Computational Methods in Fracture Mechanics

Edited by
M.H. Aliabadi and A. Cisilino

TRANS TECH PUBLICATIONS

Computational Methods in Fracture Mechanics

Edited by
M.H. Aliabadi
A. Saimoto

Computational Methods in Fracture Mechanics

Special topic volume with invited peer reviewed papers only.

Edited by

M.H. Aliabadi and A. Saimoto

TRANS TECH PUBLICATIONS LTD

Switzerland • UK • USA

Trans Tech Publications Ltd
Laubisrutistr. 24
CH-8712 Stafa-Zurich
Switzerland
http://www.ttp.net

Volume 454 of
Key Engineering Materials
ISSN 1013-9826
Full text available online at *http://www.scientific.net*

***Distributed** worldwide by*

Trans Tech Publications Ltd.
Laubisrutistr. 24
CH-8712 Stafa-Zurich
Switzerland

Fax: +41 (44) 922 10 33
e-mail: sales@ttp.net

and in the Americas by

Trans Tech Publications Inc.
PO Box 699, May Street
Enfield, NH 03748
USA

Phone: +1 (603) 632-7377
Fax: +1 (603) 632-5611
e-mail: sales-usa@ttp.net

Guest Editorial

The existence of crack-like flaws cannot be precluded in any engineering structure. At the same time, the increasing demand for energy and material conservation dictates that structures are designed with smaller safety factors. Consequently, accurate quantitative estimates of the flaw tolerance of structures are of direct concern for the prevention of fracture in load-bearing components of all kinds, ranging from space satellites and aircrafts to bone prosthesis and home appliances.

In order to sustain a reasonable cost for design and maintenance, it is generally accepted that computational analysis and simulation must partially replace full scale and laboratory testing. In general, numerical methods such as the Boundary Element Method (BEM) and the Finite Element Method (FEM) and more recently Meshless methods are used in the fracture analysis of structures, because of the complex shape and continuously changing path of the growing cracks.

This special issue of Key Engineering Materials presents nine papers that cover different aspects of the current areas of research in Fracture Mechanics using innovative and new computational approaches based on the BEM and meshless methods. A number of topics are addressed, such us dynamic and viscolastic fracture problems, crack surface contact, fatigue and cohesive crack propagation, and the analysis of cracks in composite and anisotropic bodies. There are also presented innovative formulations for fracture problems, such us Symmetric Galerkin formulations and a Local Boundary Integral Equation for the BEM and a variational element-free technique..

The editors would like to thank the contributors of papers, the reviewers and the Key Engineering Materials journal for helping put together this special issue.

Editors

Prof. M.H.Aliabadi

Department of Aeronautics

Imperial College London

UK

Prof. A Cisilino

División Soldadura y Fractomecánica - INTEMA

Facultad de Ingeniería, Universidad Nacional de Mar del Plata

Argentina

Table of Contents

Key Engineering Materials Vol. 454 (2011) pp 1-10

doi:10.4028/www.scientific.net/KEM.454.1

SGBEM for cohesive cracks in homogeneous media

Luis Távara[1,a], Vladislav Mantič[1,b], Alberto Salvadori[2,3,c], Leonard J. Gray[3,d] and Federico París[1,e]

[1]Escuela Técnica Superior de Ingenieros, Universidad de Sevilla
Camino de los Descubrimientos s/n, 41092 Sevilla, Spain

[2]Department of Civil Engineering, University of Brescia
Via Branze 38, 25123 Brescia, Italy

[3]Computer Science and Mathematics Division, Oak Ridge National Laboratory
Oak Ridge, TN 37831-6367, USA

[a]ltavara@esi.us.es, [b]mantic@esi.us.es, [c]alberto@ing.unibs.it, [d]graylj1@ornl.gov, [e]paris@esi.us.es

Keywords: Cohesive crack model, crack growth, Symmetric Galerkin Boundary Element Method, Arc-length method.

Abstract. In this paper, the Symmetric Galerkin Boundary Element Method for Linear Elastic Fracture Mechanics is extended to non-linear cohesive cracks propagating through homogeneous linear elastic isotropic media. The cohesive model adopted is based on the concept of free energy density per unit undeformed area. The corresponding constitutive cohesive equations present a softening branch which induces a potential instability. Thus, a suitable solution algorithm capable of following the growth of the cohesive zone is needed, and in the present work the numerical simulation is controlled by an arc-length method combined with a Newton-Raphson algorithm for the iterative solution of nonlinear equations. The Boundary Element Method is very attractive for modeling cohesive crack problems as all nonlinearities are located on the boundaries of linear elastic domains. Moreover a Galerkin approximation scheme, applied to a suitable symmetric boundary integral equation formulation, ensures an easy and efficient treatment of cracks in homogeneous media and an excellent convergence behavior of the numerical solution. The cohesive zone model is applied to simulate a pure mode I crack propagation in concrete. Numerical results for three-point bending test are used to check the numerical results for mode I and are compared with some numerical results obtained by FEM analysis found in the literature.

Introduction

Classical computer analysis of cracks has traditionally been based on Linear Elastic Fracture Mechanics (LEFM) assuming the presence of a crack, see [1, 2, 3] for surveys of Boundary Element Method (BEM) applications to fracture. In this LEFM approach it is difficult to study crack initiation. Furthermore LEFM is only applicable when the size of the fracture process zone at the crack tip is small compared to the size of the crack and the size of the specimen [4]. Recently, other models have been intensively developed and applied in computer crack analysis, e.g. the Cohesive Zone Models (CZMs) [5, 6, 7, 8] that assume hypotheses different from those adopted in LEFM, and avoid the presence of a stress singularity at the crack tip. The CZMs are suitable to study both crack initiation and propagation. In a cohesive crack, the propagation is governed by a traction-displacement relation across the crack faces near the tip.

In the framework of BEM [9, 10], CZM formulations have been developed by Yang and Ravi-Chandar [11] and Aliabadi and Saleh [12, 13], who implemented novel numerical procedures for cohesive crack growth by using a collocational approximation and the so-called Dual BEM. Nevertheless, the use of the Symmetric Galerkin Boundary Element Method (SGBEM) [14, 15, 16, 17, 18] for CZM implementation has several advantages in comparison with the traditional collocation

BEM [19, 20], e.g., no difficulty with smoothness requirements on displacement approximations at element junctions due to the hypersingular kernel, a consistent treatment of subdomain corners or discontinuities of boundary conditions (changing abruptly their value or kind) where traction discontinuities can take place. SGBEM provides the required number of equations and no additional equations are required as they are in the collocational BEM [9] in some cases. The SGBEM uses both the strongly singular displacement BIE and the hypersingular traction BIE in such a way that the discretizations of these BIEs lead to a symmetric linear system of algebraic equations, with positive or negative definite diagonal blocks associated to unknown tractions or displacements.

In the present work, the Ortiz - Pandolfi [7] CZM is implemented in a 2D Symmetric Galerkin BEM (SGBEM) code. The original version of this code [21] solved plane elastic problems including multi-material (piece-wise homogenous) isotropic linear-elastic solids having traction-free cracks inside the homogenous components. The materials were considered to be perfectly bonded along their interfaces. The SGBEM and the implementation details of the algorithm employed herein are discussed in [17, 18, 21]. Constitutive equations of a CZM usually include a softening branch, which induces a strong nonlinearity and potential instability. Thus, the development and implementation of a suitable solution algorithm capable of following the evolution of the cohesive zone and modeling the crack growth becomes an important issue. An arc-length control combined with a Newton-Raphson algorithm for iterative solution of nonlinear equations is used in the present work [22, 23, 24, 25].

Cohesive Zone Models

This kind of model is motivated by the fact that in some materials such as concrete, polymers, fiber-reinforced composites, tough ceramics and some alloys, the crack surfaces are usually not separated completely behind the crack tip. There exists a relatively long extension of the crack - variously called the weak zone, the bridging zone, or cohesive zone - where tractions can be transferred across the crack line. The mechanism responsible for the development of this kind of process zone can be bridging of long-chain molecules in polymers, bridging of fibers in composites, interlocking of grain boundaries in alloys and ceramics, and so on. A cohesive constitutive law is required for modeling the behavior of the material in the process zone. For these materials, the cohesive zone model of a crack seems to be the appropriate model. In a simple 2D history-independent (holonomic) CZM formulation (no friction, no plasticity, etc.) displacement discontinuities across the crack, δ_i, ($i = 1, 2$ corresponding to the normal and tangential directions to the crack respectively) are related to the traction vector, t_i, in a zone located ahead of the actual crack tip [6, 7, 8]. The constitutive law in its simplest history-independent (holonomic) version may be formally written as $\mathbf{t} = \mathbf{t}(\boldsymbol{\delta})$. A fundamental aspect in the present simple formulation of the constitutive cohesive model is the requirement that the energy dissipated at a crack propagation must be equal to the fracture energy, i.e., the following relation must be satisfied:

$$\int_0^{\delta_i^f} t_i d\delta_i = G_c \tag{1}$$

where δ_i^f is the "final" value (not necessarily finite) of the relative displacement leading to the vanishing of cohesive forces.

Ortiz-Pandolfi Model. This holonomic model is defined by three parameters $(\beta, \sigma_c, \delta_c)$. The relation between tractions and relative displacements in the cohesive zone proposed in [6, 7], requires the concept of *effective opening displacement* δ: $\delta = \sqrt{\delta_1^2 + \beta\delta_2^2}$, i.e., different weights are assigned

to the normal opening displacement (δ_1) and sliding (tangential) displacement (δ_2) through the parameter β.

Following [6, 7] the existence of a free energy density per unit undeformed area, ϕ, is postulated. Under the presence of isothermal conditions and the assumption of isotropy, it is possible to show that the cohesive law takes the form: $\boldsymbol{t} = \text{grad}_{\delta}[\phi]$ if it is assumed that the free energy ϕ depends on δ only through the effective opening displacement. This implies that:

$$\boldsymbol{t} = \text{grad}_{\delta}[\phi] = \frac{\partial \phi}{\partial \delta}\left(\frac{\delta_1}{\delta}\boldsymbol{n}_1 + \beta^2\frac{\delta_2}{\delta}\boldsymbol{n}_2\right) \tag{2}$$

where $\boldsymbol{n}_i$ is the unit vector in the i-direction. If no unloading is considered, a simple expression for the potential ϕ is furnished by the Smith and Ferrante universal binding law [7]:

$$\phi(\delta) = e\sigma_c\delta_c\left[1-\left(1+\tfrac{\delta}{\delta_c}\right)e^{-\frac{\delta}{\delta_c}}\right] \quad , \quad \tfrac{\partial\phi}{\partial\delta}(\delta) = t = e\sigma_c\tfrac{\delta}{\delta_c}e^{-\frac{\delta}{\delta_c}} \tag{3}$$

where e ≈ 2.718 is the base of the natural logarithm, σ_c is the maximum cohesive normal traction and δ_c is a characteristic opening displacement in pure fracture mode I.

Cohesive Zone Models and SGBEM

Consider a linear elastic 2D body of an arbitrary shape Ω which contains a crack. The boundary Γ of the body Ω is composed of the non-crack boundary Γ_b and the crack surface Γ_c. The crack surface Γ_c consists of two coincident surfaces Γ_c^+ and Γ_c^- which represent the upper and lower crack surfaces respectively. As explained in [19, 21] it suffices to discretize one crack surface (e.g. the upper one) as the crack surfaces are usually symmetrically loaded, verifying the equilibrium condition $\mathbf{t} = \mathbf{t}_c^+ = -\mathbf{t}_c^-$ along Γ_c. Thus, the Somigliana displacement (u-BIE) and traction (t-BIE) identities written at a point P in a smooth part of the boundary take the following form:

$$\frac{1}{2}u_k(P) = \int_{\Gamma_b}\left[U_{kj}(P,Q)t_j(Q) - T_{kj}(P,Q)u_j(Q)\right]d\Gamma Q - \int_{\Gamma_c^+}\left[T_{kj}(P,Q)w_j(Q)\right]d\Gamma Q \quad \text{on } \Gamma_u \tag{4}$$

$$\frac{1}{2}t_k(P) = \int_{\Gamma_b}\left[T^*_{kj}(P,Q)t_j(Q) - S_{kj}(P,Q)u_j(Q)\right]d\Gamma Q - \int_{\Gamma_c^+}\left[S_{kj}(P,Q)w_j(Q)\right]d\Gamma Q \quad \text{on } \Gamma_t \tag{5}$$

$$t_k(P) = \int_{\Gamma_b}\left[T^*_{kj}(P,Q)t_j(Q) - S_{kj}(P,Q)u_j(Q)\right]d\Gamma Q - \int_{\Gamma_c^+}\left[S_{kj}(P,Q)w_j(Q)\right]d\Gamma Q \quad \text{on } \Gamma_c \tag{6}$$

where $\mathbf{w} = \mathbf{u}_c^+ - \mathbf{u}_c^-$ represents relative displacement along Γ_c. U_{kj} and T_{kj} are the weakly and strongly singular kernels given by the displacement and traction fundamental solution, and T^*_{kj} and S_{kj} are the strongly singular and hypersingular corresponding derivative integral kernels. The non-crack boundary Γ_b is formed by Γ_u and Γ_t, where Γ_u is the portion of the boundary with prescribed displacements $\mathbf{u}_u$ and Γ_t is the portion of the boundary with prescribed tractions $\mathbf{t}_t$. As the primary unknowns on the crack surface are relative displacements, $\mathbf{w}$, and tractions are given in terms of $\mathbf{w}$ through the cohesive constitutive law, only t-BIE is written for points on Γ_c^+. Discretizing a weak form of Equations (4-6) in terms of rates of variables $\mathbf{u}$, $\mathbf{t}$ and $\mathbf{w}$ with respect to a "non-physical" time, associated to a load parameter λ by using a Galerkin scheme, the following linear system $[A]\{\dot{x}\} = \{\dot{b}\}$ is obtained, in block matrix form:

$$\begin{bmatrix} -\mathbf{U}_{uu} & \mathbf{T}_{ut} & \mathbf{T}_{uc} \\ \mathbf{T}^*_{tu} & -\mathbf{S}_{tt} & -\mathbf{S}_{tc} \\ \mathbf{T}^*_{cu} & -\mathbf{S}_{ct} & -\mathbf{S}_{cc}+\mathbf{K}\mathbf{M}_{cc} \end{bmatrix}\begin{Bmatrix} \dot{\mathbf{t}}_u \\ \dot{\mathbf{u}}_t \\ \dot{\mathbf{w}}_c \end{Bmatrix} = \begin{Bmatrix} -(\frac{1}{2}\mathbf{M}_{uu} + \mathbf{T}_{uu})\dot{\mathbf{u}}_u + \mathbf{U}_{ut}\dot{\mathbf{t}}_t \\ \mathbf{S}_{tu}\dot{\mathbf{u}}_u + (\frac{1}{2}\mathbf{M}_{tt} - \mathbf{T}^*_{tt})\dot{\mathbf{t}}_t \\ \mathbf{S}_{cu}\dot{\mathbf{u}}_u - \mathbf{T}^*_{ct}\dot{\mathbf{t}}_t \end{Bmatrix} \tag{7}$$

where the subscripts u, t, and c represent the terms corresponding to the non-crack boundary with prescribed displacements Γ_u, non-crack boundary with prescribed tractions Γ_t, and the crack surface

Γ_c, respectively. Thus $\mathbf{t}_u$ represents unknown tractions and $\mathbf{u}_t$ represents unknown displacements on the boundaries Γ_u and Γ_t respectively; $\mathbf{M}$ are symmetric 'mass matrixes' obtained from the free term of the integral equations.

It is important to mention that the final coefficient matrix of this system is symmetric due to the reciprocity relations of the integral kernel tensors as shown in [15, 16, 18, 26]. In [26] a similar matrix is obtained for the case of traction free cracks. The only difference is the lower right-hand diagonal block of the linear system matrix $-\mathbf{S}_{cc} + \mathbf{K}\mathbf{M}_{cc}$, where $\mathbf{K}$ is the tangent elastic stiffness matrix obtained from the cohesive law defined in a previous section. It can be shown that the product $\mathbf{K}\mathbf{M}_{cc}$ keeps the desired symmetry if $\mathbf{K}$ is symmetric, which is the case of the present cohesive law. Note that elements of $\mathbf{K}$ associated to the softening branch are negative, which implies that the block $-\mathbf{S}_{cc} + \mathbf{K}\mathbf{M}_{cc}$ may not be positive definite.

In the case of a pure traction problem ($\Gamma_u = \emptyset$) the rigid body motion in the displacement solution is removed by the use of the *Method* S introduced and studied by Vodička *et. al.* [27].

Non linear solution algorithm

The arc-length method is a powerful solution algorithm, allowing the evolution of the equilibrium states of a problem to be solved at various load levels [22, 23, 24, 25]. All these equilibrium states trace the load-displacement response of the structure in which the applied load varies proportionally as a function of a unique load parameter. In this case, for a system with n degrees of freedom (DOF), the $n + 1$ unknowns completely define the problem.

Several variants of the arc-length method, in its discrete formulation, have been proposed in the past. The one used in the present work is the normal-flow algorithm [25], where successive Newton-Raphson iterations converge to the equilibrium solution along a path which is normal (in an asymptotic sense) to the so-called Davidenko flow [25].

It should be mentioned that Risk's and Ramm's arc-length versions [22, 23] have also been implemented in the SGBEM code used. In a comparison of these three versions, the normal-flow algorithm led to a slightly faster convergence (fewer steps and/or iterations) than the other two arc-length algorithms, and for this reason it was chosen to be applied in the present work.

The solution algorithm was implemented using the full Newton-Raphson method. The prediction phase includes the determination of the arc-length step size at each increment. The first step includes the selection of an appropriate value for the arc length.

A very important issue of the procedure is to define a suitable scaling of the known and unknown variables involved in the solution of a nonlinear system of equations. The variables in the final system should have similar orders of magnitude, so as to aid the performance of the non-linear numerical solver.

Numerical Results

In order to verify the capability of the present numerical model to reproduce the cohesive zone model behavior, a three-point bending test, Fig. 1(a), for a concrete mix is modeled. The growth of a cohesive crack in such a specimen has been studied extensively in [28] using the Finite Element Method (FEM) and the node release technique for a linear cohesive law. In the present work the influence of the initial crack depth and the value of fracture energy are studied.

The dimensions of the specimen considered are height $b = 0.15m$, thickness $t = b$ and span $l = 4b$. A uniform boundary element mesh (size 0.005m) with 672 nodes and 330 quadratic elements are employed in the numerical simulation of this specimen made of a concrete-like material. The anticipated straight crack path is modeled by a mesh placed inside the single domain representing the specimen tested. The point-supports are imposed by means of the *Method* S [27]. This method

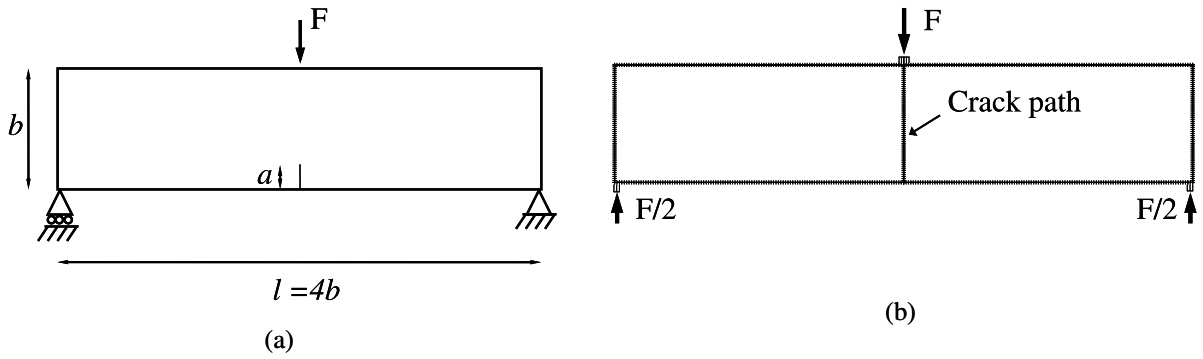

Figure 1: (a) A three-point bending specimen configuration and (b) BEM mesh used and the boundary conditions employed.

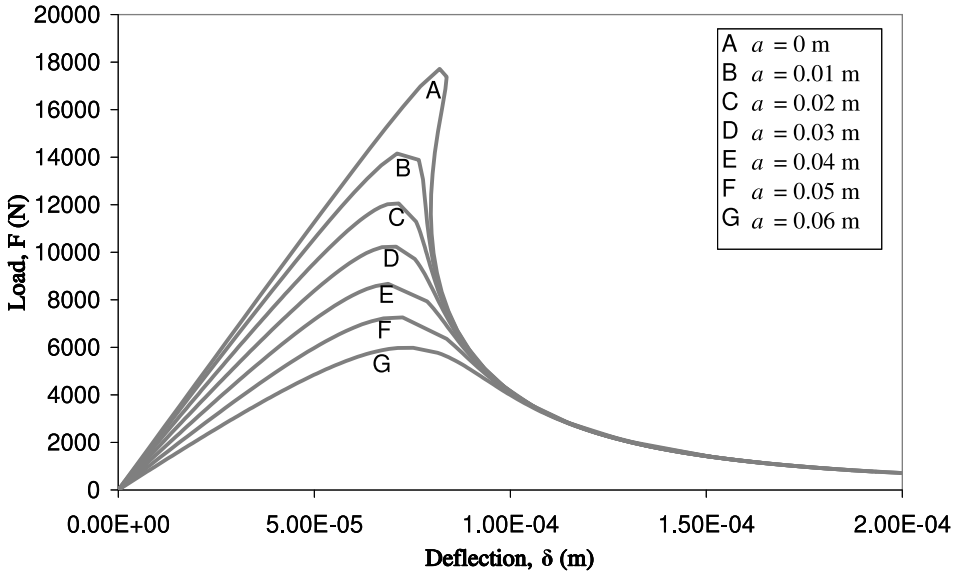

Figure 2: Load-deflection plots for different initial crack depths, a, for $G_{Ic} = 50\text{J/m}^2$.

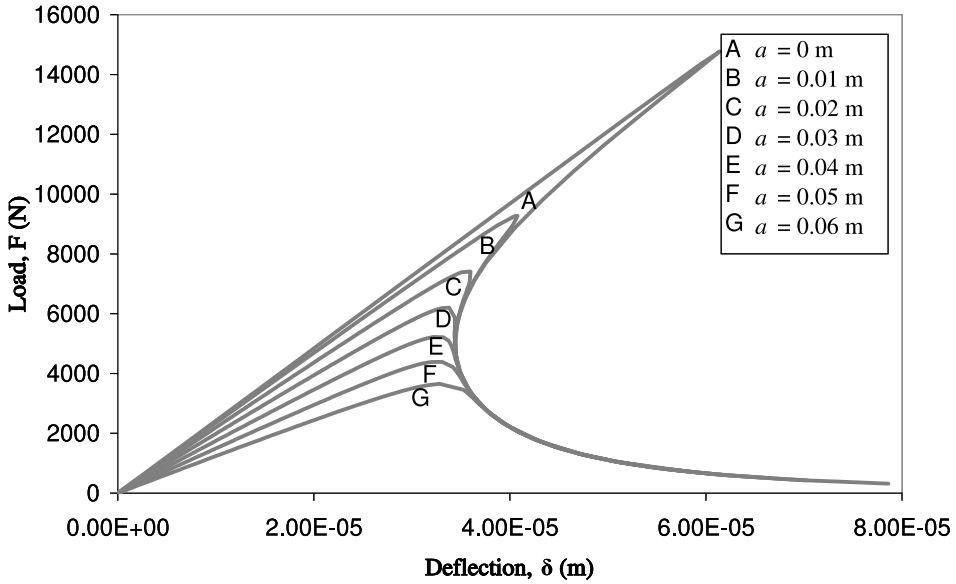

Figure 3: Load-deflection plots for several initial crack depths, a, for $G_{Ic} = 10\text{J/m}^2$.

allowed an adequate simulation of the three-point bending test, as the point-support boundary condition can be situated at a single node (similar to FEM), rather than fixing an entire element. The point supports at the two bottom corners are shown in Fig. 1(a), and as only one node is constrained at each support, rotation around these points is allowed. Constant distributions of pressures, which fulfill the condition of global equilibrium, were imposed over two elements at the centre top of the specimen and on one element at each bottom corner, Fig. 1(b). The mechanical properties of the concrete-like material are Young modulus $E = 36.5$GPa and Poisson's ratio $\nu = 0.1$. Two different values of fracture energy $G_{Ic} = 50$ and 10J/m^2 are considered. The parameter values for the Ortiz-Pandolfi model are maximum cohesive stress, $\sigma_c = 3.19$MPa, and critical opening displacement, δ_c, which has two values: $\delta_c = 5.77\text{x}10^{-6}$m and $\delta_c = 1.15\text{x}10^{-6}$m, for each of the two different values of fracture energy respectively. It is important to mention that in the present study the parameter β is irrelevant, due to the Mode I character of the problem.

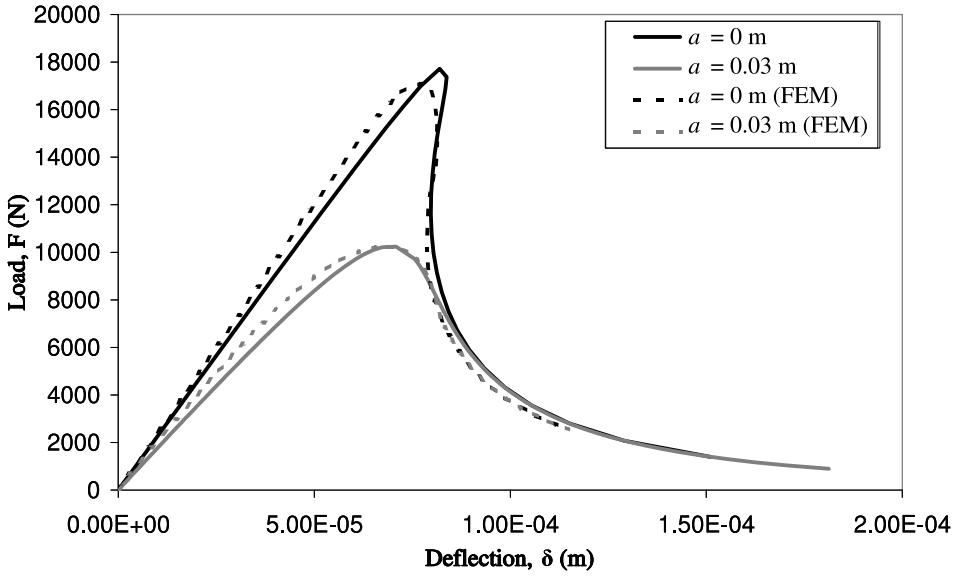

Figure 4: BEM and FEM load-deflection plots for $G_{Ic} = 50$J/m^2.

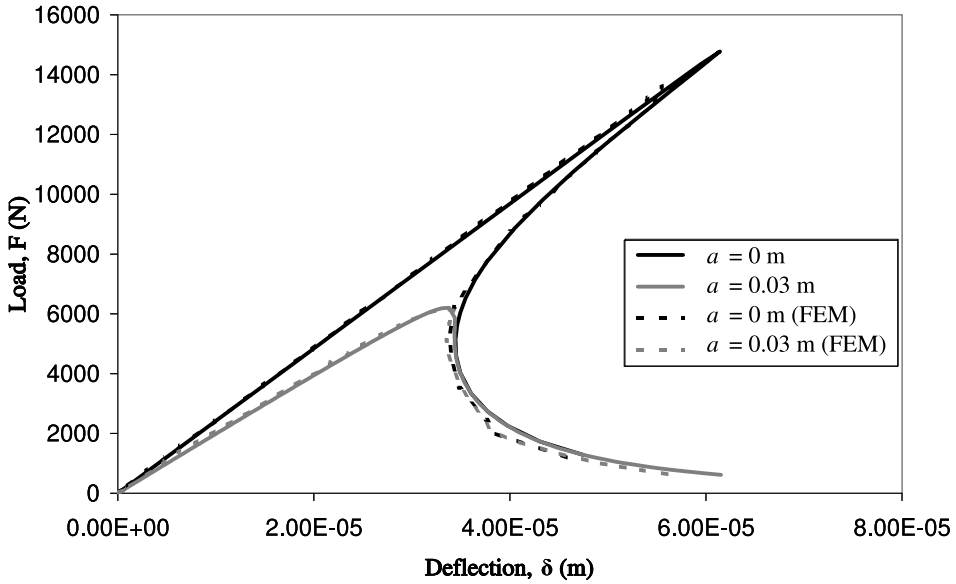

Figure 5: BEM and FEM load-deflection plots for $G_{Ic} = 10$J/m^2.

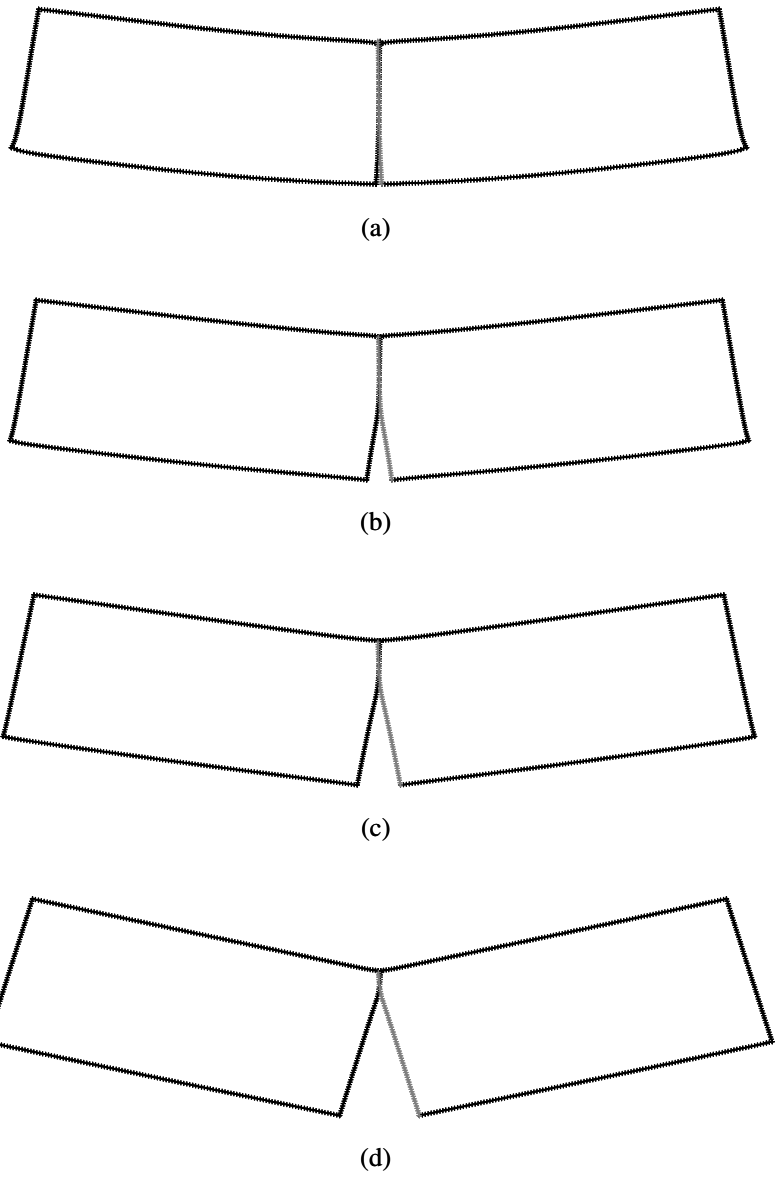

Figure 6: Deformed boundary element mesh (displacement multiplied by a factor of 500) for the initially uncracked specimen with $G_{Ic} = 50\text{J/m}^2$ for different load steps at the softening branch: (a) $F = 17718N$ (peak load), (b) $F = 9144N$, (c) $F = 4328N$ and (d) $F = 1395N$.

For each considered value of fracture energy, different initial values of crack depth, a, are considered from $a = 0$ (initially uncracked specimen) to $a = 0.06m$, with increments of $0.01m$. For all these cases considered, the load deflection (F-δ) curves are obtained. These (F-δ) curves shown in Fig. 2 for $G_{Ic} = 50\text{J/m}^2$ are related to different initial crack depths. In a similar way as in [28] initial stiffness and maximum loading capacity of the specimen decrease by increasing the initial crack depth a. Also the uncracked specimen reveals considerable instability and a nearly vertical drop in its loading capacity (a small snap-back is observed), whereas the cracked specimens appear much more "ductile". The last part of the softening branch appears as totally independent of the initial crack depth a, where all the plots superpose. The (F-δ) curves in Fig. 3 describe the specimen behavior when $G_{Ic} = 10\text{J/m}^2$. For $a \leq 0.02m$ a snap-back instability occurs, that is, a softening branch with positive slope is revealed.

Fig. 4 and Fig. 5 show a comparison between the results obtained by the SGBEM code and those

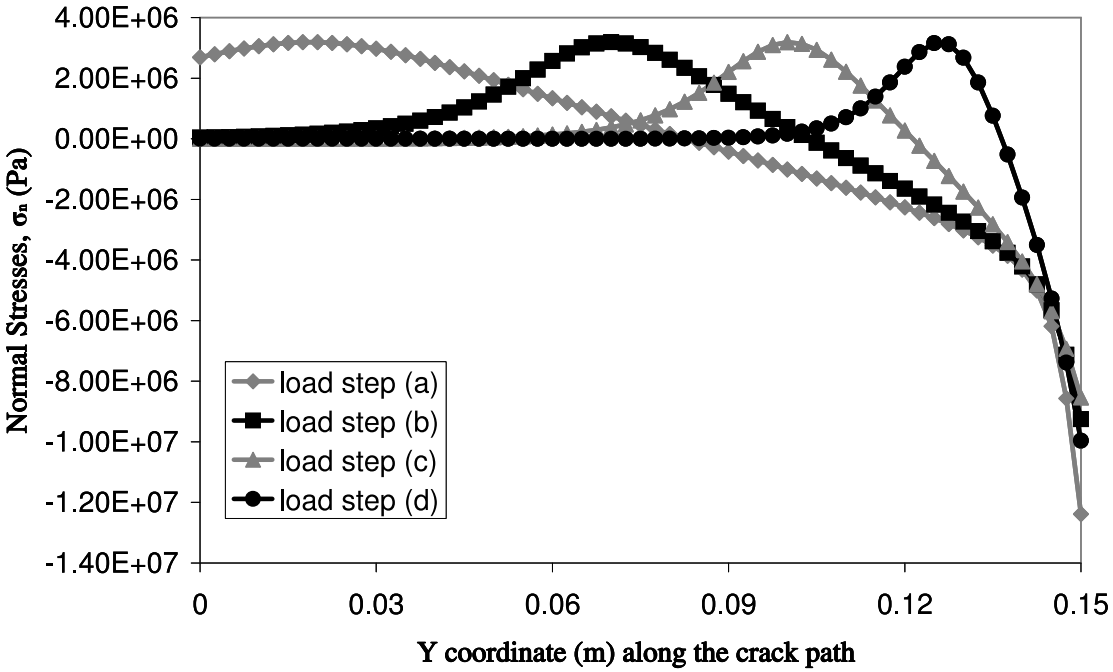

Figure 7: Normal stresses along the crack path for different load steps at the softening branch (a) $F = 17718N$ (peak load), (b) $F = 9144N$, (c) $F = 4328N$ and (d) $F = 1395N$.

obtained in Carpinteri and Colombo [28] by means of the Finite Element Method (FEM). Taking into account different cohesive laws, exponential herein and linear in [28], and different meshes, there is a very good agreement in the results. One of the reasons for the good agreement of the SGBEM and FEM results is the use of the *Method* S [27] in the SGBEM implementation to impose point-supports for the removal of rigid body motions.

Fig. 6 shows the deformed boundary element mesh of the beam at various load steps for the initially uncracked specimen with $G_{Ic} = 50\text{J/m}^2$, the crack growth being clearly observable at those stages. Notice the ticks appearing in the graphic, which represent the nodes of the SGBEM mesh. In Fig. 7 the normal stresses along the crack path for the same load steps as in Fig. 6 and same material properties are also shown. It can be observed that the expected behavior is obtained for stresses along the cohesive zone. The advancing of the so called mathematical crack tip (where the critical stress is reached) is also shown.

Conclusions

In the present work a symmetric boundary integral formulation for problems with cohesive cracks placed inside homogeneous domains has been implemented. The 2D SGBEM code used is based upon a previous implementation of crack analysis in the LEFM framework [21]. The present approach is likely to be suitable for engineering applications involving isotropic materials, e.g. for an analysis of crack initiation and growth in composites modeled as piecewise homogeneous materials at the micro-scale. The introduction of the cohesive zone requires an iterative solution procedure to solve the nonlinear equations resulting from the boundary integral formulation; the arc-length method with the normal flow procedure has been implemented.

As shown by the numerical results, the present SGBEM cohesive zone formulation agreed very well with a previous FEM crack growth analysis of the load-deflection behavior for the three-point bending test. The SGBEM analysis was capable of following the instabilities produced by a nearly vertical drop in the loading capacity and snap-back behaviors seen in some cases. Although a different cohesive law is used in [28] the SGBEM results are consistent with the results presented therein.

As can be observed by the analysis of the three point bending test, when the initial crack depth a becomes larger the specimen becomes more "ductile", and at the same time it makes the problem more stable. It is also important to mention the influence of G_{Ic}, as shown by the results. When this value is small an unstable behavior is presented, especially for small initial crack depths a.

To predict the real behavior of structures, the first step would be to determine parameters of the discrete model (σ_c and δ_c in the case of the Ortiz-Pandolfi model for Mode I), where the so-called inverse method could be very useful [29].

Acknowledgments

The work was supported by the Junta de Andalucía (Projects of Excellence TEP-1207, TEP-2045 and TEP-4051), the Spanish Ministry of Education and Science through Projects TRA2005-06764 and TRA2006-08077, and the Office of Advanced Scientific Computing Research, U.S. Department of Energy under contract DE-AC05-00OR22725 with UT-Battelle, LLC. Part of the present work was performed at the Oak Ridge National Laboratory during the research stay of L.T., V.M. and A.S., which are grateful to Dr. L.J. Gray for the opportunity of visiting and working with him. The authors thank Prof. A.-V. Phan (University of South Alabama) for the original SGBEM code employed in this work.

References

[1] Aliabadi M. H., Appl. Mech. Rev. 50 (1997), pp. 83–96.

[2] Aliabadi M. H., Int. J. Fract. 86 (1997), pp. 91–125.

[3] Cisilino A. P., Linear and Non Linear Crack Growth using Boundary Elements, Computational Mechanics Publication, WIT Press, Southampton, UK, 2000.

[4] Bažant Z.P. and Planas J., Fracture and size effect in concrete and other quasibrittle materials. CRC Press, Boca Raton, USA, 1998.

[5] Hilleborg A. Modeer M. and Petersson P.E., Cement Concrete Res. 6 (1976), pp. 773–782.

[6] Camacho G.T. and Ortiz M., Int. J. Solids Struct. 33 (1996), pp. 2899–2938.

[7] Ortiz M. and Pandolfi A., Int. J. Numer. Methods Eng. 44 (1999), pp.1267–1283.

[8] Chandra N. and Shet C., Comp. Model. Eng. Sci. 5:1 (2004), pp. 21–34.

[9] París F, Cañas J., Boundary Element Method, Fundamentals and Applications. Oxford University Press, Oxford, 1997.

[10] Aliabadi M. H., The Boundary Element Method, Vol 2 - Applications in Solids and Structures, Wiley, 2002.

[11] Yang B. and Ravi-Chandar K., Int. J. Fract. 93 (1998), pp. 115–144.

[12] Aliabadi M. H. and Saleh A.L., Eng. Fract. Mech. 69 (2002), pp. 267–280.

[13] Saleh A.L. and Aliabadi M. H., Eng. Fract. Mech. 51 (1995), pp. 533–545.

[14] Sirtori S., Meccanica, 14 (1979), pp. 210–218.

[15] Sirtori S., Maier G., Novati G. and Miccoli. S, Int. J. Numer. Meth. Eng. 35 (1992), pp. 255–282.

[16] Bonnet M., G. Maier, and C. Polizzotto, ASME Appl. Mech. Rev. 51:11 (1998), pp. 669–704.

[17] Gray L. J., In: Singular Integrals in the Boundary Element Method, edited by V. Sladek and J. Sladek, Computational Mechanics Publishers, 1998.

[18] Sutradhar A., Paulino G., Gray L., Symmetric Galerkin Boundary Element Method, Springer, 2008.

[19] Maier G., Novati G. and Cen Z., Comput. Mech. 13 (1993), pp. 74–89.

[20] Salvadori, A., Comput. Mech. 22 (2003), pp. 381–391.

[21] Phan A. V., Napier J. A. L., Gray L. J., and Kaplan T., Int. J. Numer. Methods Eng. 57:6 (2003), pp. 835–851.

[22] Crisfield M., Non-linear finite element analysis of solids and structures, Volume 1. John Wiley & Sons, 1991.

[23] Fafard M. and Massicotte B., Comput. Struct. 46 (1993), pp. 603–615.

[24] Seydel R., Practical Bifurcation And Stability Analysis - From Equilibrium to Chaos, Interdisciplinary Applied Mathematics. Springer, 1994.

[25] Ragon S.A., Grdal Z. and Watson L.T., Int. J. Solids Struct. 39 (2002), pp. 689–698.

[26] Gray L. J. and Paulino G. H., Comput. Mech. 20 (1997), pp. 26–33.

[27] Vodička R., Mantič V. and París F. Eng. Anal. Bound. Elem. 30 (2006), pp. 790–798.

[28] Carpinteri A. and Colombo G., Comput. Struct. 31 (1989), pp. 607–636.

[29] Bolzon G., Fedele R. and Maier G., Comput. Methods Appl. Mech. Engrg. 191 (2002), pp. 2847–2871.

Key Engineering Materials Vol. 454 (2011) pp 11-29

doi:10.4028/www.scientific.net/KEM.454.11

On the solution of the 3D crack surface contact problem using the boundary element method

Wilhelm Weber[a], Karsten Kolk[b], Kai Willner[c], Günther Kuhn[d]

Chair of Applied Mechanics, University of Erlangen-Nuremberg, Erlangen, Germany

[a]wilhelm.weber@ltm.uni-erlangen.de, [b]karsten.kolk@ltm.uni-erlangen.de,
[c]kai.willner@ltm.uni-erlangen.de, [d]guenther.kuhn@ltm.uni-erlangen.de

Keywords: dual boundary element method, dual discontinuity method, crack surface contact, fatigue crack propagation

Abstract. The efficient solution of the 3D crack surface contact problem utilizing the boundary element method (BEM) is presented. The dual discontinuity method (DDM), a special formulation of the BEM, is applied. This method deals directly with the relative displacements and the discontinuities of the tractions at the crack. For the normal behavior a unilateral contact is assumed and for the description of the tangential behavior Coulomb's frictional law is utilized. The hard contact formulation is regularized by the application of the penalty method. An incremental iterative procedure based on a radial return mapping algorithm is applied for the solution of this non-linear problem. Based on the stress field the fracture mechanical parameters are determined by an extrapolation method for all increments of a characteristic load cycle. By the analysis of this load cycle the cyclic fracture mechanics values are obtained. Due to the non-linear nature of crack growth the simulation is implemented in the framework of a predictor-corrector scheme. For the investigation of the influence of the crack surface roughness on the behavior of cracks two numerical examples are presented.

Introduction

The assessment of the structural integrity of components includes a fracture mechanical analysis. Therefore, an efficient numerical tool for the stress analysis in the framework of the simulation of three dimensional crack growth is required. Due to the non-linear behavior of crack growth an incremental procedure is necessary, cf. Fig. 1. Each incremental loop starts with the stress analysis of the current crack configuration including the calculation of the fracture mechanical parameters. Next, the 3D crack growth criterion based on linear-elastic fracture mechanics is evaluated for the determination of the new position of the crack front. Finally, the mesh of the numerical model is adapted in order to consider the new crack geometry in the next increment.

Due to its nature the boundary element method (BEM) in terms of the dual BEM [1, 2] is especially suited for stress concentration problems. Here, a special formulation for cracked structures of the BEM – the dual discontinuity method (DDM) [3, 4, 5, 6] – is utilized. This method offers two advantages. On the one hand, the numerical complexity is reduced. On the other hand, crack surface interaction can be easily considered by this method. Since the crack growth criterion is mainly based on the fracture mechanical parameters these values are determined from the stress field in front of the crack front by an optimized extrapolation method [6, 7].

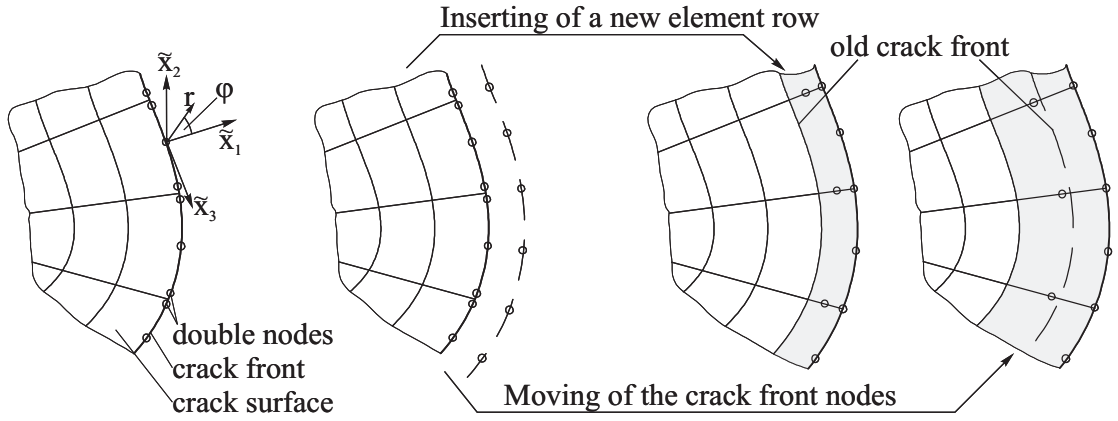

a) Calculation of the fracture mechanical parameters b) Generation of the new crack front c) Update of the discretization

Fig. 1: Three steps of an increment.

The 3D crack growth criterion is evaluated for the determination of the new crack front geometry. Since the crack surface interaction causes non-proportional mixed mode, a complete characteristic load cycle has to be evaluated for the calculation of the cyclic stress intensity factors (SIFs). For the crack propagation it has to be distinguished between the tensile mode crack growth and the shear mode growth. In this paper it is assumed that the crack grows in the tensile mode. If only the state of stress of the current crack geometry is taken into account, a linear prediction of the new crack front is obtained. In order to consider the changing stress field between two discrete crack fronts corrector steps are required. This leads directly to an implicit time integration scheme, which yields additionally an optimization of the new crack front with respect to its shape and location [8].

Finally, the numerical model has to be updated with respect to the new crack geometry. Since the BEM is utilized this task is less complicated compared to volume orientated methods, see Fig. 1c. In case of a predictor step large crack extensions along the whole crack front are present. Therefore, a new row of elements is inserted to close the gap between the old and the new crack front. Otherwise, only small changes of the crack front occur during the correction. Here, the nodes of the crack front are simply moved towards their new position. For surface breaking cracks the discretization of the outer boundary around the surface breaking points has to be modified. It is done by a local re-meshing procedure [7] using a direct paving algorithm [9].

The interaction of the crack surfaces causes a non-linear reaction of the structure on the applied load. In order to consider this behavior an incremental procedure has to be applied within the stress analysis. In principle, the state of contact is not a-priori known and has to be iteratively determined within each increment. For an efficient determination of the state of contact the hard contact formulations have to be softened. In this paper the well-known penalty method is utilized. Within this method the contact tractions are defined via a constitutive law with respect to penetrations of the hard contact formulation. Therewith, the frictional contact problem is solved by a radial return mapping scheme [10, 11, 12].

First solutions of the contact problem with the BEM trace back to Andersson et al. [13]. Later numerous investigations e.g. [14] have been carried out including the application of the penalty method [15]. The contact of the crack surfaces has been considered in [16], in which the crack is modeled via domain decomposition. Lee [17] is utilizing the dual BEM in terms

of the basic formulation. 2D cracks in unbounded domains have been analyzed by Phan [18] using the symmetric-Galerkin boundary element method (SGBEM). Here, the crack surfaces are separated by the introduction of the discontinuities of the displacements and of the tractions. Furthermore, the crack surface interaction has been taken into account. Due to the two-dimensional point of view no softening of the contact conditions is required.

3D dual boundary element method

The boundary value problem is solved by the 3D dual boundary element method (BEM). Within this method the coincident crack surfaces are separated by the utilization of the displacement and the traction boundary integral equation. Here, a special formulation namely the dual discontinuity method (DDM) is applied. It provides advantages with respect to the numerical complexity and deals directly with the relative displacements of the crack surfaces.

Due to the time dependency of the contact problem the basic equations are written in the rate formulation. The dots on the values denote the time derivatives. In the present case of a time independent formulation these values become rather incremental values.

Description of the boundary value problem. For the description of the boundary value problem (BVP) an arbitrary domain $\Omega \in \mathbb{R}^3$ containing a crack is investigated, see Fig. 2. The domain Ω is bounded by the surface Γ. The whole surface Γ consists of the normal boundary Γ^n and the coincident crack surfaces Γ^c and $\Gamma^{\bar{c}}$. The normal vector $\boldsymbol{n}$ is orientated outwards. Assuming a homogeneous and isotropic material behavior with linear elastic properties

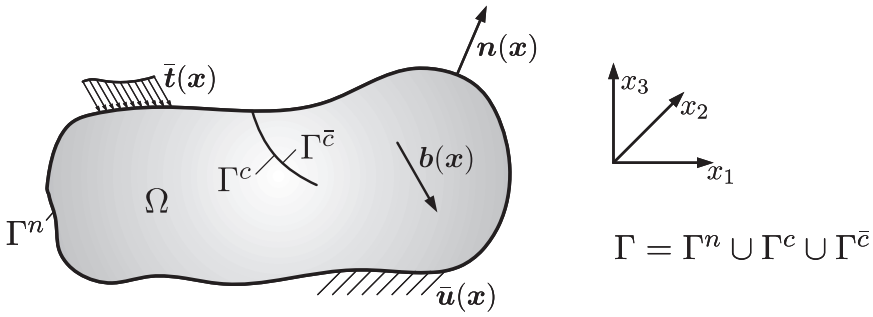

Fig. 2: Sketch of the 3D boundary value problem.

the boundary value problem is described by the Lamé-Navier equation

$$\dot{u}_{i,jj}(\boldsymbol{x}) + \frac{1}{1-2\nu}\,\dot{u}_{j,ji}(\boldsymbol{x}) + \frac{1}{G}\,\dot{b}_i(\boldsymbol{x}) = 0 \tag{1}$$

as well as by prescribed Neumann boundary conditions ($\dot{\bar{\boldsymbol{t}}}(\boldsymbol{x})$) on Γ^N and Dirichlet boundary conditions ($\dot{\bar{\boldsymbol{u}}}(\boldsymbol{x})$) on Γ^D. Between Γ^N and Γ^D the conditions $\Gamma = \Gamma^N \cup \Gamma^D$ and $\Gamma^N \cap \Gamma^D = \emptyset$ are fulfilled. The corresponding tractions are defined by the Cauchy formula

$$\dot{t}_i(\boldsymbol{x}) = \dot{\sigma}_{ij}(\boldsymbol{x}) n_j(\boldsymbol{x}), \quad \boldsymbol{x} \in \Gamma. \tag{2}$$

Without loss of generality, body forces $\dot{b}_i(\boldsymbol{x})$ are neglected in the present paper.

Boundary integral equations. Using the method of weighted residuals for the Lamé-Navier equation (1) the Somigliana equation is obtained after integration by parts twice and the choice of a fundamental solution as weighting function. The strongly singular displacement BIE results from moving the source point $\boldsymbol{\xi}$ on the boundary. It reads

$$c_{ij}(\boldsymbol{\xi})\,\dot{u}_j(\boldsymbol{\xi}) = \int_\Gamma U_{ij}(\boldsymbol{\xi},\boldsymbol{x})\,\dot{t}_j(\boldsymbol{x})\,\mathrm{d}\Gamma(\boldsymbol{x}) - \fint_\Gamma T_{ij}(\boldsymbol{\xi},\boldsymbol{x})\,\dot{u}_j(\boldsymbol{x})\,\mathrm{d}\Gamma(\boldsymbol{x}) \tag{3}$$

for source points on the normal boundary ($\boldsymbol{\xi} \in \Gamma^n$). The free term c_{ij} depends on the geometry at the source point and it is defined as $\frac{1}{2}\delta_{ij}$ for smooth boundaries. U_{ij} and T_{ij} denote the known Kelvin fundamental solutions.

For source points on a smooth crack surface ($\boldsymbol{\xi} \in \Gamma^c \cup \Gamma^{\bar{c}}$) the displacement BIE is written as

$$\frac{1}{2}\,\dot{u}_i^c(\boldsymbol{\xi}) + \frac{1}{2}\,\dot{u}_i^{\bar{c}}(\boldsymbol{\xi}) = \int_\Gamma U_{ij}(\boldsymbol{\xi},\boldsymbol{x})\,\dot{t}_j(\boldsymbol{x})\,\mathrm{d}\Gamma(\boldsymbol{x}) - \fint_\Gamma T_{ij}(\boldsymbol{\xi},\boldsymbol{x})\,\dot{u}_j(\boldsymbol{x})\,\mathrm{d}\Gamma(\boldsymbol{x}), \tag{4}$$

in which $\dot{u}_i^c(\boldsymbol{\xi})$ denotes the displacement rate of the geometric point $\boldsymbol{\xi}$ at the crack surface Γ^c and $\dot{u}_i^{\bar{c}}(\boldsymbol{\xi})$ denotes the displacement rate of the same point at the opposite crack surface $\Gamma^{\bar{c}}$. Therefore, it can not be distinguished between the coincident crack surfaces.

To overcome this problem, the corresponding hypersingular traction BIE is additionally taken into account within the concept of the dual integral formulations [1, 2]. It reads

$$\frac{1}{2}\,\dot{t}_i^c(\boldsymbol{\xi}) - \frac{1}{2}\,\dot{t}_i^{\bar{c}}(\boldsymbol{\xi}) = \fint_\Gamma D_{ij}(\boldsymbol{\xi},\boldsymbol{x})\,\dot{t}_j(\boldsymbol{x})\,\mathrm{d}\Gamma(\boldsymbol{x}) - \fint_\Gamma S_{ij}(\boldsymbol{\xi},\boldsymbol{x})\,\dot{u}_j(\boldsymbol{x})\,\mathrm{d}\Gamma(\boldsymbol{x}) \tag{5}$$

for source points on a smooth crack. The kernels D_{ij} and S_{ij} are the derivatives of the Kelvin fundamental solutions with respect to $\boldsymbol{\xi}$ multiplied by the elastic tensor and the normal vector at the source point, which are called Gebbia solutions [19, 20].

Dual discontinuity method. A special technique for crack problems within the concept of the dual integral formulations is the dual discontinuity method (DDM).

This method utilizes the symmetric properties of the fundamental solutions for the integration point $\boldsymbol{x}$ at the crack:

$$U_{ij}^c(\boldsymbol{\xi},\boldsymbol{x}) = U_{ij}^{\bar{c}}(\boldsymbol{\xi},\boldsymbol{x}) \quad , \quad T_{ij}^c(\boldsymbol{\xi},\boldsymbol{x}) = -T_{ij}^{\bar{c}}(\boldsymbol{\xi},\boldsymbol{x}), \tag{6}$$

$$Dij^c(\boldsymbol{\xi},\boldsymbol{x}) = D_{ij}^{\bar{c}}(\boldsymbol{\xi},\boldsymbol{x}) \quad , \quad S_{ij}^c(\boldsymbol{\xi},\boldsymbol{x}) = -S_{ij}^{\bar{c}}(\boldsymbol{\xi},\boldsymbol{x}). \tag{7}$$

Moreover, the special geometric situation of the crack surfaces is considered. The crack surfaces describe the same geometric surface with reversed normal vectors. By the introduction of the discontinuities of the displacements

$$\dot{\hat{u}}_i^c(\boldsymbol{x}) = \dot{u}_i^c(\boldsymbol{x}) - \dot{u}_i^{\bar{c}}(\boldsymbol{x}) \tag{8}$$

and the tractions

$$\dot{\hat{t}}_i^c(\boldsymbol{x}) = n_j^c(\boldsymbol{x})\left(\sigma_{ij}^c(\boldsymbol{x}) - \sigma_{ij}^{\bar{c}}(\boldsymbol{x})\right) = \dot{t}_i^c(\boldsymbol{x}) + \dot{t}_i^{\bar{c}}(\boldsymbol{x}) \tag{9}$$

with respect to Γ^c as new variables at the crack one crack surface e.g. $\Gamma^{\bar{c}}$ is substituted by the other one. Therewith, the displacement BIE reads as

$$c_{ij}(\boldsymbol{\xi})\,\dot{u}_j^n(\boldsymbol{\xi}) = \int_{\Gamma^n} U_{ij}(\boldsymbol{\xi},\boldsymbol{x})\,\dot{t}_j^n(\boldsymbol{x})\,\mathrm{d}\Gamma(\boldsymbol{x}) + \int_{\Gamma^c} U_{ij}(\boldsymbol{\xi},\boldsymbol{x})\,\dot{\hat{t}}_j^c(\boldsymbol{x})\,\mathrm{d}\Gamma(\boldsymbol{x}) - \int_{\Gamma^n} T_{ij}(\boldsymbol{\xi},\boldsymbol{x})\,\dot{u}_j^n(\boldsymbol{x})\,\mathrm{d}\Gamma(\boldsymbol{x}) - \int_{\Gamma^c} T_{ij}(\boldsymbol{\xi},\boldsymbol{x})\,\dot{\hat{u}}_j^c(\boldsymbol{x})\,\mathrm{d}\Gamma(\boldsymbol{x}) \tag{10}$$

for source points on the normal boundary and

$$\dot{u}_j^c(\boldsymbol{\xi}) = \frac{1}{2}\dot{\hat{u}}_j^c(\boldsymbol{\xi}) + \int_{\Gamma^n} U_{ij}(\boldsymbol{\xi},\boldsymbol{x})\,\dot{t}_j^n(\boldsymbol{x})\,\mathrm{d}\Gamma(\boldsymbol{x}) + \int_{\Gamma^c} U_{ij}(\boldsymbol{\xi},\boldsymbol{x})\,\dot{\hat{t}}_j^c(\boldsymbol{x})\,\mathrm{d}\Gamma(\boldsymbol{x}) - \int_{\Gamma^n} T_{ij}(\boldsymbol{\xi},\boldsymbol{x})\,\dot{u}_j^n(\boldsymbol{x})\,\mathrm{d}\Gamma(\boldsymbol{x}) - \int_{\Gamma^c} T_{ij}(\boldsymbol{\xi},\boldsymbol{x})\,\dot{\hat{u}}_j^c(\boldsymbol{x})\,\mathrm{d}\Gamma(\boldsymbol{x}) \tag{11}$$

for source points on the crack. The traction BIE is now written as

$$\dot{t}_j^c(\boldsymbol{\xi}) = \frac{1}{2}\dot{\hat{t}}_j^c(\boldsymbol{\xi}) + \int_{\Gamma^n} D_{ij}(\boldsymbol{\xi},\boldsymbol{x})\,\dot{t}_j^n(\boldsymbol{x})\,\mathrm{d}\Gamma(\boldsymbol{x}) + \int_{\Gamma^c} D_{ij}(\boldsymbol{\xi},\boldsymbol{x})\,\dot{\hat{t}}_j^c(\boldsymbol{x})\,\mathrm{d}\Gamma(\boldsymbol{x}) - \int_{\Gamma^n} S_{ij}(\boldsymbol{\xi},\boldsymbol{x})\,\dot{u}_j^n(\boldsymbol{x})\,\mathrm{d}\Gamma(\boldsymbol{x}) - \int_{\Gamma^c} S_{ij}(\boldsymbol{\xi},\boldsymbol{x})\,\dot{\hat{u}}_j^c(\boldsymbol{x})\,\mathrm{d}\Gamma(\boldsymbol{x}). \tag{12}$$

In all BIEs the integration is reduced by one crack surface, here $\Gamma^{\bar{c}}$.

Numerical solution. For the application of the BEM only the surface is discretized by boundary elements. The normal surface is meshed with continuous elements. For the evaluation of the hypersingular traction BIE (12) $\mathcal{C}^{0,\alpha}$-continuity for the tractions and $\mathcal{C}^{1,\alpha}$-continuity for the displacements are required and a smooth boundary is assumed [21]. Therefore, discontinuous elements are utilized at the crack. In case of surface breaking cracks, the transition to the crack surface is meshed with edge- and node-discontinuous elements.

The relevant BIEs are evaluated within the framework of a collocation procedure. Relevant in this context means that the displacement BIE (10) is applied for source points at the outer boundary. If Dirichlet boundary conditions are prescribed at the source point on both crack surfaces, the displacement BIE (11) is evaluated. Otherwise, the traction BIE (12) is applied. After a rearrangement according to the boundary conditions the linear system of equations

$$\begin{bmatrix} \boldsymbol{A}^{nn} & \boldsymbol{A}^{nc} & \boldsymbol{0} \\ \boldsymbol{A}^{cn} & \boldsymbol{A}^{cc} & \boldsymbol{0} \\ \tilde{\boldsymbol{A}}^{cn} & \tilde{\boldsymbol{A}}^{cc} & \boldsymbol{Id} \end{bmatrix} \begin{bmatrix} \dot{\boldsymbol{x}}^n \\ \dot{\hat{\boldsymbol{x}}}^c \\ \dot{\boldsymbol{x}}^c \end{bmatrix} = \begin{bmatrix} \dot{\boldsymbol{b}}^n \\ \dot{\boldsymbol{b}}^c \\ \dot{\tilde{\boldsymbol{b}}}^c \end{bmatrix} \tag{13}$$

is obtained [4, 5, 6]. The third part of the equations in (13) results from the evaluation of the remaining BIE for the source points at the crack. Here, $\boldsymbol{Id}$ denotes the identity matrix. The vector $\dot{\boldsymbol{x}}$ contains all unknown boundary values of the normal boundary $\dot{\boldsymbol{x}}^n$ and the unknown discontinuities at the crack $\dot{\hat{\boldsymbol{x}}}^c$ respectively the unknown boundary values $\dot{\boldsymbol{x}}^c$ at Γ^c. Obviously, only the reduced system of equations

$$\begin{bmatrix} \boldsymbol{A}^{nn} & \boldsymbol{A}^{nc} \\ \boldsymbol{A}^{cn} & \boldsymbol{A}^{cc} \end{bmatrix} \begin{bmatrix} \dot{\boldsymbol{x}}^n \\ \dot{\hat{\boldsymbol{x}}}^c \end{bmatrix} = \begin{bmatrix} \dot{\boldsymbol{b}}^n \\ \dot{\boldsymbol{b}}^c \end{bmatrix} \tag{14}$$

has to be solved. Here, the iterative GMRES algorithm [22] is applied. The remaining unknowns are directly calculated in a post processing step via

$$\dot{\boldsymbol{x}}^c = \dot{\boldsymbol{b}}^c - \tilde{\boldsymbol{A}}^{cn}\dot{\boldsymbol{x}}^n - \tilde{\boldsymbol{A}}^{cc}\dot{\hat{\boldsymbol{x}}}^c \tag{15}$$

to have all field quantities available e.g. for the visualization.

Due to the utilization of the discontinuous formulation the integration procedure is reduced by one crack surface. Moreover, the number of degrees of freedom (DOFs) of the linear system of equations is decreased by the number of DOFs of one crack surface.

Crack surface interaction

Since the BEM in terms of the DDM deals directly with the relative displacements (displacement discontinuities) and the discontinuities of the tractions, it is especially suited for the consideration of interaction effects of the crack surfaces. For the treatment of the contact problem it has to be distinguished between the behavior in the normal and the tangential direction. Therefore, the boundary values are defined with respect to a local orthogonal cartesian coordinate system (n, t_1, t_2) at the collocation points that is orientated in the normal n and tangential t_j directions. Possible parts of the crack surface that might get in contact belong to the Neumann boundary. Here, the total tractions are composed of the prescribed and the contact tractions ($\boldsymbol{t} = \bar{\boldsymbol{t}} + \boldsymbol{t}^{contact}$), which can be treated separately. Without loss of generality it is assumed that the crack surfaces belong to the Neumann boundary and no initial tractions are prescribed ($\bar{\boldsymbol{t}} = 0 \Rightarrow \boldsymbol{t} = \boldsymbol{t}^{contact}$).

For the collocation points at the crack surfaces three states of contact have to be distinguished. The crack could be opened or the crack surfaces can be in stick or slip mode.

Frictional contact. For the behavior of the crack surfaces in the normal direction a unilateral contact is assumed. Therefore, the crack surfaces can not penetrate each other and the gap g must fulfill the condition

$$g \geq 0. \tag{16}$$

Due to the definition of the displacement discontinuities (8) condition (16) is written as

$$\hat{u}_n^c \leq 0 \tag{17}$$

for the normal displacement discontinuity $\hat{u}_n^c$. Furthermore, only compressive tractions in the normal direction are possible

$$t_n^c \leq 0. \tag{18}$$

The behavior in the tangential direction is described by a frictional law. In the present context Coulombs frictional law is applied. Within this criterion the effective tangential traction $t_t^c = \sqrt{(t_{t_1}^c)^2 + (t_{t_2}^c)^2}$ is limited with respect to the compressive normal traction $t_n^c \leq 0$ and the frictional coefficient μ:

$$t_t^c \leq -\mu\, t_n^c = t_{\max}^c. \tag{19}$$

In case of stick t_t^c is smaller than $t_{\max}^c = -\mu\, t_n^c$. Otherwise, in case of slip t_t^c is equal to $t_{\max}^c$ and the direction of the tangential traction is opposite to the relative sliding direction $\dot{\hat{u}}_{t_i}^c$ such that energy is dissipated:

$$\dot{\hat{u}}_{t_i}^c\, t_{t_i}^c \leq 0. \tag{20}$$

Boundary integral equations for crack surface contact. As a result of the crack surface interaction contact tractions in normal and tangential direction have to be considered. Due to the principle of action and reaction the contact tractions are equal according to their amount but with opposite sign (equilibrium condition). Therewith, the discontinuities of the contact tractions vanish:

$$\hat{t}_i^c(\boldsymbol{x}) = 0 \quad \text{respectively} \quad \dot{\hat{t}}_i^c(\boldsymbol{x}) = 0. \tag{21}$$

By the consideration of this condition within the BIEs (10) - (12) the integrals concerning the traction discontinuities vanish similarly

$$\int_{\Gamma^c} U_{ij}(\boldsymbol{\xi}, \boldsymbol{x})\, \dot{\hat{t}}_j^c(\boldsymbol{x})\, \mathrm{d}\Gamma(\boldsymbol{x}) = 0, \quad \barint_{\Gamma^c} D_{ij}(\boldsymbol{\xi}, \boldsymbol{x})\, \dot{\hat{t}}_j^c(\boldsymbol{x})\, \mathrm{d}\Gamma(\boldsymbol{x}) = 0. \tag{22}$$

Therefore, the effort for the integration is reduced further. Moreover, the contact tractions remain only in the traction BIE (12) in an integral free way. In case of stick these tractions can be directly calculated in a postprocessing step. In the slip mode the tangential tractions are known from the frictional law.

It has to be mentioned that prescribed tractions $\bar{\boldsymbol{t}}$ generally do not lead to vanishing traction discontinuities. In this case the integrals (22) have to be evaluated with respect to the applied traction discontinuities.

Penalty method. For an efficient determination of the state of contact during the simulation the hard contact formulation is soften in terms of the penalty method. By the consideration of equation (17) a linear constitutive law given by

$$t_n(\hat{u}_n^c) = \begin{cases} 0 & \text{if} \quad \hat{u}_n^c \leq 0 \\ -\epsilon_n\, \hat{u}_n^c & \text{if} \quad \hat{u}_n^c > 0 \end{cases} \tag{23}$$

with a constant normal contact stiffness ϵ_n is assumed for the normal contact. In case of contact – stick or slip – the total tangential relative displacements are composed by a reversible elastic part $\hat{u}_{t_i}^{c,el}$ and the slip $\hat{u}_{t_i}^{c,sl}$:

$$\hat{u}_{t_i}^c = \hat{u}_{t_i}^{c,el} + \hat{u}_{t_i}^{c,sl}. \tag{24}$$

Between the reversible displacements and tangential tractions also a linear constitutive law with the constant tangential contact stiffness ϵ_t is assumed:

$$t_{t_i}(\hat{u}_{t_i}^c) = -\epsilon_t\, \hat{u}_{t_i}^{c,el}. \tag{25}$$

This softening of the hard contact conditions can be physically interpreted as a deformation of the surface roughness [23].

Within the traction BIE (12) the total time derivative of the traction vector is required. These values are determined by a linearization of the constitutive equations (23) and (25) under consideration of the frictional law (19) written as

$$\begin{bmatrix} \dot{t}_n \\ \dot{t}_{t_1} \\ \dot{t}_{t_2} \end{bmatrix} = \underbrace{\begin{bmatrix} \frac{\partial t_n}{\partial \hat{u}_n} & \frac{\partial t_n}{\partial \hat{u}_{t_1}} & \frac{\partial t_n}{\partial \hat{u}_{t_2}} \\ \frac{\partial t_{t_1}}{\partial \hat{u}_n} & \frac{\partial t_{t_1}}{\partial \hat{u}_{t_1}} & \frac{\partial t_{t_1}}{\partial \hat{u}_{t_2}} \\ \frac{\partial t_{t_2}}{\partial \hat{u}_n} & \frac{\partial t_{t_2}}{\partial \hat{u}_{t_1}} & \frac{\partial t_{t_2}}{\partial \hat{u}_{t_2}} \end{bmatrix}}_{=\boldsymbol{C}} \begin{bmatrix} \dot{\hat{u}}_n \\ \dot{\hat{u}}_{t_1} \\ \dot{\hat{u}}_{t_2} \end{bmatrix}. \tag{26}$$

The matrix C depends on the state of contact and it is determined during the solution procedure. If the open case is present $\boldsymbol{C}$ becomes zero, $\frac{\partial t_i}{\partial \hat{u}_j} = 0$.

Solution of the contact problem. Due to the non-linear behavior of the contact problem a time integration of the rate formulation in terms of an incremental iterative procedure has to be applied. Therefore, the rate values marked by a dot become incremental values $\Delta \boldsymbol{u}$, $\Delta \boldsymbol{t}$. Along this, the linear system of equations (14) is written as

$$\boldsymbol{A}^i \, \Delta \boldsymbol{x}^i = \Delta \boldsymbol{b}^i. \tag{27}$$

The incremental system matrix $\boldsymbol{A}^i$ of the increment i is not constant during the simulation. It depends on the state of contact of the collocation points at the crack, which has to be iteratively determined within each increment. If the state of contact is not found within a maximum number of iterations, the increment is equally split into two sub increments which are successively treated. This procedure is recursively applied until the state of contact is found.

The total boundary values of the increment i are calculated by the accumulation of the incremental values

$$\boldsymbol{u}^i = \boldsymbol{u}^{i-1} + \Delta \boldsymbol{u}^i \quad \text{respectively} \quad \boldsymbol{t}^i = \boldsymbol{t}^{i-1} + \Delta \boldsymbol{t}^i. \tag{28}$$

A radial return mapping scheme is utilized for the solution of the frictional contact problem. Since the normal traction do not depend on the tangential displacements the linearization of equation (23) reads as

$$\frac{\partial t_n}{\partial \hat{u}_n} = -\epsilon_n, \tag{29}$$

$$\frac{\partial t_n}{\partial \hat{u}_{t_j}} = 0. \tag{30}$$

Under the assumption of sticking a trial state of the tangential contact tractions considering equation (25) is calculated by

$$\tilde{t}^i_{t_j}(\hat{u}_{t_j}) = t^{i-1}_{t_j} - \epsilon_t \, \Delta \hat{u}^i_{t_j}. \tag{31}$$

The values $t^{i-1}_{t_i}$ are known from the last increment and $\Delta \hat{u}^i_{t_i}$ are calculated in the current incremental loop. After the determination of the absolute value of the tangential trial stresses $\tilde{t}^i_t = \|\tilde{t}^i_{t_j}\|$, the frictional law (19) is evaluated. In case of stick the trial state is correct and it is accepted

$$t^i_{t_j} = \tilde{t}^i_{t_j}(\hat{u}_{t_j}). \tag{32}$$

The linearization of the stick mode with respect to the tangential slip is written as

$$\frac{\partial t_{t_j}}{\partial \hat{u}_{t_k}} = -\epsilon_t \, \delta_{jk}. \tag{33}$$

Since the trial state does not depend on the normal relative displacement the corresponding partial derivatives vanish:

$$\frac{\partial t_{t_j}}{\partial \hat{u}_n} = 0. \tag{34}$$

Otherwise, if the frictional law (19) is violated with respect to the trial state, the tangential tractions are defined via

$$t^i_{t_j} = \mu t^i_n \frac{\tilde{t}^i_{t_j}}{\|\tilde{t}_{t_j}\|}. \tag{35}$$

Since the normal traction $t_n^i(\hat{u}_n)$ and the trial state $\tilde{t}_{t_j}^i(\hat{u}_{t_j})$ are depending on the relative displacements $\hat{\boldsymbol{u}}$ the linearization reads as

$$\frac{\partial t_{t_j}^i}{\partial \hat{u}_k} = \frac{\partial(\mu t_n^i)}{\partial \hat{u}_k} \frac{\tilde{t}_{t_j}^i}{\|\tilde{t}_{t_j}\|} + \mu t_n^i \frac{\partial}{\partial \hat{u}_k} \left(\frac{\tilde{t}_{t_j}^i}{\|\tilde{t}_{t_j}\|} \right) \tag{36}$$

The first part leads to the partial derivatives [10]

$$\frac{\partial t_{t_j}^i}{\partial \hat{u}_n^i} = \mu \, \epsilon_n \, \frac{\tilde{t}_{t_j}^i}{\|\tilde{t}_{t_j}\|} \tag{37}$$

and the second part to [10]

$$\frac{\partial t_{t_j}^i}{\partial \hat{u}_{t_k}^i} = \epsilon_t \frac{\mu \, t_n}{\|\tilde{t}_{t_j}\|} \left(\delta_{jk} - \frac{\tilde{t}_{t_j}^i}{\|\tilde{t}_{t_j}\|} \frac{\tilde{t}_{t_k}^i}{\|\tilde{t}_{t_j}\|} \right). \tag{38}$$

Therewith, the constitutive matrix in equation (26) is defined for all states of contact.

Crack growth algorithm

The simulation of fatigue crack propagation is implemented in the framework of linear-elastic fracture mechanics on the basis of the SIF-concept. Due to the crack closure a complete characteristic load cycle has to be analyzed for the calculation of the ranges of the SIFs. These values are utilized for the computation of crack growth in direction and magnitude. By taking into account the non-linear behavior of fatigue crack propagation an incremental iterative procedure in terms of a predictor-corrector scheme is applied for the simulation of crack growth.

Fracture mechanical parameters. Based on the state of stress and strain the fracture mechanical parameters – the stress intensity factors (SIFs) and the non-singular T-stresses – are determined. Beside the well known procedures of an extrapolation from the displacement discontinuity field [24] or the J-Integral [25] the fracture mechanical parameters in this paper are determined by an extrapolation method from the singular stress field in front of the crack front.

At smooth parts of the crack front the classical $r^{-0.5}$-stress singularity is valid. The stresses in the vicinity of a crack front point P are written with respect to the local crack front coordinate system (cf. Fig. 3) as [26]

$$\sigma_{ij}(r, \varphi, P) = \sum_{M=I}^{III} \frac{K_M(P)}{\sqrt{2\pi \, r}} f_{ij}^M(\varphi) + T_{ij}(P) + O(\sqrt{r}). \tag{39}$$

The intensity of each mode M is characterized by the corresponding SIF $K_M(P)$, while $f_{ij}^M(\varphi)$ are the angular functions. The stress field is completed by the T-stresses $T_{ij}(P)$.

The stress tensor is calculated for discrete points P_i' on a straight line in front of the point P by the evaluation of the boundary integral equation of stresses. Based on these stresses the so-called pseudo-SIFs and the pseudo-T-stresses are determined. These values are showing an error of the order $O(r)$ and $O(\sqrt{r})$, respectively [7]. Therefore, the actual fracture mechanical parameters are calculated by the extrapolation $r \to 0$ based on a regression analysis. By omitting

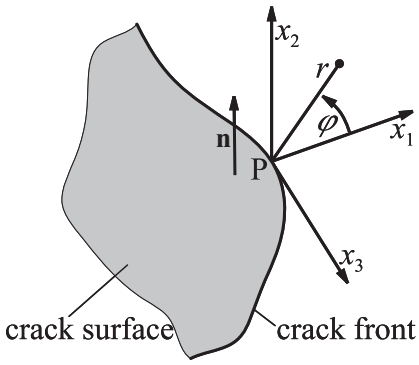

Fig. 3: Crack front coordinate system.

points at the beginning and the end of the regression line controlled by the minimization of the standard deviation very accurate values are obtained.

At non-smooth parts of the crack front and especially at the intersection points of the crack front with the outer boundary the kind of singularity is generally not a priori known. Here, the classical SIFs are no longer defined and 3D corner singularities have to be taken into account. In the vicinity of such a singular point Q (e.g. the surface breaking point in Fig. 4) the displacement field is asymptotically expanded with respect to a spherical coordinate system [27]

$$u_i(\rho, \theta, \varphi, Q) = \sum_{L=1}^{\infty} K_L^*(Q) \rho^{\alpha_L} g_i^L(\theta, \varphi, Q). \tag{40}$$

The displacement field is primarily described by the exponents α_L, which depend on the geometric situation around the singular point as well as on the material properties. They have to satisfy $\alpha_L > -0.5$ from the elastic energy point of view. The angular functions $g_i^L(\theta, \varphi, Q)$ and the generalized SIFs $K_L^*(Q)$ complete the description.

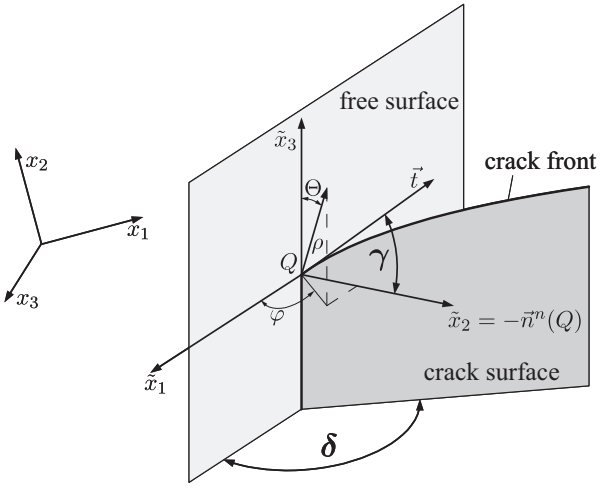

Fig. 4: Geometric situation at surface intersection point.

The exponents α_L result from the solution of a quadratic eigenvalue problem and $g_i^L(\theta, \varphi, Q)$ are the corresponding eigenvectors [27, 7]. Based on the stress field described by the leading exponent $O(\rho^{\alpha_L - 1})$ the classical SIF can be asymptotically defined [28]. If α_L is greater than 0.5, the stress singularity behaves weaker than the classical $1/\sqrt{(r)}$ stress singularity. Therefore, the

SIF is defined as $K_M \to 0$ to express this behavior within the classical SIF-concept. Otherwise, if α_L is smaller than 0.5, the stress singularity is more intensive and the SIF K_M tends to infinity.

It has been shown, that fatigue crack growth shapes a crack front, which is characterized by the $1/\sqrt{(r)}$ stress singularity at all points of the crack front including these special points [29]. Therefore, the crack front has to be smooth and a special geometric situation represented by the crack front intersection angle γ is formed (cf. Fig 4) at the surface breaking points. This angle is iteratively determined [7] and it is used to define the new position of the crack front intersection points.

Determination of the new crack front. It is a well known fact tracing back to Paris' pioneer work [30] that fatigue crack propagation depends on the cyclic values of the stresses. Due to the crack surface interaction a representative load cycle has to be evaluated for the determination of the cyclic SIFs, cf. Fig. 5. For this purpose, the equivalent SIF calculated

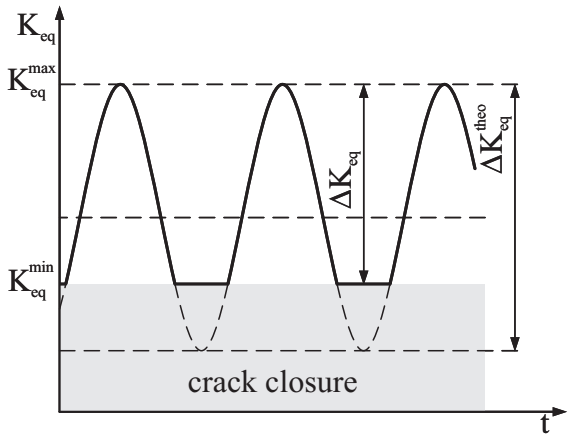

Fig. 5: Definition of the cyclic stress intensity factor.

by the criterion of the maximum energy release rate [31, 8] is taken into account. The time, when the maximum equivalent SIF is present, is denoted by $t^{\max}$ and $t^{\min}$ is the time, when the minimum equivalent SIF is present. Therewith, the cyclic equivalent SIF is defined as

$$\Delta K_{eq}(P) = K_{eq}^{\max}(P) - K_{eq}^{\min}(P) = K_{eq}(P, t^{\max}) - K_{eq}(P, t^{\min}). \tag{41}$$

According to the cyclic equivalent SIF the ranges of the SIFs are defined by

$$\Delta K_M(P) = K_M(P, t^{\max}) - K_M(P, t^{\min}). \tag{42}$$

Based on these cyclic values it is assumed that the crack starts growing in the radial direction. By excluding the generation of so-called facets (also called factory-roofs) the mode III twisting can be neglected for an infinitesimal crack extension in order to define the crack growth direction. Therefore, the kink angle $\varphi(P)$ is calculated by the maximum tangential stress (MTS) criterion of Erdogan et al. [32]. It results from the condition $\partial\sigma_\varphi/\partial\varphi = 0$ under the restriction $\partial^2\sigma_\varphi/\partial\varphi^2 < 0$ and can be explicitly written as

$$\varphi(P) = 2 \arctan\left(\frac{-2\,K_{II}(P)}{K_I(P) + \sqrt{K_I^2(P) + 8K_{II}^2(P)}}\right). \tag{43}$$

For non proportional loading conditions with changing ratios of $K_{II}(P)$ to $K_I(P)$ during the load cycle different kink angles are obtained. Following the investigation of Tanaka et al. [33] the values of $K_I(P)$ and $K_{II}(P)$ are replaced by their ranges $\Delta K_I(P)$ and $\Delta K_{II}(P)$ within the MTS-criterion (43).

The behavior of the magnitude of crack growth is described by the crack propagation rate. A widely used approach is the formula of Paris and Erdogan [34]

$$\frac{\mathrm{d}a(P)}{\mathrm{d}N} = C\ [\Delta K_{eq}(P)]^m\,. \tag{44}$$

The crack propagation rate $\mathrm{d}a(P)/\mathrm{d}N$ depends on the cyclic equivalent SIF as well as on the material parameters C and m. An extension considering the static pre-stressing of the structure is given by the formula of Hourlier et al. [35]

$$\frac{\mathrm{d}a(P)}{\mathrm{d}N} = C\ [\Delta K_{eq}(P)]^m\ \left[K_{eq}^{\max}(P)\right]^n \tag{45}$$

with the additional material parameter n.

Predictor-corrector scheme. Due to the non-linear nature of crack growth the simulation of fatigue crack propagation is implemented in the framework of a predictor-corrector scheme.

Knowing the state of stress and strain of the present crack front a new one is predicted. It is defined by the local crack extension $\Delta a(P)$ and deflection $\varphi(P)$ relative to the initial crack front. After the analysis of a characteristic load cycle in order to calculate the cyclic SIFs, the kink angle $\varphi(P)$ of each point P of the initial crack front is determined. It is obtained by the evaluation of the MTS-criterion (43) in terms of the ranges of the SIFs. For the calculation of the crack extension a crack propagation rate is evaluated for a user-specified number of load cycles ΔN_{lc}:

$$\Delta a(P) = \left[\frac{\mathrm{d}a}{\mathrm{d}N}\Big(\Delta K_{eq}(P)\Big)\right]\ \Delta N_{lc}. \tag{46}$$

Since only the SIFs of the initial crack front are considered both – the crack deflection and the crack extension – are determined in a linear way. Finally, the new position of the surface breaking points result from the geometric requirement of the crack front intersection angle ensuring the $1/\sqrt{r}$-stress singularity.

Due to the linearization of the crack growth within the predictor step the accuracy of the predicted crack front is mainly influenced by the user-specified number of load cycles ΔN_{lc}. Therefore, corrector steps including an error estimation of the predictor step are required. After the solution of the boundary value problem of the predicted crack front within the next incremental loop, the SIFs of this crack configuration are additionally known. By the consideration of these values the changing stress field is approximated by the well known relation

$$\Delta K = \Delta\sigma_n \sqrt{2\pi\, a}\, Y(a) \tag{47}$$

with the cyclic normal stress $\Delta\sigma_n$, the crack length a and the geometric function $Y(a)$ depending on the crack length. For the evaluation of this equation a virtual initial crack length $a_0(P)$ is introduced for each point along the crack front. Consequently, the crack length of the predicted crack front is written as $a_0(P)+\Delta a(P)$. For the geometric function it is assumed that $Y(a_0(P)+\Delta a(P)) \approx Y(a_0)$. On the one hand, if the crack is very small – crack in an infinite domain – the geometric function is constant. On the other hand, if the crack length has increased, the

crack extension is much smaller than the crack length: $\Delta a(P) \ll a_0(P)$. Here, the geometric function is approximately constant. Eliminating $\Delta\sigma_n$ after the evaluation of (47) at the initial (superscript in) and predicted (superscript pr) crack front the approximation of the changing stress field represented by the cyclic equivalent SIF $\Delta K_{eq}^{app}(a,P)$ is written as

$$\Delta K_{eq}^{app}(a,P) = \Delta K_{eq}^{in}(P)\sqrt{\frac{a}{a_0(P)}}, \quad a_0(P) \le a \le a_0(p) + \Delta a(P) \tag{48}$$

with

$$a_0(P) = \Delta a(P)\frac{[\Delta K_{eq}^{in}(P)]^2}{[\Delta K_{eq}^{pr}(P)]^2 - [\Delta K_{eq}^{in}(P)]^2}. \tag{49}$$

This approximation of the stress field is utilized for the re-calculation of a more accurate number of load cycles $\Delta N_{acc}(P)$ by the evaluation of the crack propagation rate:

$$\Delta N_{acc}(P) = \int_{a_0(P)}^{a_0(P)+\Delta a_0(P)} \frac{1}{\frac{\mathrm{d}a}{\mathrm{d}N}\left(\Delta K_{eq}^{app}(a,P)\right)}\mathrm{d}a. \tag{50}$$

In general, the resulting number of load cycles differs from the prescribed one. This fact is used for the correction of the predicted crack extension by replacing the predicted crack extension by

$$\Delta a_{cr}(P) = \Delta a(P) + \left[\frac{\mathrm{d}a}{\mathrm{d}N}\left(\Delta K_{eq}^{pr}(P)\right)\right] \cdot [\Delta N_{lc} - \Delta N_{acc}(P)] \tag{51}$$

until the relative error

$$\frac{|\Delta N_{lc} - \Delta N_{acc}(P)|}{\Delta N_{lc}} < \epsilon \tag{52}$$

can be neglected with respect to a user-defined accuracy ϵ for all points of the crack front.

Following [36], the directions of crack growth at the initial and predicted crack front are taken into account for the correction of the crack deflection, see Fig. 6. In principle the corrected

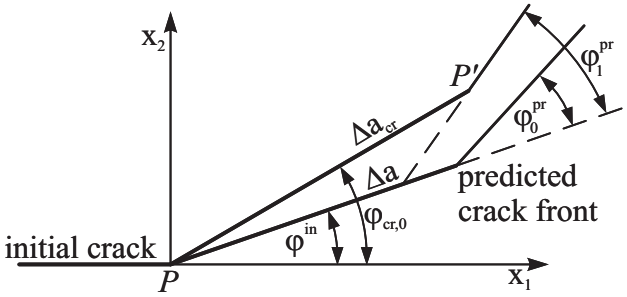

Fig. 6: Determination of crack deflection.

crack growth direction reads as

$$\varphi_{cr}(P) = \varphi^{in}(P) + c(P)\varphi^{pr}(P). \tag{53}$$

The value $c(P)$ describes the crack growth direction at the point P of the initial φ^{in} and predicted φ^{pr} crack front. On the one hand, both directions can be weighted equally

$$c(P) = 0.5. \tag{54}$$

On the other hand, the crack growth rate can be taken into account. This leads to

$$c(P) = \frac{(\Delta K_{eq}^{pr}(P))^m}{(\Delta K_{eq}^{in}(P))^m + (\Delta K_{eq}^{pr}(P))^m}. \tag{55}$$

This procedure is repeated until the modification of the crack growth direction is smaller than a user-specified tolerance.

Examples

To demonstrate the influence of the frictional contact on the behavior of cracks, two examples are presented. Within the first example the principle influence of the frictional coefficient representing the roughness of the crack surfaces is investigated. Within the second example crack propagation is analyzed.

Single edge crack specimen The first example is a single edge crack (SEC) specimen of the material steel ($E = 210\,GPa$, $\nu = 0.3$) as sketched in Fig. 7. It is loaded by a constant

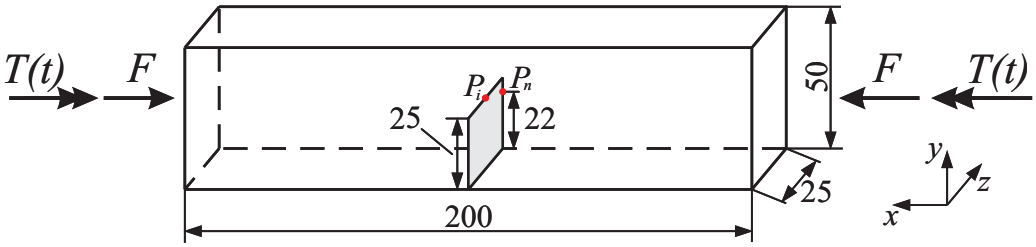

Fig. 7: Geometry and loading of SEC-specimen (dimensions in mm).

compressive force of $F = 25\,kN$ that causes a compressive stress of $\sigma_x = -20\,\frac{N}{mm^2}$. This force ensures that the crack surfaces are in contact. Beside this, the specimen is loaded with a torsional moment that increases from $0\,Nm$ to $250\,Nm$. Then, this moment is decreased to $0\,Nm$. Overall, this procedure is successively applied four times as shown in Fig. 8. Since

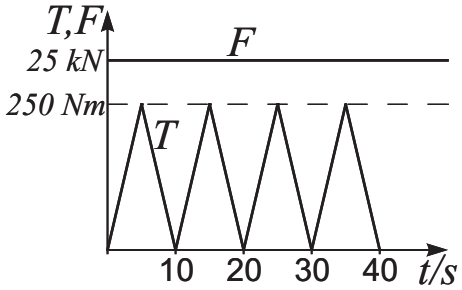

Fig. 8: Loading versus time of the specimen.

quasi static loading conditions are assumed no time dependency is present and the given time becomes more a general value.

Fig. 9 shows the displacements of the coincident points P_n on both crack surfaces for the frictional coefficient of $\mu = 0.2$ after the compression. The lower left path is linked to the point P_n on the right crack surface of the specimen and the upper right path belongs to the point on

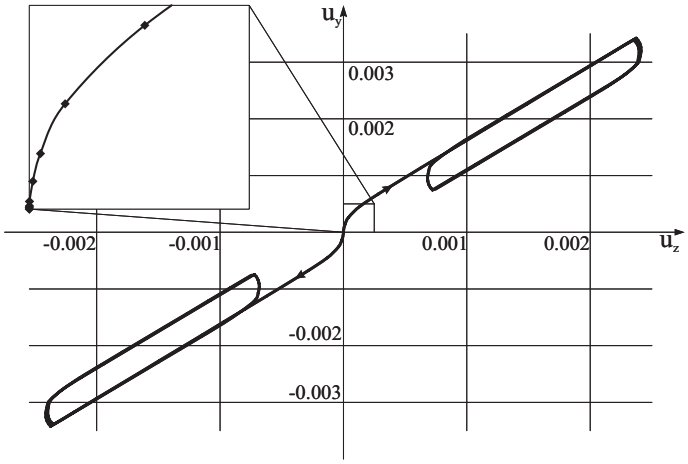

Fig. 9: Path of nodes at P_n for $\mu = 0.2$ (displacement in mm).

the crack surface at the left side with respect to Fig. 7. At the beginning of the loading process stick is present for each point of the crack surface and the specimen behaves as an un-cracked structure. Here, the maximum shear stress is present at the surface intersection points of the crack front and it is orientated in the vertical direction. Therefore, the crack surfaces start sliding in this area in vertical direction. As soon as the complete crack surfaces are sliding, they rotate around a point in the center of the specimen. This leads to a changing sliding direction during the loading procedure. When the torsional moment is decreasing, the complete crack surfaces firstly stick at each others. Then they start sliding in the same way as in the loading process. In detail, sliding begins in the vicinity of the crack front intersection points perpendicular to the deformed position followed by an approximately straight path. Due to the friction a relative displacement of the crack surfaces remains after the unloading process.

Exemplarily for all points of the crack front the state of stress at the point P_i which is located at the mid of the crack front is analyzed. Due to the symmetry of the problem only K_{III} has to be considered at this point. Fig. 10 shows the K_{III}-value versus the acting torsional moment for different frictional coefficients. For $\mu = 0$ the K_{III} is directly linked to the torsional moment.

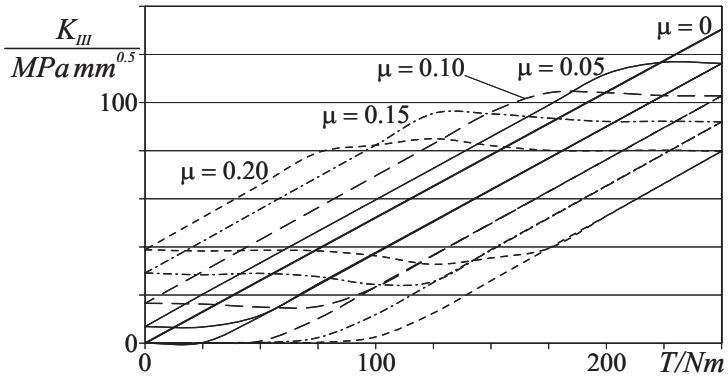

Fig. 10: K_{III} at P_i for different frictional coefficients.

In case of friction hysteresis curves are observed, which are passed counter-clockwise in this diagram. As a result of the three dimensional frictional contact problem the maximum value of K_{III} does no longer correlate with the maximum torsional moment. It occurs in the unloading process during the transition from the sticking state to the sliding of the crack surfaces. This

effect can be clearly seen for high frictional coefficients.
From the fracture mechanical point of view the ranges of the SIFs are of interest. Here, it is observed that the higher the frictional coefficient the more the maximum value is reduced and the minimum value is increased. This leads to a decreasing range of the cyclic SIF ΔK_{III} that is sketched in Fig. 11. The mean value $\overline{K}_{III}$ is approximately constant.

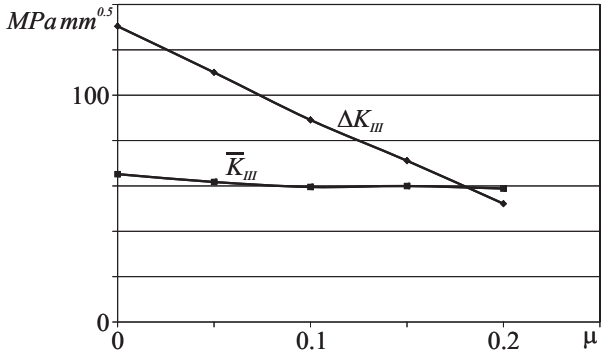

Fig. 11: Range and mean value of K_{III}.

Compressive specimen Fig. 12 shows a plate with a plane initial crack that is slanted by 45° to the mid-cross section. The plate consists of the material steel with a Young's modulus of $E = 210\,GPa$ and a Poisson ratio of $\nu = 0.3$. This specimen is loaded by a compressive force,

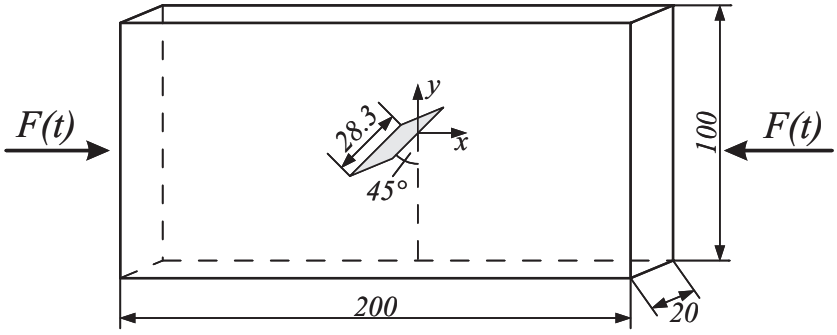

Fig. 12: Geometry of the compressive specimen (dimensions in mm).

which oscillates between $100\,kN$ and $200\,kN$, cf. Fig. 13. The crack propagation rate of this

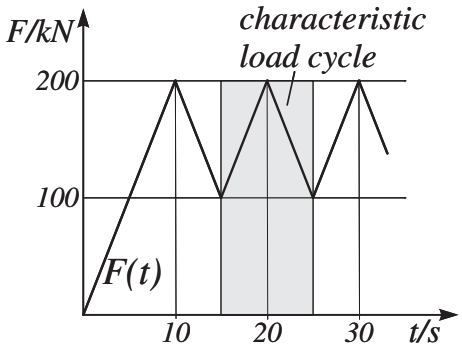

Fig. 13: Loading of the compressive specimen.

model is described by the Paris-law given by [37]

$$\frac{\mathrm{d}a}{\mathrm{d}N} = 1.27 \cdot 10^{-12} \left(\frac{\Delta K_{eq}}{MPa\, mm^{0.5}} \right)^{2.66} [mm] \,. \tag{56}$$

The simulation of crack propagation is carried out with the frictional coefficients 0.0 and 0.1. The resulting crack paths at the middle of the upper crack front are illustrated in Fig. 14. Additionally, the accumulated numbers of load cycles at selected steps of the simulation are shown. The crack paths of both simulations are approximately identical. The main difference

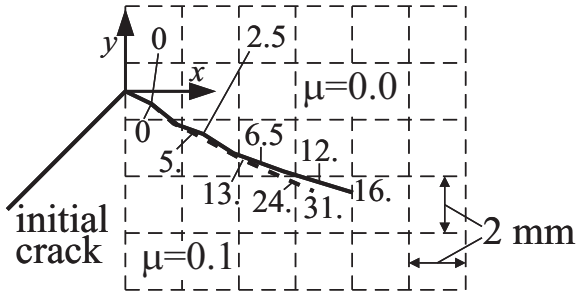

Fig. 14: Crack paths for $\mu = 0$ and $\mu = 0.1$ (load cycles in millions).

induced by friction between both simulations is in the number of load cycles. At the beginning of the simulation, the number of load cycles for $\mu = 0.1$ is approximately twice the number of load cycles as for $\mu = 0.0$. Due to the non-linear behavior of crack growth this effect is increasing when the crack grows and it ends up with a difference of the factor 2.5. Finally, it can be observed that the crack propagation slows down during crack growth independently from the frictional coefficient. At the beginning the crack needs only 5 million load cycles for a propagation of approximately 2 mm in case of $\mu = 0.1$. Afterward, 14 million load cycles are required for the same crack extension.

Conclusion

The influence of crack surface interaction on the behavior of cracks has been investigated in this paper. The main topic has been focused on the solution of the boundary value problem with the boundary element method. Here, an incremental iterative procedure has been applied in order to consider the non-linear behavior of the contact problem. The penalty method has been utilized for an efficient determination of the state of contact of the collocation points at the crack surfaces. Consistent tangential stiffness matrices for the three contact states have been obtained from a linearization procedure. For the simulation of crack propagation a predictor-corrector scheme has been applied in order to capture the changing stress field. Two examples have been presented to analyze the effect of the interaction.
It has been shown that due to friction the range of the stress intensity factors is reduced and the stress ratio acting at the crack front is different to the applied load ratio. Furthermore, the maximum and the minimum stress intensity factor correlate no longer with the maximum and minimum applied load. Therefore, a complete characteristic load cycle has to be evaluated. As a consequence of the reduced cyclic stress intensity factor, the rate of crack propagation is similarly dropped down.

References

[1] A. Portela, M.H. Aliabadi and D.P. Rooke: Int. J. Num. Meth. Eng. Vol. 33 (1992), p. 1269

[2] Y. Mi and M.H. Aliabadi: Eng. Anal. Bound. Elem. Vol. 10 (1992), p. 161

[3] T.A. Cruse: *Boundary element analysis in computational fracture mechanics* (Kluwer Academic Publishers, Dordrecht 1988).

[4] A. Cisilino and M.H. Aliabadi: Int. J. Pres. Piping Vol. 70 (1997), p. 135

[5] A. Cisilino and M.H. Aliabadi: Int. J. Num. Meth. Eng. Vol. 42 (1998), p. 237

[6] P. Partheymüller, M. Haas and G. Kuhn: Eng. Anal. Bound. Elem. Vol. 24 (2000), p. 777

[7] K. Kolk: *Automatische 2D-Rissfortschrittssimulation unter Berüsichtigung von 3D-Effekten und Anwendung schneller Randelementformulierungen* (VDI Fortschritt-Berichte, Düsseldorf 2005)

[8] W. Weber, P. Steinmann and G. Kuhn: Int. J. Fract. Vol. 149 (2008), p. 175

[9] T.D. Blacker and M.B. Stephenson: Int. J. Num. Meth. Eng. Vol. 32 (1991) p. 811

[10] T.A. Laursen: *Computational Contact and Impact Mechanics* (Springer-Verlag, Berlin Heidelberg 2003)

[11] P. Wriggers: *Computational Contact Mechanics* (John Wiley & Sons Ltd, Chichester 2002)

[12] K. Willner: *Kontinuums- und Kontaktmechanik: Synthetische und Analytische Darstellung* (Springer-Verlag, Berlin Heidelberg 2003)

[13] T. Anderson, B. Frederiksson and B.G.A. Persson: Proc. 2nd Conf. Rec. Adv. Bound. Elm. (CML Publications Southampton 1980)

[14] H. Antes and P.D. Panagiotopoulos: *The Boundary Integral Approach to Static and Dynamik Contact Problems* (Birkhäuser Verlag, Basel Boston 1992)

[15] *Yamazaki K.*: Penalty Function Method Using BEM. Chapter 5 of: *Computational Methods in Contact Mechanics* (Computational Mechanics Publications, Southampton Boston 1993)

[16] S.B. Liu and C.L. Tan: Int. J. Fract. Vol. 72 (1995) p. 39

[17] S.S. Lee: Int. J. Fract. Vol. 77 (1996) p. 323

[18] A.V. Phan, J.A.L. Napier, L.J. Gray and T. Kaplan: Int. J. Num. Meth. Eng. Vol. 57 (2003) p. 836

[19] S. Sirtori, G. Maier, G. Novati and S. Miccoli: Int. J. Num. Meth. Eng. Vol. 35 (1992) p. 255

[20] M. Gebbia: *Formule fondamentali della statica dei corpi elastici.* Rend Circ Matematico di palermo 5 (1891) p. 320

[21] M. Guiggiani, G. Krishnasamy, F.J. Rizzo and T.J. Rudolphi: J. Appl. Mech. Vol. 59 (1992) p. 604

[22] Y. Saad and M.H. Schultz: SIAM J. Sci. Stat. Comp. Vol. 7 (1986) p. 856

[23] K. Willner: J. Trib. Vol. 130 (2008) art. no. 031405

[24] A. Frangi, G. Novati, R. Springhetti and M. Rovizzi: Comp. Mech. Vol. 28 (2002) p. 220

[25] M.H. Aliabadi and D.P. Rooke: *Numerical Fracture Mechanics* (Kluwer Academic Publishers, Dordrecht 1991).

[26] J.B. Leblond and O. Torlai: J. Elast. Vol. 29 (1992) p. 97

[27] A. Dimitrov, A. Andrä and E. Schnack: Int. J. Num. Meth. Eng. Vol. 52 (2001) p. 805

[28] Z.P. Bazant and L.F. Estenssoro: Int. J. Sol. Struc. Vol. 15 (1979) p. 405

[29] M. Heyder, K. Kolk and G. Kuhn: Eng. Fract. Mech. Vol. 72 (2005) p. 2095

[30] P.C. Paris, M.P. Gomez and W.P Anderson: Trend Eng. Vol. 13 (1961) p. 9

[31] R.J. Nuismer: Int. J. Fract. Vol. 11 (1975) p. 245

[32] F. Erdogan and G.C.Sih: J. Bas. Eng. Vol. 85 (1963) p. 519

[33] K. Tanaka, Y. Akiniwa, T. Kato and T. Mikuiya: Fat. Fract. Eng. Mat. Struc. Vol. 28 (2005) p. 73

[34] P.C. Paris, F. Erdogan: J. Bas. Eng. Vol. 85 (1963) p. 528

[35] F. Hourlier and A. Pineau: Fat. Fract. Eng. Mat. Struc. Vol. 5 (1982) p. 287

[36] T. Lucht and M.H. Aliabadi: Int. J. Fract. Vol. 143 (2007) p. 195

[37] Forschungskuratorium Maschinenbau e.V.: *Bruchmechanischer Festigkeitsnachweis für Maschinenbauteile* (VDMA Verlag GmbH, Frankfurt 2006)

Key Engineering Materials Vol. 454 (2011) pp 31-46

doi:10.4028/www.scientific.net/KEM.454.31

A VARIATIONAL TECHNIQUE FOR ELEMENT FREE ANALYSIS OF STATIC AND DYNAMIC FRACTURE MECHANICS

P.H. Wen[1a] and M.H. Aliabadi[2b]

[1] Department of Engineering, Queen Mary, University of London, London, UK, E1 4NS

[2] Department of Aeronautics, Imperial College, London, UK, SW7 2BY

[a] p.h.wen@qmul.ac.uk, b m.h.aliabadi@imperial.ac.uk

Keywords: Meshless, MeshFree, Fracture Mechanics, Stress Intensity Factors, Dynamic, Laplace Doamin

Abstract. In this paper a variational technique is developed to calculate stress intensity factors with high accuracy using the element free Glerkin method. The stiffness and mass matrices are evaluated by regular domain integrals and the shape functions to determine displacements in the domain are calculated with radial basis function interpolation. Stress intensity factors were obtained by a boundary integral with a variation of crack length along the crack front. Based on a static reference solution, the transformed stress intensity factors in the Laplace space are obtained and Durbin inversion method is utilised in order to determine the physical values in time domain. The applications of proposed technique to two and three dimensional fracture mechanics are presented. Comparisons are made with benchmark solutions and indirect boundary element method.

Introduction

Crack like flaws are costly – their presence increases the time and effort spent on maintenance and repair. Cracks may ultimately lead to component fracture and subsequent structural failure, which in extreme cases can endanger human life. Since cracks cannot be eliminated totally, procedures must be devised to quantify and predict the behavior of cracked structure under service conditions.

The fundamental postulate of linear elastic fracture mechanics is that the behavior of cracks is determined solely by the stress intensity factor. Many different numerical methods have been developed over the last four decades for evaluating the stress intensity factors (see Aliabadi and Rooke[1]). The most prominent methods are the finite element method (FEM), the boundary element method (BEM) and more recently the MeshFree methods.

Early application of the finite element method to crack problems was due to Swedllow[2]. Later developments by Tracey[3], Blackburn[4], Henshell and Shaw[5] and Barsoum[6] demonstrated that accurate stress intensity factor solutions can be obtained by utilizing special crack tip elements. Virtual crack extension approach developed by Hellen[7] and Park[8] and domain integral energy approaches proposed by Shih et al [9] have helped to firmly establish FEM as an effective computational tool for cracks problems in fracture mechanics. More recent developments have been directed toward improving the FEM performance for crack growth modeling with so-called XFEM [10-12].

An early application of the BEM to crack problems was due to Cruse[13], who reported only a modest accuracy for evaluation of of the stress intensity factors. Later the sub-region BEM formulation and displacement discontinuity approaches were developed [see Aliabadi [14-15] for comprehensive reviews]. Since the early work the method has improved with the development of a new generation of BEM formulation known as the Dual Boundary Element Method [16-18]. The DEBEM has established itself as probably the most efficient and accurate method for evaluating stresses intensity factors and modeling crack growth [19-21]. Application of the method to

dynamics crack problems can be found in ref[22-29]. Other recent contributions can be found in ref[30-341].

Meshless approximations have received much interest since Nayroles et al [42] proposed the diffuse element method. Later, Belyschko et al [43] and Liu et al [44] proposed element-free Galerkin method (EFGM) and reproducing kernel particle methods, respectively. One key feature of these methods is that they do not require a structured grid and are hence meshless. Recently, Atluri et al presented a family of Meshless methods, based on the Local weak Petrov-Galerkin formulation (MLPGs) for arbitrary partial differential equations [45] with moving least-square (MLS) approximation. MLPG is reported to provide a rational basis for constructing meshless methods with a greater degree of flexibility. Local Boundary Integral Equation (LBIE) with moving least square and polynomial radial basis function (RBF) has been developed by Sladek et al [46-47] for the boundary value problems in anisotropic non-homogeneous media, i.e. functionally graded materials. Both methods (MLPG and LBIE) are meshless as no domain/boundary meshes are required in these two approaches. Other application of meshless or meshfree methods to crack problems can be found in Refs[48-58].

In this paper, the numerical implementation of element free Galerkin method for solving static/dynamic fracture problems is presented with radial basis function interpolation. The variational technique described in [29] is firstly developed with the use of element free method to determine stress intensity factor of static reference problems, which can be used to obtain the stress intensity factors in transformed domain. The accuracy of this method has been demonstrated by solving several problems in cluding: rectangular sheet and cylinder containing central/edge cracks subjected to either static or dynamic load.

Element free Galerkin method

For a linear two or three dimensional elasticity, the governing equations are written as

$$\sigma_{ij,j} + f_i = \rho \ddot{u}_i \tag{1}$$

where σ_{ij} denotes the stress tensor, f_i the body force, ρ the mass density, $\ddot{u}_i = \partial^2 u_i / \partial t^2$ the acceleration. Consider homogeneous anisotropic and linear elasticity, the relationship between the stress and strain by Hooke's law can be written as

$$\sigma_{ij} = C_{ijkl}\varepsilon_{kl} = C_{ijkl}u_{k,l} \tag{2}$$

where $\varepsilon_{kl} = \left(u_{k,l} + u_{l,k}\right)/2$, and C_{ijkl} denotes the elasticity tensor which has the following symmetries

$$C_{ijkl} = C_{jikl} = C_{klij}. \tag{3}$$

For a homogeneous isotropic solid, we have

$$C_{ijkl} = \lambda\delta_{ij}\delta_{kl} + \mu\left(\delta_{ik}\delta_{jl} + \delta_{il}\delta_{jk}\right) \tag{4}$$

where λ and μ are the Lame's constants. For two dimensional isotropic plane strain state, Hooke's law can also be written, in matrix form, as

$$\boldsymbol{\sigma} = \begin{Bmatrix} \sigma_{11} \\ \sigma_{22} \\ \sigma_{12} \end{Bmatrix} = \mathbf{D}\begin{Bmatrix} \varepsilon_{11} \\ \varepsilon_{22} \\ \varepsilon_{12} \end{Bmatrix} = \mathbf{D}\boldsymbol{\varepsilon} \tag{5}$$

where material matrix

$$\mathbf{D}=\frac{E(1-\nu)}{(1+\nu)(1-2\nu)}\begin{bmatrix}1 & \frac{\nu}{1-\nu} & 0\\ \frac{\nu}{1-\nu} & 1 & 0\\ 0 & 0 & \frac{1-2\nu}{2(1-\nu)}\end{bmatrix} \tag{6}$$

in which, E is the Young's modulus and ν the Poisson's ratio. Consider the domain Ω enclosed by boundary Γ, we have the total potential energy with

$$\Pi = U - W \tag{7}$$

where the initial elastic strain energy is defined

$$U=\frac{1}{2}\int_{\Omega}\boldsymbol{\sigma}^{\mathrm{T}}(\mathbf{y})\boldsymbol{\varepsilon}(\mathbf{y})d\Omega(\mathbf{y})=\frac{1}{2}\int_{\Omega}\boldsymbol{\varepsilon}^{\mathrm{T}}(\mathbf{y})\mathbf{D}\boldsymbol{\varepsilon}(\mathbf{y})d\Omega(\mathbf{y}) \tag{8}$$

and the external energy, the sum of contributions from known interior and boundary forces, is

$$W=\int_{\Omega}\mathbf{u}^{\mathrm{T}}(\mathbf{y})\mathbf{b}(\mathbf{y})d\Omega(\mathbf{y})-\rho\int_{\Omega}\mathbf{u}^{\mathrm{T}}(\mathbf{y})\ddot{\mathbf{u}}(\mathbf{y})d\Omega(\mathbf{y})+\int_{\Gamma}\mathbf{u}^{\mathrm{T}}(\mathbf{y})\mathbf{t}(\mathbf{y})d\Gamma(\mathbf{y}) \tag{9}$$

where $\mathbf{b}=\{b_1,b_2\}^{\mathrm{T}}$ is the body force vector, $\mathbf{t}=\{t_1,t_2\}^{\mathrm{T}}$ in which $t_i=\sigma_{ij}n_j$ or $\mathbf{t}=\boldsymbol{\sigma}\cdot\mathbf{n}$ is the vector of traction on the boundary, and n_i is a unit outward normal vector. We assume that the displacements $\mathbf{u}(\mathbf{y})$ at the field point $\mathbf{y}=(y_1,y_2)$ can be approximated in terms of the nodal values in a local domain (see Figure 1) as

$$u_i(\mathbf{y})=\sum_{k=1}^{n}\phi_k(\mathbf{y},\mathbf{x}_k)\hat{u}_i^k=\overline{\boldsymbol{\Phi}}(\mathbf{y},\mathbf{x})\hat{\mathbf{u}}_i \tag{10}$$

where $\overline{\boldsymbol{\Phi}}(\mathbf{y},\mathbf{x})=\{\phi_1(\mathbf{y},\mathbf{x}_1),\phi_2(\mathbf{y},\mathbf{x}_2),...,\phi_n(\mathbf{y},\mathbf{x}_n)\}$ and $\hat{\mathbf{u}}_i=\{\hat{u}_i^1,\hat{u}_i^2,...,\hat{u}_i^n\}^{\mathrm{T}}$, $i=1,2$, $\hat{u}_i^k(\mathbf{x}_k)$ is the nodal values at collocation point $\mathbf{x}_k=\{x_1^{(k)},x_2^{(k)}\}$, $k=1,2,...,n$, ϕ_k the shape function and $n(\mathbf{y})$ the total number of node in the local support domain, which is a function of field point $\mathbf{y}$. For two dimensional problems, we can rearrange the above relations as following

$$\begin{aligned}&\mathbf{u}(\mathbf{y})=\{u_1,u_2\}^{\mathrm{T}}=\boldsymbol{\Phi}(\mathbf{y},\mathbf{x})\hat{\mathbf{u}}\\ &\boldsymbol{\Phi}(\mathbf{y},\mathbf{x})=\begin{bmatrix}\overline{\boldsymbol{\Phi}} & 0\\ 0 & \overline{\boldsymbol{\Phi}}\end{bmatrix}=\begin{bmatrix}\phi_1 & 0 & \phi_2 & 0 & ... & \phi_n & 0\\ 0 & \phi_1 & 0 & \phi_2 & ... & 0 & \phi_n\end{bmatrix}\\ &\hat{\mathbf{u}}=\{\hat{u}_1^1,\hat{u}_2^1,\hat{u}_1^2,\hat{u}_2^2...,\hat{u}_1^n,\hat{u}_2^n\}^{\mathrm{T}}\end{aligned} \tag{11}$$

Therefore, the relationship between strains and displacements is given by

$$\boldsymbol{\varepsilon}(\mathbf{y})=\begin{bmatrix}\frac{\partial\phi_1}{\partial y_1} & 0 & \frac{\partial\phi_2}{\partial y_1} & 0 & ... & \frac{\partial\phi_n}{\partial y_1} & 0\\ 0 & \frac{\partial\phi_1}{\partial y_2} & 0 & \frac{\partial\phi_2}{\partial y_2} & ... & 0 & \frac{\partial\phi_n}{\partial y_2}\\ \frac{\partial\phi_1}{\partial y_2} & \frac{\partial\phi_1}{\partial y_1} & \frac{\partial\phi_2}{\partial y_2} & \frac{\partial\phi_2}{\partial y_1} & ... & \frac{\partial\phi_n}{\partial y_2} & \frac{\partial\phi_n}{\partial y_1}\end{bmatrix}\hat{\mathbf{u}}=\mathbf{B}(\mathbf{y})\hat{\mathbf{u}}\,. \tag{12}$$

Considering the variation of total potential energy, with respect to nodal displacement, gives

$$\delta\Pi=\delta U-\delta W=0 \tag{13}$$

Substituting $\mathbf{u}=\boldsymbol{\Phi}\hat{\mathbf{u}},\boldsymbol{\varepsilon}=\mathbf{B}\hat{\mathbf{u}}$ and $\boldsymbol{\sigma}=\mathbf{D}\boldsymbol{\varepsilon}$ into Eq.(13) yields a set of $2\times N$ linear algebraic equations in the global coordinate system

$$[\mathbf{K}]_{2N\times 2N}\hat{\mathbf{u}}_{2N}+\rho[\mathbf{C}]_{2N\times 2N}\hat{\ddot{\mathbf{u}}}=\mathbf{f}_{2N} \tag{14}$$

where N is the total number of nodes (collocation point), and the stiffness and mass matrices are defined as

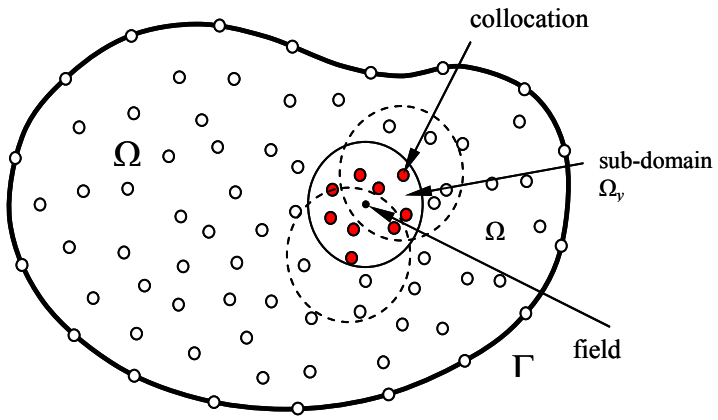

Figure 1. Sub-domain Ω_y for RBF interpolation of the field point **y** and support domains.

$$\mathbf{K} = \int_{\Omega} \mathbf{B}^{\mathrm{T}}(\mathbf{x},\mathbf{y})\mathbf{D}(\mathbf{y})\mathbf{B}(\mathbf{x},\mathbf{y})d\Omega(\mathbf{y})$$
$$\mathbf{C} = \int_{\Omega} \mathbf{\Phi}^{\mathrm{T}}(\mathbf{x},\mathbf{y})\mathbf{\Phi}(\mathbf{x},\mathbf{y})d\Omega(\mathbf{y}) \tag{15}$$

and the nodal force vector is

$$\mathbf{f} = \int_{\Omega} \mathbf{\Phi}^{\mathrm{T}}(\mathbf{x},\mathbf{y})\mathbf{b}(\mathbf{y})d\Omega(\mathbf{y}) + \int_{\Gamma_\sigma} \mathbf{\Phi}^{\mathrm{T}}(\mathbf{x},\mathbf{y})\mathbf{t}(\mathbf{y})d\Gamma(\mathbf{y}) \tag{16}$$

where Γ_σ denotes the boundary on which the traction is specified. For concentrated forces acting at the node *i,* we may determine the nodal force vector directly by

$$\mathbf{f}_i = \{F_1^i, F_2^i\}^{\mathrm{T}} \tag{17}$$

where F_1 and F_2 denote the values of concentrated force either on the boundary (external applied force) or in the domain (inner body force).

The approximation scheme

The multiquadric RBF was introduced by Hardy [59] for interpolation of topographical surfaces and an enhanced multiquadrics scheme was developed for spatial approximations by Kansa [60]. Since all radial basis functions are defined globally, the resulting matrix for interpolation is dense and can be ill-conditioned, particularly for a large number of interpolation points. It also poses serious stability problems and is computationally inefficient. To overcome this problem, a support domain technique has been introduced. A sub-domain Ω_y as shown in Figure 1 is the neighbourhood of a field point **y** and is called support domain. The distribution of function u in the sub-domain Ω_y over a number of randomly distributed notes $\{\mathbf{x}_i\}$, $i = 1,2,...,n$ can be interpolated, at a field point **y,** by

$$u(\mathbf{y}) = \sum_{i=1}^{n} R_i(\mathbf{y},\mathbf{x}_i)a_i = \mathbf{R}(\mathbf{y},\mathbf{x})\mathbf{a}(\mathbf{y}) \tag{18}$$

where $\mathbf{R}(\mathbf{y},\mathbf{x}) = \{R_1(\mathbf{y},\mathbf{x}), R_2(\mathbf{y},\mathbf{x}),..., R_n(\mathbf{y},\mathbf{x})\}$ is a set of radial basis functions centred at point **y**, $\{a_k\}_{k=1}^n$ are the unknown coefficients to be determined. The radial basis function is selected to be the following in this paper

$$R_k(\mathbf{y},\mathbf{x}_k)=\sqrt{c^2+\left|\mathbf{y}-\mathbf{x}_k\right|^2} \tag{19}$$

where c is a free parameter. From the interpolation strategy in Eq.(18), a linear system for unknown coefficients $\mathbf{a}$ become

$$\mathbf{R}_0\mathbf{a}=\hat{\mathbf{u}} \tag{20}$$

where coefficient matrix

$$\mathbf{R}_0=\begin{bmatrix} R_1(\mathbf{x}_1,\mathbf{x}_1) & R_2(\mathbf{x}_1,\mathbf{x}_2) & \dots & R_n(\mathbf{x}_1,\mathbf{x}_n) \\ R_1(\mathbf{x}_2,\mathbf{x}_1) & R_2(\mathbf{x}_2,\mathbf{x}_2) & \dots & R_n(\mathbf{x}_2,\mathbf{x}_n) \\ \cdot & \cdot & \cdots & \cdot \\ \cdot & \cdot & \cdots & \cdot \\ \cdot & \cdot & \cdots & \cdot \\ R_1(\mathbf{x}_n,\mathbf{x}_1) & R_2(\mathbf{x}_n,\mathbf{x}_2) & \dots & R_n(\mathbf{x}_n,\mathbf{x}_n) \end{bmatrix} \tag{21}$$

As the RBF are positive definite, the matrix $\mathbf{R}_0$ is assured to be invertible. Therefore, we can obtain the vector of unknowns from Eq.(20)

$$\mathbf{a}=\mathbf{R}_0^{-1}(\mathbf{x})\hat{\mathbf{u}}(\mathbf{x}) \tag{22}$$

So that the approximation $u(\mathbf{y})$ can be represented, at domain point $\mathbf{y}$, as

$$u(\mathbf{y})=\mathbf{R}(\mathbf{y},\mathbf{x})\mathbf{R}_0^{-1}(\mathbf{x})\hat{\mathbf{u}}(\mathbf{x})=\overline{\mathbf{\Phi}}(\mathbf{y},\mathbf{x})\hat{\mathbf{u}}=\sum_{k=1}^{n}\phi_k\hat{u}_k \tag{23}$$

where the shape function are defined by

$$\overline{\mathbf{\Phi}}(\mathbf{y},\mathbf{x})=\mathbf{R}(\mathbf{y},\mathbf{x})\mathbf{R}_0^{-1}(\mathbf{x}) \tag{24}$$

It is worth noticing that the shape function depends uniquely on the distribution of scattered nodes within the support domain and has the property of Kronecker Delta. As the inverse matrix of coefficient $\mathbf{R}_0^{-1}(\mathbf{x})$ is a function of distributed node $\mathbf{x}_i$ in the support domain only, it is much easier to evaluate the partial derivatives of shape function with respect to the field point. From Eq.(23), the first derivative of displacement with respect to the domain field point $\mathbf{y}$ can be obtained directly

$$u_{,k}(\mathbf{y})=\overline{\mathbf{\Phi}}_{,k}(\mathbf{y},\mathbf{x})\hat{\mathbf{u}}=\sum_{i=1}^{n}\phi_{i,k}\hat{u}_i \qquad k=1,2 \tag{25}$$

where

$$\overline{\mathbf{\Phi}}_{,k}(\mathbf{y},\mathbf{x})=\mathbf{R}_{,k}(\mathbf{y},\mathbf{x})\mathbf{R}_0^{-1}(\mathbf{x}) \tag{26}$$

From Eq. (19), we have

$$R_{i,k}(\mathbf{y},\mathbf{x}_i)=\frac{y_k-x_k^{(i)}}{\sqrt{c^2+\left|\mathbf{y}-\mathbf{x}_i\right|^2}}. \tag{27}$$

In order to guarantee unique solution of the interpolation problem, a polynomial term should be added to the interpolation in Eq.(18) as

$$u(\mathbf{y})=\sum_{k=1}^{n}R_k(\mathbf{y},\mathbf{x})a_k+\sum_{j=1}^{t}P_j(\mathbf{y})b_j=\mathbf{R}_0(\mathbf{y},\mathbf{x})\mathbf{a}+\mathbf{P}(\mathbf{y})\mathbf{b} \tag{28}$$

along with the constraints

$$\sum_{j=1}^{t}P_k(\mathbf{x}_j)a_j=0, \quad 1\le k\le t \tag{29}$$

where $\{P_k\}_{k=1}^{t}$ is a basis for P_{m-1}, the set of devariate polynomials of degree $\le m-1$, and

$$t=\binom{m+d-1}{d} \tag{30}$$

is the dimension of P_{m-1}. A set of linear equations can be written, in the matrix form, as

$$\mathbf{R}_0\mathbf{a}+\mathbf{P}^{\mathrm{T}}\mathbf{b}=\hat{\mathbf{u}},\qquad \mathbf{P}\mathbf{a}=\mathbf{0} \tag{31}$$

where matrix

$$P(\mathbf{x})=\begin{bmatrix} P_1(x_1) & P_2(x_1) & \dots & P_t(x_1)\\ P_1(x_2) & P_2(x_2) & \dots & P_t(x_2)\\ \cdot & \cdot & \cdots & \cdot\\ \cdot & \cdot & \cdots & \cdot\\ \cdot & \cdot & \cdots & \cdot\\ P_1(x_n) & P_2(x_n) & \dots & P_t(x_n)\end{bmatrix} \tag{32}$$

Solving equations in Eq.(31) gives

$$\mathbf{b}=\left(\mathbf{P}^{\mathrm{T}}\mathbf{R}_0^{-1}\mathbf{P}\right)^{-1}\mathbf{P}^{\mathrm{T}}\mathbf{R}_0^{-1}\hat{\mathbf{u}},\qquad \mathbf{a}=\mathbf{R}_0^{-1}\left[\mathbf{I}-\mathbf{P}\left(\mathbf{P}^{\mathrm{T}}\mathbf{R}_0^{-1}\mathbf{P}\right)^{-1}\mathbf{P}^{\mathrm{T}}\mathbf{R}_0^{-1}\right]\hat{\mathbf{u}} \tag{33}$$

where **I** denotes the diagonal unit matrix. It is clear that the coefficients **a** and **b** are functions of nodal coordinate **x** in the support domain only. In addition, the accuracy has been shown to be the same by using RBF with/without these polynomials. Therefore, the shape functions with radial basis function are selected by Eq.(23) for simplicity in the following analysis.

Numerical process to evaluate stiffness matrix

To determine the stiffness matrix **K** in Eq.(14), a domain integral in Eq.(15) over the domain Ω should be carried out. The 2D domain integral over a rectangular of area A is approximated by the Gaussian integration formula

$$\iint_A f(y_1,y_2)dy_1dy_2\approx A\sum_{l_2=1}^{L}\sum_{l_1=1}^{L}w_{l_1}w_{l_2}f(y_1^l,y_2^l) \tag{34}$$

where w_l denotes the weight of integral, $l=(l_1,l_2)$, L the number of Gaussian points and (y_1^l,y_2^l) the coordinate of Gaussian points. If domain Ω is divided into M sub-domains, then the stiffness and mass matrices can be written as

$$\begin{aligned}\mathbf{K}(\mathbf{x})&=\sum_{m=1}^{M}\sum_{l_2=1}^{L}\sum_{l_1=1}^{L}w_{l_1}w_{l_2}\frac{A_m}{4}\mathbf{B}^{\mathrm{T}}(\mathbf{x},\mathbf{y}^{ml})\mathbf{D}(\mathbf{y}^{ml})\mathbf{B}(\mathbf{x},\mathbf{y}^{ml})=\sum_{m=1}^{M}\sum_{l_2=1}^{L}\sum_{l_1=1}^{L}\Delta\mathbf{K}^{ml}\\ \mathbf{C}(\mathbf{x})&=\sum_{m=1}^{M}\sum_{l_2=1}^{L}\sum_{l_1=1}^{L}w_{l_1}w_{l_2}\frac{A_m}{4}\mathbf{\Phi}^{\mathrm{T}}(\mathbf{x},\mathbf{y}^{ml})\mathbf{\Phi}(\mathbf{x},\mathbf{y}^{ml})=\sum_{m=1}^{M}\sum_{l_2=1}^{L}\sum_{l_1=1}^{L}\Delta\mathbf{C}^{ml}\end{aligned} \tag{35}$$

where the integration points $\mathbf{y}^{ml}=(y_1^{ml},y_2^{ml})$ and coefficients w_l in Eq.(34) are given, if L=4, by

$$\mathbf{y}^{m(1,2,3,4)}=\left(y_1^m\pm\sqrt{\frac{1}{3}}h_1,y_2^m\pm\sqrt{\frac{1}{3}}h_2\right),\quad w_{1,2,3,4}=\frac{1}{4}, \tag{36}$$

in which (y_1^m,y_2^m) presents the centre of sub integral domain with area A_m (rectangular), h_1 and h_2 are half of the width and height of the rectangular region respectively and A_m= $4h_1h_2$. For each Gaussian point $\mathbf{y}^{ml}$, the element in the stiffness sub-matrix $\Delta\mathbf{K}^{ml}$ and mass sub-matrix $\Delta\mathbf{C}^{ml}$ can be calculated by

$$\Delta\mathbf{K}^{ml}=\frac{A_m E(1-\nu)}{4(1+\nu)(1-2\nu)}\left[\begin{array}{cc}\dfrac{\partial\phi_i}{\partial y_1}\dfrac{\partial\phi_j}{\partial y_1}+\dfrac{1-2\nu}{2(1-\nu)}\dfrac{\partial\phi_i}{\partial y_2}\dfrac{\partial\phi_j}{\partial y_2} & \dfrac{\nu}{1-\nu}\dfrac{\partial\phi_i}{\partial y_1}\dfrac{\partial\phi_j}{\partial y_2}+\dfrac{1-2\nu}{2(1-\nu)}\dfrac{\partial\phi_i}{\partial y_2}\dfrac{\partial\phi_j}{\partial y_1}\\ \dfrac{\nu}{1-\nu}\dfrac{\partial\phi_i}{\partial y_2}\dfrac{\partial\phi_j}{\partial y_1}+\dfrac{1-2\nu}{2(1-\nu)}\dfrac{\partial\phi_i}{\partial y_1}\dfrac{\partial\phi_j}{\partial y_2} & \dfrac{\partial\phi_i}{\partial y_2}\dfrac{\partial\phi_j}{\partial y_2}+\dfrac{1-2\nu}{2(1-\nu)}\dfrac{\partial\phi_i}{\partial y_1}\dfrac{\partial\phi_j}{\partial y_1}\end{array}\right]_{ij}$$

$$=\frac{A_m E(1-\nu)}{4(1+\nu)(1-2\nu)}\left[\begin{array}{cc}k_{11}^{l} & k_{12}^{l}\\ k_{21}^{l} & k_{22}^{l}\end{array}\right]_{ij} \tag{37}$$

$$\Delta\mathbf{C}^{ml}=\left[\begin{array}{cc}\phi_i\phi_j & 0\\ 0 & \phi_i\phi_j\end{array}\right]_{ij} \tag{38}$$

where i and j denote the number of nodes in the local support domain centred at $\mathbf{y}^{ml}$, $\phi_i=\phi_i(\mathbf{y}^{ml},\mathbf{x})$, i, j=1,2,…, $n(\mathbf{y}^{ml})$. Applying the Laplace transform to Eq.(14) results

$$\left(\mathbf{K}+\rho s^2\mathbf{C}\right)\tilde{\hat{\mathbf{u}}}=\tilde{\mathbf{f}} \tag{39}$$

where the Laplace transform of $f(\mathbf{x},t)$ is defined by

$$\tilde{f}(\mathbf{x},\mathrm{s})=\int_0^\infty f(\mathbf{x},t)e^{-st}dt \tag{40}$$

in which s is a Laplace parameter. Obviously the system stiffness matrix $\mathbf{K}$ and mass matrix $\mathbf{C}$ are symmetric with diagonal strip distribution similar to finite element method.

Variational technique to evaluate SIF

To obtain stress intensity factor for either static or dynamic problem, one needs a static reference problem to be solved. Let Γ_t and Γ_u be the traction and displacement boundaries respectively and consider a reference problem with a variation δa of crack length along the crack surface (see Figure 3), i.e. the collocation coordinate of crack tip $\mathbf{x}_a=(a,0)$. The variations of displacement and traction with respect to a are $\delta t_k/\delta a$ and $\delta u_k/\delta a$, respectively. Since $\delta t_k/\delta a=0$ on the traction boundary, and $\delta u_k/\delta a=0$ on displacement boundary, the stress intensity factor $K_{\mathrm{I}}^{\mathrm{static}}$ for a reference problem is determined by the following boundary integral [10]

$$K_{\mathrm{I}}^{\mathrm{static}}=\left(\frac{\mu}{(1-\nu)}\left\langle\int_{\Gamma_t}\left(\frac{\delta u_k}{\delta a}\right)t_k^0 d\Gamma-\int_{\Gamma_u}\left(\frac{\delta t_k}{\delta a}\right)u_k^0 d\Gamma\right\rangle\right)^{1/2} \tag{41}$$

where t_k^0 and u_k^0 are given boundary conditions of traction and displacement. Considering the system equation for static problem $(s=0)$ in Eq.(14) gives

$$\frac{\delta\mathbf{K}}{\delta a}\hat{\mathbf{u}}+\mathbf{K}\frac{\delta\hat{\mathbf{u}}}{\delta a}=0 \tag{42}$$

Thus we have

$$\frac{\delta\hat{\mathbf{u}}}{\delta a}=-\mathbf{K}^{-1}\frac{\delta\mathbf{K}}{\delta a}\hat{\mathbf{u}} \tag{43}$$

For each Gaussian point $\mathbf{y}^{ml}$, the element in the stiffness sub-matrix $\delta\Delta\mathbf{K}^{ml}/\delta a$ can be obtained

$$\frac{\delta(\Delta\mathbf{K}^{ml})}{\delta a}=\frac{A_m E(1-\nu)}{4(1+\nu)(1-2\nu)}\left[\begin{array}{cc}k_{11,a}^{l} & k_{12,a}^{l}\\ k_{21,a}^{l} & k_{22,a}^{l}\end{array}\right]_{ij} \tag{44}$$

where

$$k_{11,a}^{l}=\frac{\partial\phi_{i,a}}{\partial y_1}\frac{\partial\phi_j}{\partial y_1}+\frac{\partial\phi_i}{\partial y_1}\frac{\partial\phi_{j,a}}{\partial y_1}+\frac{1-2\nu}{2(1-\nu)}\left(\frac{\partial\phi_{i,a}}{\partial y_2}\frac{\partial\phi_j}{\partial y_2}+\frac{\partial\phi_i}{\partial y_2}\frac{\partial\phi_{j,a}}{\partial y_2}\right)$$

$$k_{12,a}^{l}=\frac{\nu}{1-\nu}\left(\frac{\partial\phi_{i,a}}{\partial y_1}\frac{\partial\phi_j}{\partial y_2}+\frac{\partial\phi_i}{\partial y_1}\frac{\partial\phi_{j,a}}{\partial y_2}\right)+\frac{1-2\nu}{2(1-\nu)}\left(\frac{\partial\phi_{i,a}}{\partial y_2}\frac{\partial\phi_j}{\partial y_1}+\frac{\partial\phi_i}{\partial y_2}\frac{\partial\phi_{j,a}}{\partial y_1}\right)$$

$$k_{21,a}^{l}=\frac{\nu}{1-\nu}\left(\frac{\partial\phi_{i,a}}{\partial y_2}\frac{\partial\phi_j}{\partial y_1}+\frac{\partial\phi_i}{\partial y_2}\frac{\partial\phi_{j,a}}{\partial y_1}\right)+\frac{1-2\nu}{2(1-\nu)}\left(\frac{\partial\phi_{i,a}}{\partial y_1}\frac{\partial\phi_j}{\partial y_2}+\frac{\partial\phi_i}{\partial y_1}\frac{\partial\phi_{j,a}}{\partial y_2}\right)$$

$$k_{22,a}^{l}=\frac{\partial\phi_{i,a}}{\partial y_2}\frac{\partial\phi_j}{\partial y_2}+\frac{\partial\phi_i}{\partial y_2}\frac{\partial\phi_{j,a}}{\partial y_2}+\frac{1-2\nu}{2(1-\nu)}\left(\frac{\partial\phi_{i,a}}{\partial y_1}\frac{\partial\phi_j}{\partial y_1}+\frac{\partial\phi_i}{\partial y_1}\frac{\partial\phi_{j,a}}{\partial y_1}\right) \tag{45}$$

where

$$\left\{\phi_{1,a},\phi_{2,a},\ldots,\phi_{n,a}\right\}=\frac{\delta\overline{\mathbf{\Phi}}(\mathbf{y},\mathbf{x})}{\delta a}=\frac{\delta\mathbf{R}(\mathbf{y},\mathbf{x})}{\delta a}\mathbf{R}_0^{-1}(\mathbf{x})+\mathbf{R}(\mathbf{y},\mathbf{x})\frac{\delta\mathbf{R}_0^{-1}(\mathbf{x})}{\delta a}$$

and

$$\left\{\frac{\partial\phi_{1,a}}{\partial y_i},\frac{\partial\phi_{2,a}}{\partial y_i},\ldots,\frac{\partial\phi_{n,a}}{\partial y_i}\right\}=\frac{\partial}{\partial y_i}\frac{\delta\overline{\mathbf{\Phi}}(\mathbf{y},\mathbf{x})}{\delta a}=\frac{\partial}{\partial y_i}\left(\frac{\delta\mathbf{R}(\mathbf{y},\mathbf{x})}{\delta a}\right)\mathbf{R}_0^{-1}(\mathbf{x})+\frac{\partial\mathbf{R}(\mathbf{y},\mathbf{x})}{\partial y_i}\frac{\delta\mathbf{R}_0^{-1}(\mathbf{x})}{\delta a} \tag{46}$$

As $\mathbf{R}_0^{-1}\mathbf{R}_0=\mathbf{I}$, the variations of inverse matrix $\mathbf{R}_0^{-1}$ is obtained

$$\frac{\delta\mathbf{R}_0^{-1}}{\delta a}=-\mathbf{R}_0^{-1}\frac{\delta\mathbf{R}_0}{\delta a}\mathbf{R}_0^{-1} \tag{47}$$

Therefore, by solving Eq.(43), the variations of displacement can be obtained, and then the variations of stress/traction can be written as

$$\frac{\delta\boldsymbol{\sigma}}{\delta a}=\mathbf{D}\left(\mathbf{B}\frac{\delta\hat{\mathbf{u}}}{\delta a}+\frac{\delta\mathbf{B}}{\delta a}\hat{\mathbf{u}}\right)\ \text{and}\ \frac{\delta\mathbf{t}}{\delta a}=\frac{\delta\boldsymbol{\sigma}}{\delta a}\cdot\mathbf{n} \tag{48}$$

In order to determine the transformed stress intensity factors in Laplace space for the same configuration of geometry, above variations of displacement and traction are needed. The relationship between static and transformed stress intensity factors can be written as [10]

$$\widetilde{K}_I(s)=\frac{\mu}{(1-\nu)K_{\mathrm{I}}^{\mathrm{static}}}\left[\int_{\Gamma_t}\left(\frac{\delta u_k}{\delta a}\right)\widetilde{t}_k^{0}(s)d\Gamma-\int_{\Gamma_u}\left(\frac{\delta t_k}{\delta a}\right)\widetilde{u}_k^{0}(s)d\Gamma-\rho s^2\int_{\Omega}\left(\frac{\delta u_k}{\delta a}\right)\widetilde{u}_k(s)d\Omega\right] \tag{49}$$

in which $\widetilde{u}_k^0$ and $\widetilde{t}_k^0$ are displacement and traction boundary values in the transformed domain, $K_{\mathrm{I}}^{\mathrm{static}}$ stress intensity factor for the static reference problem obtained from Eq.(41) and $\widetilde{u}_k$ displacements by Eq.(39) in the Laplace domain.

The variational technique for two-dimensional problems can be easily extended to 3D axial symmetric problems. In this case, Eq.(41) becomes

$$K_{\mathrm{I}}^{\mathrm{static}}=\left(\frac{\mu}{(1-\nu)a}\left\langle\int_{\Gamma_t}\left(\frac{\delta u_k}{\delta a}\right)t_k^0 y_1 d\Gamma-\int_{\Gamma_u}\left(\frac{\delta t_k}{\delta a}\right)u_k^0 y_1 d\Gamma\right\rangle\right)^{1/2} \tag{50}$$

for static problem and Eq.(49)

$$\widetilde{K}_I(s)=\frac{\mu}{(1-\nu)aK_{\mathrm{I}}^{\mathrm{static}}}\left[\int_{\Gamma_t}\left(\frac{\delta u_k}{\delta a}\right)\widetilde{t}_k^{0}(s)y_1 d\Gamma-\int_{\Gamma_u}\left(\frac{\delta t_k}{\delta a}\right)\widetilde{u}_k^{0}(s)y_1 d\Gamma-\rho s^2\int_{\Omega}\left(\frac{\delta u_k}{\delta a}\right)\widetilde{u}_k(s)y_1 d\Omega\right] \tag{51}$$

for dynamic problem respectively, where a is coordinate of crack tip and y_2 axis of symmetry.

In order to evaluate the stress intensity factor in the time domain, the Durbin's inverse method is employed [23]

$$f(t)=\frac{2e^{\eta t}}{T}\left[-\frac{1}{2}\widetilde{f}(\eta)+\sum_{k=0}^{K}\mathrm{Re}\left\{\widetilde{f}\left(\eta+\frac{2k\pi}{T}i\right)\exp\left(\frac{2k\pi t}{T}i\right)\right\}\right] \tag{52}$$

where $\widetilde{f}(s_k)$ is the transformed variable in the Laplace transform domain when the parameter $s_k=\eta+2k\pi i/T$, $i=\sqrt{-1}$. Numerical results show that the selections of parameters η and T affect

the accuracy slightly. In the computations, $\eta = 5/t_0$ and $T/t_0 = 20$ in the following examples, where time unit $t_0 = w/c_1$, here w is the selected length such as the width of plate for 2D or radius R of cylinder for 3D, and $c_1 = \sqrt{E(1-\nu)/\rho(1+\nu)(1-2\nu)}$ which is velocity of longitudinal waves. Obviously the total number of samples in the Laplace domain is K+1 and K is chosen as 25 in the following examples.

Examples

6.1 Central/edge cracks in rectangular sheet under uniform static load σ_0

A rectangular plate of width 2w and height 2h containing a centred crack of 2a subjected to a uniform shear load σ_0 both on the top and bottom of sheet is analysed firstly. Due to the symmetry, a quarter of plate is considered as shown in Figure 4(a). Here Poisson's ratio ν=0.3. The nodes are uniformly distributed as shown in Figure 4(b) and the total number of nodes are (m+1)×(m+1) and the integration is performed by dividing the rectangular plate into m×m cells with 4×4 Gauss points for each cell. The support domain is selected as a circle of radius d_y centered at field point **y,** which radius is determined such that the minimum number of nodes in the sub-domain $n(\mathbf{y}) \geq N_0$, here the number N_0 is chosen to be 6 for all examples. Free parameter c=w in RBF. Figure 5 shows the relative error $\eta = \left|K_{\mathrm{I}}^{\mathrm{static}} - K_{\mathrm{I}}^{0}\right| / K_{\mathrm{I}}^{0}$ against the parameter of node m when a/w=0.5, where K_{I}^{0} is accurate result presented in the handbook [24]. Excellent agreement can be achieved when m>12 with the relative error of 1%. In the following examples, m is selected to be 20. The normalize stress intensity factors $K_{\mathrm{I}}^{\mathrm{static}} / \sigma_0 \sqrt{\pi a}$ for a central or edge/double edge cracks varying with the crack length a/w and height of plate h/w are plotted in Figures 6 and 7 respectively and comparison is made with accurate solutions. Good agreement has been achieved and the results are to be found within 2% of the accurate solutions.

6.2 A Single central crack in rectangular plate/cylinder under dynamic tension

Consider a rectangular plate of width 2w and length 2h with a centrally located crack of length 2a. It is loaded dynamically in the direction perpendicular to the crack by a uniform tension $\sigma_0 H(t)$ on the top and bottom of plate, where $H(t)$ is the Heaviside function. Due to the symmetry, a quarter of plate is analysed as shown in Figure 4(a). Let Poisson ratio ν=0.3, half length of crack a=0.5w and Young's modulus a unit. Two rectangular plates are considered, i.e. h=w and h=2w. Normalize dynamic stress intensity factors $K_I(t)/\sigma_0\sqrt{\pi a}$ are plotted in Figures 8 and 9 respectively. To demonstrate the accuracy of the element free method, the results obtained by fictitious load method (FLM, also called indirect boundary element method in [25]) are plotted for comparison. Apparently before the arrival of dilatation wave traveling from the top/bottom of plate, the stress intensity factor should remain to be zero. In general, the maximum value of dynamic stress intensity factor for each case is found to be twice of that for the static. Finally a cylindrical bar of radius R and height 2h is analysed with a central circular crack of radius a subjected to a uniform Heaviside load $\sigma_0 H(t)$ at the top and bottom surfaces. Figure 10 shows the normalize dynamic stress intensity factor $K_I(t)/2\sigma_0\sqrt{a/\pi}$, where a/R=0.5, h/R=1 and Poisson ratio ν=0.2. In this figure, the results presented by Wen [25] using FLM for a central circular crack in a rectangular bar are presented for comparison. The agreement with the fictitious load method is considered to be good.

Conclusion

This paper has demonstrated the availability of the element free Galerkin method to elastostatic and elastodynamic fracture mechanics with a variational technique. Considering a static reference with same boundary configuration, the transformed stress intensity factors can be obtained by an integral in the Laplace transform domain. The accuracy of stress intensity factor by proposed method has been demonstrated by several examples. We can conclude with the following observations: (1) Element free Galerkin method with variational technique is valid to deal with static/dynamic crack problems; (2) Stiffness matrix is symmetric and strip diagonal. Therefore, the combination with different methods such as Finite Difference Method, FEM and BEM can be easily realised; (3) The high accurate solutions can be obtained with less number of samples in the Laplace space, i.e. K=25 in this paper; (4) Proposed method can be easily developed to mixed mode, three-dimensional elasticity, functionally graded material and plate bending crack problems.

References

[1] Aliabadi,M.H and Rooke,D.P. Numerical Fracture Mechanics, Computational Mechanics Publications, Southampton and Kluwer Academic Publications, Dordrecht, 1991.

[2] Swedlow,J.l., Williams,m.L. and Yang,W.H. Elasto-plastic stresses and strains in cracked plates. Proc. 1st Int. Conf. on Fracture, vol. 1, pp259-282, Sendai, Japan 1965.

[3] Tracey,D.M. Finite elements for determination of crack tip elastic stress intensity factors . Engng Fract. Mech., **3**, 255-266, 1971.

[4] Blackburn,W.S. Calculation of stress intensity factors at crack tips using special finite elements. In the Mathmatics of finite elements, edited by J.R.Williams, Academic Press, 327-336, 1973.

[5] Henshell,R.D. and Shaw, K.G. Crack tip finite elements are unnecessary. International Journal for Numerical Methods in Engineering, **9**, 495-507, 1975.

[6] Barsoum,R.S. On the use of isoparametric finite elements in linear elastic fracture mechanics, Int.J. Numer Methods in Engng, 11, 85-98 (1977).

[7] Hellen,T.K. On the method of virtual crack extensions, International Journal for Numerical Methods in Engineering, 9, 187-207, 1975.

[8] Parks,D.M. The virtual crack extension method for nonlinear material behavior, Computer methods in Applied Mechanics and Engineering, 12, 353-364, 1977.

[9] Shih,C.F, Moran,B and Nakamura,T Energy release rate along a three-dimensional crack front in a thermally stressed body. International Journal of Fracture, **30**, 79-102, 1986.

[10] Belytschko,T and Black,T Elastic crack growth in finite elements with minimal remeshing. International Journal for Numerical Methods in Engineering, **45,** 601–620, 1999.

[11] Moës,N., Dolbow,J and Belytschko,T A finite element method for crack growth without remeshing. International Journal for Numerical Methods in Engineering, **46** 131–150, 1999.

[12] Zamani, A.; Eslami, M.R. Implementation of the extended finite element method for dynamic thermoelastic fracture initiation. International Journal of Solids and Structures, **47,** 1392-404, 2010

[13] Cruse,T and Van Buren Three dimensional elastic stress analysis of a fracture specimen with an edge crack. International Journal for Fracture Mechanics, **7**, 1-15, 1971.

[14] Aliabadi,M.H. The boundary element method, Co. 2: Application in Solids and Structures, Wiley, 2002.

[15] Aliabadi,M.H. Boundary element formulation in fracture mechanics, Applied Mechanics Reviews, **50,** 83-96, 1997.

[16] Portela,A Aliabadi,M.H. and Rooke,D.P. The dual boundary element method: effective implementation for crack problems', International Journal for Numerical Methods in Engineering **33**, 1269-1287, 1992.

[17] Mi,Y and Aliabadi,M.H. Dual boundary element method for three-dimensional fracture mechanics analysis, Engineering Analysis with Boundary Elements **10**, 161-171, 1992.

[18] Aliabadi,M.H. A new generation of boundary element methods in fracture mechanics, International Journal of Fracture, **86**, 91-125, 1977

[19] Portela,A, Aliabadi,M.H. and Rooke,D.P. Dual boundary element incremental analysis of crack propagation, Computers and Structures, **46**, 237-247, 1993.
[20] Mi,Y and Aliabadi,M.H. An automatic procedure for mixed-mode crack growth analysis, Communications in Numerical Methods, **11**, 167-177, 1995.
[21] Cisilino,A.P. and Aliabadi,M.H. Three-dimensional boundary element analysis of fatigue crack growth in linear and non-linear fracture problems, Engineering Fracture Mechanics, **63**, 713-733, 1999.
[22] Wen,P.H. Dynamic Fracture Mechanics: Displacement Discontinuity Method, Computa- tional Mechanics Publications, Southampton, 1996.
[23] Wen, P.H.; Aliabadi, M.H.; Rooke, D.P. A contour integral method for dynamic stress intensity factors. Theoretical and Applied Fracture Mechanics, **27**, 29-41,1997.
[24] Wen, P.H.; Aliabadi, M.H.; Sladek, J.; Sladek, V. Displacement discontinuity method for cracked orthotropic strip: dynamic Wave Motion, **45**, 293-308, 2008.
[25] Fedelinski, P. Aliabadi, M.H.; Rooke, D.P. Single-region time domain BEM for dynamic crack problems. International Journal of Solids and Structures, **32**, 3555-3571, 1995.
[26] Fedelinski, P.; Aliabadi, M.H.; Rooke, D.P. The time-domain DBEM for rapidly growing cracks. International Journal for Numerical Methods in Engineering, **40** 1555-1572, 15 1997.
[27] Fedelinski, P., Aliabadi, M.H.; Rooke, D.P. The Laplace transform DBEM for mixed-mode dynamic crack analysis. Computers and Structures, **59**, 1021-31, 1996.
[28] Wen, P.H.; Aliabadi, M.H.; Rooke, D.P. Cracks in three dimensions: a dynamic dual boundary element analysis: Computer Methods in Applied Mechanics and Engineering, 167 139-51, 1998.
[29] Wen, P.H. Aliabadi, M.H.; Rooke, D.P. Variational technique for boundary element analysis of 3D fracture mechanics weight functions: dynamic. International Journal for Numerical Methods in Engineering, **42**, 1425-1439, 1998.
[30] Franco-Nava, J.M. and El-Zafrany, A, Hyper-singular boundary element method for elastoplastic fracture mechanics analysis with large deformation. Computational Mechanics, **37**, 15-23, 2005.
[31] Albuquerque, E.L.; Sollero, P.; Aliabadi, M.H. Dual boundary element method for anisotropic dynamic fracture mechanics. International Journal for Numerical Methods in Engineering, **59**, 1187-205, 2004.
[32] Zhao Minghao ; Liu Yuanjie; Cheng Changjun. Boundary-integral equations and the boundary-element method for three-dimensional fracture mechanic. Engineering Analysis with Boundary Elements, **13**, 333-8, 1994.
[33] Weber, W. Willner, K.; Kuhn, G. Numerical analysis of the influence of crack surface roughness on the crack path. Engineering Fracture Mechanics, **77**, 1708-1720, 2010.
[34] Gao, X.W. ; Zhang, Ch.; Sladek, J.; Sladek, V. Fracture analysis of functionally graded materials by a BEM, Composites Science and Technology, **68**, 1209-15, 2008.
[35] Sladek, J.; Sladek, V.; Fedelinski, P. Contour integrals for mixed-mode crack analysis: Effect of nonsingular terms. Theoretical and Applied Fracture Mechanics, **27**, 115-127, 1997.
[36] Williams, R.C.; Phan, A.-V.; Tippur, H.V.; Kaplan, T.; Gray, L.J. SGBEM analysis of crack-particle(s) interactions due to elastic constants mismatch. Engineering Fracture Mechanics, **74**, 314-331, 2007.
[37] Roberts, D.J.; Phan, A.-V.; Tippur, H.V.; Gray, L.J.; Kaplan, T. SGBEM modeling of fatigue crack growth in particulate composites. Archive of Applied Mechanics, **80**, 307-322, 2010.
[38] Miers, L.S. Telles, J.C.F. Two-dimensional elastostatic analysis of FGMs via BEFM Engineering Analysis with Boundary Elements, **32**, 1006-1011, 2008.
[39] Telles, J.C.F.; Guimaraes, S.On the numerical Green's function technique for cracks in Reissner's plates. Computer Methods in Applied Mechanics and Engineering, **196**, 2478-85, 2007.
[40] Leonel, Edson Denner; Venturini, W.S. Non-linear boundary element formulation with tangent operator to analyse crack propagation in quasi-brittle materials. Engineering Analysis with Boundary Elements, **34**, 122-129, 2010.

[41] Citarella, R.; Cricrì, G.Comparison of DBEM and FEM crack path predictions in a notched shaft under torsion. Engineering Fracture Mechanics, **77**, 1730-1749, 2010.
[42] Nayroles, B. Touzot, G. And Villon,P., Generalizing the finite element method: diffuse approximation and diffuse elements, Computational Mechanics 10 (1992), 307-318.
[43] Belytschko,T, Lu,Y.Y. and Gu,L., Element-free Galerkin method, Int. J. Numerical Methods in Engineering **37** 229-256, 1994.
[44] Liu,W.k., Jun,S and Zhang,Y Reproducing kernel particle methods, Int. J. Numerical Methods in Engineering **20** 1081-1106, 1995.
[45] Atluri,S.N. and Zhu,T A new meshless local Peyrov-Galerkin (MLPG) approach to nonlinear problems in computational modelling and simulation, Comput. Model. Simul. Engng **3**, 187-196, 1998.
[46] Sladek, J.; Sladek, V.; Wen, P.H.; Aliabadi, M.H. Meshless local Petrov-Galerkin (MLPG) method for shear deformable shells analysis Computer Modeling in Engineering & Sciences, **13**, 103-117, 2006.
[47] Sladek,V., Sladek,J., Tanaka,M and Zhang,Ch Local integral equation method for potential problems in functionally graded anisotropic materials, Engng Analy. with Boundary Elements, **29**, 829-843, 2005.
[48] Wen, P.H. , Aliabadi, M.H.An improved meshless collocation method for elastostatic and elastodynamic problems. Communications in Numerical Methods in Engineering, **24**, 635-651, 2008.
[49] Sladek, J.; Sladek, V.; Krivacek, J.; Aliabadi, M.H. Local boundary integral equations for orthotropic shallow shells. International Journal of Solids and Structures, **44**, 2285-303, 2007.
[50] Chen, Y.P.; Lee, J.D.; Eskandarian, A. Dynamic meshless method applied to nonlocal crack problems. Theoretical and Applied Fracture Mechanics, **38**, 293-300, 2002.
Sladek, J.; Sladek, V.; Zhang,Ch; Tan,C.L. Evaluation of fracture parameters for crack problems in FGM by a meshless method. Journal of Theoretical and Applied Mechanics, **44**, 603-36, 2006.
[51]S aldek,J, Sladek,V., Zhang,Ch., A meshless local boundary integral equation method for dynamic anti-plane shear crack problem in functionally graded materials. Engineering Analysis with Boundary Elements, **29**, 334-42, 2005.
[52] Sladek, J.; Sladek, V.; Chuanzeng Zhang Dynamic crack analysis in functionally graded piezoelectric solids by meshless local Petrov-Galerkin method. Key Engineering Materials, **348-349**, 149-52, 2007.
[53] Duflot, M. Hung Hguyen-Dang A meshless method with enriched weight functions for fatigue crack growth. International Journal for Numerical Methods in Engineering, 59, 1945-61, 2004.
[54] Zhang, Y.Y.; Chen, L. A simplified meshless method for dynamic crack growth. Computer Modeling in Engineering & Sciences, **31**, 189-99, 2008.
[55] Wen, P.H.; Aliabadi, M.H. Meshless method with enriched radial basis functions for fracture mechanics. Structural Durability & Health Monitoring, **3**, 107-19, 2007.
[56] Wen, P.H.; Aliabadi, M.H.; Liu, Y.W. Meshless method for crack analysis in functionally graded materials with enriched radial base functions. CMES - Computer Modeling in Engineering and Sciences, **30**, 133-147, 2008.
[57] Wen, P.H.; Aliabadi, M.H. Mixed-mode stress intensity factors by mesh free Galerkin method. Key Engineering Materials, **417-418**, 957-960, 2010.
[58] Wen, P.H. ; Aliabadi, M.H. Evaluation of mixed-mode stress intensity factors by the mesh-free Galerkin method: Static and dynamic. Journal of Strain Analysis for Engineering Design, **44**, 273-286, 2009.
[59] Hardy,R.L. Multiquadric equations of topography and other irregular surface, J. Geophys. Res. **76**, 1905-1915, 1971.
[60] Kansa,E.J. Multiquadrics. A scattered data approximation scheme with applications to computational fluid-dynamics. I. Surface approximations and partial derivative estimates, Computer & Mathematics with Applications **19** (8-9), 127-145, 1991.

[61] GolgergM.A., Chen,C.S. and Karur,S.R. Improved multiquadric approximation for partial differential equations, Engng Analy with Boundary Elements **18**, 9-17, 1996.
[62] Durbin,F Numerical inversion of Laplace transforms: an efficient improvement to Dubner and Abate's method, The Computer J. **17**, 371-376 1975.
[63] Rooke, D.P. and Cartwright D.J, A Compendium of Stress Intensity Factors, HMSO, London, 1976.

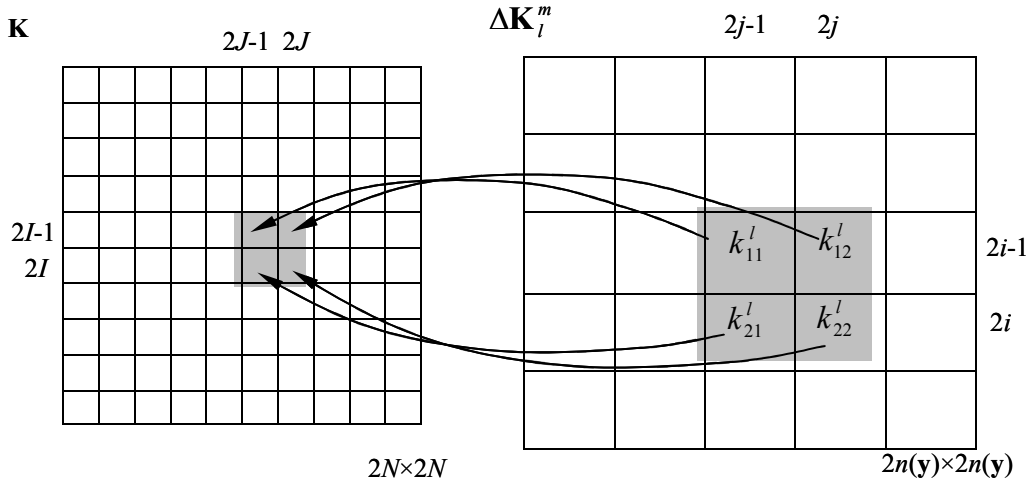

Figure 2. Stiffness matrix forming process, where *i* and *j* are node numbers in the support domain for integral Gaussian point *l*; *I* and *J* are numbers in the global system of nodes *i* and *j* respectively.

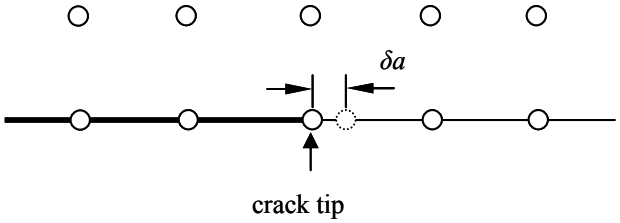

Figure 3. Variation of crack length δa along the crack surface.

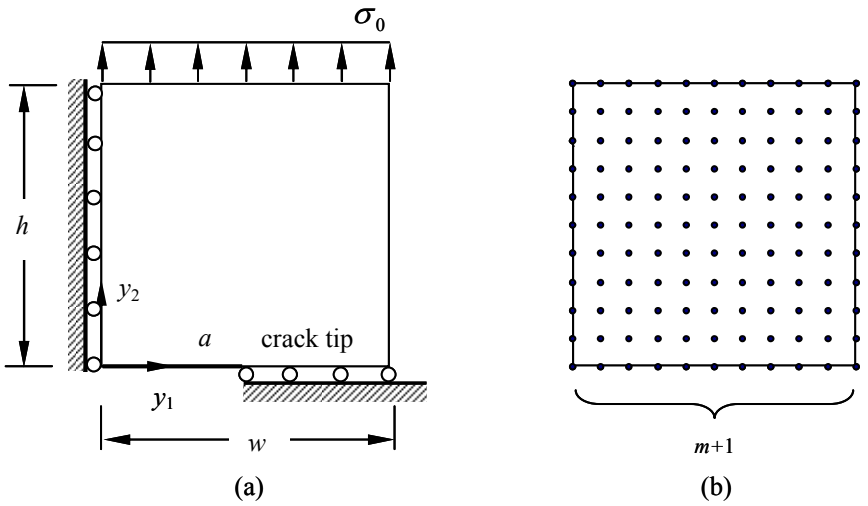

Figure 4. Rectangular sheet with central or edge/double edge crack: (a) geometry; (b) uniformly distributed nodes.

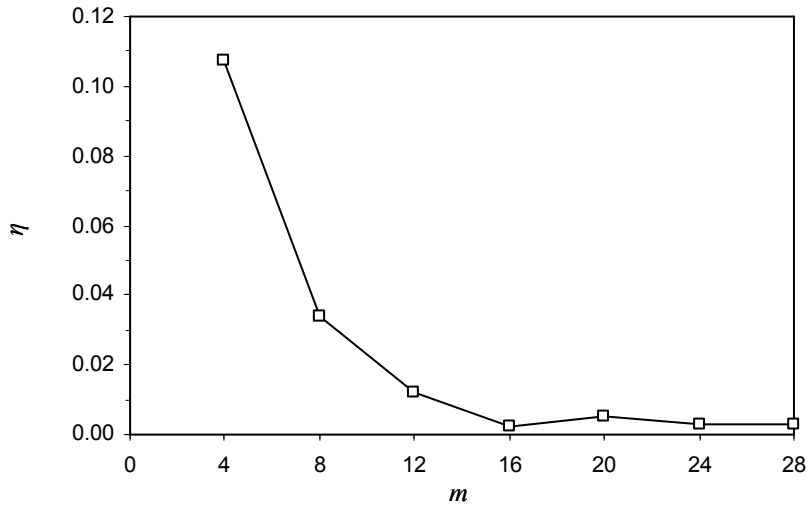

Figure 5. Relative errors and convergence for the normalized stress intensity factor of central crack under uniform tension when a/w=0.5 and h/w=1.

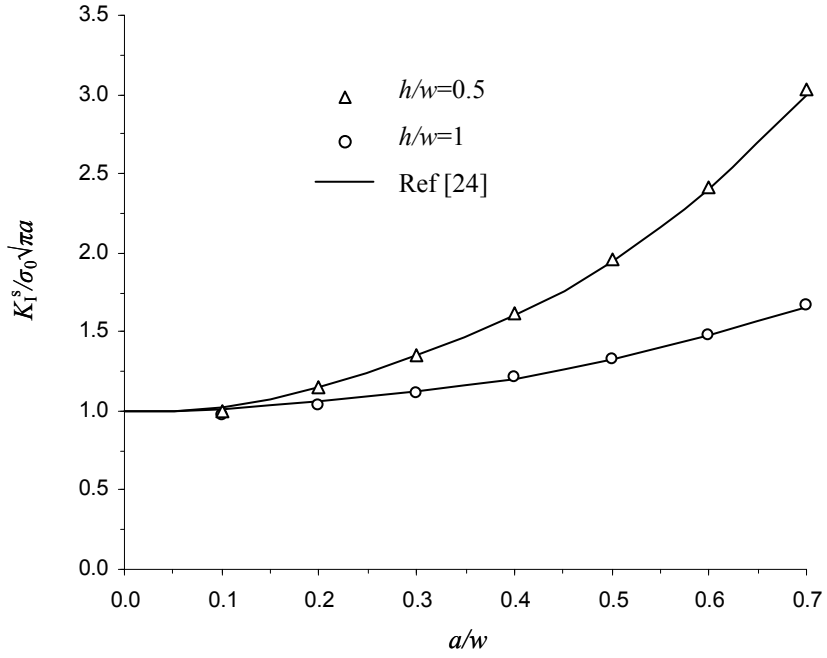

Figure 6. Normalized stress intensity factor of central crack under uniform tension.

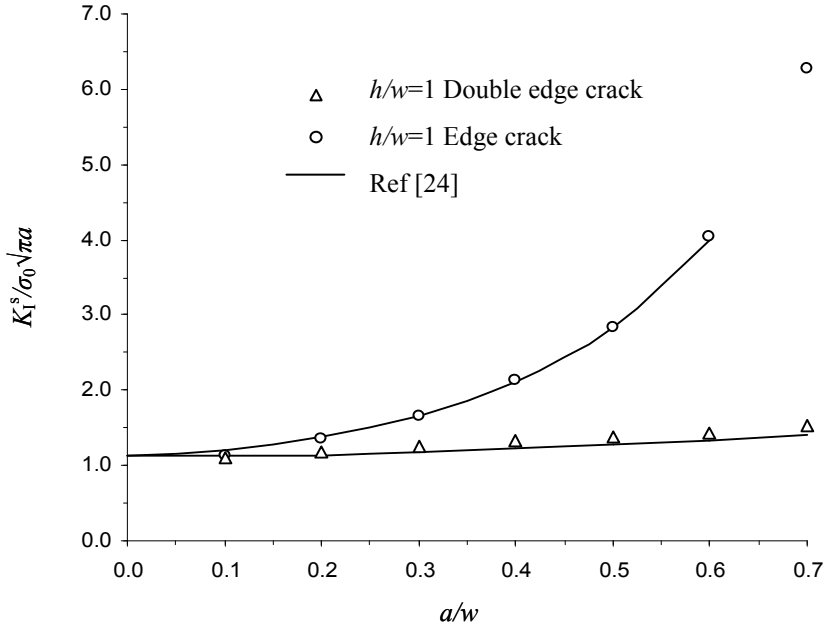

Figure 7. Normalized stress intensity factor of edge crack under uniform tension.

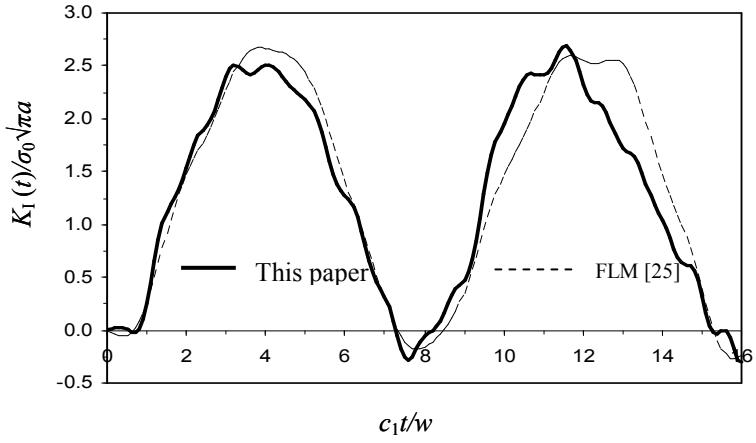

Figure 8. Normalized dynamic stress intensity factor $K_I(t)/\sqrt{\pi a}$ for a central crack under uniform tension when a/w=0.5, h/w=1 and ν=0.3.

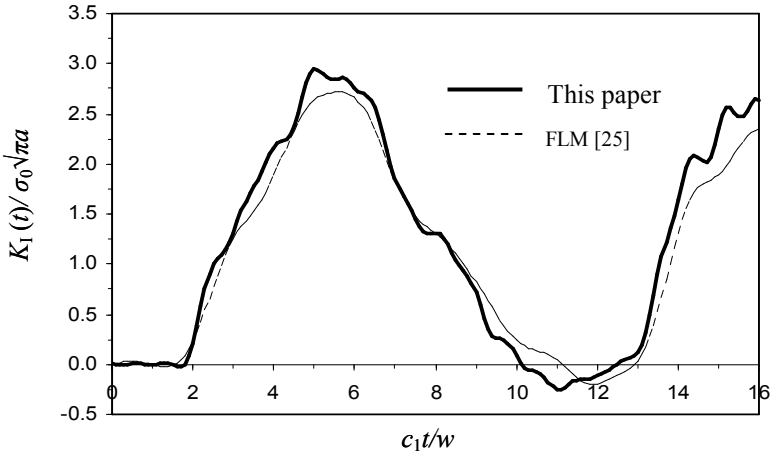

Figure 9. Normalized dynamic stress intensity factor $K_I(t)/\sqrt{\pi a}$ for a central crack under uniform tension when a/w=0.5, h/w=2 and ν=0.3.

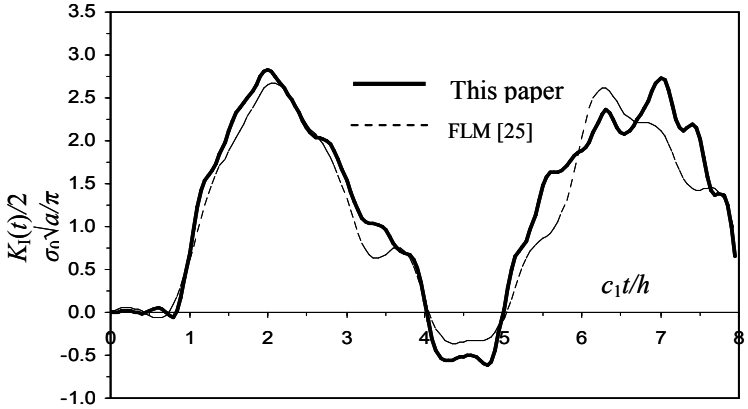

Figure 10. Normalized dynamic stress intensity factor $K_I(t)/2\sqrt{a/\pi}$ for a cylindrical bar containing a central circular crack under uniform dynamic load, where a/R=0.5, h/R=1 and ν=0.2

Key Engineering Materials Vol. 454 (2011) pp 47-77

doi:10.4028/www.scientific.net/KEM.454.47

Boundary element analysis of three-dimensional interface cracks in transversely isotropic bimaterials using the Energy Domain Integral

N.O. Larrosa[1,3], J.E. Ortiz[2] and A.P. Cisilino[3,a]

[1] Escuela Superior de Ingenieros, Escuela Superior de Ingenieros, Universidad de Sevilla. Av. de los Descubrimientos s/n, E-41092, Sevilla, España.

[2] Departamento de Mecánica de Medios Continuos, Escuela Superior de Ingenieros, Universidad de Sevilla. Av. de los Descubrimientos s/n, E-41092, Sevilla, España.

[3] División Soldadura y Fractomecánica, INTEMA. Facultad de Ingeniería, Universidad Nacional de Mar del Plata – CONICET, Av. Juan B. Justo 4302, B7608FDQ, Mar del Plata, Argentina.
[a] cisilino@fi.mdp.edu.ar

Keywords: three-dimensional interface cracks, transversely isotropic bimaterials, energy domain integral, boundary element method.

Abstract

It is presented in this paper a three-dimensional Boundary Element Method (BEM) implementation of the Energy Domain Integral for the fracture mechanical analysis of three-dimensional interface cracks in transversely isotropic bimaterials. The *J*-integral is evaluated using a domain representation naturally compatible with the BEM, in which the stresses, strains and derivatives of displacements at internal points are evaluated using their appropriate boundary integral equations. Several examples are solved and the results compared with those available in the literature to demonstrate the efficiency and accuracy of the implementation to solve straight and curved crack-front problems.

1 Introduction

The greatest advantage of composite materials is strength and stiffness combined with lightness. By choosing an appropriate combination of reinforcement and matrix material, manufacturers can produce materials with mechanical properties that fit the requirements for a particular structure for a particular purpose.

Commonly, high strength and stiffness are required in various directions within a plane. The solution is to stack and weld together a number of plies, each having the fibres oriented in different directions. Such a stack is termed a laminate. The individual plies present a macroscopic transversely isotropic behaviour with the symmetry axis in the direction of the fibres (Gibson, 2007).

Delamination is one of the most important damage mechanisms in laminate composites. It consists in the nucleation of interface cracks between the plies of the laminate as consequence of thermo-mechanical fatigue, impact or material degradation (Gibson, 2007). Once cracking initiation has arisen, preventing crack growth (propagation) is the variable to control in order the keep the material in a reliable condition. It is therefore important to develop fracture-mechanics methods for assessing interface cracks and predicting their

behaviour during the material life time.

Many questions regarding the mechanics of interface fracture have been answered during the past few decades. However, progress has been generally focused in the two-dimensional idealization of an interface crack, and not until recently major effort has been conducted on the three-dimensional aspect of interface fracture. This is in part due to the complexity of such problems and the very large computational efforts required for their numerical analysis. However, given the material mismatch at the interface boundary, it is expected that the three-dimensional effects play a more significant role in a laminate structure than in a homogenous structure.

The numerical analysis of interface cracks in transversally isotropic materials has been traditionally addressed using Finite Element Analysis (FEA) (see for example Boniface and Banks-Sills, 2002 and Freed and Banks-Sills, 2005). Besides, there is the alternative of using the Boundary Element Method (BEM). The attraction of the BEM can be largely attributed to the reduction in the dimensionality of the problem; for two-dimensional problems, only the line-boundary of the domain needs to be discretized into elements, and for three-dimensional problems only the surface of the domain needs to be discretized. This means that, compared to finite-element domain-type analysis, a boundary analysis results in a substantial reduction in data preparation. At the same time, and due to the inherent characteristics of its formulation, BEM provides very accurate results for problems containing strong geometrical discontinuities. This makes BEM a powerful numerical tool for modelling crack problems (see Aliabadi, 1997). Fracture mechanical analysis of three dimensional transversely isotropic materials using BEM has been reported by Sáez et al. (1997) and Ariza and Dominguez (2004a, 2004b) who modelled static and dynamic crack problems, Zhao et al. (1998) who derived the displacement discontinuity boundary integral equation, and more recently by Chen et al. (2009) who studied the stress intensity factors of a central square crack in a transversely isotropic cuboid with arbitrary material orientations. To our knowledge, there is no published material about the three dimensional BEM modelling of interface cracks in dissimilar transversely isotropic bimaterials.

A number of techniques have been proposed for the evaluation of fracture parameters of interface cracks using FEM and BEM. They are, among others, the virtual crack extension approach (So, Lau and Ng; 2004), contour and domain path-independent integrals (Chow and Atluri, 1998; Ortiz and Cisilino, 2005; Freed and Banks-Sills, 2005; Shah, Tan and Wang, 2006), displacement extrapolation techniques (Freed and Banks-Sills, 2005; Tan and Gao, 1990; Mao and Sun, 1995) and special crack-tip elements (He, Lin and Ding, 1994). In particular, path-independent integral techniques are derived from the *J*-integral proposed by Rice (1968). Being an energy approach, path-independent integrals eliminate the need to solve local crack tip fields accurately. If the integration domain is defined over a relatively large portion of the mesh, an accurate modelling of the crack tip is unnecessary because the crack tip field contribution to the overall energy is not significant. At the same time, it is worth noting that the *J*-integral as it was developed by Rice (1968) characterizes the crack driving force for two-dimensional problems. Therefore, for general three-dimensional cases involving cracks of arbitrary shape an alternative form for the *J*-integral is needed.

Three basic schemes have evolved for the numerical computation of the *J*-integral in three dimensions: virtual crack extension methods, generalization of Rice's contour integral, and domain integral methods (Anderson, 1994). Domain integrals are equivalent to the virtual crack extension technique and are better suited for numerical analysis than contour integral methods. Among the available domain integral methods

(see for example Nikishkov and Atluri ,1987 and Saliva et al, 2000) the Energy Domain Integral (EDI) due to Moran and Shih (1987) was chosen for this work.

The EDI can be formulated by applying the divergence theorem to Rice's *J*-integral. It produces a domain independent integral defined over finite volumes enclosing some portion of the crack front (Moran and Shih, 1987). Previous works by the authors of this paper have demonstrated the versatility and efficiency of the BEM implementation of the EDI for assessing three-dimensional cracks in elastic (Cisilino et al, 1998), elastoplastic (Cisilino and Aliabadi, 1999) and thermoelastic bodies (Balderrama et al, 2006 and 2008) and for interface cracks in dissimilar isotropic bimaterials (Ortiz and Cisilino, 2005).

It is presented in this work the BEM implementation of the EDI for the *J*-integral computation in three-dimensional interface cracks in dissimilar transversely isotropic bimaterials. The BEM solution strategy for the fracture problem and the EDI implementation is an extension of that proposed by Ortiz and Cisilino (2005) for interface cracks in dissimilar isotropic bimaterials. A number of examples demonstrate the suitability of the proposed numerical tool for assessing delamination cracks in composite laminates.

2 Transversely isotropic materials

The basic constitutive expressions governing the elastic behaviour of transversely isotropic materials are reviewed next following Ting (1996).

The general constitutive law of the anisotropic material is

$$\sigma_{ij}(x) = C_{ijkl}(x)\varepsilon_{kl}(x) = C_{ijkl}(x)u_{k,l}(x) \tag{1}$$

where $\sigma_{ij}(x)$ is the stress tensor, $\varepsilon_{ij}(x)$ is the infinitesimal strain tensor and $u_k(x)$ is the displacement vector. Partial derivatives are indicated using the comma notation. The symbol $C_{ijkl}(x)$ is the fourth-order constitutive tensor which is defined in terms of 21 independent elasticity constants.

Transversely isotropic materials are those with an axis of symmetry such that all directions perpendicular to that axis are on a plane of isotropy. In such a case the constitutive tensor can be defined in terms of 5 independent elasticity constants only. Using the Voight reduced notation (see Ting, 1996), the fourth-order constitutive tensor C_{ij} $(i,j = 1,\dots,6)$ for a transversely isotropic material with the axis of symmetry coincident with the Cartesian axis x_3 can be expressed in terms of the five following elastic constants:

$$C_{1111} = C_{11},\ C_{3333} = C_{33},\ C_{1122} = C_{12},\ C_{1133} = C_{13} \text{ and } C_{2323} = C_{44}\ . \tag{2}$$

Due to the symmetry with respect to x_3, $C_{66} = (C_{11} - C_{12})/2$.

The coefficients of the constitutive tensor C_{ij} can be written in terms of the elastic engineering constants as follows:

$$C_{11} = \frac{E(n - v'^2)}{\lambda(1+v)},\ C_{12} = \frac{E(n + v'^2)}{\lambda(1+v)}, C_{13} = \frac{Ev'}{\lambda},\ C_{33} = \frac{E(1+v)}{\lambda}, C_{44} = \mu', \tag{3}$$

being:

$$\lambda = n(1-v) - 2v'^2 \text{ and } n = E/E', \tag{4}$$

where

- E and E' are the Young's moduli in the plane of isotropy and in the directions normal to it, respectively.
- ν is the Poisson's ratio that represents the strain response in the plane of isotropy due to an action parallel to it; and ν' is the lateral strain response for the planes normal to the plane of isotropy.
- μ' is the shear modulus for the planes normal to the planes of transverse isotropy.

3 Elastic solution in the vicinity of 3D interface crack front

Consider a three-dimensional crack front with a continuously turning tangent as depicted in Figure 1*a*. Define a local coordinate system x^* at position η, where the crack energy release rate is evaluated, given by x_1^* normal to the crack front, x_2^* normal to the crack plane, and x_3^* tangent to the crack front.

The elastic solution at the neighbourhood of the interface crack front can be expressed using a double series expansion of the form:

$$u(r,\theta,\eta) = \sum_{i\geq 1}\sum_{j\geq 0} \partial_3^j K_i(\eta) r^{\alpha_i+j} \varphi_j^{(\alpha_i)}(\theta), \tag{5}$$

for $Re(\alpha_p) \leq Re(\alpha_q)$ when $p < q$. The symbol u in equation (5) is the displacement vector in cylindrical coordinates (see Figure 1*a*), $K_i(\eta)$ is the Stress Intensity Factor (SIF) associated to exponent α_i, and $\varphi_j^{(\alpha_i)}(\theta)$ is an angular function. The exponent and the angular function depend of the boundary conditions over the crack faces, solids angles of the materials and the material properties (see Omer and Yosibash, 2008).

When $j = 0$ in equation (5), α_i and $\varphi_0^{(\alpha_i)}(\theta)$ yield the solution for the two-dimensional crack problem. For a crack in a homogenous material $\alpha_1 = \alpha_2 = \alpha_3 = 1/2$, $\alpha_4 = 1$ and the coefficients K_i are the well-known stress intensity factors (SIFs) K_{I}, K_{II} and K_{III}, respectively. For interface cracks the exponents α_i are complex numbers where $Re(\alpha_1) = Re(\alpha_2) = Re(\alpha_3) = 1/2$ and $Re(\alpha_4) = 1$. The additional high order terms in Eq. (5) when $j \geq 1$ are the so-called "shadow terms" not present in the two dimensional problem. The shadow terms are originated by variation of the SIFs along the crack front.

4 The energy domain integral

Following Natha and Moran (1993), the energy release rate, $G(\eta)$, due to crack extension in its own plane along a three-dimensional crack front takes the form (see Figure 1*b*)

$$G(\eta) = \lim_{C\to 0} \xi_k(\eta) \int_{C(\eta)} \left(w \cdot \delta_{ki} - \sigma_{ij}^* u_{j,k}^*\right) n_i dC, \tag{6}$$

where w is the strain energy density, $\boldsymbol{\sigma_{ij}^*}$ and $\boldsymbol{u_{j,k}^*}$ are Cartesian components of stress and displacement derivatives expressed in the system $\boldsymbol{x^*}$, $\boldsymbol{\xi_k(\eta)}$ are the components of the unit outward normal to the crack front in the crack plane $\boldsymbol{x_1^* - x_3^*}$, $\boldsymbol{n_i}$ is the unit vector normal to the contour $\boldsymbol{C(\eta)}$ (which lies in the $\boldsymbol{x_1^* - x_2^*}$ plane), and $\boldsymbol{dC}$ is the differential of the arc length $\boldsymbol{C}$. It is worth noting that, although Eq. (6) comes from a two-dimensional analysis, it applies for a general three-dimensional case. This is because the three-dimensional stress field along a crack front of arbitrary shape is the same to that governing a two-dimensional plain strain problem (see Omer and Yosibash, 2008). Thus, the energy domain integral introduced in this section can be used for the solution of cracks of arbitrary shape in three-dimensions.

In order to derive the equivalent domain representation of Eq. (6), we consider a small segment $\boldsymbol{L_c}$ of the crack front that lies in the $\boldsymbol{x_1^* - x_3^*}$ plane as shown in Fig. 1*b*. Next we assume that the segment undergoes a virtual crack advance in the plane of the crack, and we define the magnitude of the advance at each point $\boldsymbol{\eta}$ as $\boldsymbol{\Delta a(\eta)}$. Note that $\boldsymbol{\Delta a(\eta)}$ varies continuously along $\boldsymbol{L_c}$ and it vanishes at each end of the segment. Now let

$$\bar{G}(\eta) = \int_{L_c} G(\eta)\Delta a(\eta) d\eta, \tag{7}$$

where $\boldsymbol{G(\eta)}$ is the integral defined in Eq.(6). When $\boldsymbol{G(\eta)}$ belongs to the point-wise energy release rate, $\boldsymbol{\bar{G}}$ gives the total energy released when the finite segment $\boldsymbol{L_c}$ undergoes the virtual crack advance.

The appropriate domain form of the point-wise crack-tip contour integral can be obtained from Eq. (7) by considering a tubular domain $\boldsymbol{V}$ surrounding the crack segment (see Figure 2). As it shown in the figure, the surface $\boldsymbol{S_t}$ is formed by translating the contour $\boldsymbol{C}$ along the segment $\boldsymbol{L_c}$, and $\boldsymbol{S_0}$ stands for the outer surface of $\boldsymbol{V}$ including the ends. Next an auxiliary vector function $\boldsymbol{q}$ is introduced, which is sufficiently smooth in $\boldsymbol{V}$ and it is defined on the surfaces of $\boldsymbol{V}$ as follows:

$$q_k = \begin{cases} \Delta a(\eta) \cdot \xi_k(\eta) \text{ on } S_t \\ 0 \text{ on } S_0 \end{cases} \tag{8}$$

Finally, in the limit as the tubular surface $\boldsymbol{S_t}$ is shrunk onto the crack segment $\boldsymbol{L_c}$ and in the absence of crack face tractions, we obtain the domain integral:

$$\bar{G}(\eta) = \int_V \left(\sigma_{ij}^* u_{j,k}^* - w \cdot \delta_{ki}\right) q_{k,i} dV. \tag{9}$$

In absence of body forces the integral $\boldsymbol{\bar{G}}$ given in Eq. (9) reduces to the domain representation of the familiar *J*-integral. If it is assumed that $\boldsymbol{G(\eta)}$ is constant along $\boldsymbol{L_c}$, it follows directly from Eq. (7) that:

$$J(\eta) = G(\eta) = \frac{\bar{G}}{\int_{L_c} \Delta a(\eta) d\eta}. \tag{10}$$

5 Boundary Element Analysis

In order to account for the non homogeneous material properties, a multi-domain BEM formulation is used for the problem solution. The modelling strategy is illustrated in the schematic representation in Figure 3, for a model consisting of two subdomains, $\Omega_I(x)$ and $\Omega_{II}(x)$, with external boundaries $\Gamma_I(x)$ and $\Gamma_{II}(x)$, respectively. Both subdomains share a common interface $\Gamma_{I-II}(x)$, a portion of which is debonded and thus an interface crack is introduced. The subdomains possess a linear transversely isotropic material behaviour as it has been described in Section 2. The orientation of the material is specified using a local Cartesian system (x_1^0, x_2^0, x_3^0) for each subdomain. In every case the direction of the symmetry axis of the material is chosen coincident with the direction x_3^0 (see Figure 3). In this way, it is possible to model interface cracks lying between laminates with arbitrary relative fibre orientations.

The standard BEM uses the displacement boundary integral equation to relate the displacement and traction fields, $u(x)$ and $t(x)$ over the model boundary in the global coordinate system (see Aliabadi, 2002):

$$c_{ik}(x')u_i(x') + \int_\Gamma T_{ik}(x,x')u_i(x)\mathrm{d}\Gamma(x) = \int_\Gamma U_{ik}(x,x')t_i(x)\mathrm{d}\Gamma(x), \tag{11}$$

where $U_{ik}(x,x')$ and $T_{ik}(x,x')$ are the displacement and traction fundamental solutions, respectively. The fundamental solutions account for the solution of *i-th* component of the displacement and traction fields, $u_i(x)$ and $t_i(x)$, at the field point, x, due to the action of a unit load acting in the direction j at the source point, x'. The symbol c_{ik} is the so-called jump term which depends on the local geometry at the source point, x', only. There are several expressions for the fundamental solutions for a transversely isotropic materials, see for example Pan and Chou (1976) and Loloi (2000). However, these solutions could be cumbersome to implement into a BEM code because of the multiple cases they consider to account for all possible material configurations and the relative positions of the source and field points. On the other hand, Távara et al. (2008) have recently derived completely general and unique expressions valid for all possible configurations given in terms of real functions only (no difficulties with using complex functions). The solutions due to Távara et al. (2008) have been used in this work.

According to Távara et al. (2008), the displacement fundamental solutions when $x' = 0$ has the form

$$U^0(x) = \frac{1}{4\pi r}H(x), \tag{12}$$

where $r = |x|$, and the matrix $H(x)$ is the modulation function of the displacement fundamental solution. The matrix $H(x)$ is symmetric and it depends on the direction of r but not on its magnitude (see Figure 4). A relatively simple and general expression of $H(x)$ can be obtained using the auxiliary vector $\hat{x} = (r_{12}, 0, x_3^0)$, where $r_{12} = \sqrt{(x_1^0)^2 + (x_2^0)^2}$; and the triad $[n, m, \hat{x}/r]$ with $n = (c, 0, -s)$ and $m = (0, 1, 0)$ where $c = cos\,\phi = x_3^0/r$ and $s = sin\ \phi = r_{12}/r$, and the angle $0 \le \phi \le \pi$, see Figure 4. For such a coordinate system only the coefficients $H_{ii}(\hat{x})$ and $H_{13}(\hat{x})$ are non-zeros (see Appendix A). The general expression of the tensor $H(x)$ for any x can be obtained by transformation of components:

$$H_{ij}(x) = \Omega_{ik}\,\Omega_{js}H_{ks}(\hat{x}), \tag{13}$$

where the rotation matrix Ω_{ij} is

$$\Omega_{ij} = \begin{pmatrix} \cos\theta & -\sin\theta & 0 \\ \sin\theta & \cos\theta & 0 \\ 0 & 0 & 1 \end{pmatrix}. \tag{14}$$

The computation of the traction fundamental solution, $T^0(x)$, follows a similar procedure. The details can be found in Távara et al. (2008).

Finally, the fundamental solutions $U_{ik}(x)$ and $T_{ik}(x)$ have to be transformed from the local coordinate system, (x_1^0, x_2^0, x_3^0), to the global one in order to assemble the boundary integral equation (11). The fundamental solutions are transformed from the local coordinate system to the global one via the standard transformations for second order tensors (see Ting, 1996):

$$\begin{aligned} U_{ij}(x) &= a_{ik}a_{jl}U^o_{kl}(x) \\ \text{and } T_{ij}(x) &= a_{ik}a_{jl}T^o_{kl}(x), \end{aligned} \tag{15}$$

where a_{ik} is the transformation matrix.

BEM models are discretized using 9-node quadrilateral elements. Continuous elements are used everywhere in the model, except at the intersections of the interface and the crack surfaces with model surface. In such cases one- and two-side discontinuous elements are used in order to avoid common nodes at the intersections (see Figure 5). It is worth noting that, although discontinuous elements are not strictly necessary to solve most of the practical bimaterial crack problems; they have been implemented in this work in order to develop a versatile and robust discretization strategy capable of dealing with general multiple subdomain problems (including the case of more than two subdomains sharing a single edge). At the same time, the implementation remains open to introduce further extensions to account for crack propagation which could require of the automatic model remeshing.

The regular BEM integrals over continuous and discontinuous elements are evaluated using standard Gaussian quadrature. In the case of nearly singular integrals an adaptive element subdivision technique is also employed. On the other hand, the Cauchy principal value integrals and the free terms are evaluated using the rigid body motion approach (see Aliabadi, 2002). Singular integrals are computed using the variable transformation technique due to Lachat and Watson (1976).

The equation (11) is applied to each of the subdomains while considering the orientation of the material as explained before. The equilibrium, $t_I = -t_{II}$, and continuity, $u_I = u_{II}$, conditions are enforced at the nodes used to discretize the common interface Γ_{I-II}. The resultant system of equations is solved for the unknown traction and displacement nodal values after specifying the boundary conditions. It is worth noting that the implemented BEM code is not capable of detecting contact between the crack surfaces, and so, its application is restricted to open cracks only. For further details on the multi-domain BEM formulation and implementation the reader is referred to the book by Aliabadi (2002).

The computation of the *J*-integral are included in the BEM code as a post-processing procedure, and so, it could be applied to the results from a particular model at a later stage. The required stresses, strains and derivatives of displacements at internal points are directly obtained from their boundary integral representations (Aliabadi, 2002):

$$u_{i,m}(X') = \int_{\Gamma} U_{ij,m}(x,X')t_j(x)\mathrm{d}\Gamma(x) - \int_{\Gamma} T_{ij,m}(x,X')u_j(x)\mathrm{d}\Gamma(x) \tag{16}$$

where X' is the coordinate of the internal point, $U_{ij,m}(x,X')$ and $T_{ij,m}(x,X')$ are the derivatives of the fundamental displacement $U_{ij}(x,X')$ and traction $T_{ij}(x,X')$ fundamental solutions respectively (see Távara et al., 2009). The boundary Γ corresponds to that of the subdomain where the internal point X' lies on. Strains and stresses at internal points can then be easily computed using the definition of the infinitesimal strain tensor $\varepsilon_{ij} = \frac{1}{2}(u_{i,j} + u_{j,i})$ and the constitutive relationships in equation (1).

On the other hand, the derivatives of the displacements, strains and displacements for boundary points are evaluated from the boundary displacements and tractions by means of a procedure similar to that usually used for finite elements. For further details the reader is referred to the paper by Ortiz and Cisilino (2005).

Finally, and in order to proceed with the *J*-integral computation, the resultant displacement derivatives, strains and stresses for both internal and boundary points are transformed to the local the crack-front

coordinate system (x_1^*, x_2^*, x_3^*) (see Section 4) using the standard transformation rule for second-order tensors (see Ting, 1996).

6 *J*-integral Computation

The computation of *J*-integral at any position $\boldsymbol{\eta}$ on the crack front requires of the evaluation of a volume integral within closed domains that enclose a segment of the crack front $\boldsymbol{L_c}$ (see equations 9 and 10). A natural choice here is to make $\boldsymbol{\eta}$ coincident with the element nodes on the crack front, while $\boldsymbol{L_c}$ is taken as the element or element sides at which points $\boldsymbol{\eta}$ lies (on see Figure 6). The portion of the model domain in which the volume integrals are evaluated is discretized using 27-node cells. The cells are similar to the three-dimensional finite elements and they are implemented using an isoparametric interpolation scheme, being their nodes the internal points of the BEM analysis. Thus, the values of stresses, $\boldsymbol{\sigma_{ij}^*}$, strains, $\boldsymbol{\varepsilon_{ij}^*}$, and displacements derivatives, $\boldsymbol{u_{i,m}^*}$, are interpolated by means of the cell interpolation functions, $\boldsymbol{\Psi_i}$. Besides, the boundary mesh is designed to have a web shape around the crack front in order to build the integration volumes with the shape of cylinders. This is illustrated in Figure 7, where the frontal face of the model has been partially removed to show the crack and the integration domains.

As it is depicted in Figure 6, three different cases are considered depending on whether the crack front position *M* is a mid-side node, it is shared by two elements, or it is located coincident with the external surface (surface node). If the node *M* is a mid-side node or surface node, $\boldsymbol{L_c}$ (the segment of the crack front over which the *J*-integral is computed) spans over one element, connecting nodes *M*-1, *M*, and *M*+1 and nodes *M*-2, *M*-1 and *M*, respectively. On the other hand, if *M* is a shared node, $\boldsymbol{L_c}$ spans over two elements, connecting nodes from *M*-2 to *M*+2.

The function $\boldsymbol{q}$ is defined to vary quadratically in the directions tangential and normal to the crack front. This bi-quadratic definition of $\boldsymbol{q}$ has been employed with excellent results in the computation of EDI for a variety of problems in previous works (see Cisilino et al, 1998; Cisilino and Aliabadi, 1999; Ortiz and Cisilino, 2005 and Balderrama et al., 2006 and 2008). Within this approach, and considering that the evaluation point $\boldsymbol{\eta}$ is at the middle of the crack front segment $\boldsymbol{L_c}$, and $\boldsymbol{r_0}$ is the radius of the integration domain, the function $\boldsymbol{q}$ is written as:

$$q(x^*) = \left|1 - \left(\frac{x_3^*}{\frac{L_c}{2}}\right)\right| \cdot \left[1 - \left(\frac{r}{r_0}\right)^2\right] \tag{17}$$

where $\boldsymbol{r}$ is the distance from the crack front in the $\boldsymbol{x_1^* - x_2^*}$ plane as it is depicted in Figure 1. Function $\boldsymbol{q}$ is specified at all nodes within the integration volumes. Consistent with the isoparametric formulation, the *q*-values are interpolated using

$$q = \sum_{i=1}^{27} \Psi_i Q^i, \tag{18}$$

where $\boldsymbol{\Psi_i}$ are the shape functions defined within the volume cell and $\boldsymbol{Q^i}$ are the nodal values for the *i*th node. From the definition of $\boldsymbol{q}$ (see equation 7), $\boldsymbol{Q^i = 0}$ if the *i*th node is on $\boldsymbol{S_0}$ while for nodes inside *V*, $\boldsymbol{Q^i}$ are given by interpolating between the nodal values on $\boldsymbol{L_c}$ and $\boldsymbol{S_0}$.

Following standard manipulations the derivatives of $\boldsymbol{q}$ are:

$$q_{k,j} = \sum_{i=1}^{27} \sum_{l=1}^{3} \frac{\partial \Psi_i}{\partial \zeta_l} \frac{\partial \zeta_l}{\partial x_j} Q^i, \tag{19}$$

where $\boldsymbol{\zeta_k}$ are the coordinates in the cell isoparametric space and $\boldsymbol{\partial \zeta_k / \partial x_j}$ is the Jacobian matrix of the transformation.

Finally, if Gaussian integration is used, the discretized form of expression (9) is

$$\bar{G}(\eta) = \sum_{\text{cells in } V} \sum_{p=1}^{m} \left\{ \left(\sigma_{ij}^* \, u_{j,k}^* - \sigma_{ij}^* \, \varepsilon_{ij}^* \, \delta_{ki} \right) q_{k,j} det \left(\frac{\partial x_j}{\partial \zeta_k} \right) \right\}_p w_p, \tag{20}$$

where $\boldsymbol{m}$ is the number of Gaussian points per cell, and $\boldsymbol{w_p}$ are the weighting factors.

7 Application Examples

7.1 Thick tension bimaterial plate with a centre interface crack

A thick bimaterial plate containing a through crack on the interface is considered in the first example. A schematic representation of the problem geometry, dimensions and boundary conditions are depicted in Figure 8. Model discretization is similar to that depicted in Figure 7. It consists of 658 elements and 2855 nodes. Eighteen elements are placed along the crack front, and a total of 126 elements are used in the crack discretization. Five rings of cells with normalized radii r/a = 0.1, 0.2, 0.3, 0.44 and 0.64 are accommodated around the crack front for J computations. With this purpose 648 cells and 6438 nodes are employed.

In order to validate the code and to allow comparisons with other results from the bibliography, the problem was solved first for homogeneous cases, this is, the material elastic constants and orientations were set the same for both subdomains. The first case is that of an isotropic homogeneous plate with material elastic properties E=E'=100 GPa, ν=ν'=0.3 and μ'=0.5E/(1+ν). Computed J values along the crack front are presented in Figure 9, where the origin of the normalized coordinate, z/t=0, corresponds to the specimen mid-plane (see Figure 8*b*). The reference values are those reported by Raju and Newman (1977) for a homogeneous centre cracked specimen and presented in a polynomial form by Aliabadi (1996). Since reference results are reported in terms of the mode-I stress intensity factors, K_I, they have been converted to J values using the expression (see for example Anderson, 2005)

$$J = K_I^2 / \bar{E} \tag{21}$$

where $\boldsymbol{\bar{E} = E/(1-\nu^2)}$ for the plane strain condition. It is worth mentioning that the reference results are reported in terms of stress intensity factors with an accuracy of 5%. So that, when they are converted into J values using expression (21), the error bound is increased to around 10%. The accuracy of the reference J results is indicated in Figure 9 using the error bars. Data in Figure 9 are normalized with respect to the J value for a crack in a infinite homogenous plate under plane strain condition, $\boldsymbol{J_0 = \sigma^2 \pi a / \bar{E}}$. Excellent agreement is found between the reference and computed results throughout the specimen thickness. Computed results are well within the error bounds of the reference results. Results of similar accuracy were obtained using a single-domain dual boundary element method (DBEM) in a previous work by Cisilino, et al. (1998).

For the next two homogeneous cases the direction of the axis of symmetry, $\boldsymbol{x_3^0}$, is chosen to be parallel to the crack plane, this is, coincident with the global directions x and z, respectively. For these cases the material elastic constants are chosen the same to those of the laminated used by Ariza and Dominguez (2004b). The five independent values of the coefficients of the tensor $\boldsymbol{C_{ij}}$ (see equation 3) are

$$C_{11} = 5.37 \text{ GPa},\ C_{12} = 1.34 \text{ GPa},\ C_{13} = 3.35 \text{ GPa},\ C_{33} = 251.168 \text{ GPa}, \text{ and } C_{44} = 5 \text{ GPa}. \quad (22)$$

The associated elastic properties are: E= 5 GPa, E'= 247.83 GPa, ν=0.245, ν'= 0.01 and μ'= 2.5. The material orientation is specified for each subdomain by means of the angles $(\boldsymbol{\alpha, \beta, \gamma})$ which define the orientation of $\boldsymbol{x_3^0}$, the material axis of symmetry, with respect to the global coordinate system $(\boldsymbol{x, y, z})$. In this way, for the material axis of symmetry oriented in the direction global direction x, the orientation angles are are 0°/90°/90°, while for the material axis of symmetry oriented in the global direction z, the angles are 90°/90°/0°.

Computed results along the crack front are presented in Figure 10. In other to compare with other results, data in Figure 10 is presented in terms of normalized stress intensity factors, $\boldsymbol{K_I/K_0}$, where $\boldsymbol{K_0 = \sigma\sqrt{\pi a}}$. To compute the stress intensity factors from the J results, the problem was assimilated to a two-dimensional one in the xy plane. Stress intensity factors were computed from the J results using the expressions (see Chu and Hong, 1990),

$$J_1 = a_{11}K_I^2 + a_{12}K_IK_{II} + a_{22}K_{II}^2 \quad (23)$$
$$\text{and } J_2 = b_{11}K_I^2 + b_{12}K_IK_{II} + b_{22}K_{II}^2,$$

where the coefficients a and b depend on the elastic material properties and the material orientation. The coefficients $\boldsymbol{a_{12}}$, $\boldsymbol{a_{22}}$ and the three coefficients $\boldsymbol{b}$ are zero when one of the principal axes of the material is parallel to the crack plane. Thus, for the cases considered in this work

$$J_1 = a_{11}K_I^2. \quad (24)$$

The values for the coefficient $\boldsymbol{a_{11}}$ as a function of the ratio between the Young modulus in the xy plane, $\boldsymbol{E_x/E_y}$, are reported in Table 1.

It can be seen in Figure 10 that with the only exceptions of the regions next to the lateral faces of the specimen (say, $\boldsymbol{|z/t| > 0.45}$) where the boundary layer effect takes place, the stress intensity factor value is nearly constant along the crack front. Also plotted in Figure 10 there are two sets of results computed using a two-dimensional high-resolution finite element model. The finite element model was solved using Abaqus (2009), and it was discretized using a fine regular mesh consisting of 9,600 8-node biquadratic, plane stress elements (CPS8R). The stress intensity factors were computed using an Abaqus built-in facility. The resultant normalized stress intensity factors are $\boldsymbol{K_I/K_0 = 1.124}$ and $\boldsymbol{K_I/K_0 = 1.184}$ for the material axis of symmetry oriented in the global directions x and z, respectively. The difference between the BEM and FEM results is less than 2%.

The final case consists in a heterogeneous plate with the axis of symmetry of the material oriented in the global directions z and y for the subdomains I and II, respectively; this is, 90°/90°/0° for the subdomain I and 90°/0°/90° for the subdomain II. The material elastic properties are the same of the previous cases. Computed results are presented in Table 2. The results are normalized with respect to $\boldsymbol{J_0 = \sigma^2\pi a/E'}$. It can be seen that J value is nearly constant along the complete crack front. Besides, the path independence is found excellent with a standard deviation of around 5% for the results computed using the domains with radii $\boldsymbol{r/a \geq 0.20}$. The only exceptions are the positions next to the lateral face of the specimen, where the

boundary layer effect takes place and the applicability of the *J*-integral is not strictly valid. The smallest integration domains with $\boldsymbol{r/a = 0.10}$ do not provide accurate results. This is attributed to the fact that these domains are discretized using a single cell in the radial direction. Similar behaviours were found in previous works by the authors (see for example Cisilino et al., 1998 and Ortiz and Cisilino, 2005).

7.2 Bimaterial laminate with an edge interface crack

It is considered in this example the analysis of an edge crack in a bimaterial laminate. The model geometry and discretization are depicted in Figure 11. Model dimensions are: crack length a=10 mm, specimen width b=4a, height h=a and thickness $2t$=1.5a. Material properties are the same used by Ariza and Dominguez (2004b) and reported in Equation (22) in the previous example. The discretization of the model is that illustrated in Figure 7, using 596 elements. Five rings of cells with normalized radii r/a = 0.05, 0.1, 0.15, 0.22 and 0.32 are accommodated around the crack front for the *J* computations. Five hundred and four cells are used in the construction of the integration domains.

The model was solved for a number of relative orientations of the axis of symmetry of the material in both subdomains. The computed results are reported in Figure 12. *J*-results in Figure 12 are normalized with respect to $\boldsymbol{J_0 = \sigma^2 \pi a / E'}$. It can be seen that when one of the principal axes of the material is specified perpendicular to the crack front direction for both subdomains, the *J*-integral results along the crack front are symmetric with respect to the specimen mid-plane (z/t=0). These are the cases for the results labelled 90°/90°/0°-90°/90°/0° and 0°/90°/90°-90°/90°/0° in the figure. On the other hand, when the orientation of the principal axes of the material are arbitrary in at least one of the two subdomains, the *J*-integral results along the crack front are not symmetric with respect to the specimen mid-plane. The extreme values for the *J*-integral are attained at the free surface.

7.3 A circumferential interface crack in a cylindrical bimaterial bar

The last example consists in a cylindrical bimaterial bar containing a circumferential crack subjected to remote axial tension σ, see Figure 13*a*. The radius of the bar is b=5a and its height h=24a, being a the crack depth. A total of 684 elements are employed in the model discretization. Four rings of cells with radii r/a = 0.25, 0.5, 0.75 and 1 are accommodated around the crack front for the *J* computations. Integration domains are constructed using 672 cells. The model discretization is illustrated in Figure 13*b*. Material properties are the same reported in Equation 22 for a previous example.

The problem was solved considering different material orientations. The results are reported in Figure 14. In every case the results are normalized with respect to $\boldsymbol{J_0 = \sigma^2 \pi a / E'}$. The first solution is for an isotropic homogeneous material and it was used with validation purposes. The *J* result is constant along the complete crack front. The difference between the computed result and that reported by Murakami and Okazaki (1976) is 5% (it is worth noting that the reported precision for the reference solution is 3%). The second solution is for a homogeneous transversely-isotropic case, with the material symmetry axis specified coincident with the direction y for both subdomains (results labeled 90°/0°/90°-90°/0°/90° in Figure 14). Once again, and as it was expected, the computed *J* values are constant along the complete crack front. In the third case the orientation of the material axis of symmetry are different in each subdomain: for the subdomain I the

material axis of symmetry is oriented in the z-direction, while for the subdomain II it is oriented in the y-direction (results labelled 90°/90/0°-90°/0°/90° in Figure 14). The J results exhibit a periodic variation along the crack front. Minimum values occur in the positions coincident with the direction of the z-axis, while the maximums are in the positions coincident with the direction of the x-axis. In the last case, the orientation of the material axis of symmetry is specified in the x-direction for both subdomains (results labelled 0°/90/90°-0°/90°/90° in Figure 14). As for the previous case, the J results exhibit a periodic variation along the crack front. However, in this case minimum values occur in the positions coincident with the direction of the x-axis, while the maximums are in the positions coincident with the direction of the z-axis.

8 Conclusions

A boundary element methodology for the analysis of three-dimensional interface cracks in transversely isotropic bimaterials has been presented in this paper. The analysis is addressed using a multidomain BEM formulation in order to account for the different material properties at both sides of the crack. The J-integral is computed along the crack front using the Energy Domain Integral (EDI) methodology. This is implemented as a post-processing technique, and so, it can be applied to the results from a particular model at a later stage. The implementation takes advantage of the efficiency of the boundary integral equation to directly obtain the required displacement derivatives, stress and strain fields from their boundary integral representations.

The efficiency and accuracy of the proposed implementation has been addressed by analysing a number of examples with straight and curved crack fronts. The computed results compared very well with those reported in the literature for benchmark problems. Besides, the implemented algorithm allowed studying the effect of the relative orientations of the materials on both sides of the crack on the J integral values.

Maximum errors and dependence of the computed results with the integration paths occur for surface cracks at the intersection of the crack front with a free surface. In this sense it is worth noting that the formulation of EDI methodology used in this work is based on the assumption that the near-crack tip fields asymptote to the plane strain fields along the crack front. But it turns out that this assumption does not hold at the intersection of the crack front and a free surface, and so the proposed methodology is not strictly applicable. This problem remains unsolved in this work. Following previous work (Cisilino and Ortiz, 2005), alternative approaches for the selection of the auxiliary function $\boldsymbol{q}$ for the implementation of the EDI could be explored to improve the accuracy of the computations.

Acknowledgements

This work has been partially supported by the Agencia Nacional de Promoción Científica y Tecnológica (ANPCyT) of Argentina through the grant PICT 2007 Nº 1154. J.E. Ortiz has been supported by the Programa Ramón y Cajal of the Spanish Ministry of Science and Innovation.

References

Abaqus 6.9-1 (2009). Dassault Systemes, Providence, RI, USA

Aliabadi M.H. (1996): Database of Stress Intensity Factors. *Computational Mechanics Publications*, Southampton, UK.

Aliabadi M.H. (1997). Boundary element formulations in fracture mechanics. *Applied Mechanics Review*, 50: 83-96.

Aliabadi M.H. (2002). *The Boundary Element Method, Volume II: Applications in Solids and Structures*. Wiley, Chichister, UK.

Anderson T.L. (2005). *Fracture Mechanics: Fundamentals and Applications*. Second Edition, CRC Press, Boca Ratón, USA.

Ariza M.P. and Dominguez J. (2004a). Dynamic BE analysis of 3-D cracks in transversely isotropic solids. *Computer Methods in Applied Mechanics and Engineering*, 193/9-11: 765-779.

Ariza M.P. and Dominguez J. (2004b). Boundary element formulation for 3D transversely isotropic cracked bodies. *International Journal for Numerical Methods in Engineering*, 60/4: 719-753.

Balderrama R., Cisilino A.P., Martinez M. (2006). BEM analysis of three-dimensional fracture problems using the energy domain integral. *ASME Journal of Applied Mechanics*, 73/6:959-969.

Balderrama R., Cisilino A.P., Martinez M. (2008). Boundary element analysis of three-dimensional mixed-mode thermoelastic crack problems using the interaction and the energy domain integrals. *International Journal for Numerical Methods in Engineering*, 74/2: 294-320.

Boniface V. and Banks-Sills L. (2002). Stress intensity factors for finite interface cracks between a special pair of transversely isotropic materials. *ASME Journal of Applied Mechanics*, 69/3: 230-239.

Bowie, O.L.; Freese, C.E. (1972) Central crack in plane orthotropic rectangular sheet. *International Journal of Fracture Mechanics*, vol. 8/1, pp. 49-58.

Chen C-S, Chen C-H and Pan E. (2009). Three-dimensional stress intensity factors of a central square crack in a transversely isotropic cuboid with arbitrary material orientations. *Engineering Analysis with Boundary Elements*, 33: 128– 136

Chow W. T. and Atluri S. N. (1998). Stress intensity factors as the fracture parameters for delamination crack growth in composite laminates. Computational Mechanics, 21: 1-10.

Chu S.J. and Hong C.S. (1990). Application of the J_k integral to mixed mode crack problems for anisotropic composite laminates. *Engineering Fracture Mechanics*, 35/6:1093-1103.

Cisilino A.P., Aliabadi M.H. and Otegui J.L. (1998). Energy domain integral applied to solve centre and double-edge crack problems in three dimensions. *Theoretical and Applied Fracture Mechanics*, 29:181-194.

Cisilino A.P. and Aliabadi M.H. (1999). Elastoplastic BEM implementation of the energy domain integral for the analysis of 3D fracture problems. *International Journal of Fracture*, 96:229-245.

Freed Y. and Banks-Sills L. (2005). A through interface crack between a ±45◦ transversely isotropic pair of materials. *International Journal of Fracture* , 133: 1–41.

Gibson R.F. (2007). *Principles of Composite Material Mechanics*. CRC Press, London.

He W.J., Lin D.S. and Ding, H.J. (1994). A boundary element for crack analysis at a bimaterial interface. *Engineering Fracture Mechanics*, 49/3:405-410.

Lachat J.C. and Watson J.O. (1976). Efective numerical treatment of boundary integral equations: a formulation for three-dimensional elastostatics. *International Journal for Numerical Methods in Engineering*, 10: 991-1005.

Loloi M. (2000). Boundary integral equation solution of three-dimensional elastostatic problems in transversely isotropic solids using closed-form displacement fundamental solutions. *International Journal for Numerical Methods in Engineering*, 48: 823-842.

Mao R. and Sun G. (1995). A study of the interaction between matrix crack and matrix-fibre interface. *Engineering Fracture Mechanics*, 51/3: 469-477.

Moran B. and Shih C.F. (1987). A general treatment of crack tip contour integrals. International *Journal of Fracture*, 35/4: 295-310.

Murakami Y. and Okazaki Y. (1976). A simple procedure for the accurate determination of stress intensity factors by finite element method. *Trans. Japan Soc. Mech. Engrs.*, 42/364: 3679-3687

Natha R. and Moran B. (1993). Domain integrals for axisymmetric interface crack problems. *International Journal of Solids & Structures*, 30/15: 2027-2040.

Nikishkov G.P. and Atluri S.N. (1987). Calculation of fracture mechanics parameters for an arbitrary three-dimensional crack by the equivalent domain integral method. *International Journal of Numerical Methods in Engineering*, 24/9:1801-1821.

Omer N. and Yosibash Z. (2008). Edge singularities in 3-D elastic anisotropic and multi-material domains. *Computer Methods in Applied Mechanics and Engineering*, 197: 959-978.

Ortiz J.E. and Cisilino A.P. (2005). Boundary element method for J-integral and stress intensity factor computations in three-dimensional interface cracks. *International Journal of Fracture*, 133:197-222.

Pan Y. and Chou, T. (1976). Point solution for an infinite transversely isotropic solid. *Journal of Applied Mechanics*, 98: 608-612.

Raju I.S. and Newman J.C. (1977). Three-dimensional finite-element analysis of fnite-thickness fracture specimens. *Technical Report NASA TN D-8414*.

Rice J.R. (1968). A path independent integral and the approximate analysis of strain concentration by notches and cracks. *ASME Journal of Applied Mechanics*, 379-386.

Sáez A., Ariza, M.P. and Dominguez J. (1997) Three-dimensional fracture analysis in transversely isotropic solids. *Engineering Analysis with Boundary Elements*, 20/4: 287-298.

Saliva R., Vénere M.J., Padra C., Taroco E. y Feijoó R.A. (2000). Shape sensitivity analysis and energy release rate of planar cracks embedded in three-dimensional bodies. *Computer Methods in Applied Mechanics and Engineering*, 188: 649-664.

Shah P.D., Tan C.L. and Wang X. (2006). Evaluation of T-stress for an interface crack between dissimilar anisotropic materials using the boundary element method. *Computer Modeling in Engineering & Science*, 13/3:185-197.

So W.M.G., Lau K.J. and Ng S.W. (2004). Determination of stress intensity factors for interfacial cracks using the virtual crack extension approach. *Computer Modeling in Engineering & Science*, 5/3:189-200.

Synge J.L.; Schild A. (1978). Tensor Calculus, Dover Publications, New York.

Tan C.L. and Gao Y.L. (1990). Treatment of bimaterial interface crack problems using the boundary element method. *Engineering Fracture Mechanics*, 36: 919-932.

Távara L., Ortiz J.E., Mantic, V. and París, F. (2008). Unique real-variable expressions of displacement and traction fundamentals solutions covering all transversely isotropic elastic materials for 3D BEM. *International Journal for Numerical Methods in Engineering*, 74:776-798.

Távara L., Mantic V., Ortiz J.E. and París F. (2009). Unique real-variable expressions of the integral kernels in the stress hypersingular boundary integral equation covering all transversely isotropic elastic materials for 3D BEM. *Submitted to the International Journal for Numerical Methods in Engineering*.

Ting T.C.T. (1996). *Anisotropic Elasticity: Theory and Applications*. Oxford University Press, Oxford, UK.

Appendix A

Non-zero components of the tensor $\boldsymbol{H}(\hat{\boldsymbol{x}})$:

$$\boldsymbol{H_{11}} = \frac{\mathbf{1}}{\mathbf{C_{66}}\boldsymbol{\beta_3}} + \frac{\mathbf{C_{44}}\boldsymbol{c^2} + \mathbf{C_{33}}\boldsymbol{s^2}}{\mathbf{C_{11}}\mathbf{C_{44}}\boldsymbol{gh}} - \frac{\boldsymbol{f}}{\boldsymbol{\xi}} \tag{A1}$$

,

$$\boldsymbol{H_{22}} = \frac{\mathbf{1}}{\mathbf{C_{11}}\boldsymbol{g}} + \frac{\boldsymbol{f}}{\boldsymbol{\xi}}, \tag{A2}$$

,

$$\boldsymbol{H_{33}} = \frac{\mathbf{1}}{\boldsymbol{gh}}\left\{\frac{\boldsymbol{h} + \boldsymbol{c^2}}{\mathbf{C_{44}}} + \frac{\boldsymbol{s^2}}{\mathbf{C_{11}}}\right\}, \tag{A3}$$

$$H_{13} = \frac{(\mathrm{C}_{13} + \mathrm{C}_{44})sc}{\mathrm{C}_{11}\mathrm{C}_{44}gh}, \tag{A4}$$

$$\beta_3 = \left\{\frac{\mathrm{C}_{44}c^2 + \mathrm{C}_{33}s^2}{\mathrm{C}_{66}}\right\}^{1/2}, \tag{A5}$$

$$h = \left\{c^4 + \frac{\eta s^2 c^2}{\mathrm{C}_{11}\mathrm{C}_{44}} + \frac{\mathrm{C}_{33}s^4}{\mathrm{C}_{11}}\right\}^{1/2}, \tag{A6}$$

$$g = \left\{2(h + c^2) + \frac{\eta s^2}{\mathrm{C}_{11}\mathrm{C}_{44}}\right\}^{1/2}, \tag{A7}$$

$$\xi = g(h + g\beta_3 + \beta_3^2), \tag{A8}$$

$$\eta = \mathrm{C}_{11}\mathrm{C}_{33} - \mathrm{C}_{13}^2 - 2\mathrm{C}_{13}\mathrm{C}_{44}, \tag{A9}$$

where $= \cos\phi = x_3/r$, $s = \sin\phi = r_{12}/r$ and the angle ϕ is indicated in Figure 4.

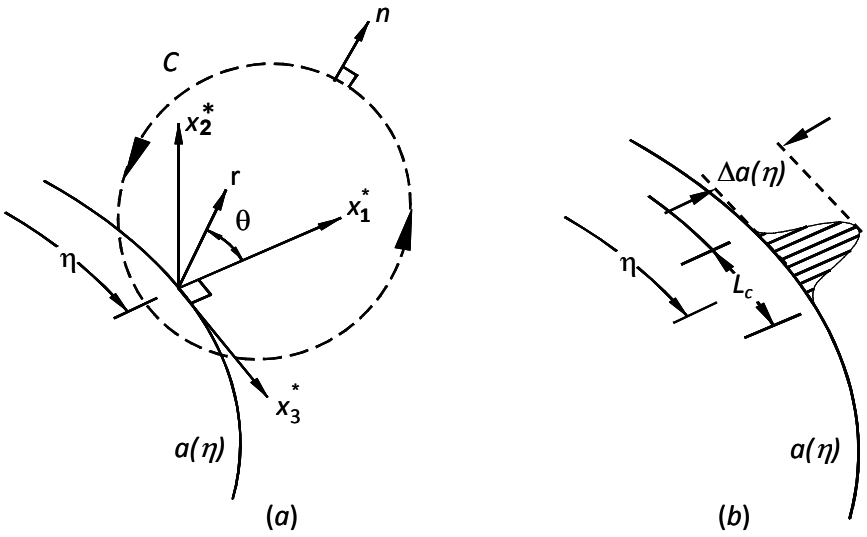

Figure 1: (*a*) Definition of the local orthogonal Cartesian coordinates at point η on the crack front, (*b*) Virtual crack front advance.

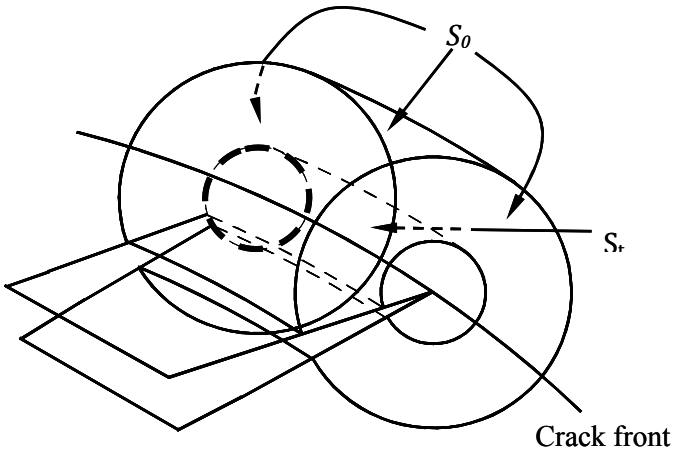

Figure 2: Tubular domain surrounding a segment of the crack front.

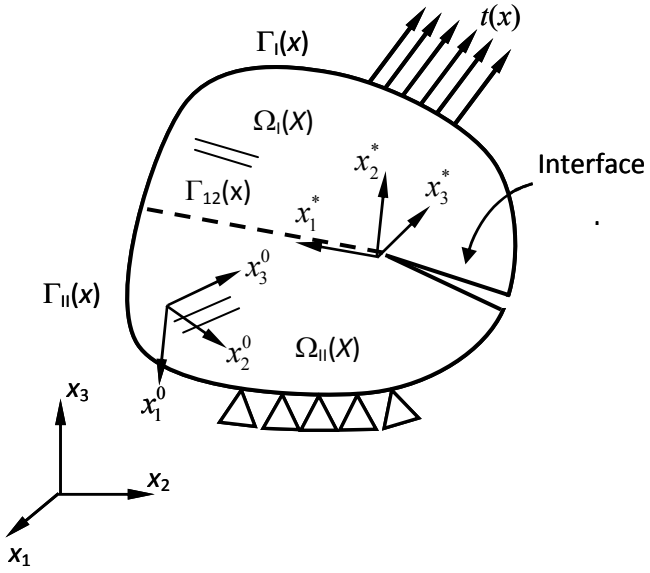

Figure 3: Schematic two-dimensional representation of the multi-domain BEM model with an interface crack.

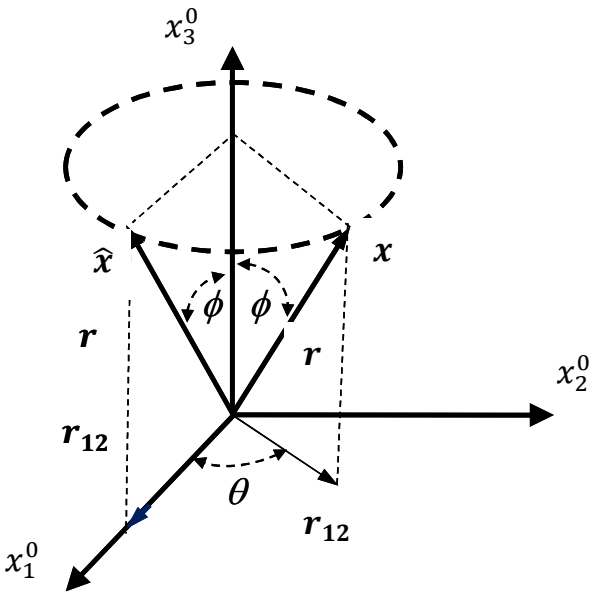

Figure 4: Point **x** and $\hat{\mathbf{x}}$ associated with a transversely isotropic material.

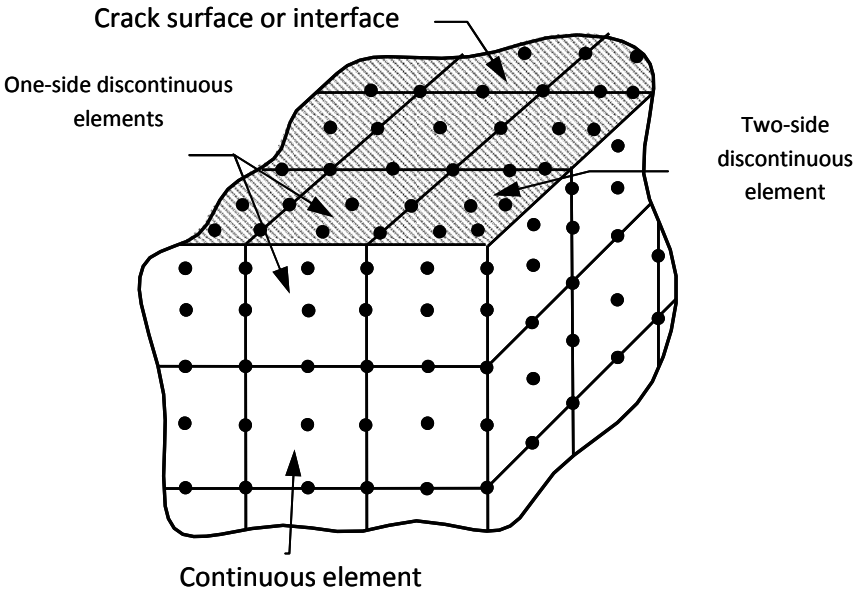

Figure 5: Model discretization strategy using continuous and

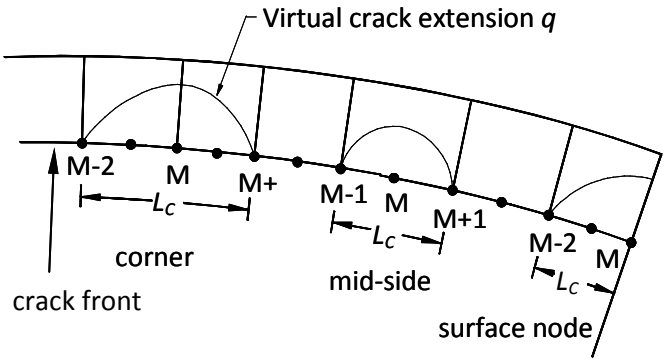

Figure 6: Schematic of the crack front region illustrating the virtual crack extensions for a corner node, a mid-node and a surface node.

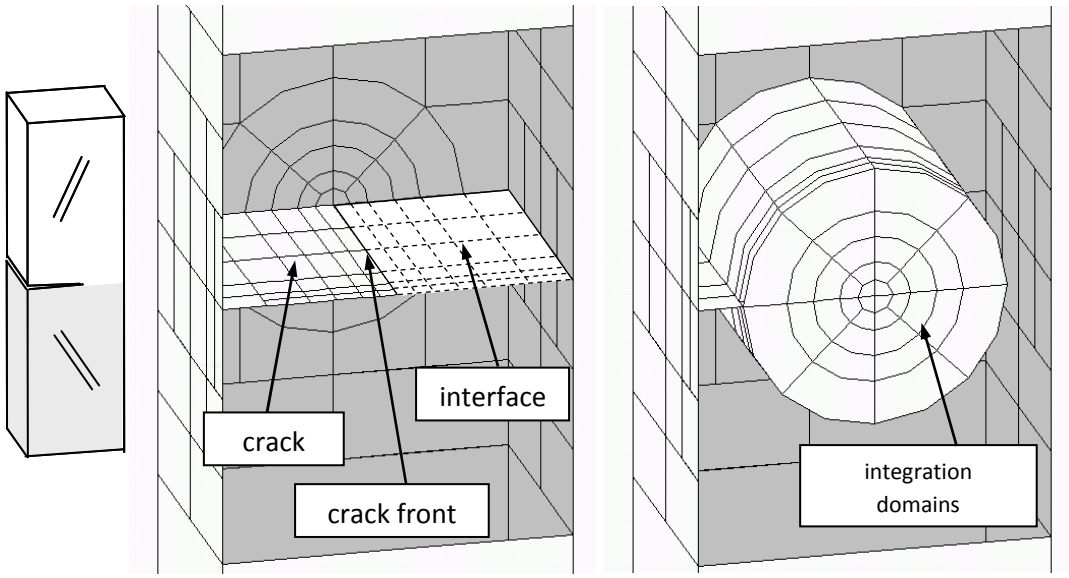

Figure 7: (*a*) Problem geometry, (*b*) Boundary Element discretization,

(*c*) Integration domains.

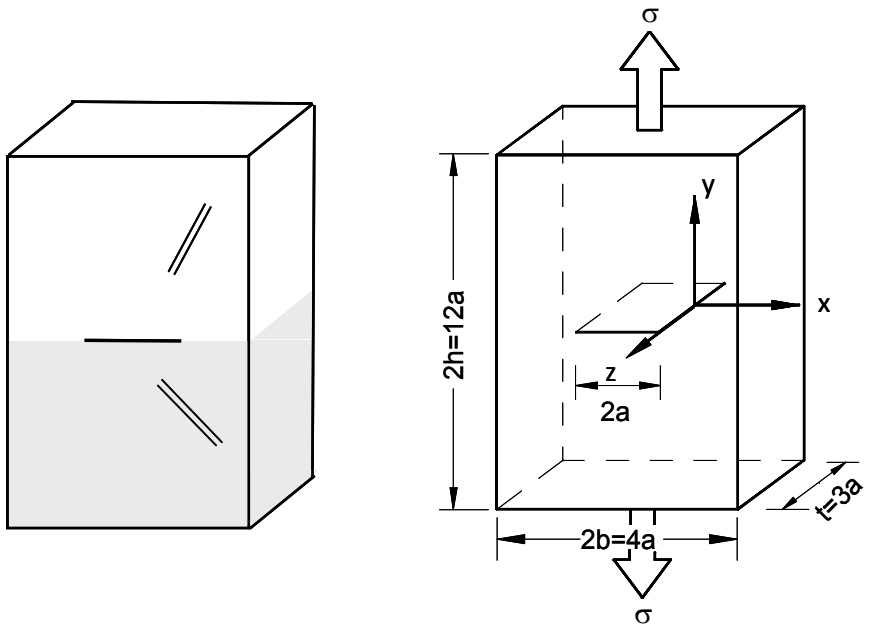

Figure 8: (*a*) Schematic representation of the thick tension plate with a centre interface crack, (*b*) Model dimensions.

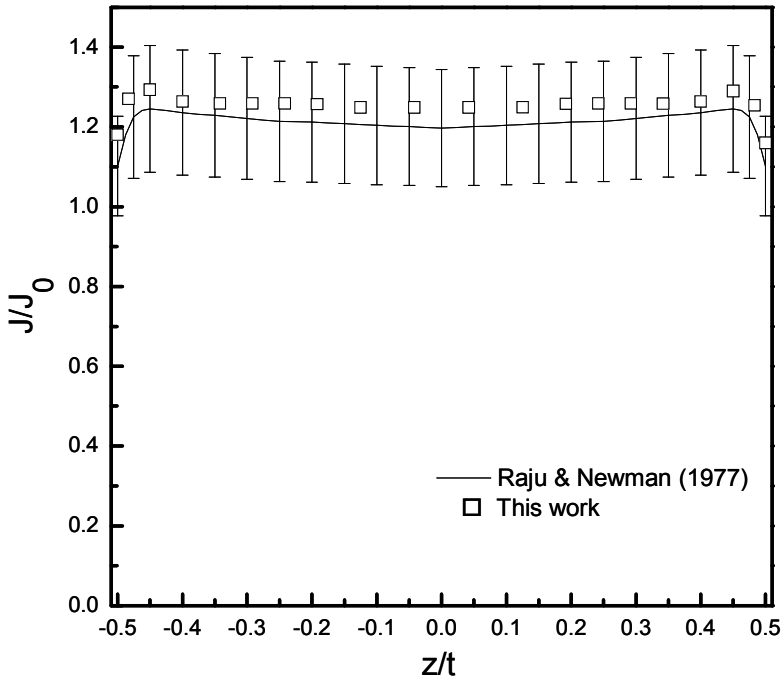

Figure 9: Normalized *J*-integral results along the crack front for the homogeneous isotropic centre crack specimen.

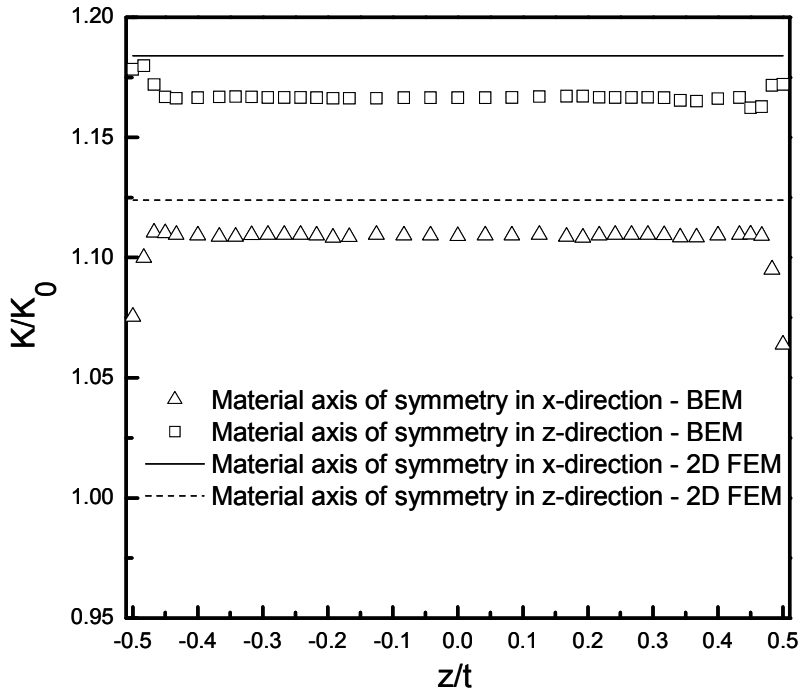

Figure 10: Normalized *SIF* results along the crack front for the homogeneous transversely-isotropic centre crack specimen.

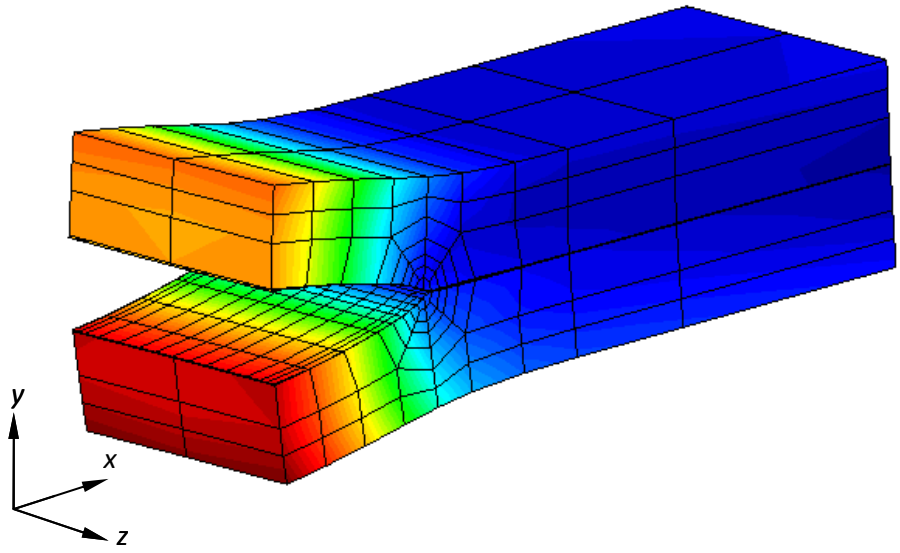

Figure 11: Bimaterial laminate with an edge crack (deformed geometry)

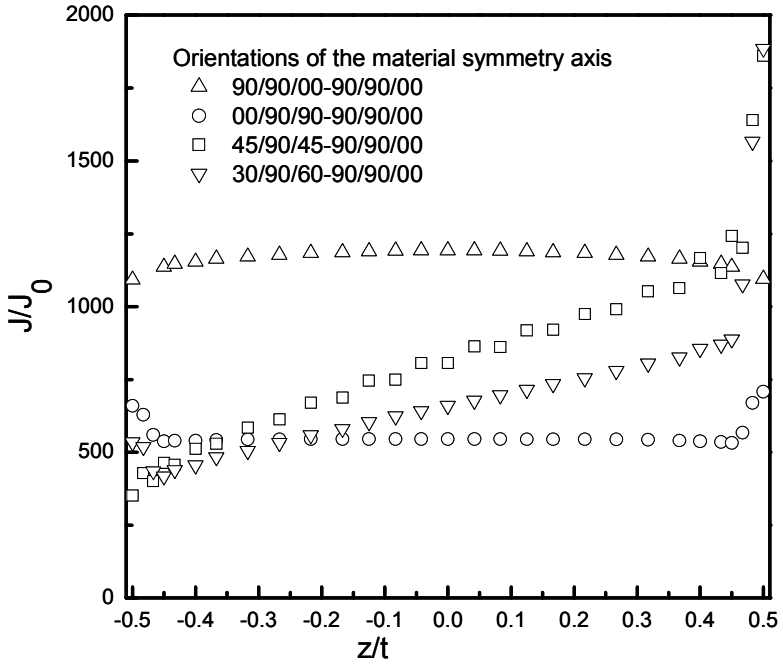

Figure 12: Normalized *J*-integral results along the crack front of the edge crack in the ply.

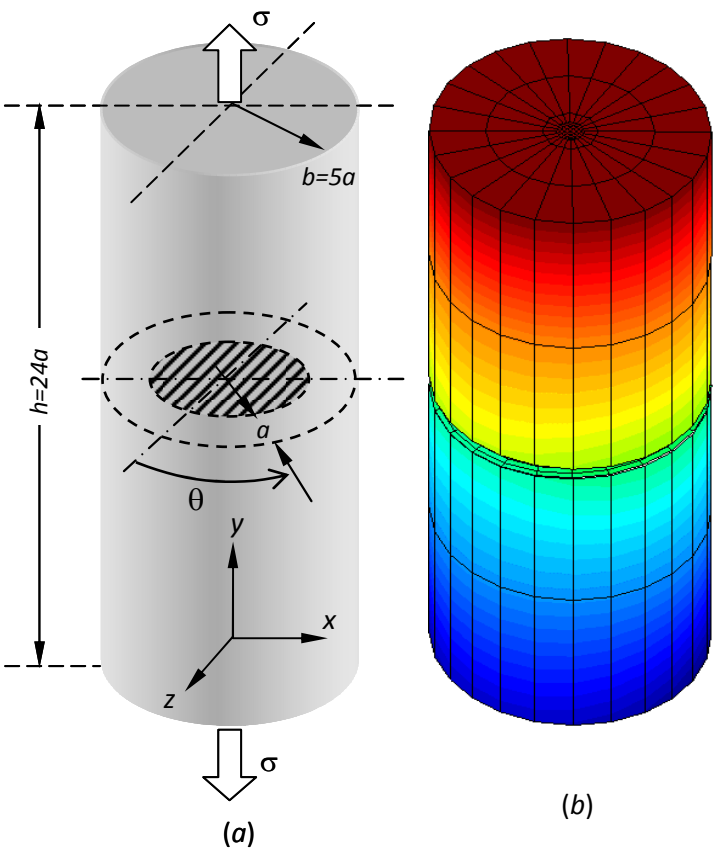

Figure 13: External circumferential interface crack in a cylindrical bimaterial bar, (*a*) model geometry and dimensions, (*b*) model discretization (deformed mesh)

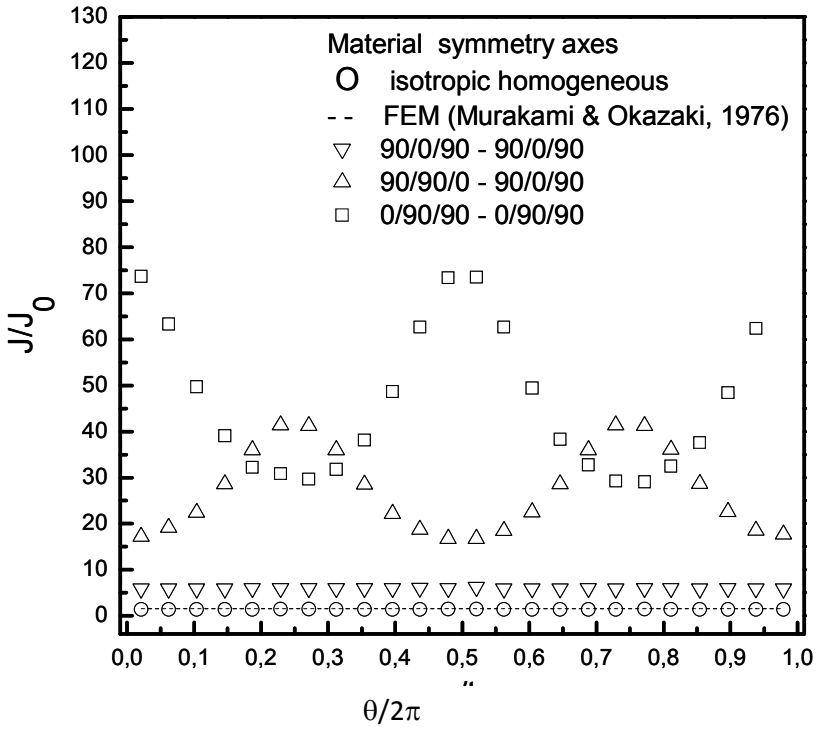

Figure 14: Normalized *J*-integral results along the crack front of the circumferential crack in the biomaterial bar.

Table 1: Resulting values for the coefficients a_{11} and Young Modulus ratios used to compute stress intensity factors from the *J* results.

Case	a_{11}	E_x/E_y
Material symmetry in *x*- direction	$0.112\ 10^{-9}$	49.57
Material symmetry in *z*- direction	$0.2\ 10^{-9}$	1

Table 2: Normalized *J*-integral results for the heterogeneous plate as a function of the integration domain size. The results for the smallest integration domains, *r/a*=1 (shaded column in the table) are excluded for the computation of the average value and the STD.

z/t	*r/a*					Average	STD
	0.10	0.20	0.30	0.44	0.64		
0.000	25.6382	30.4503	30.7658	30.7658	30.6081	30.5613	0.49
0.042	25.6382	30.4503	30.7658	30.7658	30.6081	30.5566	0.49
0.083	25.6382	30.4503	30.7658	30.7658	30.6081	30.5512	0.49
0.125	25.6382	30.4503	30.7658	30.7658	30.6081	30.5452	0.49
0.167	25.6382	30.4503	30.7658	30.7658	30.6081	30.5384	0.49
0.192	25.6382	30.4503	30.6869	30.7658	30.6081	30.5306	0.44
0.217	25.6382	30.4503	30.6869	30.7658	30.6081	30.5231	0.44
0.242	25.6382	30.4503	30.6869	30.7658	30.6081	30.5144	0.44
0.267	25.6382	30.4503	30.6869	30.7658	30.6081	30.5041	0.44
0.292	25.6382	30.4503	30.6869	30.7658	30.6081	30.4917	0.44
0.317	25.6382	30.3714	30.6869	30.6869	30.5292	30.4766	0.50
0.342	25.6382	30.3714	30.6081	30.6869	30.4503	30.4651	0.47
0.367	25.6382	30.3714	30.6081	30.6081	30.4503	30.4559	0.39
0.400	25.5593	30.3714	30.6081	30.6081	30.4503	30.4470	0.39
0.433	25.5593	30.2925	30.6081	30.6081	30.4503	30.4345	0.50
0.450	25.5593	30.2925	30.5292	30.6081	30.4503	30.4207	0.44
0.467	25.4804	30.2925	30.6869	30.7658	30.6869	30.4043	0.70
0.483	25.0071	29.9770	30.7658	31.1603	31.2391	30.3024	1.91
0.500	23.5871	28.5570	29.7403	30.3714	30.6081	29.8192	3.08

Key Engineering Materials Vol. 454 (2011) pp 79-96

doi:10.4028/www.scientific.net/KEM.454.79

Symmetric-Galerkin boundary element transient analysis of the DSIFs for the interaction of a crack with a circular inclusion

A.-V. Phan[1,a] , L. J. Gray[2,b] and A. Salvadori[3,c]

[1]Department of Mechanical Engineering, University of South Alabama, Mobile, AL 36688, USA
[2]CSM Division, Oak Ridge National Laboratory, Oak Ridge, TN 37831, USA
[3]DICATA, Università di Brescia, via Branze 38, 25123 Brescia, Italy

[a]vphan@jaguar1.usouthal.edu, [b]graylj1@ornl.gov, [c]alberto.salvadori@ing.unibs.it

Keywords: symmetric-Galerkin boundary element method, elastodynamics, crack-inclusion interaction, dynamic stress intensity factors, transient responses.

Abstract. A dynamic analysis of crack-inclusion interaction is described in this paper. The analysis employs a two-dimensional symmetric-Galerkin boundary integral formulation for multi-domain elastodynamic fracture analysis in the frequency domain. The multi-domain technique is based on the assumption of perfectly bonded inclusions. The numerical implementation of this boundary integral formulation is carried out with standard quadratic elements, allowing the use of an improved quarter-point element for accurately determining frequency responses of the dynamic stress intensity factors (DSIFs). To deal with singular and hypersingular integrals, the formulation is decomposed into two parts: the first part is identical to that for elastostatics while the second part contains at most logarithmic singularities. The treatment of the elastostatic singular and hypersingular singular integrals employs an exterior limit to the boundary, while the weakly singular integrals in the second part are handled by Gauss quadrature. Time histories (transient responses) of the DSIFs are obtained in a post-processing step by applying the standard fast Fourier transform algorithm to the frequency responses of these DSIFs. Two numerical examples are presented for the computation of the DSIFs due to crack-inclusion interaction under two types of impact loading: Heaviside step loading and blast loading. The numerical results are consistent and confirm the well known crack tip shielding mechanism observed during the interaction between a crack and a much stiffer inclusion.

Introduction

As the use of composite materials in industry (*e.g.*, airframes) has expanded, there is an increasing interest in their fracture behavior under impact loading conditions. Of particular interest is the dynamic fracture behavior due to crack-inclusion interaction in these materials. Among numerical methods available for this class of problems, boundary element method (BEM, *e.g.*, [1]) has emerged as an effective tool. The key feature of the BEM is that only the boundary of the domain is discretized. For wave problems posed as scattering from a finite body in an infinite domain, this means that an artificial truncation of the domain is not required. For fracture analysis the important implications are that the singular stress field ahead of the crack is not approximated, and that remeshing a propagating crack is an easier task. There are two types of BEM formulations in dynamics: frequency domain (FD, *e.g.*, [2–8]) and time domain (TD, *e.g.*, [8–10]). Nonlinear elastodynamics by means of incremental schemes requires the use of TD formulation [1] while a FD formulation is better suited for parallel computing and analyses of the same structure under different dynamic loading conditions (frequency responses are independent of each other as well as the loading). Although the FD formulation requires the

use of Fourier/Laplace transform if time solutions are needed, its implementation is generally simpler than for the TD formulation. For BEM works on the dynamic crack-inclusion interaction, FD formulation has been employed by Mykhas'kiv and Khay [11] while TD formulation has been preferred by several other research groups (*e.g.*, [12–15]).

A variant of the BEM, employing a Galerkin approximation of both the displacement boundary integral equation (BIE) and the hypersingular traction BIE, has been known as the symmetric-Galerkin BEM (SGBEM) (*e.g.*, [16]). Compared with the dual BEM (DBEM), the SGBEM is potentially more time-consuming as the Galerkin procedure is based upon an additional boundary integration. However, the SGBEM also offers several key advantages in fracture applications: (a) SGBEM uses the displacement BIE on the boundary part where displacement is prescribed and traction BIE on the boundary part where traction is known. As the name implies, this results in a symmetric coefficient matrix, and this remains true for fracture problems, with the proviso that the unknowns on the crack faces are the jumps in displacement. Thus, the extra computational expense can be partially offset by exploiting this symmetry, both in the matrix construction phase and in solving the linear system of equations; (b) unlike the DBEM or other collocation methods, there is no smoothness requirement on the displacement (*e.g.*, [17]) in order to evaluate the hypersingular integral; thus, standard *continuous* elements can be employed. The Galerkin approach can therefore easily exploit the highly effective quarter-point quadratic element to accurately capture the crack tip behavior. On the other hand, internal collocation, as often employed by the DBEM, results in a physically unappealing *discontinuous* interpolation; and (c) the weighted averaging formulation of Galerkin, by avoiding direct collocation at corners and junction points, provides a smoother solution in the neighborhood of geometric discontinuities. This is especially useful for dealing with kinked crack problems.

In addition to important developments of the SGBEM for stress and fracture analysis in elastostatics, the SGBEM for elastodynamics has been reported in the time domain (*e.g.*, [18,19]) and frequency domain (*e.g.*, [20–24]). However, to the best knowledge of the authors, no work on dynamic crack-inclusion interaction using SGBEM has been reported in the literature. This paper presents a study on the interaction between a crack and a circular inclusion using a symmetric-Galerkin boundary integral formulation for elastodynamics in the frequency domain (Fourier space).

In both finite and boundary element modeling of discrete cracks, the standard approach consists of incorporating the quarter-point (QP) element [25, 26] to improve the accuracy of stress intensity factor (SIF) calculations (*e.g.*, [27,28]). Nevertheless, in either finite or boundary element analyses, the prediction of K_{II} and K_{III} has not been nearly as accurate as for K_{I}. Recently, Gray and Paulino [29] have proved that, for an arbitrary crack geometry, a constraint exists in the series expansion of the crack opening displacement at the tip (see also [30]). As discussed in [29], the standard QP (SQP) element in general fails to satisfy this constraint, and this has led to the development of an improved modified QP (MQP) element [31]. It was demonstrated in [31–33] that the accuracy of the computed SIFs and/or T-stress can be significantly improved by incorporating this MQP element into the SGBEM. As a result, the MQP element is employed to determine the dynamic SIFs (DSIFs) in this work. Note that a recent development of the so-called enhanced QP (EQP) element [34] has suggested that EQP would provide even a better accuracy than MQP in evaluating the SIFs.

As the FD formulation is employed in this work, the DSIFs produced from any SGBEM analysis are a function of frequency. If time histories (transient responses) of the DSIFs are needed, the standard fast Fourier transform (FFT) algorithm can be used to obtain these time-dependent quantities.

Two numerical examples are reported to demonstrate the effectiveness of using the SGBEM for frequency-domain elastodynamics and Fourier transforms in the analysis of crack-inclusion interaction. These problems involve the determination of transient responses of the DSIFs for a crack interacting with a circular inclusion in a finite plate and a three-point bend beam.

Boundary Integral Equations for Elastodynamic Fracture Analysis

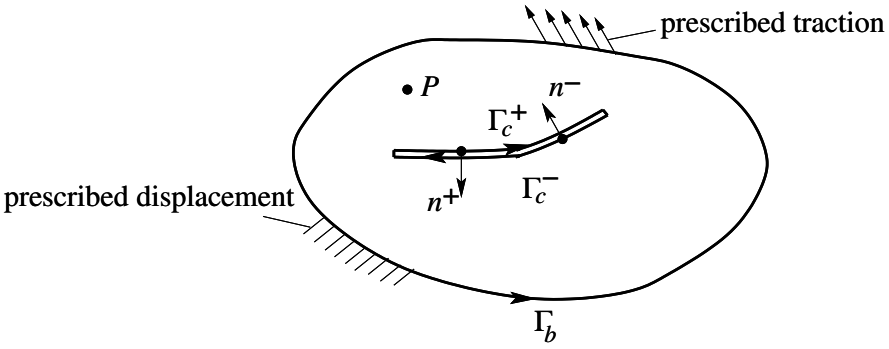

Fig. 1: A domain containing a crack

Consider a finite domain containing a crack as shown in Fig. 1. The crack is composed of two symmetrically loaded surfaces Γ_c^+ and Γ_c^- which are initially coincident. Let the boundary of the domain be Γ and $\Gamma = \Gamma_b \cup \Gamma_c^+ \cup \Gamma_c^-$. Also, let $\Gamma_b = \Gamma_{bu} \cup \Gamma_{bt}$ where Γ_{bu} is part of Γ_b where displacement is specified and Γ_{bt} is part of Γ_b where traction is prescribed. Finally, let $\Gamma_t = \Gamma_{bt} + \Gamma_c^+$ and note that traction is supposed to be known on $\Gamma_c = \Gamma_c^+ \cup \Gamma_c^-$. The Navier-Cauchy governing equation for elastodynamics without body force is given by

$$(c_p^2 - c_s^2)u_{i,ij}(Q,t) + c_s^2 u_{j,ii}(Q,t) - \ddot{u}_j(Q,t) = 0\,. \tag{1}$$

where commas and dots denote space and time differentiations, respectively, and $u_i(Q,t)$ represents the displacement vector at a field point Q and at time t. The compressional (c_p) and shear (c_s) velocities are known to be

$$c_p^2 = \frac{\lambda + 2\mu}{\rho}\,, \qquad c_s^2 = \frac{\mu}{\rho}\,. \tag{2}$$

where λ and μ are the Lamé constants, and ρ is the mass density.

The Fourier transform of Eq. (1) gives the following frequency domain representation:

$$(c_p^2 - c_s^2)u_{i,ij}(Q,\omega) + c_s^2 u_{j,ii}(Q,\omega) + \omega^2 u_j(Q,\omega) = 0\,. \tag{3}$$

Use of the reciprocal relation for two elastodynamic states of the same angular frequency ω results in the following displacement BIE for a source point P interior to the domain in question:

$$\begin{aligned}\mathcal{U}(P,\omega) \;\equiv\; & u_k(P,\omega) - \int_{\Gamma_b} [U_{kj}(P,Q,\omega)\, t_j(Q,\omega) - T_{kj}(P,Q,\omega)\, u_j(Q,\omega)]\, \mathrm{d}Q \\ & + \int_{\Gamma_c^+} T_{kj}(P,Q,\omega)\, \Delta u_j(Q,\omega)\, \mathrm{d}Q = 0\,.\end{aligned} \tag{4}$$

where Q denotes a field point, u_j and t_j are the displacement and traction vectors, respectively, and Δu_j is the displacement jump vector across the crack surfaces. As Δu_j is used as the unknown on the crack, only one crack surface, *e.g.*, Γ_c^+, needs to be discretized.

For P off the boundary, the kernel functions are not singular and it is permissible to differentiate Eq. (4) with respect to P, yielding the displacement gradients. Substitution of these gradients into Hooke's law and then Cauchy's relation results in the following BIE for surface traction:

$$\mathcal{T}(P,\omega) \equiv t_k(P,\omega) - n_\ell(P) \int_\Gamma [D_{kj\ell}(P,Q,\omega)\, t_j(Q,\omega) - S_{kj\ell}(P,Q,\omega)\, u_j(Q,\omega)]\, \mathrm{d}Q + n_\ell^+(P) \int_{\Gamma_c^+} S_{kj\ell}(P,Q,\omega)\, \Delta u_j(Q,\omega)\, \mathrm{d}Q = 0\,. \tag{5}$$

where n_ℓ is the outward normal vector to the related boundary. It is well known that this traction BIE is essential for treating crack geometries. As it is difficult to find correct expressions for the elastodynamic kernel tensors $U_{kj}, T_{kj}, D_{kj\ell}$ and $S_{kj\ell}$, these formulas are given in the Appendix.

It can be shown that the limits of the integrals in Eqs. (4) and (5) as P approaches the boundary exist. From now on, for $P \in \Gamma$, the BIE is understood in this limiting sense.

The Galerkin boundary integral formulation is obtained by taking the shape functions ψ_m employed in approximating the boundary tractions and displacements as weighting functions for Eqs. (4) and (5). For a symmetric-Galerkin approximation, Eq. (6) needs to be employed on the boundary part Γ_{bu} where displacements are prescribed, and Eq. (7) is used on the boundary part Γ_t where tractions are prescribed,

$$\int_{\Gamma_{bu}} \psi_m(P)\, \mathcal{U}(P,\omega)\, \mathrm{d}P = 0\,. \tag{6}$$

$$\int_{\Gamma_t} \psi_m(P)\, \mathcal{T}(P,\omega)\, \mathrm{d}P = 0\,. \tag{7}$$

The additional boundary integration is the key to obtaining a symmetric coefficient matrix (as the name implies), as this ensures that the source point P and field point Q are treated in the same manner.

As mentioned earlier, standard (continuous) quadratic shape functions are used in this work to exploit the highly accurate MQP element for fracture analysis. One of the advantages of the frequency-domain analysis is that Eqs. (4) and (5) have a similar form as those in elastostatics. Thus, the reader is referred to, for example, Ref. [16] for more details on the SGBEM.

Multi-domain Analysis

The above SGBEM formulations need to be extended to deal with multi-domain problems such as those involving crack-inclusion interaction. The multi-domain technique is based upon the assumption of a perfect bonding between inclusions and the matrix which requires the displacement continuity and traction equilibrium conditions to be enforced on the interface.

Without loss of generality, consider a problem with two domains A and B as shown in Fig. 2. The coefficient matrix is partitioned into a 4×4 block structure as follows:

$$\begin{bmatrix} S_{AA} & 0 & S_{Au_I} & S_{At_I} \\ 0 & S_{BB} & S_{Bu_I} & -S_{Bt_I} \\ S_{u_IA} & S_{u_IB} & S_{u_Iu_I} & S_{u_It_I} \\ BS_{t_IA} & S_{t_IB} & S_{t_Iu_I} & S_{t_It_I} \end{bmatrix}\,. \tag{8}$$

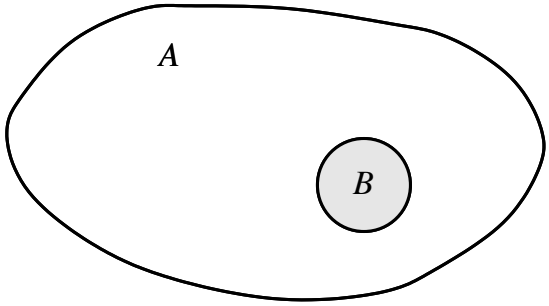

Fig. 2: A multi-domain problem

where S_{AA} and S_{BB} refer to Eqs. (6) and (7), depending on the boundary conditions, written for the non-interface boundaries of domains A and B, respectively, and S_{Au_I}, S_{At_I}, *etc.*, correspond to the unknown interface displacement (u_I) and interface traction (t_I). As both displacements and tractions are the unknowns on the interface, both Eqs. (6) and (7) need to be employed on this interface.

As a result of the symmetric-Galerkin (SG) procedure, S_{AA} and S_{BB} are symmetric matrices. The (1,2) and (2,1) blocks are equal to zero as the SG equations for domain A do not involve the geometry of domain B, and *vice versa*. The minus sign in the (2,4) block is due to the change in sign for the interface traction. The key in obtaining a symmetric coefficient matrix is to complete rows three and four with appropriate interface equations. More details of multi-domain techniques for the SGBEM can be found in, *e.g.*, [18, 36, 37].

Treatment of Singular Integrals

The main computational task in implementing Eqs. (6) and (7) is the evaluation of the singular and hypersingular integrals [24]. For this type of evaluation, one can employ a direct regularization approach (*e.g.*, [38]) or a decomposition technique as adopted herein: the elastodynamics formulation is decomposed into two parts as follows:

$$\int\int I \,\mathrm{d}Q \,\mathrm{d}P = \int\int I^s \,\mathrm{d}Q \,\mathrm{d}P + \int\int (I - I^s) \,\mathrm{d}Q \,\mathrm{d}P \,. \tag{9}$$

where I and I^s denote an elastodynamic kernel and its elastostatic counterpart, respectively. As seen in the Appendix, I involves modified Bessel functions of the second kind.

The first part $\int\int I^s \,\mathrm{d}Q \,\mathrm{d}P$ is identical to that for elastostatics. The treatment of the singular and/or hypersingular integrals in this part is carried out by means of an exterior limit to the boundary (the needed analytic integrations and limit are aided by symbolic computation). As the general procedure for this treatment has been presented in [16, 39], we therefore focus on the second term.

As the distance r between P and Q tends to zero ($\forall \omega > 0$), the modified Bessel functions of the second kind take the following forms:

$$K_0(z) = -\ln\frac{z}{2} - \gamma + \mathcal{O}(z)\,, \tag{10}$$

$$K_1(z) = \frac{1}{z} + \frac{z}{2}\left(\ln\frac{z}{2} + \gamma - \frac{1}{2}\right) + \mathcal{O}(z^2)\,, \tag{11}$$

$$K_2(z) = \frac{1}{z^2} - \frac{1}{2} + \mathcal{O}(z^3)\,, \tag{12}$$

where z could be either z_1 or z_2 (see Eq. (31)), and γ is Euler's constant.

Use of these above equations in the elastodynamic kernels results in the following asymptotic behavior for the kernel functions,

$$U^d_{kj} - U^s_{kj} = \frac{E_\omega}{2\pi\mu}\,\delta_{kj} = \mathcal{O}(1)\,, \tag{13}$$

$$T^d_{kj} - T^s_{kj} = \mathcal{O}(r\ln r)\,, \tag{14}$$

$$D^d_{kj\ell} - D^s_{kj\ell} = \mathcal{O}(r\ln r)\,, \tag{15}$$

$$S^d_{kj\ell} - S^s_{kj\ell} = \mathcal{O}(\ln r)\,, \tag{16}$$

where $i^2 = -1$, ν is Poisson's ratio and

$$E_\omega = \frac{-1}{4(1-\nu)}\left[(3-4\nu)\left(\ln\frac{i\omega}{2}+\gamma\right)+\frac{1}{2}\right]+\frac{1}{2}\left[\ln c_s + \left(\frac{c_s}{c_p}\right)^2 \ln c_p\right]. \tag{17}$$

It can be seen that the second part $\int\int (I - I^s)\,\mathrm{d}Q\,\mathrm{d}P$ is regular except when the integrand is $S^d_{kj\ell} - S^s_{kj\ell}$. However, this logarithmic singularity can be treated straightforwardly by Gauss quadrature using the following conversion [40]:

$$\int_0^1 f(r)\ln r\,\mathrm{d}r = -\int_0^1\int_0^1 f(sr)\,\mathrm{d}s\,\mathrm{d}r\,. \tag{18}$$

Finally, it should be noted that, since both I and I^s are singular, the singular terms in the kernel difference $(I - I^s)$ must be algebraically canceled out to avoid large round-off errors. By doing that, the integrand $(I - I^s)$ can be accurately obtained by using Eqs. (29) and (30), where $K_0(z)$, $K_1(z)$, $K_2(z)$ are given by Eqs. (10) through (12), and $\psi_{,r}$, $\chi_{,r}$, $\psi_{,rr}$, $\chi_{,rr}$ are replaced by $\psi_{,r} - AA$, $\chi_{,r} - AA + BB$, $\psi_{,rr} - CC$, $\chi_{,rr} + DD$, respectively. Here,

$$AA = \frac{z_2^2}{2r}\left(\ln\frac{z_2}{2}+\gamma-\frac{1}{2}\right),$$

$$BB = \left(\frac{c_s}{c_p}\right)^2\frac{z_1^2}{2r}\left(\ln\frac{z_1}{2}+\gamma-\frac{1}{2}\right),$$

$$CC = \left[\left(\frac{c_s}{c_p}\right)^2\frac{z_1^2}{2}\left(\ln\frac{z_1}{2}+\gamma-\frac{1}{2}\right)+\frac{z_2^2}{2}\right]\frac{1}{r^2},$$

$$DD = \left[-\left(\frac{c_s}{c_p}\right)^2\frac{z_1^2}{2}\left(\ln\frac{z_1}{2}+\gamma-\frac{3}{2}\right)+\frac{z_2^2}{2}\left(\ln\frac{z_2}{2}+\gamma-\frac{3}{2}\right)\right]\frac{1}{r^2}\,. \tag{19}$$

Dynamic Stress Intensity Factors

In this work, the DSIFs are numerically evaluated using the displacement correlation technique (DCT). This technique is based upon the crack displacement jump in the vicinity of the crack tip and the jump is determined by the SGBEM described earlier. According to the DCT,

$$K_{\mathrm{I}}(\omega) = \beta\mu\lim_{r\to 0}\sqrt{\frac{2\pi}{r}}\,\Delta u_n(\omega)\,,$$

$$K_{\mathrm{II}}(\omega) = \beta\mu\lim_{r\to 0}\sqrt{\frac{2\pi}{r}}\,\Delta u_t(\omega)\,, \tag{20}$$

where Δu_n and Δu_t are the normal and tangential components of the crack displacement jump vector, respectively, and r is the distance to the crack tip. In Eq. (20),

$$\beta = \frac{4\beta_p\beta_s - (1+\beta_s^2)^2}{4\beta_p(1-\beta_s^2)}\,, \tag{21}$$

and

$$\beta_p = \sqrt{1-(c/c_p)^2}\,, \qquad \beta_s = \sqrt{1-(c/c_s)^2}\,, \tag{22}$$

where c is the crack growth velocity. For stationary cracks such as those considered in this work, $c = 0$ and

$$\lim_{c\to 0}\beta = \frac{c_p^2 - c_s^2}{2c_p^2} = \frac{1}{4(1-\nu)}\,. \tag{23}$$

The dynamic fracture analysis calculations reported in this work are performed using the MQP element developed in [31]. By using the MQP shape functions in Eq. (20), the DCT-based DSIFs are obtained as

$$\begin{aligned} K_{\mathrm{I}}(\omega) &= \frac{\beta\mu}{3}\sqrt{\frac{2\pi}{L}}\left(8\Delta u_n^{(2)} - \Delta u_n^{(3)}\right)\,, \\ K_{\mathrm{II}}(\omega) &= \frac{\beta\mu}{3}\sqrt{\frac{2\pi}{L}}\left(8\Delta u_t^{(2)} - \Delta u_t^{(3)}\right)\,, \end{aligned} \tag{24}$$

where L is the distance between the tip and ending nodes, and the superscripts (2) and (3) denote the quarter-point and ending nodes of the crack-tip element, respectively.

As the DSIFs are directly given in terms of the nodal values of the displacement jump of the crack-tip element, and the MQP element enhances the accuracy of the nodal displacement jump, this enhances the accuracy of the obtained DSIF frequency responses.

Obtaining Time Histories from Frequency Response Analysis

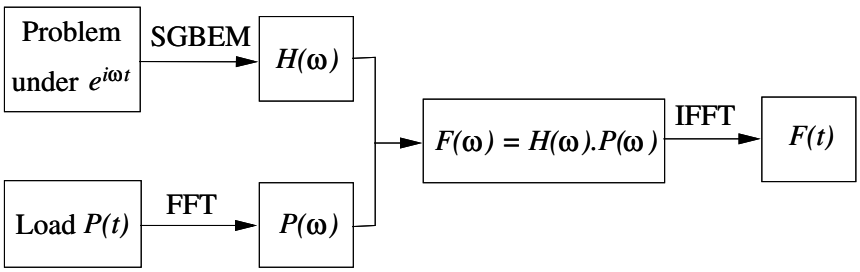

Fig. 3: A model for obtaining time histories using the standard FFT algorithm

To simplify the notations used in this paper, $X(\omega)$ is understood as the Fourier transform of $X(t)$ and vice versa.

The solution of a dynamic problem for a system can be viewed as an input/output relation where the input is the load P and the output is the dynamic response F of the system. If P and F are in the frequency domain, the relation can be written as

$$F(\omega) = H(\omega)P(\omega)\,. \tag{25}$$

In Eq. (25), $H(\omega)$ is called the frequency response which is the response of the system due to a unit harmonic load $P(\omega) = e^{i\omega t}$.

Figure 3 depicts a model for obtaining time histories (transient responses) from frequency response analysis of damped systems. In this model, the problem under a unit harmonic load ($e^{i\omega t}$) is analyzed first using SGBEM to obtain the frequency response $H(\omega)$. In the mean time, the time-dependent load $P(t)$ is converted to the frequency domain ($P(\omega)$) by means of FFT. Relation (25) is then employed to obtain the dynamic response $F(\omega)$ in the frequency domain. Finally, IFFT is used to transform $F(\omega)$ into the time domain ($F(t)$).

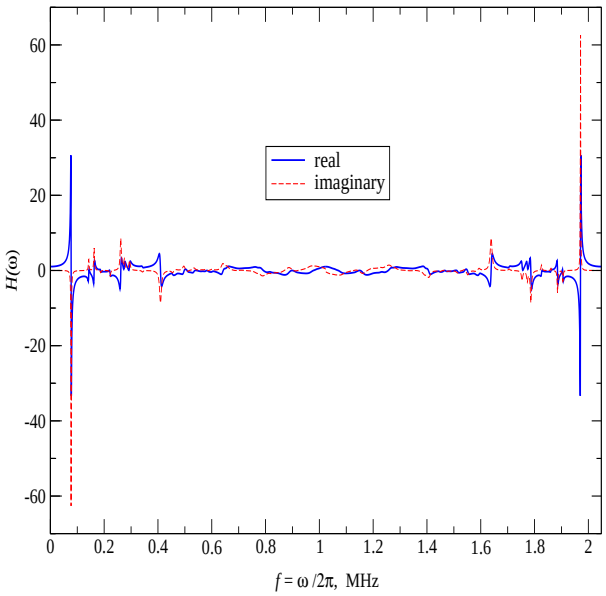

Fig. 4: Conjugate symmetry about Nyquist's frequency of frequency response $H(\omega)$

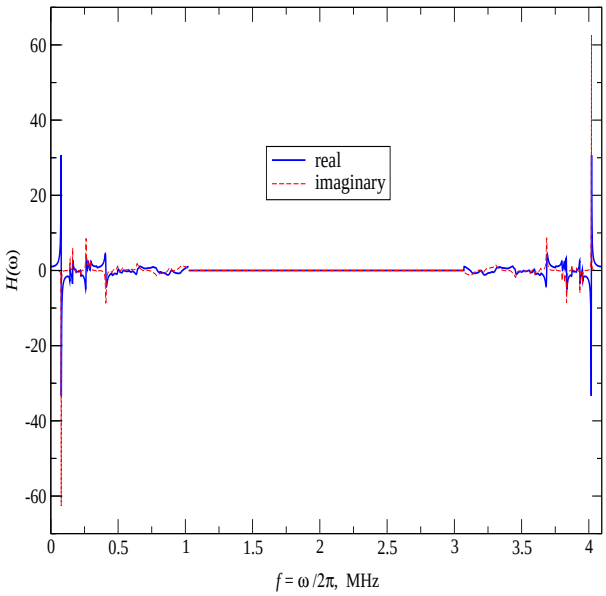

Fig. 5: Doubling time resolution by doubling Nyquist's frequency

A procedure for obtaining the transient responses by the standard FFT algorithm can be summarized as follows:

(a) Determine a frequency resolution Δf ($f = 2\pi\omega$) which needs to be small enough to minimize the loss of frequency information.

(b) Perform SGBEM analysis for $f = 0, \Delta f, 2\Delta f, \ldots, \frac{N}{2}\Delta f = f_{\text{Nyq}}$, where $N = 2^m$ and m is a positive integer, to obtain the frequency response $H(\omega)$ for the first $(\frac{N}{2} + 1)$ samples. The Nyquist frequency f_{Nyq} needs to be chosen such that frequency responses above f_{Nyq} are not significant and can thus be discarded. Note that the very first sample ($j = 1$) is the static sample ($f = 0$);

(c) For the last $(\frac{N}{2} - 1)$ samples ($j = \frac{N}{2} + 2 \ldots N$), $H(\omega)$ must be determined such that it is conjugate symmetric about the Nyquist frequency, i.e.,

$$H(j) = \text{conj}(H(N - j + 2)) \qquad (j = \frac{N}{2} + 2 \ldots N)\,. \tag{26}$$

Figure 4 depicts an example of a frequency response $H(\omega)$ constructed from using $\Delta f = 0.001$ MHz, $N = 2^{11} = 2,048$ and $f_{\text{Nyq}} = 1.024$ MHz.

(d) Perform FFT for the time-dependent load $P(t)$ for the first N samples ($j = 1 \ldots N$);

(e) Calculate $F(\omega) = H(\omega)P(\omega)$;

(f) Perform IFFT for $F(\omega)$ to obtain the transient response $F(t)$. Note that the period and time resolution (sampling interval) of this transient response are $T_f = 1/\Delta f$ and $\Delta t = T_f/N$, respectively;

(g) If the calculated Δt does not give a very good indication of the shape of the transient curves, interpolation [41] can be used. This is done by increasing the value of Nyquist's frequency while requiring no extra SGBEM analysis as extra zeros are added to the frequency response. As a result, the number of samples N is increased accordingly which improves the resolution of the transient curves.

Figure 5 shows an example of a frequency response $H(\omega)$ for which Nyquist's frequency f_{Nyq} is doubled from 1.024 MHz to 2.048 MHz. Thus, Δt is reduced in half.

More mathematical details of this frequency domain analysis can be found in [42] where some studies on the effects of f_{Nyq} and Δf on the computational cost were given.

Numerical Examples

Two numerical examples involving viscoelastic materials are given in this Section to illustrate the effectiveness of using frequency-domain elastodynamic SGBEM and the standard FFT algorithm in transient analysis of the DSIFs in case of crack-inclusion interaction. The internal damping of the viscoelastic materials is considered by means of a complex shear modulus defined as $\mu_c = \mu(1 + 2i\zeta)$ where ζ is the damping ratio. Note that undamped cases ($\zeta = 0$) are not considered here as their transient responses never decay which violate the periodic nature of the standard FFT algorithm presented in Section 6 (*e.g.*, [41]). That's why some studies in the literature reported that zero damping ratio would result in spurious oscillations in the time solution [6, 42]). Two types of impact loading are considered as depicted in Fig. 6: a Heaviside step function and a blast loading function. Note in the standard implementation of the FFT that a quiet zone, where the applied load $\sigma(t) = 0$, needs to be added to the end of the duration of the load. This zone and T_f must be long enough in order to obtain accurate transient results.

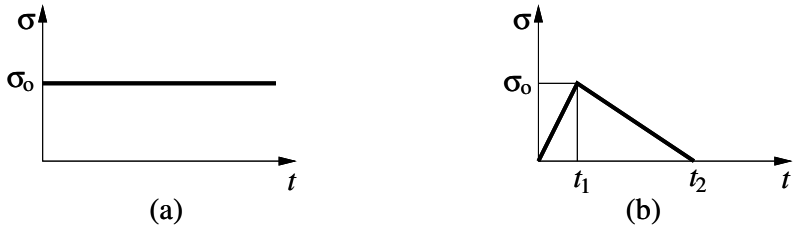

Fig. 6: (a) Heaviside step loading; (b) Blast loading

Crack-inclusion interaction in a finite plate

The first example deals with a plate of size $(2W \times 2H) = (30 \text{ mm} \times 40 \text{ mm})$ containing a 30°-oriented crack of length $2a = 4.8$ mm and an inclusion of diameter $d = 4$ mm as shown in Fig. 7. The plate is subjected to a uniaxial tension $\sigma(t)$ in the form of a Heaviside step or blast loading ($t_1 = 2$ μs, $t_2 = 8$ μs) as depicted in Fig. 6. Crack tip A is eccentrically positioned relative to the inclusion center as shown, and the eccentricity is denoted as e. The material properties for the matrix and inclusion are respectively assumed to be: $\mu = 260$ GPa and 640

GPa, $\nu = 0.08$ and 0.01, and $\rho = 3,220$ kg/m^3 and 3,515 kg/m^3. Let the normalized mode-I and mode-II DSIFs be defined as

$$F_{\rm I} = \frac{K_{\rm I}}{\sigma_o\sqrt{\pi a}}\,, \qquad F_{\rm II} = \frac{K_{\rm II}}{\sigma_o\sqrt{\pi a}}\,. \tag{27}$$

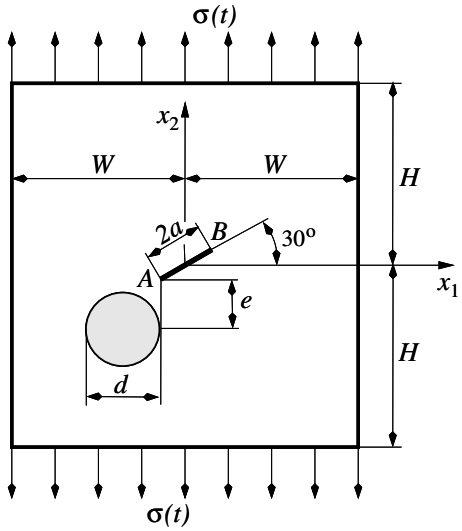

Fig. 7: Crack-inclusion interaction in composite plate.

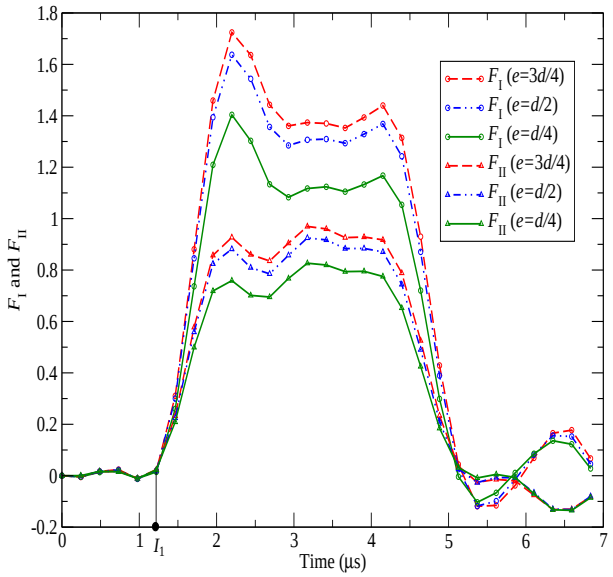

Fig. 8: $F_{\rm I}$ and $F_{\rm II}$ at tip A ($\zeta = 1\%$, Heaviside step loading).

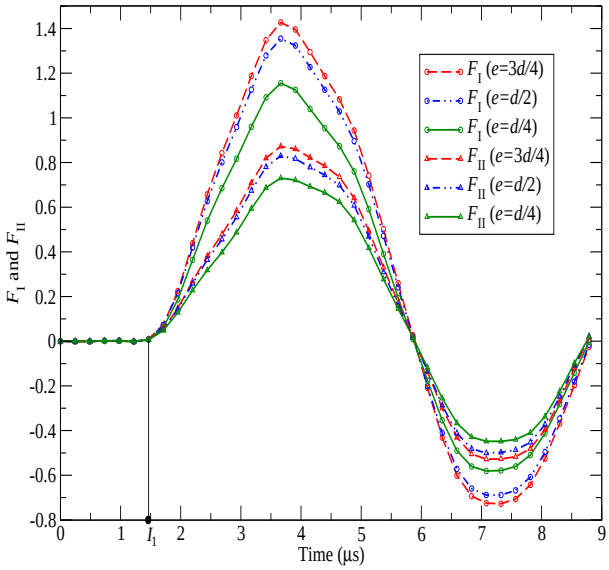

Fig. 9: $F_{\rm I}$ and $F_{\rm II}$ at tip A ($\zeta = 1\%$, blast loading).

Due to the interaction between the inclusion and a very nearby crack, a dense mesh needs to be employed for the SGBEM frequency response analysis of the normalized DSIFs. Per convergence study, 20 elements is used on the plate boundary, 20 equal-length elements on the crack and 64 elements on the inclusion boundary. Here, $\Delta f = 0.001$ MHz, $N = 2^{11} = 2,048$ and $f_{\rm Nyq} = 1.024$ MHz are selected which results in a period of $T_f = 1/\Delta f = 1,000\,\mu$s and a time resolution of $\Delta t = T_f/N = 0.4883\,\mu$s. To double the resolution of the transient responses

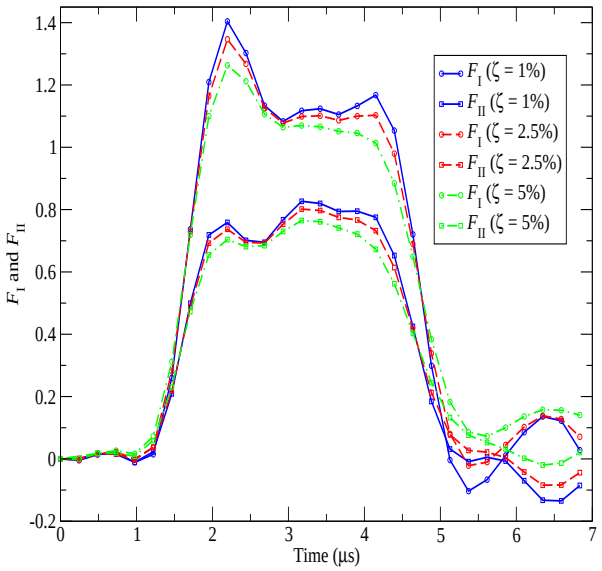

Fig. 10: F_{I} and F_{II} at tip A ($e = d/4$, Heaviside step loading).

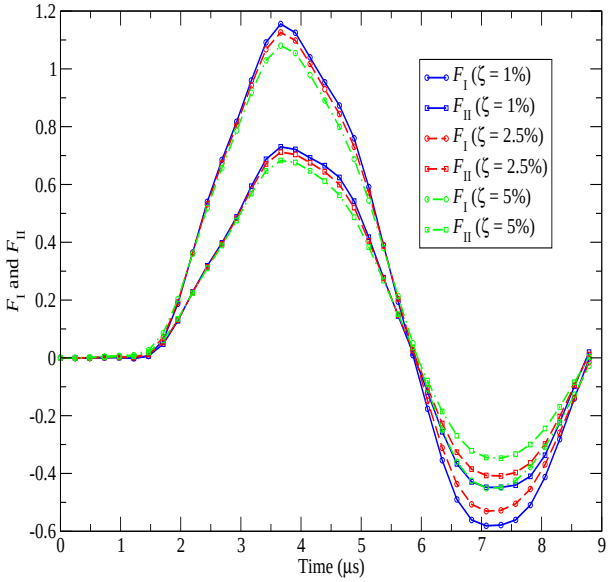

Fig. 11: F_{I} and F_{II} at tip A ($e = d/4$, blast loading).

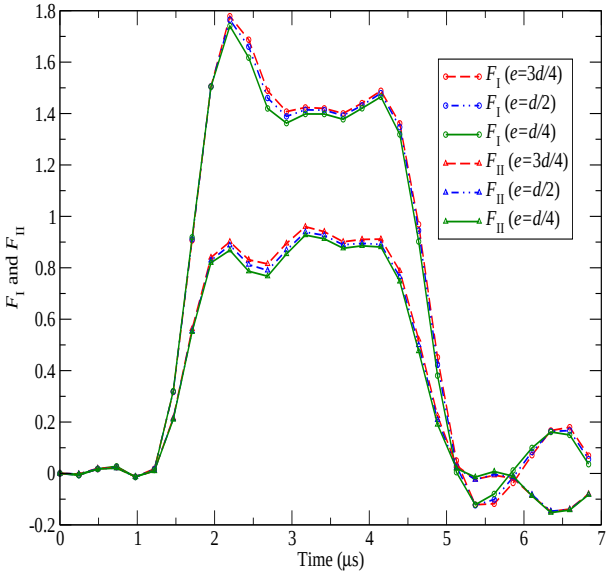

Fig. 12: F_{I} and F_{II} at tip B ($\zeta = 1\%$, Heaviside step loading).

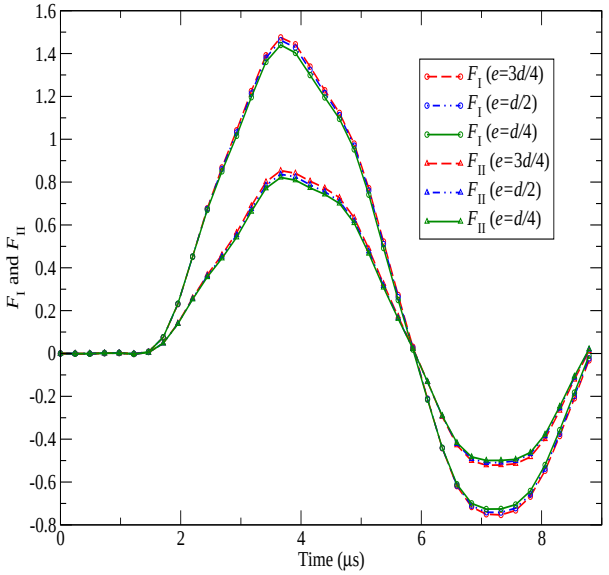

Fig. 13: F_{I} and F_{II} at tip B ($\zeta = 1\%$, blast loading).

for this problem, N is doubled from 2,048 to 4,096 which cuts the time resolution in half at $\Delta t = 0.2441\,\mu$s.

First of all, it can be observed that there are many oscillations on the time-history DSIF curves in Figs. 8 through 15. These oscillations are caused by the wave scattering from the crack tip, inclusion and plate boundary. The first oscillation occurs at time T_1 which is the time needed for the incident longitudinal wave to reach the crack ($T_1 \simeq 1.25\,\mu$s and $1.5\,\mu$s for the Heaviside and blast loading, respectively).

Figures 8 through 11 and 12 through 15 show the time histories of the normalized DSIFs at crack tip A and B, respectively, during the first $7\,\mu$s for the Heaviside step loading and the

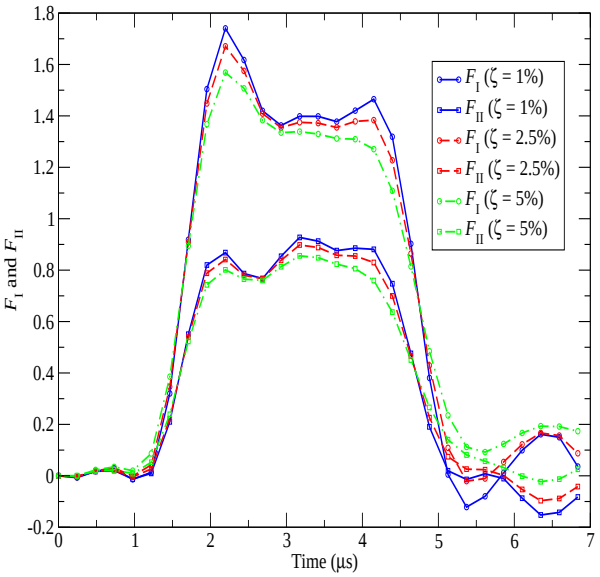

Fig. 14: F_{I} and F_{II} at tip B ($e = d/4$, Heaviside step loading).

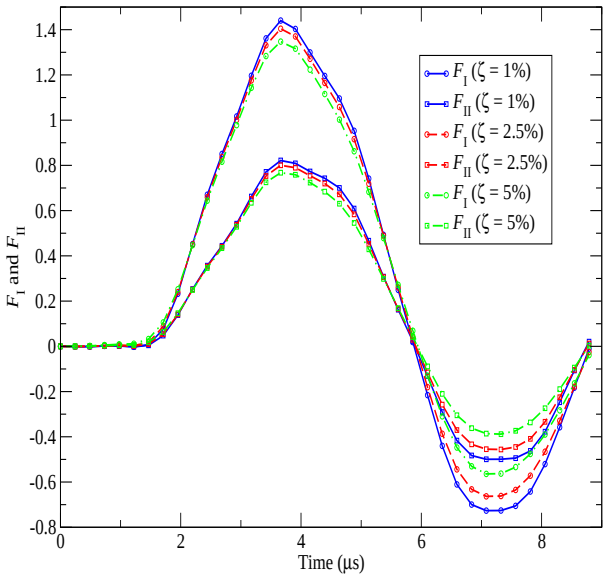

Fig. 15: F_{I} and F_{II} at tip B ($e = d/4$, blast loading).

first 9 μs for the blast loading. Figures 8 and 12 depict F_{I} and F_{II} as functions of three different eccentricities, namely $e = 3d/4, d/2$ and $d/4$, under the Heaviside step loading while Figs. 9 and 13 show the same type of solution, but under the blast loading. These figures confirm a mechanism known as crack-tip shielding: the SIFs/DSIFs decrease as the crack tip approaches a much stiffer inclusion (as e decreases). As crack tip B is located further away from the inclusion, the interaction between this crack tip and the inclusion is less significant as seen in Figs. 12 and 13.

Figures 10 and 14 show F_{I} and F_{II} as functions of three different damping ratios under the Heaviside step loading while Figs. 11 and 15 depict the same type of solution, but under the blast loading. It can be seen that the DSIF solutions are dampened accordingly as ζ increases. Finally, the crack tip shielding mechanism at A can also be observed by noticing that F_{I} at tip A (Figs. 10 and 11) are smaller than that at tip B (Figs. 14 and 15).

Crack-inclusion interaction in a three-point bend beam

The last example deals with a three-point bend beam of width $L = 200$ mm and depth $W = 50$ mm, containing an edge crack of length $a = 10$ mm and an inclusion of diameter $d = 2R = 5$ mm as shown in Fig. 16. The crack is eccentrically positioned relative to the inclusion center as shown, and the eccentricity in the x- and y-direction are denoted as e_x and e_y, respectively. The material properties for the matrix and inclusion are respectively assumed to be; $\mu = 4.1$ GPa and 15 GPa, $\nu = 0.34$ and 0.3, and $\rho = 1,175$ kg/m^3 and 1,500 kg/m^3. The beam is subjected to an impact load $P(t)$ per unit thickness of the beam. Again, both types of impact: Heaviside step function and blast function (with $t_1 = 100\,\mu$s and $t_1 = 400\,\mu$s) are considered (see Fig. 6 where σ and σ_o are replaced by P and P_o, respectively). The normalized mode-I and mode-II DSIFs are defined as

$$F_{\mathrm{I}} = \frac{K_{\mathrm{I}}}{P_o L/W^{3/2}}\,, \qquad F_{\mathrm{II}} = \frac{K_{\mathrm{II}}}{P_o L/W^{3/2}}\,. \tag{28}$$

A convergence test suggests a total of 125 elements for the beam boundary, 5 equal-length elements for the crack and 68 uniform elements for the matrix-inclusion interface. The frequency

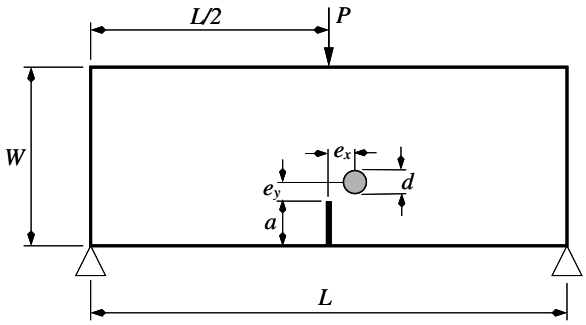

Fig. 16: Crack-inclusion interaction in a three-point bend beam.

responses of the mode-I DSIF are obtained using the following data: $\Delta f = 25$ Hz, $N = 2^{11} = 4,096$, $f_{\text{Nyq}} = 51.2$ KHz. This results in the following values for the transient analysis using the standard FFT algorithm: $T_f = 1/\Delta f = 40$ ms and $\Delta t = T_f/N = 9.766\,\mu$s.

Again, the oscillations on the time-history DSIF curves in Figs. 17 through 22 are due to wave scattering from the inclusion, crack tip, supports and beam boundary. As shown in Figs. 17 and 18, the first oscillation occurs at time $T_1 \simeq 30\,\mu$s and $35\,\mu$s for the Heaviside and blast loading, respectively). These are times needed for the incident longitudinal wave to travel from the top surface of the beam to the crack tip.

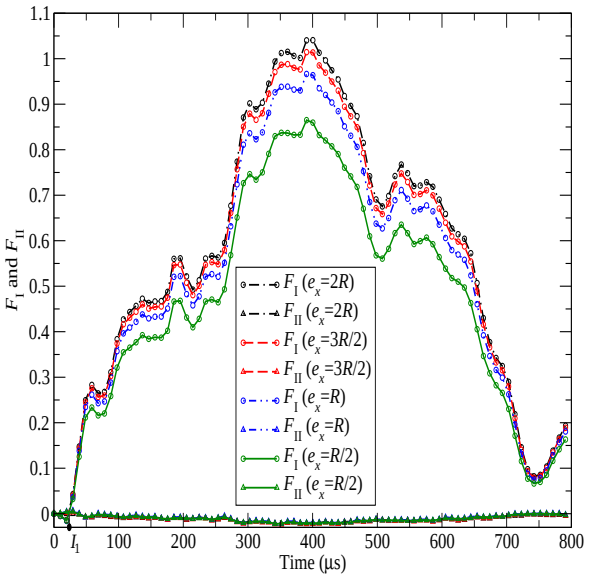

Fig. 17: Effect of e_x on F_{I} under Heaviside step loading ($e_y = R$).

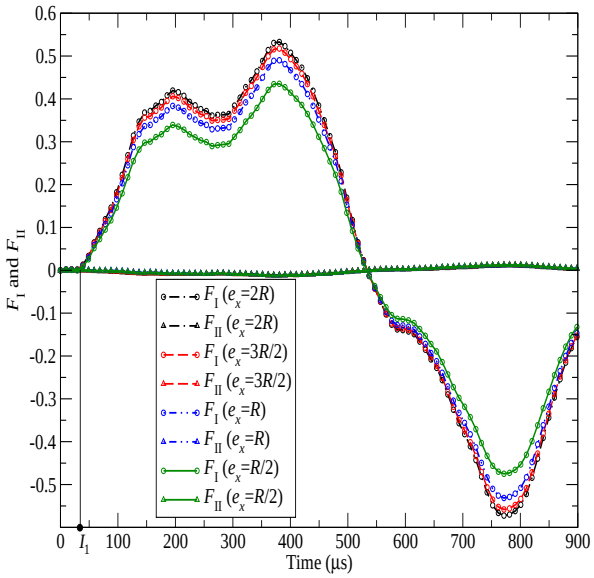

Fig. 18: Effect of e_x on F_{I} under blast loading ($e_y = R$).

Figures 17 and 19 depict the effect of the eccentricities e_x and e_y, respectively, on the normalized DSIFs during the first 800 μs under the Heaviside step loading, while Figs. 18 and 20 show the same effects during the first 900 μs under the blast loading. Again, the results exhibit the increase of crack-tip shielding for F_{I} and amplification for F_{II} as the tip approaches the inclusion. Actually, due to the position of the inclusion relative to the crack tip in this case, the shielding of F_{I} is more pronounced and the amplification of F_{II} is not noticeable (Figs. 17 and 18) as the horizontal eccentricity e_x decreases (the approaching direction of the stiff inclusion is perpendicular to the crack which mainly decreases the crack opening displacement (COD)) while the shielding of F_{I} is less pronounced and the amplification of F_{II} is noticeable

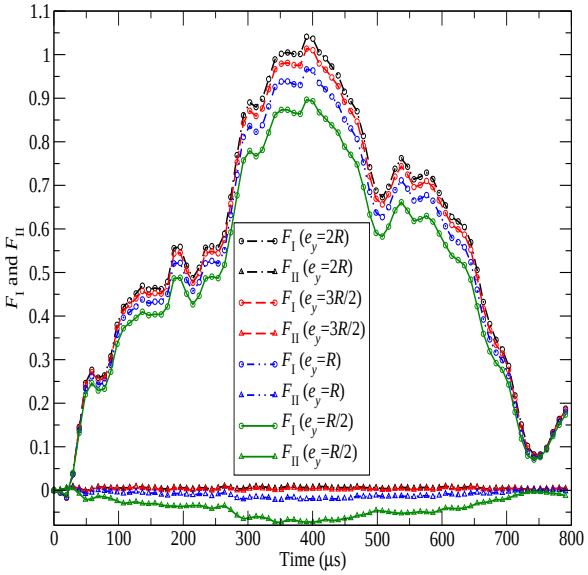

Fig. 19: Effect of e_y on F_{I} under Heaviside step loading ($e_x = R$).

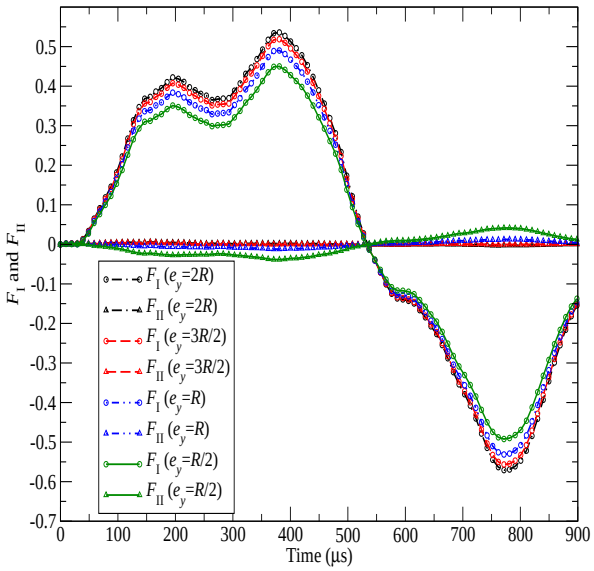

Fig. 20: Effect of e_y on F_{I} under blast loading ($e_x = R$).

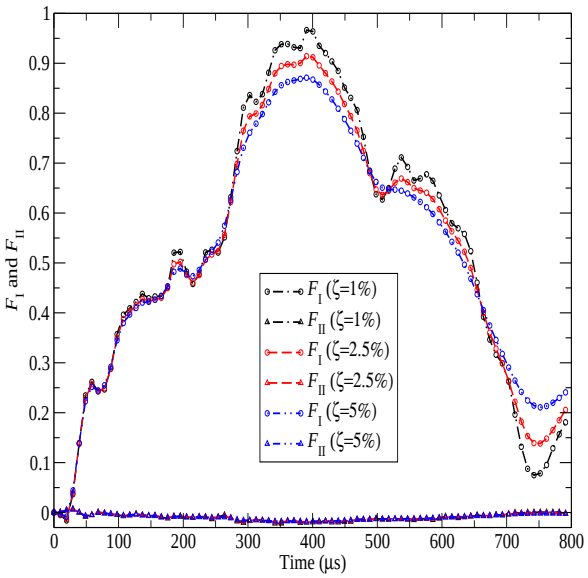

Fig. 21: Effect of ζ on F_{I} under Heaviside step loading ($e_x = e_y = R$).

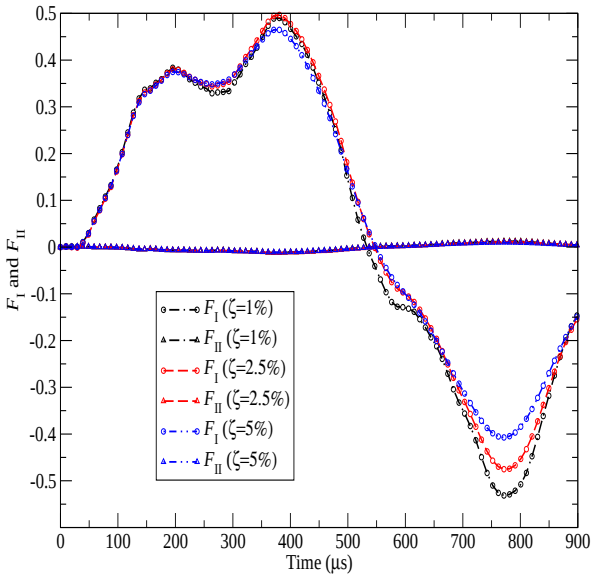

Fig. 22: Effect of ζ on F_{I} under blast loading ($e_x = e_y = R$).

(Figs. 19 and 20) as the vertical eccentricity e_y decreases (the approaching direction of the stiff inclusion is parallel to the crack which decreases the COD and increases the crack sliding displacement).

Finally, Figs. 21 and 22 show the effect of three different damping ratios, namely $\zeta = 1\%, 2.5\%$ and 5%, on the transient responses of F_{I} and F_{II} under the Heaviside and blast loading, respectively. Again, the DSIF solutions are dampened accordingly as ζ increases.

Conclusion

A 2-D symmetric-Galerkin boundary integral formulation for multi-domain elastodynamic fracture analysis in the frequency domain, together with a post-processing procedure for obtaining transient responses using the standard FFT algorithm, were described in this paper. The formulation was successfully employed for analyzing the dynamic interaction between a crack and a circular inclusion in a finite plate and a three-point bend beam. There are several major advantages of this dynamic fracture modeling technique: (a) Compared to a static counterpart, this formulation only requires additional integrals that are either regular or weakly singular. However, care should be taken to avoid large round-off errors in evaluating the additional weakly singular integrals; (b) Unlike in the conventional collocation dual BEM, standard continuous elements can be employed in the SGBEM, allowing the use of SQP/MQP/EQP elements to accurately capture the crack tip behavior; (c) The FD formulation is suitable for arbitrarily time-dependent loading often seen in practical engineering, as the handling of this type of loading by means of the standard FFT algorithm is inexpensive; and (d) The FD formulation is also known to result in stable transient responses as it is easier to select an appropriate frequency step for the FD formulation than a suitable time step for the TD formulation. The transient responses of the DSIFs obtained for the two examples considered in this paper are reasonable, consistent and suggest that the dynamic fracture modeling technique discussed herein is very effective. The results also confirm the well-known crack tip shielding mechanism due to crack-inclusion interaction. A potential extension of this work is the modeling of dynamic crack growth through a cluster of particles.

Acknowledgments. This research was supported in part by the NSF Grant CMMI-0653796, and by the Office of Advanced Scientific Computing Research, U.S. Department of Energy, under contract DE-AC05-00OR22725 with UT-Battelle, LLC.

Appendix

The elastodynamic kernels in Eqs. (4) and (5) are given by

$$
\begin{aligned}
U_{kj} &= \frac{1}{2\pi\mu}(\psi\delta_{kj} - \chi r_{,k} r_{,j})\,, \\
T_{kj} &= \frac{1}{2\pi}\left[B_1\left(\frac{\partial r}{\partial n}\delta_{kj} + r_{,j}n_k\right) - \frac{2\chi}{r}\left(r_{,k}n_j - 2r_{,k}r_{,j}\frac{\partial r}{\partial n}\right) - 2\chi_{,r}r_{,k}r_{,j}\frac{\partial r}{\partial n} + \frac{\lambda}{\mu}B_2 r_{,k}n_j\right]\,, \\
D_{kj\ell} &= \frac{1}{2\pi}\left[\left(\frac{2\chi}{r} - \frac{\lambda}{\mu}B_2\right)\delta_{k\ell}r_{,j} - B_1(\delta_{kj}r_{,\ell} + \delta_{\ell j}r_{,k}) + 2\left(\chi_{,r} - 2\frac{\chi}{r}\right)r_{,k}r_{,j}r_{,\ell}\right]\,, \\
S_{kj\ell} &= \frac{\mu}{2\pi}\left\{\frac{\partial r}{\partial n}\left[4\left(\chi_{,rr} - 5\frac{\chi_{,r}}{r} + 8\frac{\chi}{r^2}\right)r_{,k}r_{,j}r_{,\ell} - B_3(\delta_{kj}r_{,\ell} + \delta_{\ell j}r_{,k}) + B_4\delta_{k\ell}r_{,j}\right] + B_4 r_{,k}r_{,\ell}n_j\right. \\
&\quad - B_3\left(r_{,\ell}n_k + r_{,k}n_\ell\right)r_{,j} + \left[4\frac{\chi}{r^2} - 4\frac{\lambda}{\mu}\frac{B_2}{r} + \left(\frac{\lambda}{\mu}\right)^2\left(\chi_{,rr} + 2\frac{\chi_{,r}}{r} - \psi_{,rr} - \frac{\psi_r}{r}\right)\right]\delta_{k\ell}n_j \\
&\quad \left. -2\frac{B_1}{r}\left(\delta_{j\ell}n_k + \delta_{jk}n_\ell\right)\right\}\,,
\end{aligned}
\tag{29}
$$

where n_j is the normal vector to the boundary, δ_{ij} is the Kronecker delta, and

$$
\begin{aligned}
B_1 &= \psi_{,r} - \frac{\chi}{r}\,, \\
B_2 &= B_1 - \chi_{,r}\,, \\
B_3 &= \psi_{,rr} - \frac{\psi_{,r}}{r} - 3\frac{\chi_{,r}}{r} + 6\frac{\chi}{r^2}\,,
\end{aligned}
$$

$$
\begin{aligned}
B_4 &= 2\left[2\frac{\chi_{,r}}{r} - 4\frac{\chi}{r^2} + \frac{\lambda}{\mu}\left(\chi_{,rr} - 2\frac{\chi}{r^2} - \psi_{,rr} + \frac{\psi_{,r}}{r}\right)\right], \\
\psi &= K_0(z_2) + \frac{1}{z_2}\left[K_1(z_2) - \frac{c_s}{c_p}K_1(z_1)\right], \\
\chi &= K_2(z_2) - \left(\frac{c_s}{c_p}\right)^2 K_2(z_1), \\
\psi_{,r} &= \frac{1}{z_2 r}\left[\frac{c_s}{c_p}z_1 K_2(z_1) - z_2 K_2(z_2) - z_2^2 K_1(z_2)\right], \\
\chi_{,r} &= \frac{1}{r}\left\{\left(\frac{c_s}{c_p}\right)^2\left[z_1 K_1(z_1) + 2K_2(z_1)\right] - z_2 K_1(z_2) - 2K_2(z_2)\right\}, \\
\psi_{,rr} &= \frac{1}{z_2 r^2}\left\{-\frac{c_s}{c_p}\left[3z_1 K_0(z_1) + (z_1^2+6)K_1(z_1)\right] + 3z_2 K_0(z_2) + (z_2^2+6)K_1(z_2)\right. \\
&\quad \left. + z_2^2\left[z_2 K_0(z_2) + K_1(z_2)\right]\right\}, \\
\chi_{,rr} &= \frac{1}{r^2}\left\{-\left(\frac{c_s}{c_p}\right)^2\left[z_1^2 K_0(z_1) + 3z_1 K_1(z_1) + 6K_2(z_1)\right]\right. \\
&\quad \left. + z_2^2 K_0(z_2) + 3z_2 K_1(z_2) + 6K_2(z_2)\right\}. \qquad (30)
\end{aligned}
$$

In Eq. (30), $K_n(z)$ is the modified Bessel function of the second kind and order n, and

$$
\begin{aligned}
z_1 &= \frac{i\omega r}{c_p}, \\
z_2 &= \frac{i\omega r}{c_s}, \\
r &= \sqrt{[x_1(Q) - x_1(P)]^2 + [x_2(Q) - x_2(P)]^2}. \qquad (31)
\end{aligned}
$$

References

[1] J. Dominguez: *Boundary Elements in Dynamics*(Computational Mechanics Publications, Southampton 1997).

[2] J. Sladek and V. Sladek: Int. J. Numer. Meth. Eng., Vol. 23 (1986), p. 919.

[3] P. Fedeliński, M.H. Aliabadi and D.P. Rooke: Comput. Struct., Vol. 59 (1996), p. 1021.

[4] P.H. Wen, M.H. Aliabadi and D.P. Rooke: Comput. Method Appl. M., Vol. 167 (1998), p. 139.

[5] P. Fedeliński: Eng. Anal. Bound. Elem., Vol. 28 (2004), p. 1135.

[6] F. Chirino and J. Dominguez: Eng. Fract. Mech., Vol. 34 (1989), p. 1051.

[7] M.P. Ariza and J. Dominguez: Eng. Anal. Bound. Elem., Vol. 26 (2002), p. 639.

[8] F. Chirino, R. Gallego, A. Sáez and J. Dominguez: Eng. Anal. Bound. Elem., Vol. 13 (1994), p. 11.

[9] P. Fedeliński, M.H. Aliabadi and D.P. Rooke: Comput. Struct., Vol. 32 (1995), p. 3555.

[10] P. Fedeliński and M.H. Aliabadi: Int. J. Numer. Meth. Eng., Vol. 40 (1997), p. 1555.

[11] V.V. Mykhas'kiv and O.M. Khay: Int. J. Solids Struct., Vol. 46 (2009), p. 602.

[12] J. Lei, Y.-S. Wang and D. Gross: Eng. Anal. Bound. Elem., Vol. 29 (2005), p. 802.

[13] J. Lei, Q. Yang, Y.-S. Wang and C. Zhang: Compos. Sci. Technol., Vol. 69 (2009), p. 1279.

[14] M. Wünsche, C. Zhang, F. Garcia-Sánchez, A. Sáez, J. Sladek and V. Sladek: Comput. Method Appl. M., Vol. 198 (2009), p. 2812.

[15] Z.M. Xiao and J. Luo: Eng. Fract. Mech., Vol. 71 (2004), p. 1635.

[16] A. Sutradhar, G.H. Paulino and L.J. Gray: *Symmetric Galerkin Boundary Element Method* (Springer-Verlag, Berlin 2008).

[17] L.J. Gray: Math. Comput. Model., Vol. 15 (1991), p. 165.

[18] G. Maier, M. Diligenti and A. Carini: Comput. Method Appl. M., Vol. 92 (1991), p. 193.

[19] A. Frangi and G. Maier: Comput. Method Appl. M., Vol. 171 (1999), p. 281.

[20] J. Bielak, R.C. MacCamy, D.S. McGhee and A. Barry: J. Eng. Mech.-ASCE, Vol. 117 (1991), p. 2265.

[21] G. Davi and A. Milazzo: Eng. Anal. Bound. Elem., Vol. 14 (1994), p. 343.

[22] J.J. Pérez-Gavilá and M.H. Aliabadi: Comput. Struct., Vol. 79 (2001), p. 2621.

[23] A.-V. Phan, L.J. Gray and A. Salvadori: Comput. Method Appl. M., doi:10.1016/j.cma.2010.06.019.

[24] A.-V. Phan, L.J. Gray and A. Salvadori: Mech. Res. Commun., Vol. 37 (2010), p. 177.

[25] R.D. Henshell and K.G. Shaw: Int. J. Numer. Meth. Eng., Vol. 9 (1975), p. 495.

[26] R.S. Barsoum: Int. J. Numer. Meth. Eng., Vol. 10 (1976), p. 25.

[27] G.E. Blandford, A.R. Ingraffea and J.A. Liggett: Int. J. Numer. Meth. Eng., Vol. 17 (1981), p. 387.

[28] L. Banks-Sills: Appl. Mech. Rev., Vol. 44 (1991), p. 447.

[29] L.J. Gray and G.H. Paulino: SIAM J. Appl. Math., Vol. 58 (1998), p. 428.

[30] M. Costabel, M. Dauge and R. Duduchava: Commun. Part. Diff. Eq., Vol. 28 (2003), p. 869.

[31] L.J. Gray, A.-V. Phan, G.H. Paulino and T. Kaplan: Eng. Fract. Mech., Vol. 70 (2003), p. 269.

[32] A.-V. Phan, L.J. Gray and T. Kaplan: J. Appl. Mech., Vol. 74 (2007), p. 1282.

[33] A. Sutradhar and G.H. Paulino: Eng. Anal. Bound. Elem., Vol. 28 (2004), p. 1335.

[34] A. Salvadori and L.J. Gray: Int. J. Numer. Meth. Eng., Vol. 70 (2007), p. 445.

[35] M. Bonnet: textslBoundary Integral Equation Methods for Solids and Fluids (John Wiley & Sons, England 1995).

[36] S.M. Hölzer: Commun. Numer. Meth. En., Vol. 9 (1993), p. 219.

[37] L.J. Gray and G.H. Paulino: Int. J. Numer. Meth. Eng., Vol. 40 (1997), p. 3085.

[38] A. Frangi and G. Novati: Comput. Mech., Vol. 22 (1998), p. 50.

[39] L.J. Gray, in: Singular Integrals in the Boundary Element Method. Advances in Boundary Element, edited by V. Sladek and J. Sladek, chapter 2, Computational Mechanics Publishers (1998).

[40] B. Danloy: Math. Comput., Vol. 27 (1973), p. 861.

[41] E.O. Brigham: textslThe Fast Fourier Transform and Its Applications (Prentice Hall, New Jersey 1988).

[42] Z.J. Yang, A.J. Deeks and H. Hao: Eng. Fract. Mech., Vol. 74 (2007), p. 669.

Key Engineering Materials Vol. 454 (2011) pp 97-112

doi:10.4028/www.scientific.net/KEM.454.97

Stress Intensity Factor Evaluation of Anisotropic Cracked Sheets Under Dynamic Loads Using Energy Domain Integral

M. Mauler[1], P. Sollero[2], E. L. Albuquerque[3]

[1,2] Faculty of Mechanical Engineering, University of Campinas
13083-970, Campinas, Brazil, [martimmn,sollero]@fem.unicamp.br

[3]Faculty of Technology, University of Brasilia
70910-900, Brasilia, Brazil, eder@unb.br

Keywords: Boundary Element Method, Anisotropy, Energy Domain Integral, Dynamic Fracture Mechanics.

Abstract. The aim of this paper is to present a procedure to perform the evaluation of dynamic stress intensity factors of composite cracked sheets. The numerical method that is used to perform the modeling of the crack is the dual boundary element method. The inertial effects are modeled using the dual reciprocity boundary elements method. The Houbolt Method is used to integrate time, and the energy domain integral is used to evaluate stress intensity factors.

INTRODUCTION

The presence of cracks in mechanical or structural components decreases its mechanical and fatigue resistance due to the high stress concentration at the crack tip. Under dynamic loads, a crack can be still more dangerous due to wave propagations that increase magnitude of stress intensity factors. Stress intensity factors can be obtained in the boundary element analyses by different methods, such as the the crack tip opening displacement [1, 8], special crack tip elements [2, 3], and path independent integrals based on conservation principles [5]. Among these methods, path independent integrals, as J and M integrals, have the advantage that they do not require an elaborate representation of the crack tip singular fields, due to the relatively small contribution that the crack tip fields make to the total strain energy of the body. The contour integrals in the J and M-integral expressions can be evaluated at points far away from the crack tip, hence the accuracy of the these methods is expected to be higher. The M integral has some advantages over J integral. For example, a unique relation between the M-integral and T-stress can be found. However, the expression of M integral has more terms and its implementation is not justified if the interest is only in the computation of stress intensity factors.

The successful application of high performance composites is reflected in many of the mechanical properties such as strength, ductility, toughness, and fatigue resistance. Composite materials are ideal for components which require high strength per weight and stiffness per weight ratios. For example, aircraft are typically weight sensitive structures in which composite materials are effective. Typical, composite weight saving of 30 % has been reported. However, the application of composite materials in critical components has lagged behind, due to the lack of sufficient knowledge about composite damage tolerance properties. Wave propagation in cracked laminated (anistropic) materials, for example, is one of the area that still demands a lot of research. Dynamic fracture mechanics in anisotropic materials has been investigated with boundary elements [7, 8] and by other numerical methods. However, none of the literature articles presented the computation of dynamic stress intensity factors using path independent integrals.

In this paper, the boundary element method (BEM) is applied for the analysis of the dynamic response of composite cracked sheets. The elastodynamic response of cracked sheets has been previously presented by Albuquerque et al. [7, 8]. The dual boundary element method (DBEM) is a boundary modelling technique aiming fracture mechanics problems, allowing to discretize the

crack in a single region. This technique has been successfully described and implemented by Portela et al. [9], and regarded as an efficient technique to simulate fracture mechanics problems. The consideration of inertial effects of the component introduces domain integrals in the boundary equilibrium equations, which must be transformed into boundary integrals. The dual reciprocity method (DRBEM) has been successfully used to overcome this problem for isotropic and anisotropic sheets, as shown by Kögl and Gaul [10] and Albuquerque, Sollero and Aliabadi [7, 8]. A transient procedure is adopted using the Houbolt [11] time integration. Finally, the evaluation of the dynamic stress intensity factors is performed using the energy domain integral (EDI). The EDI for fracture mechanics problems has been described by Cisilino, Aliabadi and Otegui [12] and by Balderrama, Cisilino, and Martinez [13]. To the best of authors knowledge, it is the first time that EDI is been used in the computation of dynamic stress intensity factors for anisotropic materials.

BOUNDARY ELEMENT FORMULATION

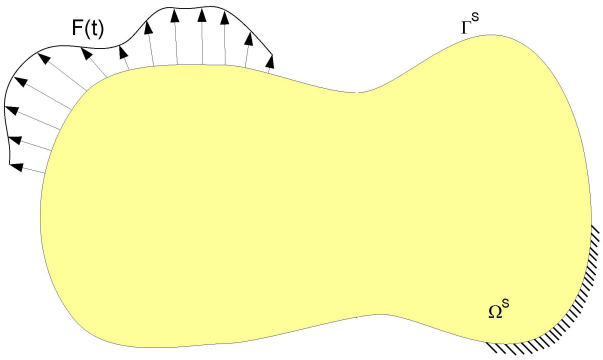

Figure 1: Illustration of cracked plate

Considering that the sheet shown in Fig.(1) is under a dynamic load, the integral equation for the sheet in a source point (x') is given by [8]:

$$c_{ij}\left(x'\right)u_j\left(x'\right)+\int_{\Gamma}T_{ij}\left(x',\,x\right)u_j\left(x'\right)d\Gamma=\int_{\Gamma}U_{ij}\left(x',\,x\right)t_j\left(x'\right)d\Gamma+\int_{\Omega}U_{ij}\left(x',\,x\right)\rho\ddot{u}_j\left(x'\right)d\Omega\quad.\tag{1}$$

The coefficient $c_{ij}\left(x'\right)$ depends on the position of the source point (x') in relation to the boundary which is being integrated, $t_j\left(x'\right)$ and $u_j\left(x'\right)$ are nodal tractions and displacements, $T_{ij}\left(x',\,x\right)$ and $U_{ij}\left(x',\,x\right)$ are anisotropic fundamental solutions for tractions and displacements, and ρ is the mass density of the material. The first three terms from eq.(1) refer to the classical elastostatics formulation, and the last term refers to the effect of body forces due to the mass of the sheet under dynamic load.

DUAL BOUNDARY ELEMENT METHOD (DBEM)

The DBEM consists on applying a displacement equation in the boundary and in one of the sides of the crack, and a traction equation in the remaining side of the crack. The displacement equation is given by eq.(1). The traction equation, obtained by the differentiation of eq.(1) [8], is given by:

$$\frac{1}{2}t_j\left(x'\right)+n_{(i)}\left(x'\right)\int\limits_{\Gamma}S_{ijk}\left(x',\,x\right)u_k\left(x'\right)d\Gamma=n_{(i)}\left(x'\right)\int\limits_{\Gamma}D_{ijk}\left(x',\,x\right)t_k\left(x'\right)d\Gamma+$$
$$n_{(i)}\left(x'\right)\int\limits_{\Omega}D_{ijk}\left(x',\,x\right)\rho\ddot{u}_k\left(x'\right)d\Omega \quad , \tag{2}$$

where $S_{ijk}\left(x',\,x\right)$ and $D\left(x',\,x\right)$ are linear combinations of derivatives of $T_{ij}\left(x',\,x\right)$ and $U_{ij}\left(x',\,x\right)$. When $x'\rightarrow x$, $S_{ijk}\left(x',\,x\right)$ exhibits hypersingularity $O\left(r^{-2}\right)$, and $D\left(x',\,x\right)$ exhibits strong singularity $O\left(r^{-1}\right)$, where $r\left(x',\,x\right)$ is the distance between the source and the integration points and $n_i\left(x'\right)$ is a unitary vector, normal to the boundary at the source point. Eq.(2) is known as hypersingular equation for plane elasticity, and, together with eq.(1), constitutes the basis of the DBEM technique.

DUAL RECIPROCITY BOUDARY ELEMENT METHOD (DRBEM)

Eq.(1) contains both, domain and boundary integrals. The DRBEM allows approximating a domain integral by a sum of boundary integrals. Applying the DRBEM in this elastodynamic problem consists on approximating the inertial effects of eq.(1) by [8]:

$$\rho\ddot{u}_j\left(x'\right)=\sum_{e=1}^{E}\beta_k^e q_{jk}^e\left(x',\,x\right) \quad , \tag{3}$$

where E is number of nodes. Coefficients β_k^e are interpolation coefficients and $q_{jk}^e\left(x',\,x\right)$ are interpolation functions, which, for the anisotropic sheet, are given by[8]:

$$q_{jk}^e\left(x^e,\,x\right)=C_{jilm}\left[c\,r\left(r_{,m}\,r_{,i}\,\delta_{lk}+\delta_{im}\,\delta_{lk}\right)\right] \quad , \tag{4}$$

where C_{jilm} is the elastic constant tensor from the equilibrium equation. The constant c is arbitrary, $\hat{u}_{kj}\left(x'\right)$ and $\hat{t}_{kj}\left(x'\right)$ are given by[7]:

$$\hat{u}_{kj}=c\,r^3\,\delta_{kj} \qquad \text{and} \qquad \hat{t}_{kj}=\sigma_{kjm}\,n_m \quad , \tag{5}$$

where n_m is a unitary vector, normal to the boundary at the source point and σ_{kjm} is given by[8]:

$$\sigma_{kjm}=C_{kmrs}\left[c\,\frac{3r^2}{2}\left(r_{,s}\,\delta_{jr}+\,r_{,r}\,\delta_{js}\right)\right] \quad . \tag{6}$$

Coupling eq.(3) with eq.(1), the integral equation is given by:

$$c_{ij}\left(x'\right)u_j\left(x'\right)+\int\limits_{\Gamma}T_{ij}\left(x',\,x\right)u_j\left(x'\right)d\Gamma=\int\limits_{\Gamma}U_{ij}\left(x',\,x\right)t_j\left(x'\right)d\Gamma+$$
$$\sum_{e=1}^{E}\beta_k^e\left[c_{ij}\left(x^e\right)\hat{u}_{kj}^e\left(x^e\right)+\int\limits_{\Gamma}U_{ij}\left(x^e,\,x\right)t_{kj}^e\left(x^e\right)d\Gamma-\int\limits_{\Gamma}T_{ij}\left(x^e,\,x\right)\hat{u}_{kj}^e\left(x^e\right)d\Gamma\right] \quad . \tag{7}$$

DISCRETIZED BOUNDARY ELEMENT FORMULATION

In order to obtain the elastodynamic response of the system, the boundary is divided into boundary elements. Quadratic elements are used to model the sheet. For matters of convenience, four vectors with dimension $(2 \times E)$ are created:

$$\mathbf{u} = \boldsymbol{\varphi} u^{(i)} \quad ; \quad \hat{\mathbf{u}} = \boldsymbol{\varphi} \hat{u}^{(i)} \quad ; \quad \mathbf{t} = \boldsymbol{\varphi} t^{(i)} \quad ; \quad \hat{\mathbf{t}} = \boldsymbol{\varphi} \hat{t}^{(i)} \quad , \tag{8}$$

where $\boldsymbol{\varphi}$ is the vector of quadratic shape functions, $\mathbf{u}\,(2 \times E)$ and $\mathbf{t}\,(2 \times E)$ are vectors of nodal displacements and tractions of the system, and $\hat{\mathbf{u}}\,(2 \times E)$ and $\hat{\mathbf{t}}\,(2 \times E)$ are the vectors of particularly solutions for nodal displacements and tractions of the system. Coupling eq.(8) with eq.(7), and calling

$$\int_{\Gamma_j} U \boldsymbol{\varphi} d\Gamma = \mathbf{G} \qquad \text{and} \qquad \int_{\Gamma_j} T \boldsymbol{\varphi} d\Gamma = \mathbf{H} \quad , \tag{9}$$

it is possible to rewrite the integral equation (7) as:

$$\mathbf{H}_{\mathrm{lj}} \mathbf{u}_{\mathrm{j}} = \mathbf{G}_{\mathrm{lj}} \mathbf{t}_{\mathrm{j}} + \sum_{e=1}^{E} \left[\mathbf{H}_{lj} \mathbf{u}_j^e - \mathbf{G}_{\mathrm{lj}} \mathbf{t}_{\mathrm{j}}^{\mathrm{e}} \right] \boldsymbol{\beta}_{\mathrm{e}} \quad . \tag{10}$$

The E vectors $\boldsymbol{\beta}_{\mathrm{e}}\,(2 \times 1)$ can be assembled in one vector $\boldsymbol{\beta}\,(2E \times 1)$. Therefore, eq.(3) can be rewritten as:

$$\mathbf{p} = \mathbf{Q} \boldsymbol{\beta} \quad , \tag{11}$$

where $\mathbf{p}$ contains the body forces of the component under consideration for each one of its nodes. The matrix $\mathbf{Q}$ contains values of the function $q_j^e\,(x',\, x)$ for the nodes of the component which is being considerate. The matrix form for the equilibrium equations of the component is obtained coupling eq.(11) with eq.(10), and can be written as:

$$\mathbf{H}_{\Gamma} \mathbf{u}_{\Gamma} - \mathbf{G}_{\Gamma} \mathbf{t}_{\Gamma} = \mathbf{B}_{\Gamma} \mathbf{p}_{\Gamma} \tag{12}$$

where $\mathbf{B}$ is given by:

$$\mathbf{B} = \left[\mathbf{H} \hat{\mathbf{U}}_{\mathrm{E}} - \mathbf{G} \hat{\mathbf{T}}_{\mathrm{E}} \right] \mathbf{Q}^{-1} \quad . \tag{13}$$

$\hat{\mathbf{T}}$ and $\hat{\mathbf{U}}$ are matrices of traction and displacement particular solutions. Finally, coupling equations for boundary and domain, the equation system, can be written as:

$$\mathbf{H}\mathbf{u} = \mathbf{G}\mathbf{t} + \mathbf{B}\mathbf{p}. \tag{14}$$

TRANSIENT SOLUTION

To solve the linear system given by eq.(14), a transient solution procedure is used. This procedure was proposed by Houbolt[11]. Considering that the inertial effects of the components are due to an acceleration field given by:

$$\mathbf{p} = \rho \ddot{\mathbf{u}} = \mathbf{Q} \boldsymbol{\beta} \quad , \tag{15}$$

eq.(14) can be rewritten for an instant of time $\tau + \triangle\tau$ as:

$$\mathbf{H}\mathbf{u}_{\tau+\triangle\tau} = \mathbf{G}\mathbf{t}_{\tau+\triangle\tau} + \mathbf{B}\rho\ddot{\mathbf{u}}_{\tau+\triangle\tau} \quad . \tag{16}$$

In order to proceed with the time integration, the period τ is divided in N time steps , where:

$$\tau = N\triangle\tau \quad . \tag{17}$$

Assuming that the solution for eq.(16) is known at $\tau = 0, \triangle\tau, 2\triangle\tau...$, the acceleration at $\tau + \triangle\tau$ is approximated by the expression[11]:

$$\ddot{\mathbf{u}}_{\tau+\triangle\tau} = \frac{1}{\triangle\tau^2}\left(2\mathbf{u}_{\tau+\triangle\tau} - 5\mathbf{u}_{\tau} + 4\mathbf{u}_{\tau-\triangle\tau} - \mathbf{u}_{\tau-2\triangle\tau}\right) \quad . \tag{18}$$

Inserting eq.(18) into eq.(16), the following system of equation is obtained:

$$\left[\mathbf{H} - \rho\frac{2}{\triangle\tau^2}\mathbf{B}\right]\mathbf{u}_{\tau+\triangle\tau} = \mathbf{G}\mathbf{t}_{\tau+\triangle\tau} + \mathbf{B}\rho\frac{1}{\triangle\tau^2}\left(-5\mathbf{u}^{\mathrm{S}}_{\tau} + 4\mathbf{u}^{\mathrm{S}}_{\tau-\triangle\tau} - \mathbf{u}^{\mathrm{S}}_{\tau-2\triangle\tau}\right). \tag{19}$$

Energy Domain Integral

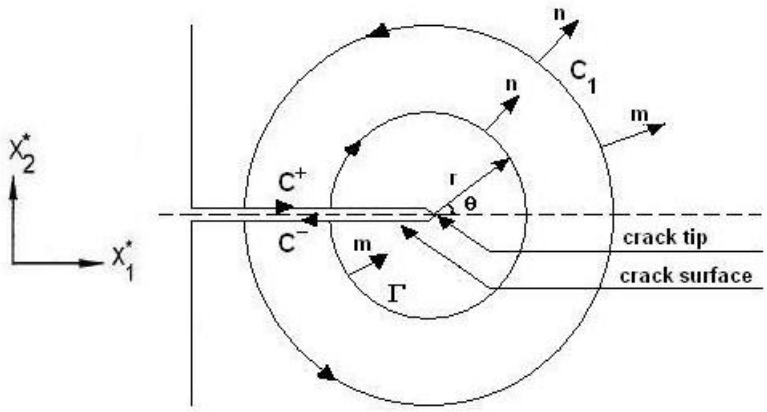

Figure 2: Integration limits for J-Integral.

The linear elastic fracture mechanics theory is only suitable for problems with a small area of non-linear deformation around the crack tip. When this criteria is not verified, an alternative theory must be applied [12]. Furthermore, the evaluation of stress intensity factors using numerical solutions of stresses and strains near the crack tip, usually require a fine mesh of elements and often do not provide accurate results for stress intensity factors [5]. Among the most used parameters to overcome these problems, are the J Integral and the energy domain integral. Those parameters consider a virtual energy release rate for stationary cracks, and can be used as failure criteria.

The EDI methodology is a general domain integral method for the computation of J proposed by [14], [15], and [16]. The methodology can be applied to quasi-static and dynamic problems with elastic, plastic, or viscoplastic material response, as well as thermal loading. The EDI methodology

is equivalent to the virtual crack extension technique but has the advantage that only one computer run is necessary to evaluate the point wise energy release rate along the complete crack front. Besides, the domain integral formulation is efficient and relatively simple to implement numerically.

Considering the simplified example given by Fig.(2), the energy release rate per unit of crack length advance along the x_1^* axis under quasi-static conditions is given by [12]:

$$J_k = \lim_{\Gamma \to 0} \int_{\Gamma} \left(w\delta_{ik} - \sigma_{ij}^* u_{j,k}^* \right) n_i dC \quad , \tag{20}$$

where w is the strain energy density, σ_{ij}^* and $u_{j,1}^*$ are Cartesian components of stress and displacement expressed in the local system x^*, n_i is the unit vector that is normal to the contour Γ, and dC is the differential of the arc length C , as depicted in Fig.(2). Although is possible to compute J_k integral, these methods are generally quite time consuming, as they require internal evaluations at Gauss points of all quantities. In order to overcome this drawback, the EDI is the method implemented in this work.

Let δl denote the local crack front advance in the normal to the crack front direction in the plane of the crack. Thus, the energy released J_k per unit of finite segment of crack advance Δa, for quasi-static conditions, can be obtained by:

$$-\delta\pi = J_k \Delta a \quad , \tag{21}$$

where $-\delta\pi$ is the decrease in potential energy.

Inducing $h \to 0$, as depicted in Fig.(3), means that the surfaces S^+ and S^- will have normal vectors m_k along the x_2^* axis, and the surface S_t will have its normal vector m_k along the x_1^* axis. Hence, the local crack front advance δl is given by:

$$\delta l = \Delta a \, l_k \, m_k \quad . \tag{22}$$

where $\Delta a l_k$ denotes the crack advance in the x_k^* direction.

Furthermore, restricting l_k to lie along S_t and to be a function of x_1^*, we obtain:

$$J_k \Delta a = \Delta a \int_{S_t} \left(\sigma_{ij}^* u_{j,k}^* - w\delta_{ki} \right) l_k \, m_i \, dS \quad . \tag{23}$$

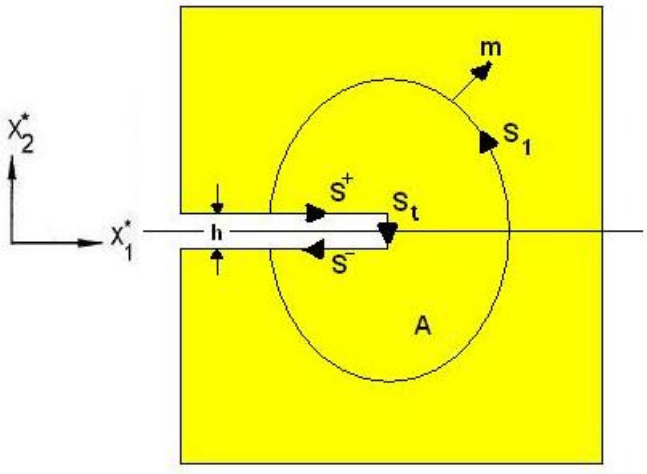

Figure 3: Integration limits for J-Integral.

To develop an domain integral, we consider the simply connected area S enclosed by the surfaces S^+, S^-, S_t and S_1, as depicted in Fig.(3). Furthermore, introduce the functions[12]:

$$q_k = l_k \quad \text{em} \quad S_t \quad \text{and} \quad q_k = 0 \quad \text{em} \quad S_1 \quad , \tag{24}$$

and consider that q_k is a smooth function in the area S . Using eq.(24), we can re-write eq.(23) as:

$$J_k = \int_S \left(\sigma_{ij}^* u_{j,k}^* - w\delta_{ki}\right) m_i \, q_k \, dS \; - \int_{S^+ + S^-} \sigma_{2j}^* u_{j,k}^* \, m_2 \, q_k \, dS \quad . \tag{25}$$

To obtain eq.(25), we consider that $m_1 = 0$ and $m_2 = \pm 1$ on the crack surfaces. It may be noted that $q_2 = l_2 = 0$ everywhere. In the absence of crack face tractions, the second term of eq.(25) vanishes. Finally, applying the divergence theorem to the closed surface integral eq.(25), we obtain:

$$J_k = \int_V \left(\sigma_{ij}^* u_{j,k}^* - w\delta_{ki}\right) q_{k,i} \, dV. \tag{26}$$

Notice that the integration presented by eq.(26) is path independent. Thus, any area may be used to perform the integration, regardless of shape, or symmetry.

Taking into consideration the inertial effects of the sheet, another term is added to eq.(20). Thus, the energy release rate can be re-written as [12]:

$$\hat{J}_k = \lim_{\Gamma \to 0} \left(\int_\Gamma \left(w\delta_{ik} - \sigma_{ij}^* u_{j,k}^*\right) n_i dC + \int_V \rho \ddot{u_i}^* u_{i,k}^* dV \right), \tag{27}$$

where $\rho \ddot{u_i}^*$ are inertial effects active near the crack tip.

Considering the inertial effects acting in the sheet, eq.(26) can be re-written as:

$$\hat{J}_k = \int_V \left(\sigma_{ij}^* u_{j,k}^* - w\delta_{ki}\right) q_{k,i} \, dV + \int_V \rho \ddot{u_i}^* u_{i,1}^* dV. \tag{28}$$

The function q_k was introduced in order to model the virtual crack front advance. Cisilino et al. [12] have presented a bi-quadratic function for a three dimensional problem, which has been widely tested. The two dimensional form of this function is given by:

$$q_k\left(x^*\right) = \left[1 - \left(\frac{r}{r_0}\right)^2\right], \tag{29}$$

where r is the distance of the crack tip on the plane given by $x_1^* - x_2^*$. Notice that q_k, given by eq.(29), fulfills the condition of smoothness inside the integration area S. The shape of the function q_k is quadratic in order to interpolate the contribution of the stress intensity factors in the stress distribution at the crack region.

COMPUTATIONAL IMPLEMENTATION OF THE EDI

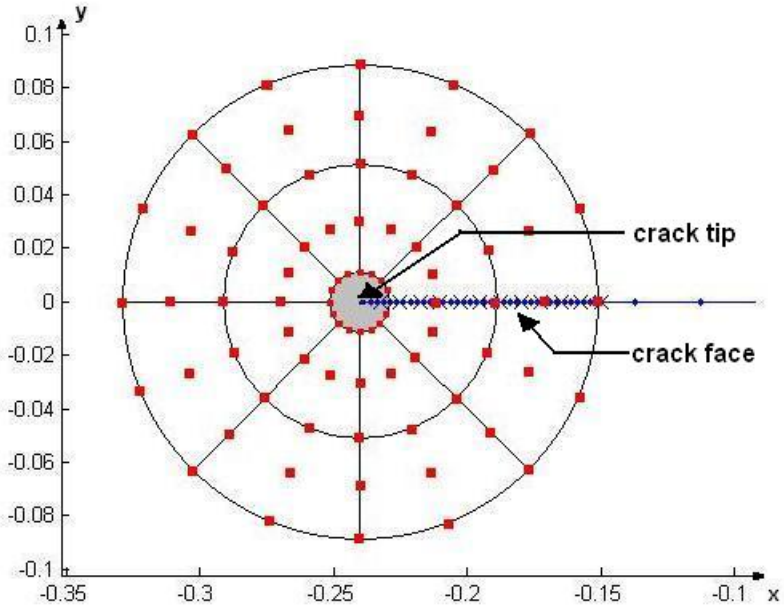

Figure 4: EDI integration domain.

In possession of eq.(28), it is necessary to perform the domain integration around the crack tip, in order to obtain $\hat{J}$. An alternative to proceed with the analysis, is to perform the isoparametric integration of cells created around the crack tip with bi-quadratic elements, as shown in the Fig.(4), thus fulfilling the derivative condition of q_k. The portion of the domain in which area integrals are performed is discretized using 9-node isoparametric cells, over which stresses, strains and displacements derivatives are approximated by products of the interpolation function Φ_i, and the nodal values of σ_{ij}, ε_{ij} and $\ddot{u}_i$, known at the end of each time step of the solution procedure. Functions q_k are specified at all nodes within the integration area. Thus, it can be written in isoparametric form as:

$$q_k = \sum_{i=1}^{NCells} \Phi_i Q_i^k, \tag{30}$$

where Q_i^k are the nodal values of q_k in the ith node. From eq.(24), it is possible to realize that Q_i^1 and Q_i^2 are equal to zero. Therefore, we have:

$$\frac{\partial q_1}{\partial x_j} = \sum_{i=1}^{NCells} \left(\frac{\partial \Phi_i}{\partial \varepsilon} \frac{\partial \varepsilon}{\partial x_j} + \frac{\partial \Phi_i}{\partial \eta} \frac{\partial \eta}{\partial x_j} \right). \tag{31}$$

Considering the matrix:

$$\mathbf{B}_{iso} = \begin{bmatrix} \frac{\partial \Phi_1}{\partial \varepsilon} & \frac{\partial \Phi_2}{\partial \varepsilon} & \frac{\partial \Phi_3}{\partial \varepsilon} & \frac{\partial \Phi_4}{\partial \varepsilon} & \frac{\partial \Phi_5}{\partial \varepsilon} & \frac{\partial \Phi_6}{\partial \varepsilon} & \frac{\partial \Phi_7}{\partial \varepsilon} & \frac{\partial \Phi_8}{\partial \varepsilon} & \frac{\partial \Phi_9}{\partial \varepsilon} \\ \frac{\partial \Phi_1}{\partial \eta} & \frac{\partial \Phi_2}{\partial \eta} & \frac{\partial \Phi_3}{\partial \eta} & \frac{\partial \Phi_4}{\partial \eta} & \frac{\partial \Phi_5}{\partial \eta} & \frac{\partial \Phi_6}{\partial \eta} & \frac{\partial \Phi_7}{\partial \eta} & \frac{\partial \Phi_8}{\partial \eta} & \frac{\partial \Phi_9}{\partial \eta} \end{bmatrix}, \tag{32}$$

it is possible to obtain the values of $\partial u_i/\partial x_j$ by the product:

$$\begin{bmatrix} \frac{\partial u_1}{\partial x_1} & \frac{\partial u_1}{\partial x_2} \\ \frac{\partial u_2}{\partial x_1} & \frac{\partial u_2}{\partial x_2} \end{bmatrix} = \mathbf{B}_{iso} \begin{bmatrix} u_1^1 & u_2^1 \\ u_1^2 & u_2^2 \\ u_1^3 & u_2^3 \\ u_1^4 & u_2^4 \\ u_1^5 & u_2^5 \\ u_1^6 & u_2^6 \\ u_1^7 & u_2^7 \\ u_1^8 & u_2^8 \\ u_1^9 & u_2^9 \end{bmatrix}, \tag{33}$$

where u^k is the displacement value in the kth node, known after each time-step of the solution procedure. Applying the Gaussian integration, the discretized form of eq.(28) is given by:

$$\hat{J}_1 = \sum_{NCells} \sum_{p=1}^{m} \left\{ \left(\sigma_{ij} \frac{\partial u_j}{\partial x_1} - w\delta_{1i} \right) \frac{\partial q_1}{\partial x_i} + \rho \ddot{u}_j \frac{\partial u_j}{\partial x_1} + \frac{1}{h_S} b_j \frac{\partial u_j}{\partial x_1} \right\}_p det\left(Jac\right)_p W_p, \tag{34}$$

where W_p are the weighting factors, m is the number of Gaussian points per cell, and Jac is the Jacobian matrix given by:

$$Jac = \begin{bmatrix} \partial x/\partial \varepsilon & \partial x/\partial \eta \\ \\ \partial y/\partial \varepsilon & \partial y/\partial \eta \end{bmatrix}. \tag{35}$$

OBTAINING K_I AND K_{II}

The J_k-integral is related to the stress intensity factors of a cracked homogeneous anisotropic plate by

$$\hat{J}_1 = \alpha_{11} K_I^2 + \alpha_{12} K_I K_{II} + \alpha_{22} K_{II}^2, \tag{36}$$

$$\hat{J}_2 = \beta_{11} K_I^2 + \beta_{12} K_I K_{II} + \beta_{22} K_{II}^2, \tag{37}$$

where the α_{ij} are defined by

$$\begin{aligned} \alpha_{11} &= -\frac{a_{22}}{2} \mathrm{Im}\left(\frac{\mu_1 + \mu_2}{\mu_1 \mu_2} \right), \\ \alpha_{22} &= \frac{a_{11}}{2} \mathrm{Im}\left(\mu_1 + \mu_2 \right), \\ \alpha_{12} &= -\frac{a_{22}}{2} \mathrm{Im}\left(\frac{1}{\mu_1 \mu_2} \right) + \frac{a_{11}}{2} \mathrm{Im}(\mu_1 \mu_2), \end{aligned} \tag{38}$$

the β_{ij} are defined by

$$\begin{aligned}
\beta_{11} &= \frac{1}{2}\mathrm{Im}[\omega_{11}\omega_{21} + \omega_{31}\omega_{41}], \\
\beta_{12} &= \frac{1}{2}\mathrm{Im}[\omega_{11}\omega_{22} + \omega_{12}\omega_{21} + \omega_{31}\omega_{42} + \omega_{32}\omega_{41}], \\
\beta_{22} &= \frac{1}{2}\mathrm{Im}[\omega_{12}\omega_{22} + \omega_{32}\omega_{42}],
\end{aligned} \tag{39}$$

and the ω_{ij} by

$$\begin{aligned}
\omega_{11} &= \frac{\mu_1\mu_2}{\mu_1-\mu_2}\left(-\frac{\mu_1}{\sqrt{\mu_1}} + \frac{\mu_2}{\sqrt{\mu_2}}\right) & \omega_{12} &= \frac{1}{\mu_1-\mu_2}\left(-\frac{\mu_1^2}{\sqrt{\mu_1}} + \frac{\mu_2^2}{\sqrt{\mu_2}}\right) \\
\omega_{21} &= \frac{\mu_1\mu_2}{\mu_1-\mu_2}\left(-\frac{p_{11}}{\sqrt{\mu_1}} + \frac{p_{22}}{\sqrt{\mu_2}}\right) & \omega_{22} &= \frac{1}{\mu_1-\mu_2}\left(-\frac{p_{11}\mu_1}{\sqrt{\mu_1}} + \frac{p_{12}\mu_2}{\sqrt{\mu_2}}\right) \\
\omega_{31} &= \frac{\mu_1\mu_2}{\mu_1-\mu_2}\left(-\frac{1}{\sqrt{\mu_2}} + \frac{1}{\sqrt{\mu_1}}\right) & \omega_{32} &= \frac{1}{\mu_1-\mu_2}\left(\frac{\mu_1}{\sqrt{\mu_1}} - \frac{\mu_2}{\sqrt{\mu_2}}\right) \\
\omega_{41} &= \frac{\mu_1\mu_2}{\mu_1-\mu_2}\left(-\frac{p_{21}}{\sqrt{\mu_1}} + \frac{p_{22}}{\sqrt{\mu_2}}\right) & \omega_{42} &= \frac{1}{\mu_1-\mu_2}\left(-\frac{p_{21}\mu_1}{\sqrt{\mu_1}} + \frac{p_{22}\mu_2}{\sqrt{\mu_2}}\right)
\end{aligned} \tag{40}$$

where a_{ij} are the compliance coefficients, μ_k are roots of the characteristic polynomial and p_{ij} are material constants [17].

For traction free cracks the J_1-integral vanishes along the crack surfaces, whereas the J_2-integral would involve integration of highly singular integrands along each surfaces. In order to avoid this difficulty an auxiliary relationship in terms of displacements ratios is developed here to be used together with J_1 for decoupling of the stress intensity factors K_I and K_{II}.

The coupling of the stress intensity factors has been a limiting factor in the analysis of cracked composite materials under mixed mode loading. However, a simple procedure can be introduced for the decoupling of mode I and mode II stress intensity factors, based on the ratio of relative displacements and equation (36), the relation of the J-integral for anisotropic materials, and K_I and K_{II}.

The relative sliding and opening displacements δ_n, for $\theta = \pm\pi$ are given by

$$\delta_1 = 2\sqrt{\frac{2r}{\pi}}(D_{11}K_I + D_{12}K_{II}) \tag{41}$$

and

$$\delta_2 = 2\sqrt{\frac{2r}{\pi}}(D_{21}K_I + D_{22}K_{II}) \ , \tag{42}$$

where D_{ij} are functions of the complex parameters of the anisotropic material [17].

The ratio of relative displacements is

$$S = \frac{\delta_2}{\delta_1} = \frac{D_{21}K_I + D_{22}K_{II}}{D_{11}K_I + D_{12}K_{II}} \ , \tag{43}$$

and the ratio of stress intensity factors

$$F = \frac{K_I}{K_{II}} = \frac{SD_{12} - D_{22}}{D_{21} - SD_{11}} \ , \tag{44}$$

or

$$K_I = FK_{II} \ . \tag{45}$$

Substituting equation (36) into equation (45), and solving for K_{II} gives the following relationship:

$$K_{II} = \left(\frac{J_1}{\alpha_{11} F^2 + \alpha_{12} F + \alpha_{22}} \right)^{\frac{1}{2}} \quad . \tag{46}$$

Thus K_{II} and K_I are now decoupled and can be obtained from a knowledge of S, F, J_1 and α_{ij}.

EXAMPLES

1-Rectangular quasi-isotropic plate with central crack

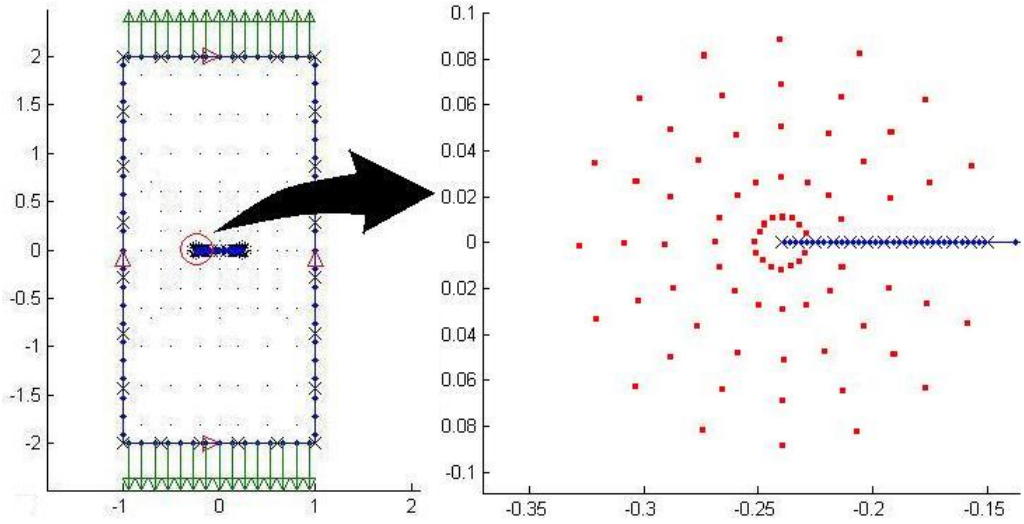

Figure 5: Rectangular plate with central crack.

A rectangular plate with central crack, as depicted in Fig.(5), is instantaneously loaded by a uniform tensile stress $\sigma_0 = 100$ MPa at time $\tau = 0$. The plate has the following dimensions: the length is 400 mm; the width is 200 mm; and crack length is 48 mm. The plate has the following material properties: Young modulus E_1 and E_2 equal to 220 GPa lying respectively on the sheet's width and length directions; shear modulus of 77 GPa; Poisson modulus $\nu = 0.3$; and density $\rho = 5000$ Kg/m^3. A state of plane stress is assumed. This Problem was studied by Chen [18] using the finite difference method, and by Dominguez and Gallego [2] using the time domain BEM, both applied to isotropic materials. The structure was discretized using 80 discontinuous elements and 246 domain points, from which, 75 are used for the energy domain integration. The normalized dynamic stress intensity factor K_I/K_0 versus time is shown in Fig.(6).

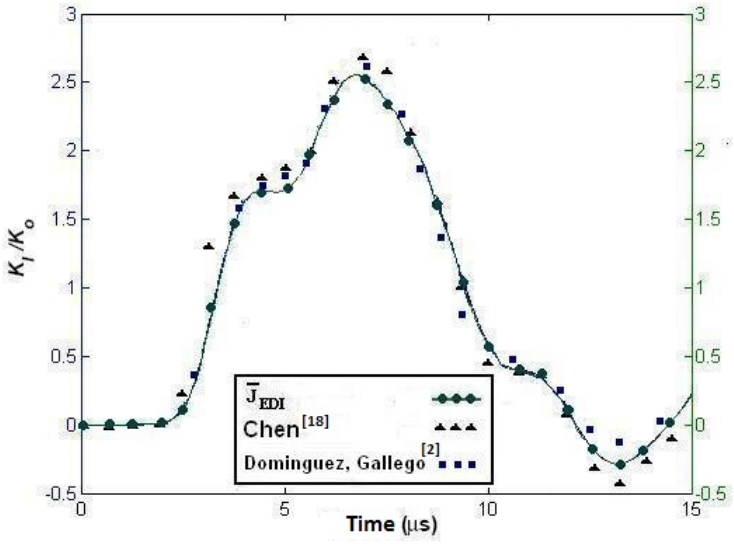

Figure 6: K_I/K_0 for rectangular quasi-isotropic plate with central crack.

2-Rectangular orthotropic plate with central crack

A rectangular plate with central crack, as depicted in Fig.(5), is instantaneously loaded by a uniform tensile stress $\sigma_0 = 100$ MPa at time $\tau = 0$. The plate has the following dimensions: the length is 400 mm; the width is 200 mm; and crack length is 48 mm. The plate has the following material properties: Young moduli $E_1 = 118.3$ GPa and $E_2 = 54.8$ GPa, lying respectively on the sheet's width and length directions; shear modulus of $G_{12} = 8.79$ GPa; Poisson modulus $\nu = 0.4286$; and density $\rho = 1900$ Kg/m^3. A state of plane stress is assumed. This problem was studied by Hua, Tian-You and Lan-Quao[19] using the finite difference method applied do anisotropic materials. The discretization if the structure is similar to the discretization of the previous example. The normalized dynamic stress intensity factor K_I/K_0 versus time is shown in Fig.(7).

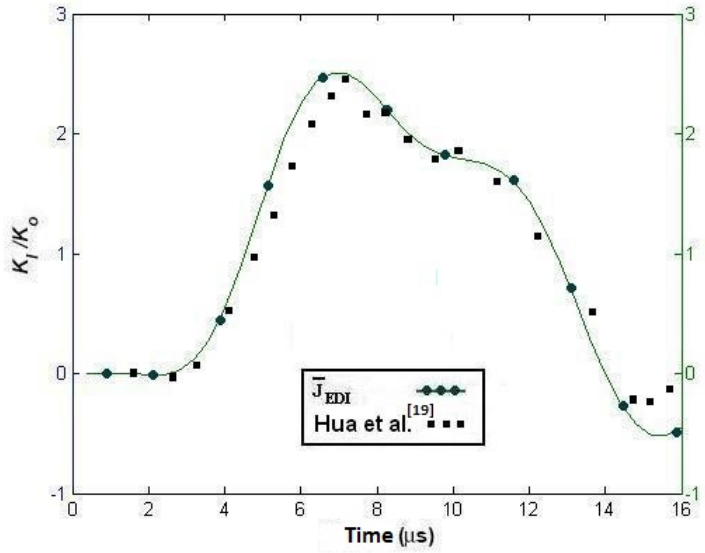

Figure 7: K_I/K_0 for rectangular orthotropic plate with central slanted crack.

3-Rectangular orthotropic plate with central crack

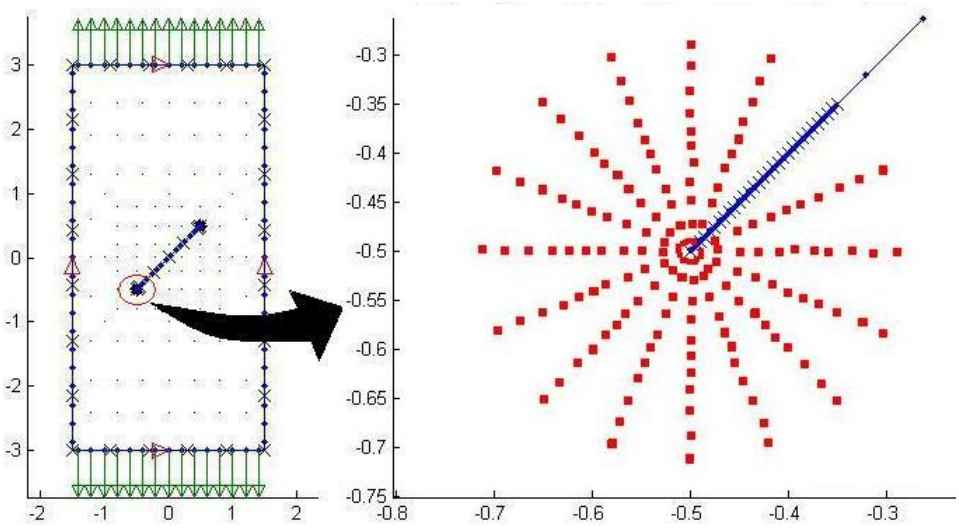

Figure 8: Rectangular plate with central inclinated crack.

A rectangular plate with central crack, with inclination of 45^o, as depicted in Fig.(8), is instantaneously loaded by a uniform tensile stress $\sigma_0 = 100$ MPa at time $\tau = 0$. The plate has the following dimensions: the length of 600 mm; the width is 300 mm; and crack length is 141.4 mm. The plate has the following material properties: Young moduli $E_1 = 220$ GPa and $E_2 = 110$ GPa, lying respectively on the sheet's width and length directions; shear modulus $G_{12} = 76.93$ GPa; Poisson modulus $\nu = 0.4286$; and density $\rho = 5000$ Kg/m^3. A state of plane stress is assumed. This Problem was studied by Albuquerque, Sollero and Aliabadi [7, 8] using the DBEM and DRBEM techniques. The structure was discretized using 96 discontinuous elements and 304 domain points, from which, 105 are used for the energy domain integration. The normalized dynamic stress intensity factors K_I/K_0 and K_{II}/K_0 are shown versus time in Fig.(9) and Fig.(10), respectively.

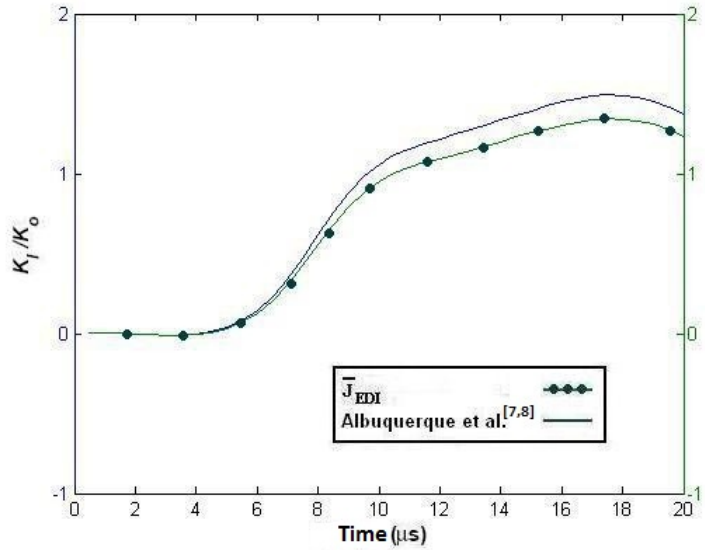

Figure 9: K_I/K_0 for rectangular orthotropic plate with central inclinated crack.

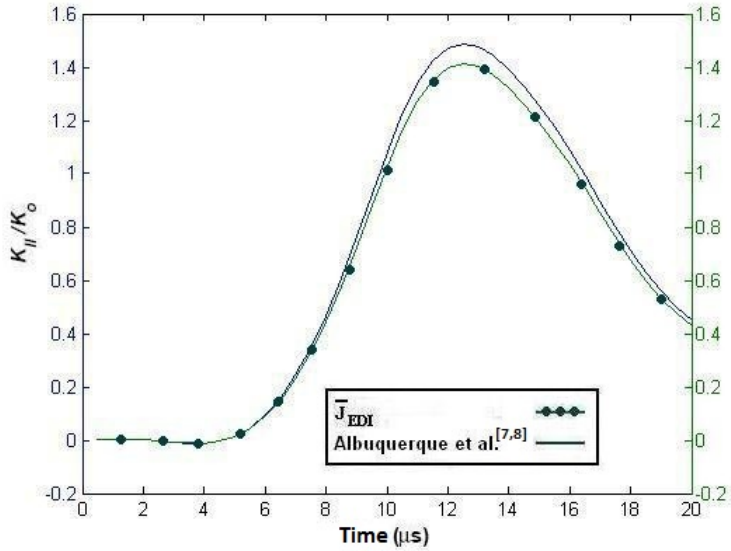

Figure 10: K_{II}/K_0 for rectangular orthotropic plate with central inclinated crack.

Conclusions

In this paper, a formulation for dynamic analysis of composite cracked sheets was presented, and a procedure to solve the problem was proposed as well. The procedure described in this paper is more time consuming than a procedure on a frequency domain. However, allows a broader range of solutions with application of different load cycles. A procedure for the evaluation dynamic stress intensity factors was also presented. The EDI is computationally more expensive than the Crack Tip Opening Displacement (DTOD) method. However, it allows the implementation of other mechanical phenomena, as plasticity effects at the crack tip, and crack propagation. The EDI integration is derived from the $\hat{J}_k$ integral, but it is easier to calculate since all of its terms are domain integrals. It

also allows the isoparametric derivation of the values of displacements. Hence, it is not necessary to integrate the values of displacement derivatives, which is a much more time consuming procedure.

Acknowledgments

The authors would like to thanks FAPESP (The State of São Paulo Research Foundation) and CNPq (National Research Council) for the financial support of this work.

References

[1] G. E. Blandford, A. R. Ingraffea, and J. A. Ligget, Two dimensional stress intensity factor computation using the boundary element method. International Journal for Numerical Methods in Engineering 17:387–404 (1981).

[2] J. Domdinguez and R. Gallego, Time domain boundary element method for dynamic stress intensity factor computation. International Journal of Numerical Methods in Engineering 33: 635-647 (1992).

[3] F. Garcia-Sanchez, C. Z. Zhang, A. Saez. A two-dimensional time-domain boundary element method for dynamic crack problems in anisotropic solids. Engineering Fracture Mechanics 75:1412-1430 (2008).

[4] P. Fedelinski and M. H. Aliabadi, The Dual boundary element method in dynamic fracture mechanics. Engineering Analysis with Boundary Elements 12: 203-210 (1993).

[5] P. Fedelinski and M. H. Aliabadi, The Dual boundary element method: $\hat{J}$-integral for dynamic stress intensity factors. International Journal of Fracture 65: 369-381 (1994).

[6] J. Sladek, V. Sladek, and P. Fedelinski, Computation of the second fracture parameter in elastodynamics by the boundary element method. Advances in Engineering Software 30:725-734 (1999).

[7] E. L. Albuquerque, P. Sollero, and M. H. Aliabadi, The boundary element method applied to time dependent problems in anisotropic materials. International Journal of Solids and Structures, 39:1405-1422 (2002).

[8] E. L. Albuquerque, P. Sollero, and M. H. Aliabadi, Dual boundary element method for anisotropic dynamic fracture mechanics. International Journal for Numerical Methods in Engineering, 59:1187-1205 (2004).

[9] A. Portela, M. H. Aliabadi, and D. P. Rooke, The dual boundary element method: Effective implementation for crack problems. International Journal for Numerical Methods in Engineering, 33:1269-1287 (1982).

[10] M. Kögl and L. Gaul, A boundary element method for transient piezoelectric analysis. Engineering Analysis with Boundary Elements, 24:591-598 (2000).

[11] J. C. Houbolt, A recurrence matrix solution for the dynamic response of elastic aircraft. Journal of Aeronautical and Science, 17:540-550 (1950).

[12] A. P. Cisilino, M. H. Aliabadi, and J. L. Otegui. Energy domain integral applied to solve center and double edge crack problems in three-dimensions. Theoretical and Applied Fracture Mechanics 29:181-194 (1998).

[13] R. Balderrama, A. P. Cisilino, and M. Martinez. Boundary element analysis of three-dimensional mixed-mode thermoelastic crack problems using the interaction and energy domain integrals. International Journal for Engineering Material 74:294-320 (2008).

[14] B. Moran and C. F. Shih. A general treatment of crack tip contour integrals. International Journal of Fracture 35:295-310 (1987).

[15] C. F. Shih, B. Moran, and A. Neddleman. Energy release rate along a three-dimensional crack front in a thermally stresses body. International Journal of Fracture 30:79-102 (1986).

[16] F. Z. Li, , C. F. Shih, and A. Needleman. A comparison of methods for calculating energy release rates. Engineering in Fracture Mechanics 21:405-421 (1985).

[17] P. Sollero and M. H. Aliabadi. Crack growth analysis in homogeneous orthotropic laminates. Composites Science and Technology 58:1697-1703 (1998).

[18] Y. M. Chen, Numerical computation of dynamic stress intensity factors by a Lagrangian finite-difference method. Engineering Fracture Mechanics, 7:653-660 (1975).

[19] Z. Hua, F. Tian-You, and T. Lan-Quao, Composite materials dynamic fracture studies by generalized Shmuely difference algorithm. Engineering Fracture Mechanics, 54:869-877 (1996).

Key Engineering Materials Vol. 454 (2011) pp 113-125

doi:10.4028/www.scientific.net/KEM.454.113

Computer Modelling of Dynamic Fracture Experiments

Piotr Fedelinski[1, a]

[1]Silesian University of Technology, Gliwice, Poland

[a]Piotr.Fedelinski@polsl.pl

Keywords: fracture, crack growth, stress intensity factors, dynamic loading, experiment, boundary element method.

Abstract. In this work the time-domain boundary element method (BEM) is applied to simulate dynamic fracture experiments. The fast fracture is modelled by adding new boundary elements at the crack tip. The direction of crack growth is perpendicular to the direction of maximum circumferencial stress. The time dependent loading of specimens and velocities of crack growth are taken from experiments as input data for computer simulations. The method is used to analyze: a short beam specimen, a special mixed-mode specimen and a three-point bend specimen subjected to impact loads. The dynamic stress intensity factors (DSIF) and the crack paths are compared with the results obtained by other authors who used the finite element method (FEM) and experimental methods.

1. Introduction

The analysis of rapidly growing cracks is one of the important subjects of dynamic fracture mechanics [1]. The path and velocity of crack growth depend on the magnitude and distribution of the stress field in the vicinity of the crack tip, which can be characterized by dynamic stress intensity factors. The aim of dynamic fracture experiments is the determination of fracture toughness, the time dependence of DSIF, the crack growth direction, velocity and shape. These results can be used to establish laws, which define the dependence of crack direction and velocity on DSIF.

Analytical methods are limited to cracked bodies with simple geometries and boundary conditions. Consequently, numerical methods are needed to analyze more general and practical problems. Recently numerical methods are combined with experiments. During the numerical simulation it is assumed that the dimensions of a specimen, its material properties, initial and boundary conditions are known. Additionally the following parameters are specified or searched:

- crack-path history - $x_i(t)$,
- crack-growth history - $a(t)$, $c(t)$,
- crack-growth criterion - $c(K)$,
- crack-direction criterion - $\alpha(K)$,
- crack tip parameters - $K(t)$,

where x_i are the coordinates of crack tip, a is the crack length, c is the crack growth velocity, α is the crack growth angle, K are dynamic stress intensity factors and t is time.

Nishioka et al. [2,3] proposed three types of numerical simulation depending on which parameters are known from the experiments and which are searched. The classification of the methods is given in Table 1.

Table1. Types of numerical simulation of dynamic fracture

Simulation	Known quantities	Unknown quantities
generation phase	$x_i(t)$, $a(t)$, $c(t)$	$K(t)$, $c(K)$, $\alpha(K)$
application phase	$c(K)$, $\alpha(K)$	$x_i(t)$, $a(t)$, $c(t)$, $K(t)$
mixed-phase (type a)	$a(t)$, $c(t)$, $\alpha(K)$	$x_i(t)$
mixed-phase (type b)	$x_i(t)$, $c(K)$	$a(t)$, $c(t)$

The most frequently used computer method in numerical simulations of fracture experiments is the finite element method (FEM). Bui, Maigre and Rittel [4,5,6,7] applied the FEM to analyze a special specimen with a crack of constant length, which was loaded by the split Hopkinson bar. Numerically computed DSIF and velocities of loaded surfaces of the specimen were compared with experimental results. Weisbrod and Rittel [8] analyzed a one-point bend short specimen loaded by a bar. They compared DSIF computed by the FEM with the experimental solutions till the moment of propagation of the crack. Nishioka et al. [3] analyzed by the FEM a three-point bend specimen loaded by a dropping hammer. The numerically computed DSIF and crack paths were compared with the experimental results for various loading points. Gregorie et al. [9] and Combescure et al. [10] applied the extended finite element method (X-FEM) to analyze a special mixed-mode compression specimen. A comparison of numerically computed crack paths and velocities of loaded edges of the specimen with experimental results was presented in that work.

The boundary element method (BEM) is particularly suitable to analysis of crack growth. The computer modelling is simplified in comparison to the FEM since only external boundaries and crack surfaces are divided into boundary elements. The crack growth is modelled by adding new elements at the crack tip. Because of the reduced interpolation to the boundaries of the body the method gives very accurate results. The dynamic crack growth problems are modelled by the time-domain BEM (Dominguez [11]). This formulation was applied to dynamic analysis of stationary cracks by Fedelinski et al. [12]. The same authors applied for the first time the method to dynamically growing cracks without predefined crack paths [13]. Practical applications of the method were presented in [14]. Sellig et al. [15,16] presented the formulation of the method for fast growing cracks with variable velocity and they take into account contact of crack surfaces. Sellig et al. [17] applied the method to simulation of the dynamic fracture test which was earlier analyzed by Bui et al. [4]. They considered additionally dynamic crack growth. The results computed by the BEM and FEM were compared with experiments.

In this work the fundamentals of the time-domain BEM for structures with growing cracks are given for completeness. The method is used to simulate three different dynamic fracture experiments. The numerical examples show possible applications of the method and its accuracy.

The type of the present computer simulation can be classified as the mixed-phase simulation (type a), called the fracture-path prediction mode. In the numerical examples dynamic loading and velocities of crack growth are taken from experiments. The computer code is used to calculate dynamic stress intensity factors and crack paths. The aim of this kind of simulation is to determine DSIF for growing cracks, which is difficult to measure experimentally, and to verify the crack growth direction criterion.

2. Boundary integral equations

The method is applied to a linear elastic, homogeneous and isotropic body containing a rapidly growing crack. The boundary of the body, denoted by $\Gamma(t)$, is a function of time t because of the crack growth. The boundary Γ consists of the external boundary Γ^{e} and two crack surfaces Γ^{+} and Γ^{-}, as shown in Fig. 1. For a body which is not subjected to body forces and which has zero initial displacements and velocities, the displacement of a point x' can be represented by the following boundary integral equation [11]:

$$c_{ij}(x')u_j(x',t) = \int_0^t [\int_\Gamma U_{ij}(x',t,x,\tau)t_j(x,\tau)d\Gamma(x)]d\tau - \int_0^t [\int_\Gamma T_{ij}(x',t,x,\tau)u_j(x,\tau)d\Gamma(x)]d\tau , \quad (1)$$

where $U_{ij}(x',t,x,\tau)$ and $T_{ij}(x',t,x,\tau)$ are the fundamental solutions of elastodynamics, $u_j(x,\tau)$ and $t_j(x,\tau)$ are the boundary displacements and tractions respectively, $c_{ij}(x')$ is a constant which depends on the position of the collocation point, x' is the collocation point, x is a boundary point and t is the observation time.

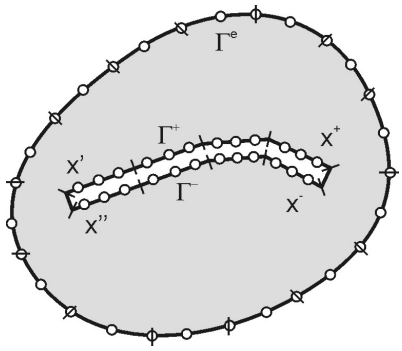

Fig. 1 Boundary element modelling of the body with the crack

The displacement equation for points, which belong to the smooth crack surfaces, has the form:

$$\frac{1}{2}u_i(x',t)+\frac{1}{2}u_i(x'',t)=\int_0^t[\int_\Gamma U_{ij}(x',t,x,\tau)t_j(x,\tau)d\Gamma(x)]d\tau-\int_0^t[\int_\Gamma T_{ij}(x',t,x,\tau)u_j(x,\tau)d\Gamma(x)]d\tau\,, \tag{2}$$

where *x'* and *x''* are coincident points on the opposite crack surfaces. The traction equation for the same points is:

$$\frac{1}{2}t_j(x',t)-\frac{1}{2}t_j(x'',t)=n_i(x')\{\int_0^t[\int_\Gamma U_{kij}(x',t,x,\tau)t_k(x,\tau)d\Gamma(x)]d\tau-\int_0^t[\int_\Gamma T_{kij}(x',t,x,\tau)u_k(x,\tau)d\Gamma(x)]d\tau\}\,, \tag{3}$$

where $U_{kij}(x',t,x,\tau)$ and $T_{kij}(x',t,x,\tau)$ are the fundamental solutions of elastodynamics and $n_i(x')$ is an outward normal unit vector at the collocation point.

3. Numerical formulation

The numerical modelling requires discretization of both space and time variations. The boundary $\Gamma(\tau)$ of the body is divided into boundary elements. The observation time t is divided into N time steps. The crack growth is modelled by adding new elements ahead of the crack tip [13]. A distinct set of boundary integral equations is obtained by applying the displacement equation (1) for collocation nodes along the external boundary, the displacement equation (2) and the traction equation (3) simultaneously for coincident nodes along both crack faces. Quadratic elements are used for the discretization of the boundary, as shown in Fig. 1. Within each time step the displacements are approximated by using linear interpolating functions and the tractions are piecewise constant. After discretization and integration the following matrix equation is obtained for time t, that is after N time steps:

$$\boldsymbol{H}^{NN}\boldsymbol{u}^{N}=\boldsymbol{G}^{NN}\boldsymbol{t}^{N}+\sum_{n=1}^{N-1}(\boldsymbol{G}^{Nn}\boldsymbol{t}^{n}-\boldsymbol{H}^{Nn}\boldsymbol{u}^{n})\,, \tag{4}$$

where $\boldsymbol{u}^n$, $\boldsymbol{t}^n$ contain nodal values of displacements and tractions at the time step n; $\boldsymbol{H}^{Nn}$ and $\boldsymbol{G}^{Nn}$ depend on the fundamental solutions and interpolating functions. The columns of matrices $\boldsymbol{H}^{NN}$, $\boldsymbol{G}^{NN}$ are reordered according to the boundary conditions, giving new matrices $\boldsymbol{A}^{NN}$ and $\boldsymbol{B}^{NN}$. The matrix $\boldsymbol{A}^{NN}$ is multiplied by the vector $\boldsymbol{x}^N$ of unknown displacements and tractions and the matrix $\boldsymbol{B}^{NN}$ by the vector $\boldsymbol{y}^N$ of the known boundary conditions; thus:

$$\boldsymbol{A}^{NN}\boldsymbol{x}^{N} = \boldsymbol{B}^{NN}\boldsymbol{y}^{N} + \sum_{n=1}^{N-1}(\boldsymbol{G}^{Nn}\boldsymbol{t}^{n} - \boldsymbol{H}^{Nn}\boldsymbol{u}^{n}). \tag{5}$$

The matrix equation is solved step-by-step giving the unknown displacements and tractions at each time step.

4. Modelling of crack growth

The dynamic stress intensity factors (DSIF) are obtained from the crack opening displacements [13]:

$$K_I = 2\mu\sqrt{\frac{\pi}{2r}}\frac{4\beta_1\beta_2 - \left(1+\beta_2^2\right)^2}{4\beta_1\left(1-\beta_2^2\right)}\Delta u_2, \tag{6}$$

$$K_{II} = 2\mu\sqrt{\frac{\pi}{2r}}\frac{4\beta_1\beta_2 - \left(1+\beta_2^2\right)^2}{4\beta_2\left(1-\beta_2^2\right)}\Delta u_1, \tag{7}$$

where:

$$\beta_1 = \sqrt{1-(c/c_1)^2}\,,\ \beta_2 = \sqrt{1-(c/c_2)^2}\,, \tag{8}$$

where μ is the shear modulus; Δu_1 and Δu_2 are the relative displacements in the tangential and perpendicular direction of corresponding points on opposite crack faces; r is the distance of points from the crack tip, c is the velocity of crack growth, c_1 and c_2 are the velocities of longitudinal and shear waves respectively. In the present work the relative displacements of the third pair of coincident nodes of boundary elements at the crack tip were used to calculate dynamic stress intensity factors for growing cracks. The stress distribution in the vicinity of a crack tip is calculated using DSIF and current tip velocity. The crack will grow in the direction of maximum circumferential stress. The crack growth is modelled by adding a new pair of boundary elements of length Δa at the crack tip:

$$\Delta a = c\Delta\tau, \tag{9}$$

where $\Delta\tau$ is a time step.

4. Numerical examples

4.1. One point bend short beam specimen. An unsupported short beam specimen is in contact with a single bar. The striker hits the bar, the stress wave propagates through the bar and loads the specimen. Strains in the bar and the specimen are measured by strain gauges. The experimental setup is shown in Fig. 2. This problem was analyzed by the FEM and experimentally in [8]. The loading of the specimen is determined from the incident and reflected strains recorded by the gauge 1. The onset of crack propagation is detected by gauges 2 and 3. The dimensions of the specimen in millimeters and loading are given in Fig. 3. The specimen is made of a commercial tungsten base heavy alloy. The dynamic Young modulus of the material is equal to E=338 GPa, Poisson's ratio ν=0.3 and mass density ρ=17100 kg/m^3. The specimen is in plane strain conditions. The experimentally determined loading is shown in Fig. 4 [8].

The specimen is divided into 84 boundary elements and the time step is $\Delta\tau$=1 μs. The computer modelling was performed for a stationary crack. The experimentally detected crack propagation started at 21 μs after the specimen was loaded [8]. Therefore the numerical results are valid for times smaller than 21 μs.

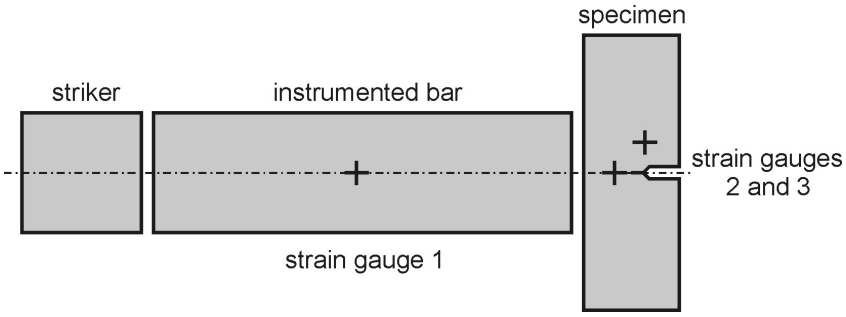

Fig. 2. Measurement system [8]

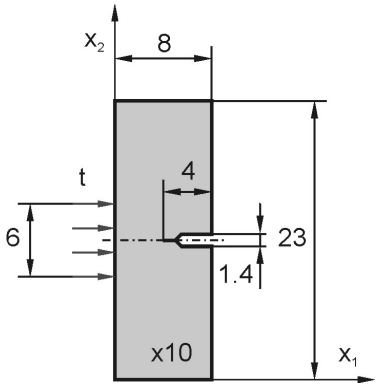

Fig.3. Dimensions of the short beam specimen and loading [8]

The comparison of boundary element method (BEM), finite element method (FEM) and experimental (EXP) dynamic stress intensity factors [8] is shown in Fig. 5. The quality of computer simulation strongly depends on the accuracy of experimentally determined dynamic loading. The results of the BEM simulation better agree with the FEM simulation, than with experimental results, because the same dynamic boundary conditions were used in computer simulations.

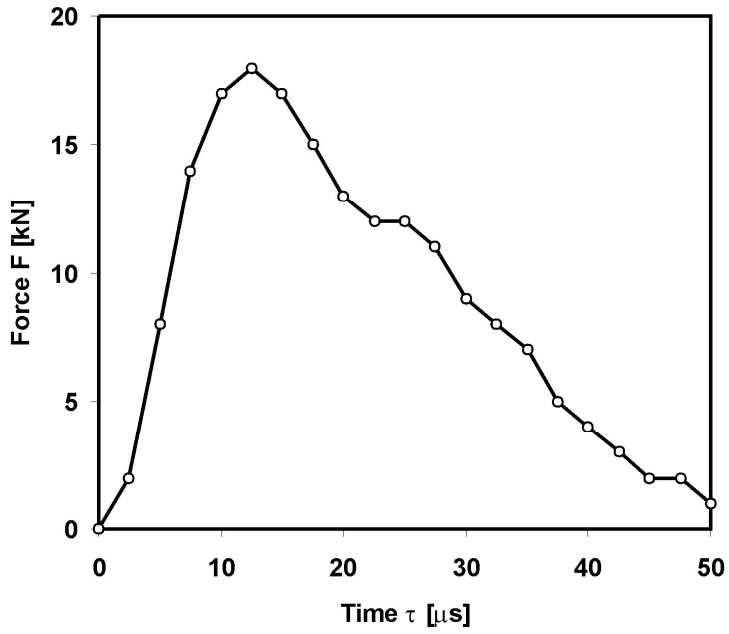

Fig. 4. Time variation of loading for the short beam specimen [8]

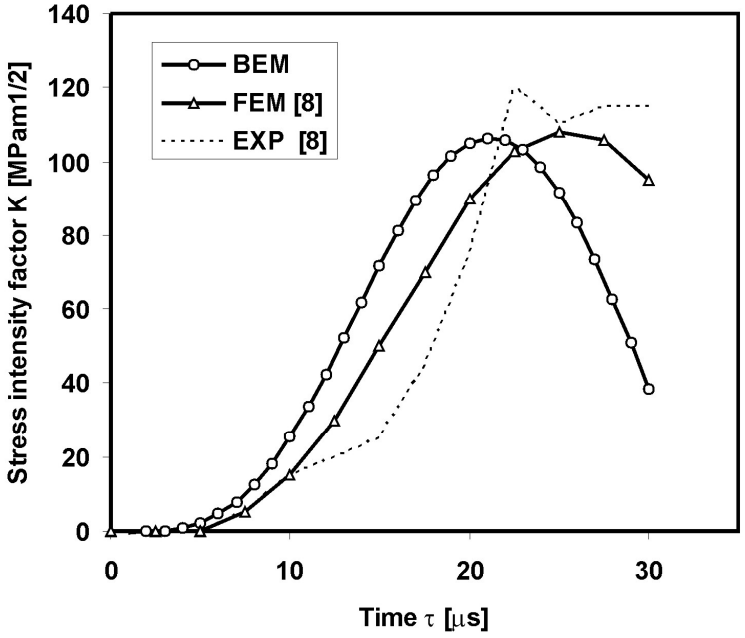

Fig. 5. Dynamic stress intensity factors for the short beam specimen

4.2. Special mixed-mode specimen. The method is applied to analyze a special cracked specimen loaded by the split pressure Hopkinson bar. The experimental results and the computer modelling of this specimen by using the X-FEM are presented in works [9,10]. The data, which are necessary for computer simulation, are taken from the work [9]. The special specimen is placed between the split Hopkinson bars shown in Fig 6. The input bar is loaded by the striker. The velocity of the striker is measured by the optical gauge. The strains in the input bar are measured by strain gauges 1 and 2 and strains in the output bar by the strain gauge 3. The specimen is lighted and 4 cameras register the state of the specimen during the experiment. The striker hits the input bar and the stress wave propagates through the input bar, the specimen and the output bar. The dimensions of the specimen are given in millimeters in Fig 7. The initial crack, which is situated above the axis of symmetry of the specimen, is subjected simultaneously to tension and shear mode of loading when the specimen is compressed.

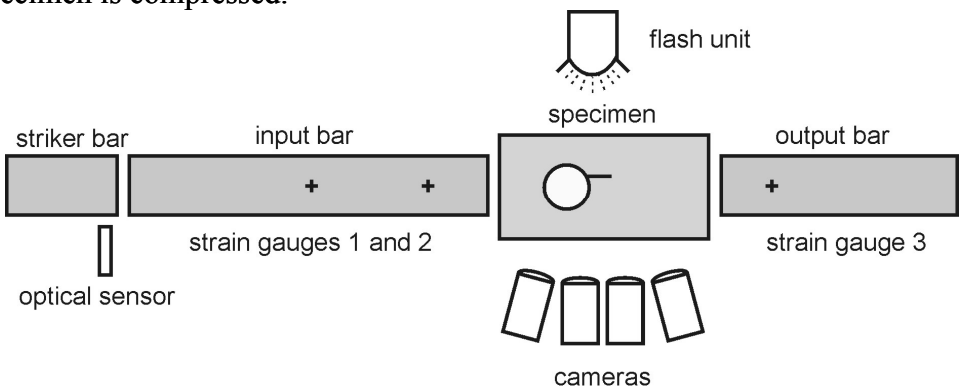

Fig. 6. Measurement system [9]

The specimen is made of polymethyl methacrylate (PMMA) and has the following material properties: Young's modulus E=3.3 GPa, Poisson's ratio ν=0.42, mass density ρ=1180 kg/m^3, and the structure is in plane strain. Only the specimen is modelled using 70 boundary elements. During the crack growth in each time step two boundary elements are added at the crack tip. The final number of elements is equal to 130. The time step is equal to Δt= 10 μs.

The left and right edge is loaded by the uniformly distributed tractions t_1 and t_2, which were measured during the experiment. The time dependence of resultant forces on both edges of the specimen F_1 and F_2 is given in Fig 8. The crack is stationary from the beginning of loading till 200 μs, next it grows with a velocity 210/m/s, during the period of time from 270 till 320 μs it arrests, and later it grows with the velocity 160 m/s. The process is simulated till 500 μs.

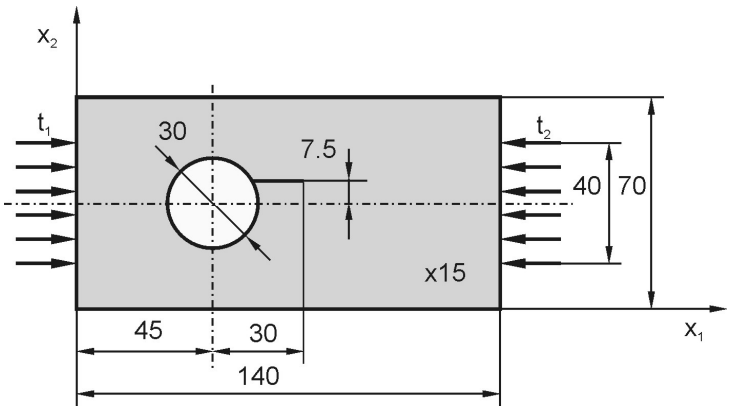

Fig. 7. Dimensions of the special mixed-mode specimen and loading [9]

The comparison of computed and experimental velocities of the edges of the specimen is shown in Fig. 9. Time variations of DSIF K_I and K_{II} are presented in Fig 10. When the longitudinal wave reaches the crack tip the DSIF increase. When the crack starts to grow the DSIF decrease. During the period of time from 270 till 320 μs, when K_I has the minimal value, the crack arrests. After the increase of K_I the crack grows again. The DSIF K_{II} has small values during the growth of the crack. Gregorie et al. [9] assumed in the computer simulation of this experiment that the critical value of DSIF is K_{IC}=1.33 MPam$^{1/2}$. In Fig. 10 it can bee seen that K_I has smaller value than the critical DSIF during the arrest of the crack. The specimen with the final crack is shown in Fig 11. The shape of the crack computed numerically is compared with the experimental crack [9] in Fig 12. A good agreement of shapes of the crack can be seen.

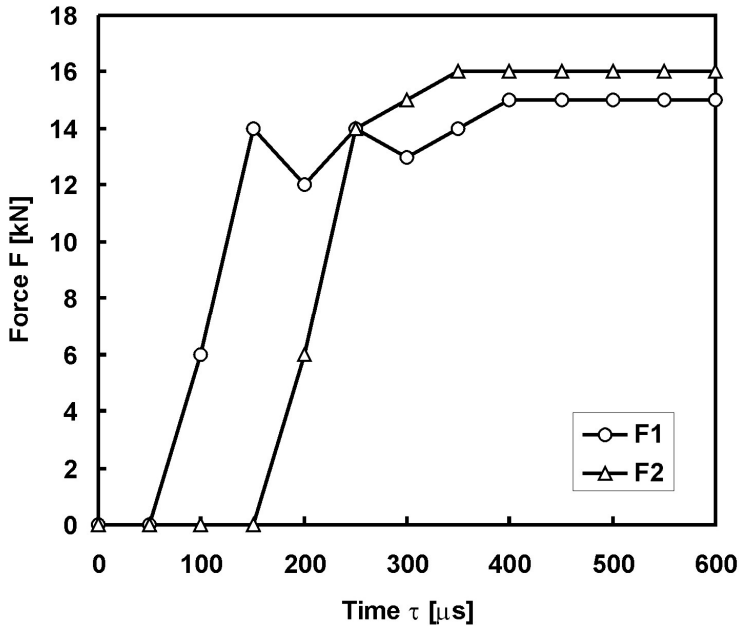

Fig. 8. Time variation of resultant tractions on edges of the special mixed-mode specimen [9]

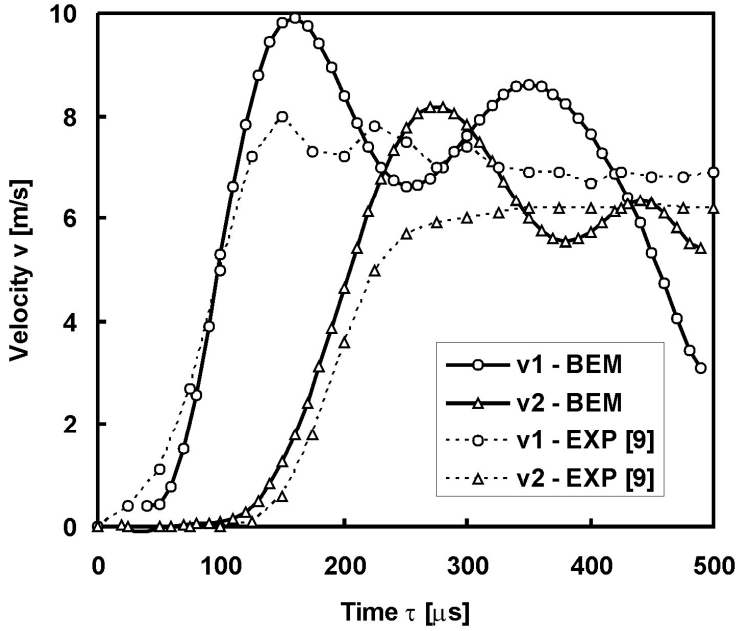

Fig. 9. Time variation of velocities of edges of the special mixed-mode specimen

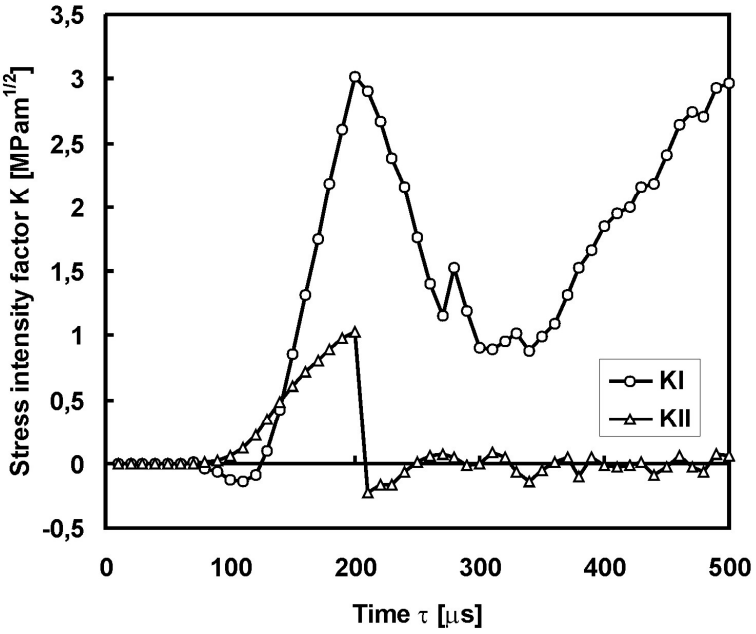

Fig. 10. Dynamic stress intensity factors for the special mixed-mode specimen

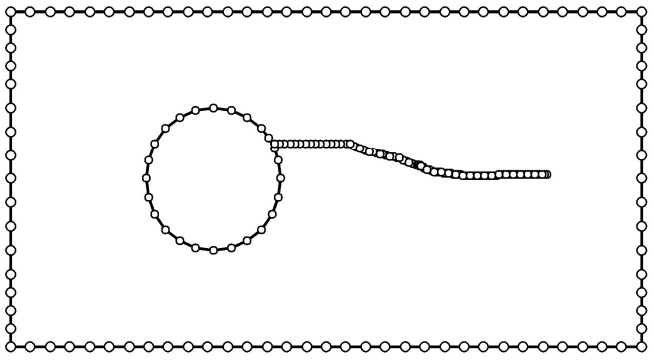

Fig. 11. The special mixed-mode specimen with the final crack

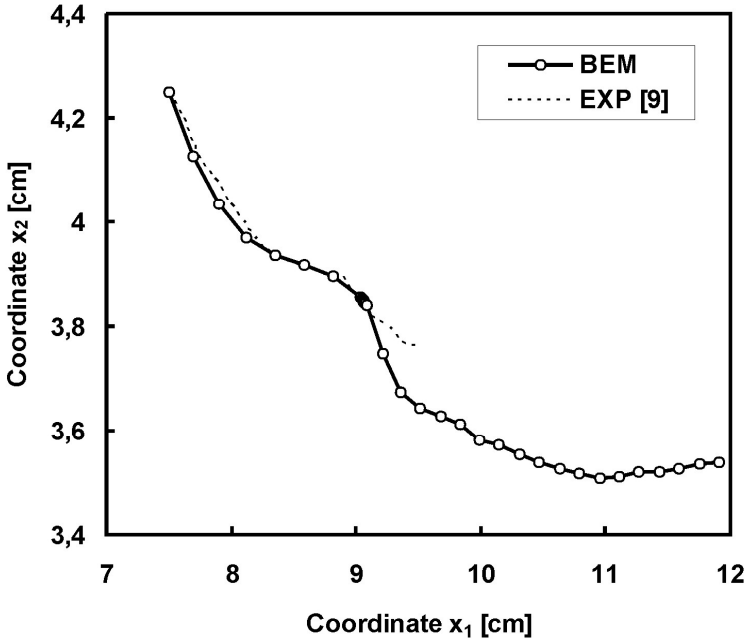

Fig.12. Crack paths for the special mixed-mode specimen

4.3. Three-point bend specimen. A three-point bend specimen for a mixed-mode fracture is shown in Fig. 13. Experimental results and numerical simulation by the FEM for this problem were presented in [3]. The dimensions of the plate are given in millimeters. The specimen is made of PMMA, which has the following material properties: Young's modulus E=2.94 GPa, Poisson's ratio ν=0.3 and mass density ρ=1190 kg/m^3. It is assumed that the plate is under plane stress conditions. The load is applied by a dropping hammer. The mass of the hammer is m=5.05 kg and its velocity v=5m/s. The specimen is loaded symmetrically e=0 and eccentrically e=0.1, where the relative loading eccentricity e equals the ratio of the distance of loading point from the line of symmetry to half the distance between the supports.

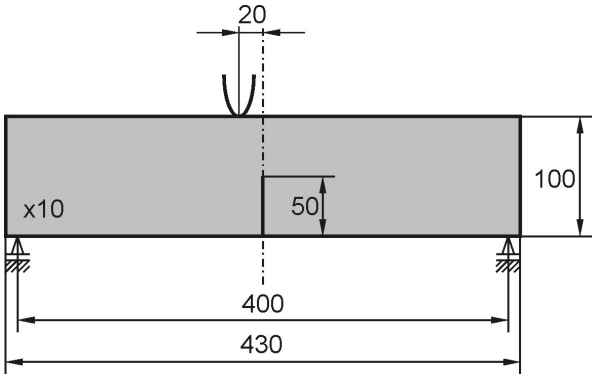

Fig. 13. Dimensions of the three-point bend specimen and boundary conditions for eccentric loading [3]

The variations of forces at the loading point measured experimentally [3] are shown in Fig. 14. The load has the maximum value F=6000 N at about 225 μs for e=0 and F=6400 N at about 210 μs for e=0.1. Dynamic fracture starts at t=156 μs for e=0 and at t=120 μs for e=0.1. The variations of velocity of crack growth determined experimentally [3] are shown in Fig. 15. The maximum crack velocity is c=250 m/s for e=0, and c=300 m/s for e=0.1. It is assumed that the specimen is always in contact with the supports.

The initial boundary of the plate is divided into 78 quadratic elements. The time step is Δt=5 μs.

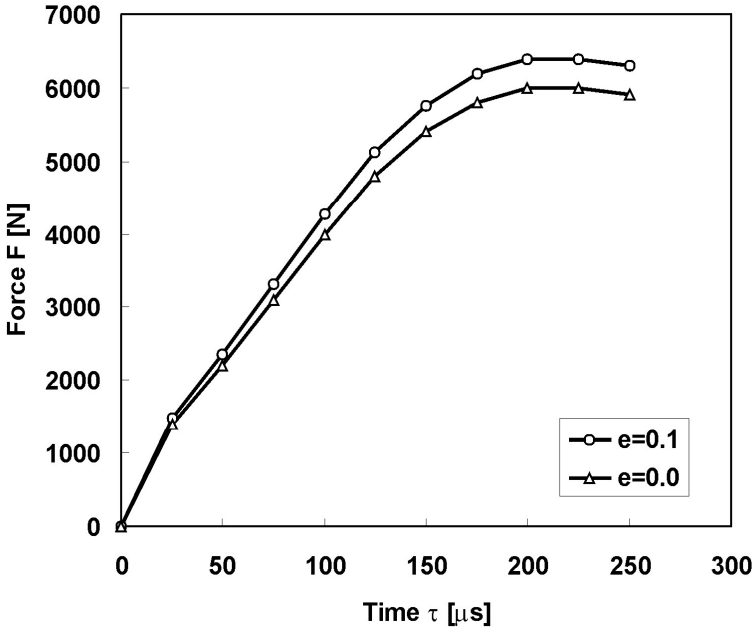

Fig. 14. Time variation of loading for the three-point bend specimen [3]

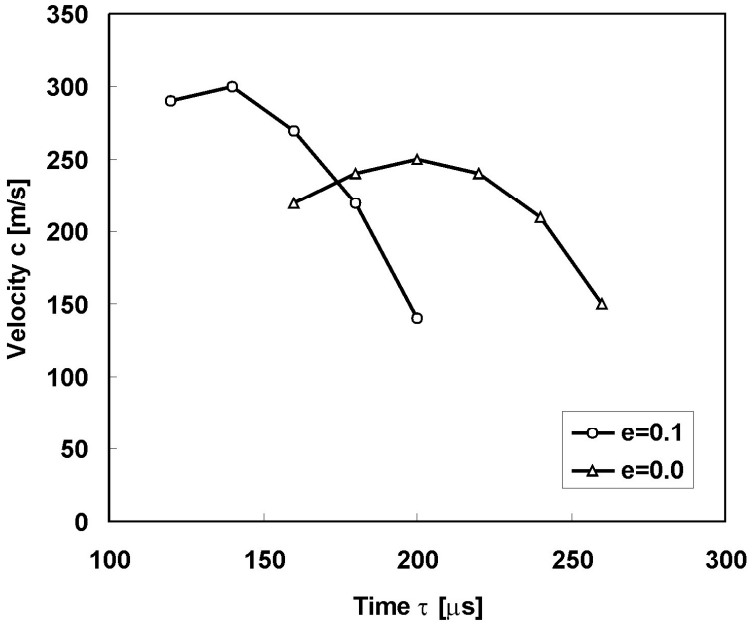

Fig. 15. Velocity of crack growth for the three-point bend specimen [3]

In Fig. 16 and 17 dynamic stress intensity factors for symmetric and eccentric loading are shown respectively. The BEM results are compared with the FEM solutions and experimental results obtained by the caustic method. The experimental results are not shown in Fig. 17 because they are almost the same as the FEM results. For eccentric loading all results agree well. For symmetric loading the DSIF obtained by the FEM, for times longer than 150 μs, are smaller than the BEM and experimental results. For the symmetric loading when the compressive longitudinal wave arrives at the crack tip, K_I becomes slightly negative. In this work a contact of crack surfaces is not taken into account and small overlapping is allowed. For symmetric case the crack path is straight and vertical.

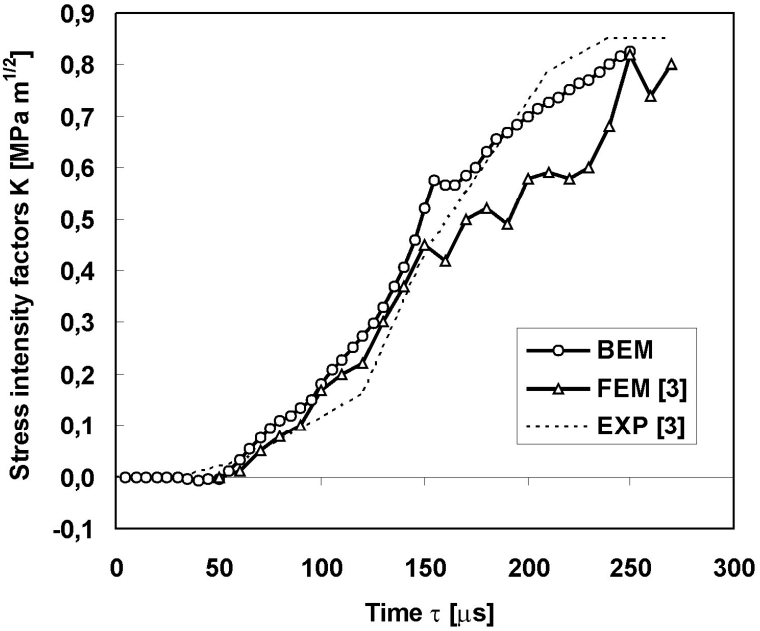

Fig. 16. Dynamic stress intensity factors for symmetric loading e=0 for the three-point bend specimen

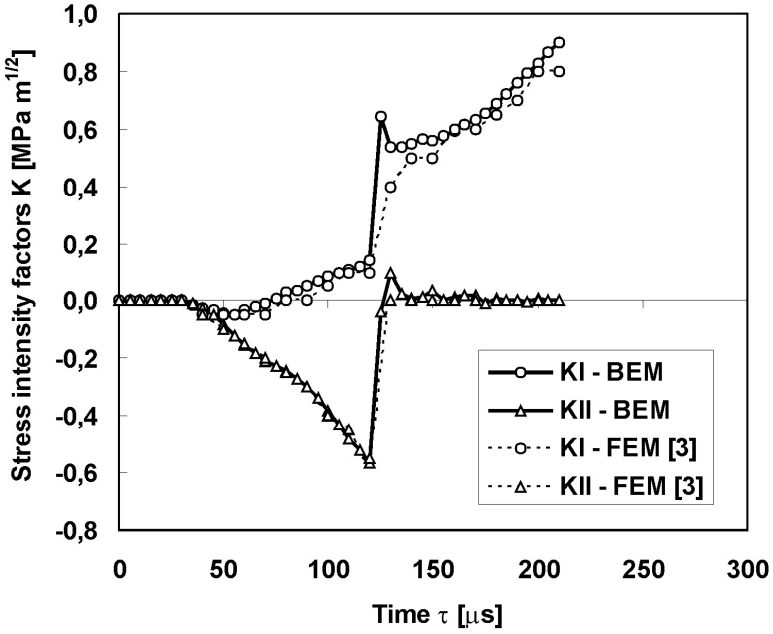

Fig. 17. Dynamic stress intensity factors eccentric loading e=0.1 for the three-point bend specimen

For the eccentric loading the K_I is positive and increases when the shear wave arrives at the crack tip. The absolute value of K_{II} increases up to the onset of crack propagation. During the dynamic crack growth the K_{II} are zero. The crack paths are shown in Fig. 18. The shape of the growing crack is compared with that computed by FEM and the experimental one. The crack paths obtained by computer simulations agree well. The real crack path is more curved. The crack grows towards the loading point.

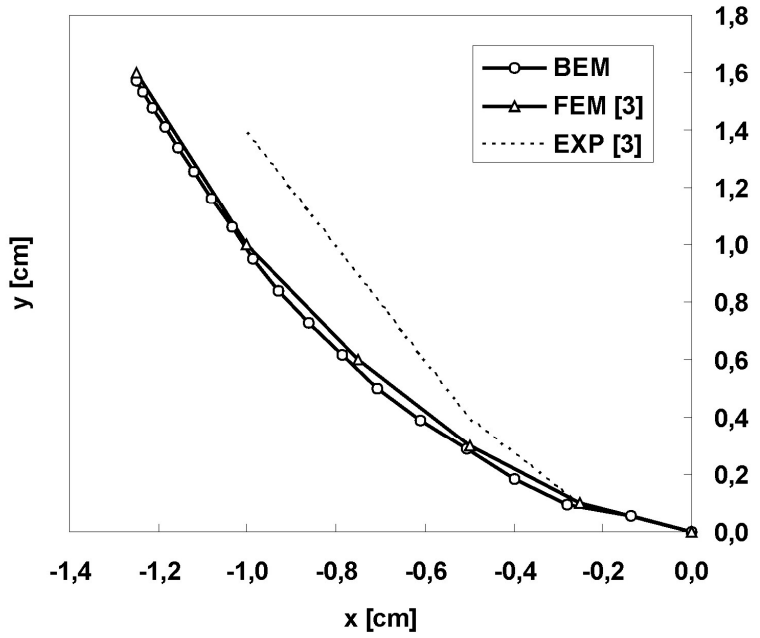

Fig. 18. Crack paths for eccentric loading e=0.1 for the three-point bend specimen

5. Conclusions

The time domain boundary element method is applied to model three dynamic fracture experiments: a short beam specimen with a stationary crack, a special mixed-mode specimen and a three-point bend specimen with fast growing cracks subjected to impact loads. The experimentally measured impact forces and crack tip velocities as a function of time are used as the data in computations. It is assumed in the numerical simulations that the cracks grow in the direction perpendicular to the maximum circumferencial stress. This type of computer simulation can be classified as the fracture-path prediction mode. The dynamic stress intensity factors and crack paths are computed and compared with the finite element method or experimental results presented in literature.

The numerical examples show good agreement of the BEM solutions with the FEM and experimental results. These results confirm accuracy of DSIF and the assumed crack growth direction criterion. The quality of the computer simulation strongly depends on the experimentally measured dynamic loading and crack growth velocity. Usually the BEM results agree better with the FEM solutions, than with the experimental results because the same quality input data are used in computer simulations. The comparison of numerically computed and experimentally measured crack shapes is more reliable than the comparison of DSIF, which are more difficult to measure.

References

[1] L.B. Freund: *Dynamic fracture mechanics*, Cambridge University Press, Cambridge (1990).

[2] T. Nishioka: Optics Lasers Eng., Vol. 32 (1999), pp. 205-255.

[3] T. Nishioka, H. Tokudome and M. Kinoshita: Int. J. Solids Struct., Vol. 38 (2001), pp. 5273-5301.

[4] H.D. Bui, H. Maigre and D.Rittel: Int. J. Solids Struct., Vol. 29 (1992), pp. 2881-2895.

[5] H. Maigre and D. Rittel: Int. J. Solids Struct., Vol. 30 (1993), pp. 3233-3244.

[6] H. Maigre and D. Rittel: Int. J. Fract., Vol. 73 (1995), pp. 67-79.

[7] D. Rittel and H. Maigre: Mech. Mater., Vol. 23 (1996), pp. 229-239.

[8] G. Weisbrod and D. Rittel: Int. J. Fract., Vol. 104 (2000), pp. 89-103.

[9] D. Gregorie, H. Maigre, J. Rethore and A. Combescure: Int. J. Solids Struct., Vol. 44 (2007), pp. 6517-6534.

[10] A. Combescure, A. Gravouil, D. Gregorie and J. Rethore: Comp. Meth. Appl. Mech. Eng. Vol. 197 (2008), pp. 309-318.

[11] J. Dominguez: *Boundary elements in dynamics*, Computational Mechanics Publications, Southampton (1993).

[12] P. Fedelinski, M.H. Aliabadi and D.P. Rooke: Int. J. Solids Struct., Vol. 32 (1995), pp. 3555-3571.

[13] P. Fedelinski, M.H. Aliabadi and D.P. Rooke: Int. J. Numer. Meth. Eng., Vol. 40 (1997), pp. 1555-1572.

[14] P. Fedelinski: Eng. Anal. Bound. Elem., Vol. 28 (2004), pp. 1135-1147.

[15] Th. Sellig and D. Gross: Int. J. Solids Struct., Vol. 34 (1997), pp. 2087-2103.

[16] Th. Seelig and D. Gross: Acta Mech., Vol. 132 (1999), pp. 47-61.

[17] Th. Seelig, D. Gross and K. Pothmann: Int. J. Fract., Vol. 99 (1999), pp. 325-338.

Key Engineering Materials Vol. 454 (2011) pp 127-135

doi:10.4028/www.scientific.net/KEM.454.127

On NGF applications to LBIE potential and displacement discontinuity analyses

L. S. Miers[1,a], J. C. F. Telles[1,b]

[1]Programa de Engenharia Civil – COPPE/Univ. Federal do Rio de Janeiro,

Caixa Postal 68506, Cep 21941-972, Rio de Janeiro / RJ – Brasil

[a]lsmiers@coc.ufrj.br, [b]telles@coc.ufrj.br

Keyword: Local boundary integral equation, numerical Green's function, meshless methods.

Abstract: This work aims at extending the concept of the Numerical Green's Function (NGF), known from boundary element applications to potential and fracture mechanics problems, to the Local Boundary Integral Equation (LBIE) context. As a "companion" solution, the NGF is used to remove the integrals of the main discontinuities over the crack boundary and is to be introduced only for source points whose support touches or contains the actual crack surfaces.

Introduction

Meshless methods are increasingly proving to be accurate for the analysis of the most common problems found in engineering applications. They can be quite efficient, in terms of computer time, in the solution of problems that need a great number of node repositioning during the analysis, sometimes more expensive than the analysis itself, in comparison to mesh-based methods.

Normally, a meshless method is a mesh-free counterpart of a well-established mesh-based method [1,2] and because of this, there is no reason to believe that the improvements made for the mesh-based procedures cannot be implemented in their mesh-free versions. In the context of standard boundary integral equations, the so-called local boundary integral (LBIE) method has emerged as a possible mesh-free boundary element (BEM) alternative and can profit from many previous alternative procedures developed for the original BEM procedure.

In this work, the concept of the numerical Green's function (NGF) for potential discontinuity problems and 2-D elastostatic fracture mechanics is implemented in the local boundary integral equation method. LBIE has been brought into existence from the boundary integral equation, basic to the standard BEM whereas the NGF version of this applications was first used in a BEM context [3] during the last decade.

The approximation scheme for the trial function used here is the well-known moving least squares (MLS) method, which is the most common alternative in the bibliography [4]. The singular integrals are computed using Kutt's quadrature [5] procedure, well-known from previous BEM implementations. The starting ideas applied here originate from References [6-10].

LBIE for potential problems

To demonstrate the formulation, only the linear Poison equation is used, even though the approach is suitable for solving nonlinear problems as well. Poison's equation can be written as

$$\nabla^2 u(\mathbf{x}) = p(\mathbf{x}), \quad \mathbf{x} \in \Omega \tag{1}$$

and the boundary conditions

$$u = \bar{u} \text{ on } \Gamma_u$$
$$\frac{\partial u}{\partial n} = q = \bar{q} \text{ on } \Gamma_q \tag{2}$$

Here, p is a domain distributed function, Ω the domain bounded by Γ and Γ_u and Γ_q the portions of the boundary with potential and flux prescribed respectively.

A weak formulation of the problem can be written as

$$\int_{\Omega} u^G \left(\nabla^2 u - p\right) d\Omega = 0 \tag{3}$$

where u^G is the Green's function used as the test function for the weighted residual statement and u is the trial function. The test function satisfies the following equation

$$\nabla^2 u^G(\xi, \mathbf{x}) + \delta(\xi, \mathbf{x}) = 0 \tag{4}$$

in which $\delta(\xi,\mathbf{x})$ is the Dirac delta function.

By integrating eq.(3) by parts twice, the global boundary integral equation is obtained as follows

$$u(\xi) = \int_{\Gamma} u^G(\xi, \mathbf{x}) \frac{\partial u(\mathbf{x})}{\partial n} d\Gamma - \int_{\Gamma} u(\mathbf{x}) \frac{\partial u^G(\xi, \mathbf{x})}{\partial n} d\Gamma - \int_{\Omega} u^G(\xi, \mathbf{x}) p(\mathbf{x}) d\Omega \tag{5}$$

where n is the outward normal vector to Γ, $\mathbf{x} = [x, y, z]^T$ is the set of co-ordinates and $\xi = [x_\xi, y_\xi, z_\xi]^T$ is defined as the source point.

To obtain the local formulation of eq.(5), a local sub-domain Ω_s and its boundary $\partial\Omega_s$ are considered instead of Ω and Γ respectively, leading to the following form

$$u(\xi) = \int_{\partial\Omega_s} u^G(\xi, \mathbf{x}) \frac{\partial u(\mathbf{x})}{\partial n} d\Gamma - \int_{\partial\Omega_s} u(\mathbf{x}) \frac{\partial u^G(\xi, \mathbf{x})}{\partial n} d\Gamma - \int_{\Omega_s} u^G(\xi, \mathbf{x}) p(\mathbf{x}) d\Omega \tag{6}$$

Eq.(6) indicates that the value of the unknown function at ξ can be obtained by carrying out the integrals over a sub-domain within the closed outer boundary Γ.

It should be noted that eq.(6) holds regardless of the shape and size of $\partial\Omega_s$, which can be deliberately chosen according to the characteristics of the functions used in the method. The most regular shape of a sub-domain is an n-dimensional sphere, centered at ξ, for a problem defined on an n-dimensional space.

For 2-D potential problems, Ω_s is a circle of radius r_0, and the Green's function and its normal derivative are

$$\begin{aligned} u^G &= -\frac{1}{2\pi} \ln(r) + u^C \\ \frac{\partial u^G}{\partial n} &= -\frac{1}{2\pi r} \frac{\partial r}{\partial n} + q^C \end{aligned} \tag{7}$$

where u_c an q_c are the complementary solutions for potential and flux respectively, which are added to the classic fundamental solution in order to obtain the Green's function corresponding to the desired problem. The use of the Green's function instead of the conventional fundamental solution precludes the use of the so-called "companion" solution [1,2], which is commonly added to the fundamental solution in order to make it vanish over the circular part of the sub-domain boundary $\partial\Omega_s$.

When ξ lies on the global boundary Γ, the sub-domain can still be taken as a part of a circle centered at ξ, but now its boundary includes the part of the circumference (L_s) and the part of Γ limiting Ω_s (Γ_s). The local integral equation for a nodal point ξ at Γ becomes

$$\alpha(\xi) u(\xi) = \int_{\Gamma_s + L_s} u^G(\xi, \mathbf{x}) \frac{\partial u(\mathbf{x})}{\partial n} d\Gamma - \int_{\Gamma_s + L_s} u(\mathbf{x}) \frac{\partial u^G(\xi, \mathbf{x})}{\partial n} d\Gamma - \int_{\Omega_s} u^G(\xi, \mathbf{x}) p(\mathbf{x}) d\Omega \tag{8}$$

where $\alpha(\xi)$ is a free coefficient depending on the shape of Γ at ξ.

LBIE for liner elasticity problems

Consider the following 2-D linear elasticity problem defined within the domain Ω and boundary Γ,

$$\sigma_{ij,j} + b_j = 0 \tag{9}$$

where σ_{ij} is the stress tensor, b_i is the body force and $(\,)_{,i}$ denotes the derivative with respect to x_i. The boundary conditions are

$$\begin{aligned} u_i &= \overline{u}_i \quad \text{on } \Gamma_u \\ p_i &\equiv \sigma_{ij} n_j = \overline{p}_i \quad \text{on } \Gamma_p \end{aligned} \tag{10}$$

where the bar indicates prescribed values, respectively, for displacements u and tractions p and Γ_u and Γ_p are the parts of the boundary Γ where they are prescribed.

Using u_i^G as test function, the weak form of Equation (17) can be written as

$$\int_\Omega \left(\sigma_{ij,j} + b_j\right) u_i^G d\Omega = 0 \tag{11}$$

and integrating Eq.(11) by parts twice, the following expression is obtained:

$$-\int_\Omega \sigma_{ij,j}^G u_i d\Omega + \int_\Gamma p_i^G u_i d\Gamma = \int_\Gamma p_i u_i^G d\Gamma + \int_\Omega b_i u_i^G d\Omega \tag{12}$$

In the present case, u_i^G is chosen to be the solution of a unit load in an infinite plane containing cracks, to be discussed later on. This solution satisfies the following condition

$$\sigma_{ij,j}^G(\xi, \mathbf{x}) + \delta(\xi, \mathbf{x}) e_i = 0 \tag{13}$$

where $\delta(\xi, \mathbf{x})$ is the Dirac delta function and e_i is the unit load vector on the x_i direction. The test functions can be rewritten as

$$\begin{aligned} u_i^G &= u_{ki}^G e_k \\ p_i^G &= p_{ki}^G e_k \end{aligned} \tag{14}$$

where u_{ki}^G and p_{ki}^G are, respectively, the i-th components of displacements and tractions due to a unit load in the x_k direction.

Substituting Eqs.(14) and (13) in Eq.(11) leads to the so-called Somigliana's identity, which gives the values of displacements in any point of the domain in terms of the boundary values of displacements and tractions:

$$u_i(\xi) = \int_\Gamma u_{ij}^G(\xi, \mathbf{x}) p_j(\mathbf{x}) d\Gamma - \int_\Gamma p_{ij}^G(\xi, \mathbf{x}) u_j(\mathbf{x}) d\Gamma + \int_\Omega u_{ij}^G(\xi, \mathbf{x}) b_j(\mathbf{x}) d\Omega \tag{15}$$

where ξ is the source point and $\mathbf{x}$ is the field (generic) point.

If instead of the real domain Ω and boundary Γ of the problem, a sub-domain Ω_s and its boundary $\partial\Omega_s$ located entirely inside Ω are considered, Eq.(15) becomes

$$u_i(\xi) = \int_{\partial\Omega_s} u_{ij}^G(\xi, \mathbf{x}) p_j(\mathbf{x}) d\Gamma - \int_{\partial\Omega_s} p_{ij}^G(\xi, \mathbf{x}) u_j(\mathbf{x}) d\Gamma + \int_{\Omega_s} u_{ij}^G(\xi, \mathbf{x}) b_j(\mathbf{x}) d\Omega \tag{16}$$

For a source point located on the global boundary Γ, Eq.(16) can be rewritten as

$$\alpha_{ij}(\xi) u_i(\xi) = \int_{L_s + \Gamma_s} u_{ij}^G(\xi, \mathbf{x}) p_j(\mathbf{x}) d\Gamma - \int_{L_s + \Gamma_s} p_{ij}^G(\xi, \mathbf{x}) u_j(\mathbf{x}) d\Gamma + \int_{\Omega_s} u_{ij}^G(\xi, \mathbf{x}) b_j(\mathbf{x}) d\Omega \tag{17}$$

and considering two dimensions only, its matrix form is as follows,

$$\boldsymbol{\alpha}\mathbf{u} = \int_{L_s + \Gamma_s} \mathbf{u}^{\mathbf{G}} \mathbf{p} d\Gamma - \int_{L_s + \Gamma_s} \mathbf{p}^{\mathbf{G}} \mathbf{u} d\Gamma + \int_{\Omega_s} \mathbf{u}^{\mathbf{G}} \mathbf{b} d\Omega \tag{18}$$

where

$$\mathbf{u}^G = \begin{bmatrix} u_{11}^G & u_{12}^G \\ u_{21}^G & u_{22}^G \end{bmatrix}; \quad \mathbf{p}^G = \begin{bmatrix} p_{11}^G & p_{12}^G \\ p_{21}^G & p_{22}^G \end{bmatrix}; \quad \mathbf{u} = \begin{bmatrix} u_1 \\ u_2 \end{bmatrix}; \quad \mathbf{p} = \begin{bmatrix} p_1 \\ p_2 \end{bmatrix}; \quad \mathbf{b} = \begin{bmatrix} b_1 \\ b_2 \end{bmatrix}. \tag{19}$$

and α_{ij} ($\boldsymbol{\alpha}$) is a constant matrix that depends on the shape of the boundary at ξ.

$$\boldsymbol{\alpha}(\xi) = \begin{bmatrix} \frac{\theta}{2\pi} - \frac{\sin 2\theta_1 - \sin 2\theta_2}{8\pi(1-\bar{\nu})} & \frac{\cos 2\theta_1 - \cos 2\theta_2}{8\pi(1-\bar{\nu})} \\ \frac{\cos 2\theta_1 - \cos 2\theta_2}{8\pi(1-\bar{\nu})} & \frac{\theta}{2\pi} + \frac{\sin 2\theta_1 - \sin 2\theta_2}{8\pi(1-\bar{\nu})} \end{bmatrix} \tag{20}$$

where θ, θ_1 and θ_2 are defined in Fig.1 and

$$\bar{\nu} = \begin{cases} \nu & \text{for plane strain} \\ \dfrac{\nu}{1+\nu} & \text{for plane stress} \end{cases}$$

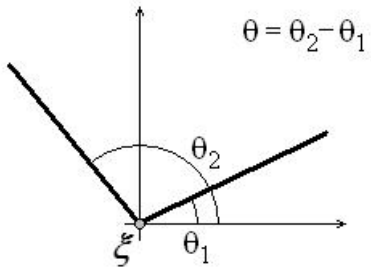

Figure 1 – definition of internal angle θ, θ_1 and θ_2.

Moving least squares (MLS) approximation scheme

The MLS scheme is by far the most used in meshless methods to approximate the trial function $u^h(\mathbf{x})$. Its definition will be briefly presented in this section; for further details, see [4,1,2,6]. It has the following form

$$u^h(\mathbf{x}) = \sum_{i=1}^{n} \phi_i(\mathbf{x})\hat{u}_i = \boldsymbol{\Phi}^T \cdot \hat{\mathbf{u}} \quad \forall \mathbf{x} \in \Omega_x; \tag{21}$$

where $\boldsymbol{\Phi}$ is the MLS shape function, $\hat{\mathbf{u}}$ is the "fictitious" nodal values of the trial function and n is the number of nodes inside the domain of definition Ω_x of the considered node. The domain of definition of a certain node $\mathbf{x}$ is composed by the nodes who have $\mathbf{x}$ inside their support.

Complementary solution for potential problems

The complementary solution – $(\,)^C$ – is a function added to the fundamental solution – $(\,)^*$ – to generate the Green's function – $(\,)^G$ – suited to certain types of problems.

$$\begin{aligned} u^G(\xi,\mathbf{x}) &= u^*(\xi,\mathbf{x}) + u^C(\xi,\mathbf{x}) \\ \frac{\partial u^G(\xi,\mathbf{x})}{\partial n} &= q^G(\xi,\mathbf{x}) = q^*(\xi,\mathbf{x}) + q^C(\xi,\mathbf{x}) \end{aligned} \tag{22}$$

Here, two GFs for potential problems are proposed: an exact solution for a unit source in a semi-infinite plane and a numerical solution for an infinite plane containing unloaded lines of potential discontinuity.

Semi-infinite plane

In this work, the flux-free surface $\overline{\Gamma}$ of the half-plane is assumed to be represented by a horizontal line. The complementary part for this problem is a function of the coordinates of the image of the load point with respect to $\overline{\Gamma}$ as shown in Fig.2

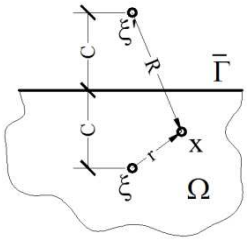

Figure 2 – half-plane Green's Function

The complementary functions are shown as follows

$$u^C = -\frac{1}{2\pi}\ln(R)$$
$$\frac{\partial u^C}{\partial n} = q^C = -\frac{1}{2\pi r}\frac{\partial R}{\partial n} \tag{23}$$

For more details, see Brebbia, Telles and Wrobel [5].

Infinite plane with internal lines of potential discontinuity

Consider an infinite plane, with a line of potential discontinuity within, under the action of a unit point source applied at ξ. In what follows, the Green's function for this problem is written in terms of a superposition of the fundamental solution for Laplace's equation plus a complementary part which provides satisfaction of the flux-free requirement over the internal line of potential discontinuity (see Fig.3).

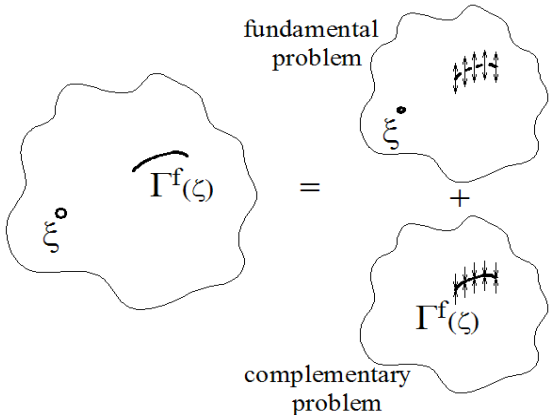

Figure 3 – Numerical Green's Function (NGF)

The Laplace's solution u^* and q^* produces nonzero flux values across the barrier line $\Gamma^f(\zeta)$, these are then counterbalanced by the complementary fluxes. Hence, an infinite plane with an impervious slit is simulated.

The complementary part of the GF can be written in terms of boundary integral equations as

$$u^C(\xi,\mathbf{x}) = \int_{\Gamma^-} q^*(\mathbf{x},\zeta)\cdot c(\xi,\zeta)d\Gamma(\zeta)$$
$$q^C(\xi,\mathbf{x}) = \int_{\Gamma^-} Q^*(\mathbf{x},\zeta)\cdot c(\xi,\zeta)d\Gamma(\zeta) \tag{24}$$

where $q^*(x,\zeta)$ and $Q^*(x,\zeta)$ are the free (Laplace's) fundamental flux and its derivative referred to the source point as used in the classical and hypersingular boundary integral equations. These equations produce the complementary potential and flux at an internal point **x** due to a unit point

source at ξ, as a function of the potential discontinuity $c(\xi,\zeta) = u(\xi,\zeta^+) - u(\xi,\zeta^-)$. Note that here the source point of the complementary problem is $\mathbf{x}$; point ξ is introduced only to guarantee that the complementary solution is computed with the same notation as eq.(22). The boundary Γ^- corresponds to the inferior surface of the line of potential discontinuity, whose superior surface is Γ^+. The numerical value of $c(\xi,\zeta)$ is computed using an efficient implementation of the hypersingular boundary integral equation.

Complete details of the procedure can be found in [7].

Numerical Green's function for fracture mechanics

Consider an infinite elastic plane with an unloaded crack inside under the action of a unit point load applied at ξ. The fundamental displacements and tractions for this case can be calculated by the superposition shown in Fig.4, which mathematically reads

$$\begin{aligned} u_{ij}^G(\xi,\mathbf{x}) &= u_{ij}^*(\xi,\mathbf{x}) + u_{ij}^c(\xi,\mathbf{x}) \\ p_{ij}^G(\xi,\mathbf{x}) &= p_{ij}^*(\xi,\mathbf{x}) + p_{ij}^c(\xi,\mathbf{x}) \end{aligned} \tag{25}$$

where $(\,)^*$ refers to Kelvin's fundamental solution (Fig.3B) and $(\,)^c$ indicates the complementary part (Fig.3C).

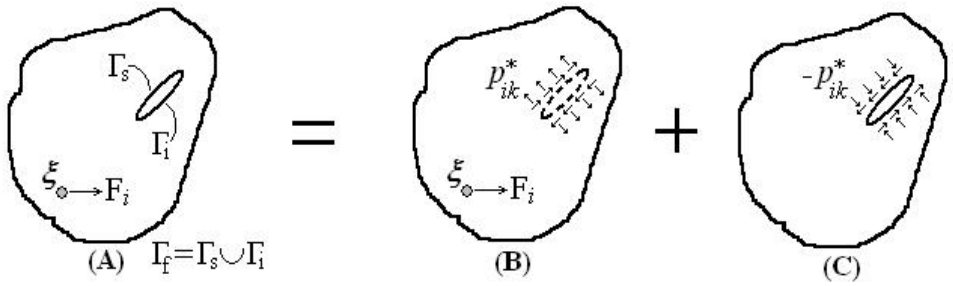

Figure 4 – superposition of effects

According to [3], the complementary part of the solution can be calculated as follows

$$\begin{aligned} u_{ij}^c(\xi,\mathbf{x}) &= \int_{\Gamma_i} p_{jk}^*(\mathbf{x},\zeta)\cdot c_{ik}(\xi,\zeta)\,d\Gamma(\zeta) \\ p_{ij}^c(\xi,\mathbf{x}) &= \int_{\Gamma_i} P_{jk}^*(\mathbf{x},\zeta)\cdot c_{ik}(\xi,\zeta)\,d\Gamma(\zeta) \end{aligned} \tag{26}$$

where ζ is a point on Γ_i and $c_{ik}(\xi,\zeta)$ are the crack openings (see Fig.5)

$$c_{ik}(\xi,\zeta) = u_{ik}^c(\xi,\zeta^s) - u_{ik}^c(\xi,\zeta^i) \tag{27}$$

which can be calculated by solving the following system of equations

$$\mathbf{S}\mathbf{c}_{ij}(\xi,\zeta) = \mathbf{p}_{ij}^*(\xi,\zeta) \tag{28}$$

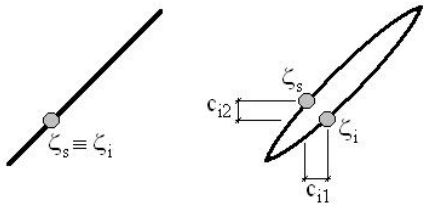

Figure 5 – crack openings

Matrix **S** is square of dimension $2N$ (N is the number of points on ζ_i) that depends only of the crack geometry. This complete formulation can be seen in [3].

It is worth noticing that the complementary part vanishes if the actual crack, or part of it, does not pertain to the integration boundary, here no longer the global boundary Γ, but the boundary of the sub-domain of integration $\partial\,\Omega_s$. Hence, only the nodes whose sub-domains contain part of the crack have non-zero complementary parts whereas for all other nodes the NGF becomes Kelvin's solution only.

The numerical implementation of these equations can be seen in detail in Reference [3].

Examples

To illustrate the presented techniques, two examples are proposed, one for each theory presented. The results are compared with sufficiently refined ones obtained with a BEM potential and elasticity codes using quadratic elements.

Potential problems: cofferdam-type problem

In this example there are two sheet piles enclosing a permeable soil to be excavated. The problem geometry, node cloud and boundary conditions are presented in Fig.6. Because of the symmetry, only half of the geometry was analyzed.

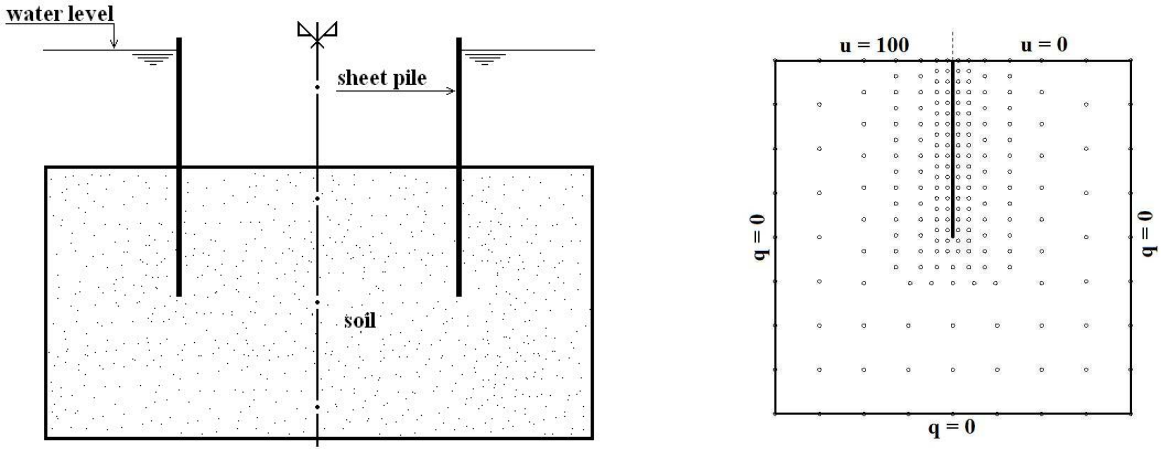

Figure 6 – cofferdam-type problem geometry, node cloud and boundary conditions

The results obtained with the NGF-LBIE and NGF-BEM were almost the same and could not be distinguishable (see Fig.7).

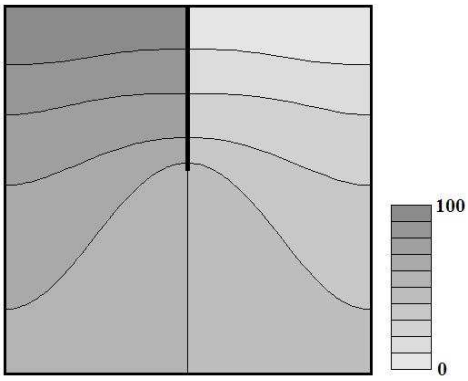

Figure 7 – cofferdam-type problem results

Fracture mechanics: stress intensity factor

In this example, the stress intensity factor K_I is the result compared. The relation (r_i/c_i) for the MLS weight function is equal to 4.0. This value can guarantee a good "decay" of *w*.

It can be seen in Fig. 8 that the node cloud is denser in the neighborhood of the crack, but without any node positioned on it. The distribution of nodes influenced by the presence of the crack can be uniform or not, but the crack edges require denser clouds due to the natural difficulty to represent the behavior of stresses in that region. Good results were obtained when at least 10% of the total number of nodes was influenced by the crack.

The results are compared with the ones presented in [3]. For this example it is considered: $E = 50000$, $\nu = 0.2$ and number of nodes $N = 210$.

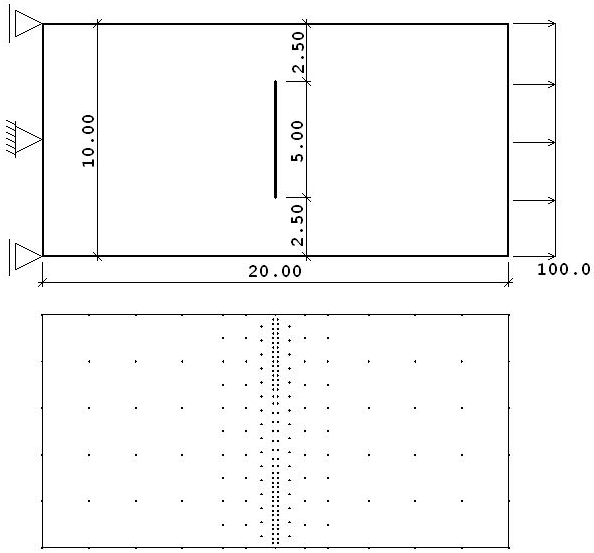

Figure 8 – geometry and node cloud of fracture mechanics example

The stress intensity factor K_I is obtained here using the following relation [8]

$$K_I = \frac{G\sqrt{2\pi}}{4(1+\nu)} \sum_{i=1}^{np} \frac{c_{11}(\zeta_i,\zeta)\sqrt{r_i}}{r_i} \tag{29}$$

where G is the shear modulus, $c_{11}(\zeta_i,\zeta)$ is the value of the crack opening at node ζ_i, r_i is the distance between ζ_i and the nearest crack edge and $np=6$ is the number of nodes considered. The chosen positions of the nodes ζ_i are presented in Fig.9, in intrinsic coordinates.

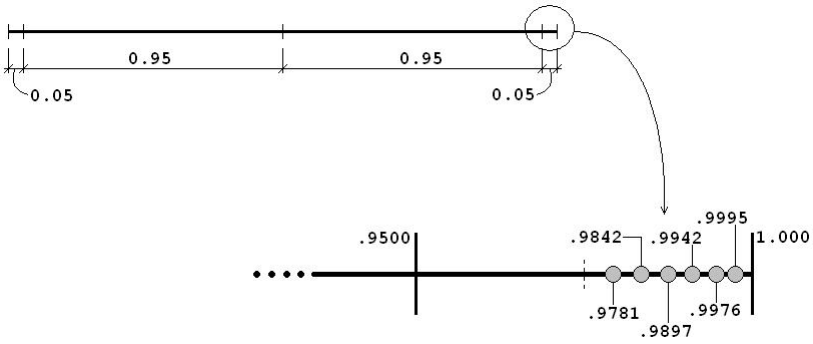

Figure 9 – position of ζ_i for K_I calculation

The comparison of the results obtained with this technique and those found with NGF-BEM (numerical Green's function with BEM) and AGF-BEM (analytical Green's function with BEM) are presented in Table 1

Table 1 – comparison of results

Method	K_I/K_0	Error (%)
NGF-LBIE	1.182	0.51
NGF-BEM	1.1877	0.99
AGF-BEM	1.1871	0.94
estimated	1.176 ± 1%	-

In order to present the results in non-dimensional form, they are divided by $K_0 = \sigma\sqrt{\pi a}$, where σ is the applied load and a is the half-length of the crack.

Conclusion

The present work aimed at introducing the concept of the NGF to potential problems and fracture mechanics applications in the context of the LBIE method. Here the LBIE formulation was presented for potential and elastostatic problems, as well as the procedure for obtaining the NGF for potential discontinuity and fracture mechanics. The MLS approximation scheme was used to interpolate the trail function.

As demonstrated by the results, the LBIE is shown to be suitable for a Green's function type of implementation and the development of the NGF for infinite planes with unloaded lines of discontinuity has proven to be worth of attention, especially for elastic fracture mechanics applications.

References

[1] S.N.Atluri and S.Shen: Comput. Mod. Eng. Sci. Vol. 3 (2002), pp. 11-51.
[2] S.N.Atluri, J.Sladek, V.Sladek and T.Zhu: Comput. Mech. Vol. 25 (2000), pp. 180-198.
[3] J.C.F.Telles, G.S.Castor and S.Guimarães: Int. J. Num. Methods Eng. Vol. 38 (1995), pp. 3259-3274.
[4] P.Lancaster and K.Salkauskas: Math. Comput. Vol. 37 (1981), pp. 141-158.
[5] C.A.Brebbia, J.C.F.Telles and L.C.Wrobel: Boundary Element Techniques: Theory and Application in Engineering (Springer, Berlin 1984).
[6] Y.P.Chen, A.Eskandarian and M.Oskard: Theor. App. Frac. Mech. Vol. 41 (2004), pp. 83-94.
[7] J.C.F.Telles, C.A.R. Vera-Tudela, S.Guimarães: El. Journal Bound. Elem. Vol. BeTeq2001 (2002), pp. 136-150.
[8] L.P.S.Barra and J.C.F.Telles: Eng. Anal. Bound. Elem. Vol 23 (1999), pp. 77-87.
[9] L. S. Miers and J. C. F. Telles: CMES Vol. 14 (3), (2006), pp. 661-669
[10] C. A. R.Vera-Tudela, T. C. F. Luiz and J. C. F.Telles: Comput. Mech. Vol. 39, (2006), pp. 15- 23

Key Engineering Materials Vol. 454 (2011) pp 137-148

doi:10.4028/www.scientific.net/KEM.454.137

Nonlinear Viscoelastic Fracture Mechanics using Boundary Elements

Stavros Syngellakis[1,a] and Jiangwei Wu[2,b]

[1]School of Engineering Sciences, University of Southampton, Southampton SO17 1BJ, UK,

[2]Department of Mechanical Engineering, Shanghai Maritime University, 1550 Pu Dong Avenue, Shanghai 200135, P. R. China,

[a]ss@soton.ac.uk, [b]jiangwei_wu@hotmail.com

Keywords: Polymers, viscoelasticity, non-linearity, fracture, strain-softening, boundary elements.

Abstract. The boundary element methodology is applied to the fracture mechanics of non-linear viscoelastic solids. The adopted non-linear model is based on the 'free volume' concept, which is introduced into the relaxation moduli entering the linear viscoelastic relations through a time shift depending on the volumetric strain. Nonlinearity generates an irreducible domain integral into the original boundary integral equation governing the behaviour of linear viscoelastic solids. This necessitates the evaluation of domain strains, which relies on a non-standard differentiation of an integral with a strong kernel singularity. A time domain formulation based on constant shape functions over boundary elements and domain cells is computer-implemented through a numerical integration algorithm. The effectiveness of the developed numerical tool is demonstrated through the analysis of a plate with a central crack. The predicted stress field around the crack tip is compared with respective results obtained by the finite element method.

Introduction

The importance of polymers and other viscoelastic materials to modern engineering practice has prompted extensive research on their failure mechanisms. The issue of viscoelastic fracture, in particular, was addressed in many early experimental and theoretical studies [1]. Crack propagation was linked to material properties through an experimentally validated model [2]. A sound theoretical basis for assessing crack initiation and growth was achieved by combining classical fracture mechanics concepts with viscoelastic material modelling [3-5]. An energy criterion for crack growth was proposed and tested against experimental evidence [6-7]. More recent studies explored the relevance of *J*-integral as a criterion for crack growth [8-9].

It was noted quite early that viscoelastic behaviour becomes highly nonlinear in the presence of cracks [5]. Such non-linearity manifests itself as considerable strain softening near the crack tip. Schapery [10] proposed a quite general and frequently applied nonlinear constitutive model, which includes the principle of time-stress superposition. The latter is accounted for through the definition of 'reduced time', a concept originally introduced to account for temperature variation [11]. Based on experimental studies, Knauss and Emri [12-13] linked the time-stress superposition model to the concept of free volume. This model has been applied to various problems [14-15] and found to be a very effective analysis tool for assessing the effect of nonlinearity on the behaviour of polymer materials. Dooling et al proposed a constitutive model based on the hypothesis of a non-Newtonian flow process [16]. A wider view of trends and developments in non-linear viscoelastic modelling has been provided by Schapery [17]. Schapery also proposed a theoretical model accounting for nonlinearity in the evaluation of *J*-like path independent integrals [18]. Knauss and Losi [19] used the 'free volume' concept to study crack propagation through nonlinear viscoelastic material in the context of adhesive bond failure.

The development of numerical techniques for the implementation of linear and nonlinear constitutive models in the solution of fracture problems has been an important research objective. Applications of the finite element method (FEM) to linear viscoelastic fracture mechanics (LVFM) have been mainly concerned with the simulation of crack growth in the polymer matrix of

composites [20]. Moran and Knauss [14] used FEM modelling to introduce the 'free volume' concept into a fracture mechanics context. Non-linear FEM algorithms and codes, based on the Schapery model [10], have also been developed and tested for efficiency and stability [21].

The boundary element method (BEM) has been extensively and very effectively used in modelling linear viscoelastic behaviour [22]. It seems, however, that there has been only one previous attempt to extend such formulations to nonlinear problems [23]. On the other hand, BEM has been shown to be a reliable tool for performing LVFM analyses. An early such three-dimensional formulation [24], based on the Laplace transform approach, predicted the crack opening displacement of a penny-shaped crack in a viscoelastic material characterised by a three-parameter Kelvin model. Two-dimensional stress and displacement fields were later analysed in the neighbourhood of a crack filled with failed, so-called craze material [25]. Laplace transform-based BEM was also used for the evaluation of dynamic stress intensity factors in cracked viscoelastic plates under suddenly applied loads [26]. More recently, a direct, time domain BEM formulation was applied to the evaluation of an expression for the strain energy release rate derived from a functional corresponding to the potential energy in elasticity [27-28]. Further results have confirmed the effectiveness of both Laplace transform and time domain BEM in predicting time-dependent stress intensity factors and energy release rates under constant and time dependent loads [29]. In parallel with viscoelastic material modelling for polymers, BEM analyses, based on viscoplasticity, have also been developed for predicting metal creep and rupture [30-32].

The non-linear visco-elastic model employed in the present BEM analysis of fractured polymers is based on the reduced time concept, which is, in turn, considered as a function of mechanical free-volume changes. The relaxation moduli of linear visco-elasticity are thus employed in the Boltzmann constitutive equations with a time shift depending on the volumetric strain. The difference between the actual and a pseudo stress tensor, the latter linearly related to the actual strains, generates an irreducible domain integral into the original integral equation derived for linear viscoelastic solids. Domain strains are obtained by differentiation of a domain integral with a strong kernel singularity resulting in a singular integral and a regular free term. A time domain formulation is implemented through a numerical integration algorithm. The effectiveness of the developed numerical tool is demonstrated through the analysis of a plate with a central crack subjected to remote tension. The results are compared with respective predictions by the finite element method.

Background Theory

The linear viscoelastic model adopted in earlier BEM formulations [33] is, in accordance with Boltzmann's principle, of hereditary integral type

$$\sigma_{ij} = G_{ijkl}(t)\varepsilon_{kl}(0) + \int_0^t G_{ijkl}(t-\tau)\frac{\partial \varepsilon_{kl}(\tau)}{\partial \tau}\,\mathrm{d}\tau \tag{1}$$

where σ_{ij}, ε_{ij} are the stress and small strain tensors, respectively, and $G_{ijkl}(t)$ the relaxation moduli in the general case of an anisotropic medium. The problem is described relative to a Cartesian frame of reference x_i, i =1,2,3, adopting the summation convention for repeated indices. Introducing the notation for the Stieltjes convolution of two functions [34], Eq. 1 can be more concisely written as

$$\sigma_{ij} = G_{ijkl} * \mathrm{d}\varepsilon_{kl} \tag{2}$$

For an isotropic material characterised by shear and relaxation moduli $\mu(t)$ and $K(t)$, respectively, Eq. 2 becomes

$$\sigma_{ij} = 2\mu * \mathrm{d}\varepsilon_{ij} + \frac{1}{3}(3K - 2\mu) * \mathrm{d}\varepsilon_{kk}\,\delta_{ij} \tag{3}$$

The nonlinear constitutive equations adopted here are [14]

$$\sigma_{ij} = \int_{-\infty}^{t} G_{ijkl}[\zeta(t)-\zeta(\tau)]\frac{\partial \varepsilon_{kl}(\tau)}{\partial \tau}\mathrm{d}\tau = G_{ijkl}[\zeta(t)]\varepsilon_{kl}(0) + \int_{0}^{t} G_{ijkl}[\zeta(t)-\zeta(\tau)]\frac{\partial \varepsilon_{kl}(\tau)}{\partial \tau}\mathrm{d}\tau \tag{4}$$

where $\zeta(t)$ is the reduced or intrinsic time, which may account for the effect of temperature [11], moisture and pressure variations on the relaxation moduli. A general definition of $\zeta(t)$ is

$$\zeta(t) = \int_{0}^{t} \frac{\mathrm{d}\tau}{\phi[v(\tau)]} \tag{5}$$

where ϕ is a shift factor, which depends on the fractional free volume v, that is, the ratio of free volume to the total polymer volume. The free volume itself is a measure of molecular packing irregularities. Here, only the influence of mechanically induced aging is considered, thus v is expressed only in terms of volumetric strain as

$$v = v_0 + C\varepsilon_{kk} \tag{6}$$

where v_0 is the fractional free volume at some reference state and C is a material parameter which, in many cases, may be taken equal to unity. A possible expression for ϕ is [12]

$$\phi = \exp\left[b\left(\frac{1}{v} - \frac{1}{v_0}\right)\right] \tag{7}$$

where b is another experimentally determined material parameter.

Formulation

The derivation of an integral equation for non-linear viscoelastic problems begins with the reciprocal theorem of linear viscoelasticity [34]. Given two linear viscoelastic states (ε_{ij}, σ_{ij}) and ($\tilde{\varepsilon}_{ij}, \tilde{\sigma}_{ij}$), satisfying the constitutive Eq. 2 in the viscoelastic domain Ω, then

$$\int_{\Omega} \tilde{\varepsilon}_{ij} * \mathrm{d}\sigma_{ij}\mathrm{d}\Omega = \int_{\Omega} \varepsilon_{ij} * \mathrm{d}\tilde{\sigma}_{ij}\mathrm{d}\Omega \tag{8}$$

In a non-linearly deformed viscoelastic material, it is possible to define the notional pseudo stress field σ_{ij}^{L} related to the actual strain components by

$$\sigma_{ij}^{L} = G_{ijkl} * \mathrm{d}\varepsilon_{kl} \tag{9}$$

Then, the actual stress developing in the non-linear material can be written as

$$\sigma_{ij} = \sigma_{ij}^{L} + \sigma_{ij}^{NL} \tag{10}$$

where σ_{ij}^{NL} represents the effect of material non-linearity on stress, that is, the stress difference resulting from using constitutive Eq. 4 rather than Eq. 2. The reciprocity relation, Eq. 8, is only valid for σ_{ij}^{L}; hence, for the non-linear problem, it should take the form

$$\int_{\Omega} \tilde{\varepsilon}_{ij} * \mathrm{d}(\sigma_{ij} - \sigma_{ij}^{NL})\mathrm{d}\Omega = \int_{\Omega} \varepsilon_{ij} * \mathrm{d}\tilde{\sigma}_{ij}\mathrm{d}\Omega \tag{11}$$

Substitution of the small strain-displacement relations into Eq. 11, integration by parts and the application of divergence theorem, gives

$$\int_{\Gamma} \tilde{u}_i * \mathrm{d}p_i \mathrm{d}\Gamma + \int_{\Omega} \tilde{u}_i * \mathrm{d}f_i \mathrm{d}\Omega = \int_{\Gamma} u_i * \mathrm{d}\tilde{p}_i \mathrm{d}\Gamma + \int_{\Omega} u_i * \mathrm{d}\tilde{f}_i \mathrm{d}\Omega + \int_{\Omega} \tilde{\varepsilon}_{ij} * \mathrm{d}\sigma_{ij}^{NL} \mathrm{d}\Omega \tag{12}$$

where Γ is the boundary of Ω while u_i, p_i and f_i are, respectively, the components of the displacement, traction and body force corresponding to the actual, nonlinear problem while $\tilde{u}_i, \tilde{p}_i$ and $\tilde{f}_i$ are the respective quantities associated with the second hypothetical linear stress-strain field ($\tilde{\varepsilon}_{ij}, \tilde{\sigma}_{ij}$). The latter is assumed to arise from the body forces

$$\tilde{f}_{ki} = \delta_{ki} \delta(\mathbf{x}-\boldsymbol{\xi}) H(t) \tag{13}$$

acting on an infinite isotropic linearly viscoelastic domain, where δ_{ki} is the Kronecker delta, $\delta(\mathbf{x}-\boldsymbol{\xi})$ the delta function and $H(t)$ the Heaviside step function. Then, Eq. 12 is transformed to

$$\kappa_{ij} u_j(t) = \int_{\Gamma} (\tilde{u}_{ij} * \mathrm{d}p_j - \tilde{p}_{ij} * \mathrm{d}u_j) \mathrm{d}\Gamma + \int_{\Omega} \tilde{u}_{ij} * \mathrm{d}f_j \mathrm{d}\Omega - \int_{\Omega} \tilde{\varepsilon}_{ijk} * \mathrm{d}\sigma_{jk}^{NL} \mathrm{d}\Omega \tag{14}$$

where $\tilde{u}_{ki}(\mathbf{x}-\boldsymbol{\xi}, t)$ is the time-dependent fundamental solution while $\tilde{\varepsilon}_{ijk}$ and $\tilde{p}_{ij}$ are the corresponding strain and edge traction components. In Eq. 14, $\kappa_{ij} = \delta_{ij}$ for interior source points and $\kappa_{ij} = (1/2)\delta_{ij}$ for points on a smooth boundary. Expressions for κ_{ij} when the source point is a corner boundary point can be found in the boundary element literature [35].

The Laplace transform of $\tilde{u}_{ki}$ can be derived from the fundamental solution of the respective elastic problem via the correspondence principle. Inversion from the transform to the real time domain leads to the general form [33]

$$\tilde{u}_{ij}(\mathbf{x}-\boldsymbol{\xi}, t) = A(t) g_{ij}(\mathbf{x}-\boldsymbol{\xi}) + B(t) h_{ij}(\mathbf{x}-\boldsymbol{\xi}) \tag{15}$$

where the time functions $A(t)$ and $B(t)$ also depend implicitly on the relaxation moduli of the material while the spatial functions $g_{ij}(\mathbf{x}-\boldsymbol{\xi})$ and $h_{ij}(\mathbf{x}-\boldsymbol{\xi})$ also depend on the dimensionality of the problem. In two-dimensions,

$$g_{ij}(\mathbf{x}-\boldsymbol{\xi}) = -\frac{\delta_{ij}}{8\pi} \ln r$$

$$h_{ij}(\mathbf{x}-\boldsymbol{\xi}) = \frac{1}{8\pi} r_{,i} r_{,j}$$

where $r = |\mathbf{x}-\boldsymbol{\xi}|$.

Eq. 14 is not a true boundary integral equation because of the presence of an irreducible domain integral dependent on material non-linearity. An iterative scheme accounting for that integral complements an existing time-stepping boundary element formulation [33] for solving the linear part of Eq. 14. The scheme relies on the evaluation of σ_{ij}^{NL} at internal points using Eq. 10 and the constitutive relations (1) and (4). The strains are given in terms of the displacement gradients, which are obtained by spatial differentiation of the domain displacement components given by Eq. 14 with $\kappa_{ij} = \delta_{ij}$:

$$\frac{\partial u_i(\boldsymbol{\xi},t)}{\partial \xi_l}=\int_{\Gamma}\left[\frac{\partial \tilde{u}_{ij}}{\partial \xi_l}*\mathrm{d}p_j-\frac{\partial \tilde{p}_{ij}}{\partial \xi_l}*\mathrm{d}u_j\right]\mathrm{d}\Gamma+\int_{\Omega}\frac{\partial \tilde{u}_{ij}}{\partial \xi_l}*\mathrm{d}f_j\mathrm{d}\Omega-\frac{\partial}{\partial \xi_l}\int_{\Omega}\tilde{\varepsilon}_{ijk}*\mathrm{d}\sigma_{jk}^{NL}\mathrm{d}\Omega \tag{16}$$

The small strain-displacement relations are then applied while the linear pseudo stress as well as the actual stress components are calculated using the constitutive Eqs. 1 and 4, respectively.

Differentiation of the Singular Domain Integral. The strong singularity of the kernel $\partial\tilde{\varepsilon}_{ijk}/\partial\xi_l$, whose behaviour is of order O(r^{-2}), does not allow differentiation under the domain integral sign in the third term on the right-hand side of Eq. 16. The correct expression for that gradient is derived using a method proposed by Bui [36]. Thus, the irreducible domain integral is separated into two parts,

$$\frac{\partial}{\partial \xi_l}\int_{\Omega}\tilde{\varepsilon}_{ijk}*\mathrm{d}\sigma_{jk}^{NL}\mathrm{d}\Omega=\lim_{R\to 0}\left[\frac{\partial}{\partial \xi_l}\int_{\Omega-\Omega_R}\tilde{\varepsilon}_{ijk}*\mathrm{d}\sigma_{jk}^{NL}\mathrm{d}\Omega+\frac{\partial}{\partial \xi_l}\int_{\Omega_R}\tilde{\varepsilon}_{ijk}*\mathrm{d}\sigma_{jk}^{NL}\mathrm{d}\Omega\right] \tag{17}$$

where Ω_R is a small circle of radius R, centred at the source point $\boldsymbol{\xi}$.

It can be shown that the second volume integral on the right-hand side of Eq. 17 is of the order O(R^2). The proof requires σ_{ij}^{NL} as well as its first and second partial derivatives to be continuous functions of $\mathbf{x}$ in the neighbourhood of $\boldsymbol{\xi}$. Then, a Taylor's series expansion of σ_{ij}^{NL} around $\boldsymbol{\xi}$ leads to

$$\int_{\Omega_R}\tilde{\varepsilon}_{ijk}(\mathbf{x},\boldsymbol{\xi},t)*\mathrm{d}\sigma_{jk}^{NL}(\mathbf{x},t)\mathrm{d}\Omega=R^2D_{ijkm}(t)*\mathrm{d}\sigma_{jk}^{NL}{}_{,m}(\boldsymbol{\xi},t) \tag{18}$$

where $D_{ijkm}(t)$ are linear combinations of $A(t)$ and $B(t)$, independent of $\boldsymbol{\xi}$. Hence the spatial derivatives of the right-hand side of Eq. 18 are expressed in terms of second partial derivatives of σ_{ij}^{NL} and therefore vanish as $R\to 0$.

Since Ω_R depends on $\boldsymbol{\xi}$, differentiation of the first domain integral on the right-hand side of Eq. 17 produces an additional convective term. Thus

$$\frac{\partial}{\partial \xi_l}\int_{\Omega-\Omega_R}\tilde{\varepsilon}_{ijk}*\mathrm{d}\sigma_{jk}^{NL}\mathrm{d}\Omega=\int_{\Omega-\Omega_R}\frac{\partial \tilde{\varepsilon}_{ijk}}{\partial \xi_l}*\mathrm{d}\sigma_{jk}^{NL}\mathrm{d}\Omega-\int_{\Gamma_R}n_l\tilde{\varepsilon}_{ijk}*\mathrm{d}\sigma_{jk}^{NL}\mathrm{d}\Gamma \tag{19}$$

where Γ_R is the periphery of the circle with radius R and $\mathbf{n}$ is the outward unit normal to that circle. Using the formulas [37]

$$\int_{\Gamma_R}r_{,i}\,r_{,j}\,\mathrm{d}\Gamma=\pi R\delta_{ij},\quad\int_{\Gamma_R}r_{,i}\,r_{,j}\,r_{,k}\,r_{,l}\,\mathrm{d}\Gamma=\frac{\pi R}{4}(\delta_{ij}\delta_{kl}+\delta_{ik}\delta_{jl}+\delta_{il}\delta_{jk}) \tag{20}$$

the last convective term on the right-hand side of Eq. 19 is transformed to

$$\int_{\Gamma_R}n_l\tilde{\varepsilon}_{ijk}*\mathrm{d}\sigma_{jk}^{NL}\mathrm{d}\Gamma=-\frac{1}{8}A(t)*\mathrm{d}\sigma_{il}^{NL}(\boldsymbol{\xi},t)+\frac{1}{16}B(t)*\mathrm{d}\sigma_{jj}^{NL}(\boldsymbol{\xi},t)\delta_{il} \tag{21}$$

that is, a sum of simple convolution integrals.

As $R\to 0$, the first integral on the right-hand side of Eq. 19 becomes the Cauchy principal value of the singular integral, whose existence has been proved and the method to evaluate it is presented next. The strain components corresponding to $\tilde{u}_{ij}$ and their gradients are obtained by successive differentiation of Eq. 15.

Evaluation of the Cauchy Principal Value. The domain integral on the right-hand side of Eq. 19 is evaluated by dividing the domain into cells, that is, two-dimensional subdomains Ω_c bounded by contours Γ_c. The integration is performed over each cell using an approximate model for the unknown σ_{ij}^{NL}. The radial integration method [37] was used to evaluate the Cauchy principal value of that integral over the cell containing the source point. The integration over all other cells was performed using numerical quadrature.

The domain integral on the right-hand side of Eq. 19 can be expressed as

$$\int_{\Omega_c} \frac{\partial \tilde{\varepsilon}_{ijk}(\mathbf{x},\boldsymbol{\xi},t)}{\partial \xi_l} * \mathrm{d}\sigma_{jk}^{NL}(\mathbf{x},t)\mathrm{d}\Omega = \left[\int_{\Omega_c} \frac{\partial \tilde{\varepsilon}_{ijk}(\mathbf{x},\boldsymbol{\xi},t)}{\partial \xi_l}\mathrm{d}\Omega\right] * \mathrm{d}\sigma_{jk}^{NL}(\boldsymbol{\xi},t)$$

$$+ \int_{\Omega_c} \frac{\partial \tilde{\varepsilon}_{ijk}(\mathbf{x},\boldsymbol{\xi},t)}{\partial \xi_l} * \left[\mathrm{d}\sigma_{jk}^{NL}(\mathbf{x},t) - \mathrm{d}\sigma_{jk}^{NL}(\boldsymbol{\xi},t)\right]\mathrm{d}\Omega \tag{22}$$

The strong singularity persists in the first integral on the right-hand side of Eq. 22 while the second integral can be shown to be regular and therefore evaluated by standard numerical schemes. A polar coordinate system (r, θ) is defined with the origin at the source point $\boldsymbol{\xi}$. It can be shown that, relative to this system, the singular integral on the right-hand side of Eq. 22 can be transformed to

$$\int_{\Omega_c} \frac{\partial \tilde{\varepsilon}_{ijk}(\mathbf{x},\boldsymbol{\xi},t)}{\partial \xi_l}\mathrm{d}\Omega = \int_{\Gamma_c}\left[\frac{1}{r}\frac{\partial r}{\partial n}\right]_{\Gamma} \psi_{ijkl}(\theta,t)\int_0^{r(\Gamma)}\frac{\mathrm{d}r}{r}\mathrm{d}\Gamma \tag{23}$$

where

$$\frac{\partial \tilde{\varepsilon}_{ijk}}{\partial \xi_l} = \frac{1}{r^2}\psi_{ijkl}(\theta,t)$$

Since the integration is carried out in the Cauchy principal value sense, a small circle of radius R around the singular point $\boldsymbol{\xi}$ can be cut off. Thus, Eq. 23 becomes,

$$\int_{\Omega_c-\Omega_R} \frac{\partial \tilde{\varepsilon}_{ijk}(\mathbf{x},\boldsymbol{\xi},t)}{\partial \xi_l}\mathrm{d}\Omega = \int_{\Gamma_c}\left[\frac{\ln r}{r}\frac{\partial r}{\partial n}\right]_{\Gamma} \psi_{ijkl}(\theta,t)\mathrm{d}\Gamma + \ln R\int_0^{2\pi}\psi_{ijkl}(\theta,t)\mathrm{d}\theta \tag{24}$$

where $\partial r/\partial n = -1$ has been used in the second integral along the circle Γ_R. Using relations (20), it can be shown that the last integral on the right-hand side of Eq. 24 is identical to zero; this is an intrinsic property of ψ_{ijkl}. Hence, as $R \to 0$, Eq. 24 becomes

$$\int_{\Omega_c} \frac{\partial \tilde{\varepsilon}_{ijk}(\mathbf{x},\boldsymbol{\xi},t)}{\partial \xi_l}\mathrm{d}\Omega = \int_{\Gamma_c}\left[\frac{\ln r}{r}\frac{\partial r}{\partial n}\right]_{\Gamma} \psi_{ijkl}(\theta,t)\mathrm{d}\Gamma \tag{25}$$

Now the strongly singular domain integral has been transformed into a boundary integral. Since the source point is located inside the domain, no singularity occurs and standard Gaussian quadrature formulas can be used to calculate this integral.

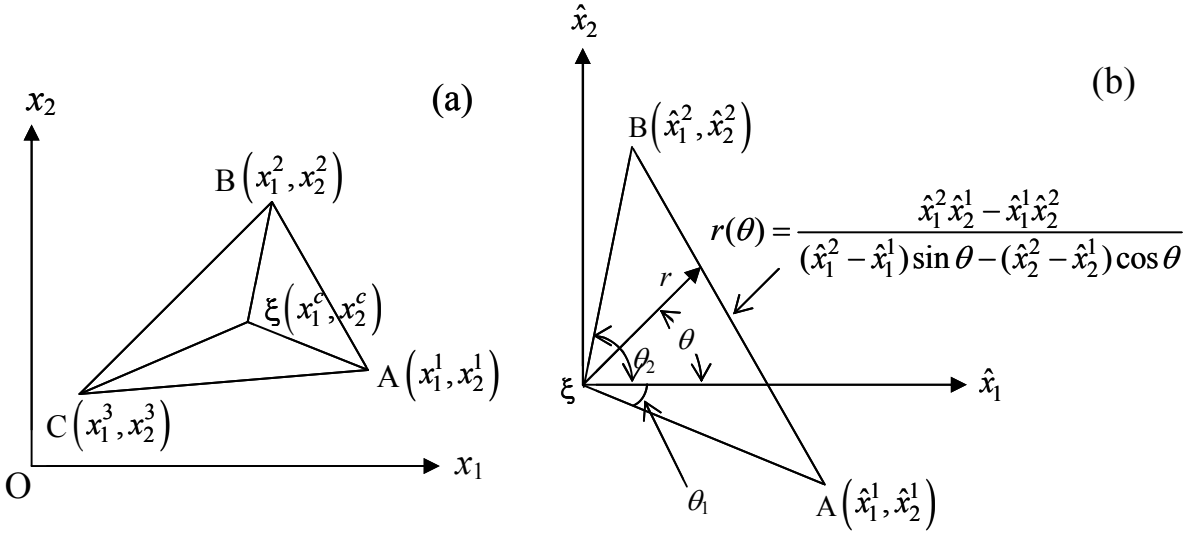

Figure 1 Triangular cell (a) and polar coordinate system with origin at the singular point ξ (b)

The domain was divided into small triangular cells, such as the one shown in Fig. 1(a), with the source point ξ at the centre of the triangle. Relative to a polar frame of reference with origin at the centre of the triangle, the equation of side A($\hat{x}_i^1$)-B($\hat{x}_i^2$) of the triangle, shown in Fig. 1(b), can be expressed in terms of the local corner co-ordinates $\hat{x}_i^j = x_i^j - \xi_i$, where x_i^j are the co-ordinates of corner *j*.

Thus, in this case, the contour integral on the right-hand side of Eq. 25 is evaluated along each side of the triangle. Adopting a 'constant' cell model for σ_{jk}^{NL}, the stress difference in Eq. 22 vanishes and therefore

$$\int_{\Omega_c} \frac{\partial \tilde{\varepsilon}_{ijk}(\mathbf{x},\xi,t)}{\partial \xi_l} * \mathrm{d}\sigma_{jk}^{NL}(\mathbf{x},t)\mathrm{d}\Omega = \left[\sum \int_{\theta_m}^{\theta_n} \ln[r(\theta)]\psi_{ijkl}(\theta,t)\mathrm{d}\theta\right] * \mathrm{d}\sigma_{jk}^{NL}(\xi,t) \tag{26}$$

The integrals on the right-hand side of Eq. 26 are calculated using the standard Gaussian quadrature formulas.

Numerical Algorithm

Constant boundary elements were used in the present numerical implementation of BEM formulation based on integral Eq. 14, which also requires modelling in the time dimension. If the boundary surface Γ is discretised in E elements Γ_e, the following representation can be adopted,

$$u_j(\mathbf{x},t) = u_j^e(t), \quad p_j(\mathbf{x},t) = p_j^e(t) \tag{27}$$

where $u_j^e(t)$ and $p_j^e(t)$ are the time dependent nodal values of displacement and traction, respectively. Over a cell, strain was modelled as uniform and, as a consequence of Eqs. 1, 4, 6 and 7, the shift factor as well as both linear and non-linear contributions to the stress are also constant within each cell.

It was assumed that the boundary variables $u_i(x,t)$ and $p_i(x,t)$ as well as the nonlinear part of total stress $\sigma_{jk}^{NL}(\mathbf{x},t)$ in the domain are linear with respect to time t within a small time step $\Delta t_\kappa = t_\kappa - t_{\kappa-1}$. The viscoelastic fundamental solutions were written in the general form:

$$\tilde{u}_{ij} = b_{ij}^0 + \sum_{n=1}^{N} b_{ij}^n \mathrm{e}^{-\beta_n t}, \ \tilde{p}_{ij} = a_{ij}^0 + \sum_{m=1}^{M} a_{ij}^m \mathrm{e}^{-\alpha_m t}, \ \tilde{\varepsilon}_{ijk} = c_{ijk}^0 + \sum_{q=1}^{Q} c_{ijk}^q \mathrm{e}^{-\gamma_q t} \tag{28}$$

where the coefficients a_{ij}^m, b_{ij}^n and c_{ijk}^q are spatial functions of $r = |\mathbf{x} - \boldsymbol{\xi}|$. Then, the discretised form of Eq. 14 was obtained as

$$\kappa_{ij}(\xi)u_i^{(K)}(\xi) = \sum_{n=0}^{N} B_j^{n(K)}(\xi) + \sum_{\kappa=1}^{K}\sum_{n=1}^{N}[B_j^{n(\kappa-1)}(\xi)\mathrm{e}^{-\beta_n(t_K - t_\kappa)}(\mathrm{e}^{-\beta_n \Delta t_\kappa} - 1)]$$

$$-\sum_{m=0}^{M} A_j^{m(K)}(\xi) - \sum_{\kappa=1}^{K}\sum_{m=1}^{M}[A_j^{m(\kappa-1)}(\xi)\mathrm{e}^{-\alpha_m(t_K - t_\kappa)}(\mathrm{e}^{-\alpha_m \Delta t_\kappa} - 1)]$$

$$-\sum_{q=0}^{Q} C_j^{q(K)}(\xi) - \sum_{\kappa=1}^{K}\sum_{q=1}^{Q}[C_j^{q(\kappa-1)}(\xi)\mathrm{e}^{-\gamma_q(t_K - t_\kappa)}(\mathrm{e}^{-\gamma_q \Delta t_\kappa} - 1)] \tag{29}$$

where, for simplicity, the body force was assumed to be zero and

$$A_i^{m(\kappa)}(\xi) = \int_\Gamma a_{ij}^m u_j^{(\kappa)} \mathrm{d}\Gamma\,,\ B_i^{n(\kappa)}(\xi) = \int_\Gamma b_{ij}^n p_j^{(\kappa)} \mathrm{d}\Gamma\,,\ C_i^{q(\kappa)}(\xi) = \int_\Omega c_{ijk}^q \sigma_{jk}^{NL(\kappa)} \mathrm{d}\Omega$$

$$u_i^{(\kappa)}(\mathbf{x}) = u_i(\mathbf{x}, t_\kappa)\,,\ p_i^{(\kappa)}(\mathbf{x}) = p_i(\mathbf{x}, t_\kappa)\,,\ \sigma_{jk}^{NL(\kappa)}(\mathbf{x}) = \sigma_{jk}^{NL}(\mathbf{x}, t_\kappa)$$

An iterative scheme is proposed for solving Eq. 29 since the current values of the stresses σ_{jk}^{NL} are not known at the beginning of a time step. At the first iteration, the boundary displacements and tractions are determined at time $t = t_\kappa$ assuming $\sigma_{jk}^{NL}(t_\kappa) = \sigma_{jk}^{NL}(t_{\kappa-1})$. Then displacement gradients are determined from Eq. 16 leading to initial estimates of domain strains and subsequently of stresses through constitutive Eqs. 1 and 4. The value of the domain integral can thus be revised and the procedure repeated until results from two successive iterations agree within an acceptable tolerance. Convergence of boundary displacements was the adopted criterion for terminating the iteration. This was assumed to occur when

$$\left|\frac{u^i - u^{i-1}}{u^i}\right| \le 0.0001$$

where u^i is any nodal displacement at iteration i.

It should be noted that, at $t = 0$ all unknown boundary values can be calculated when the integral Eq. 14 governs only the initial elastic response due to any non-zero initial values of the boundary or loading conditions. At the following time $t = t_1$ (step $\kappa = 1$), the respective unknown boundary values can be obtained from Eq. 29 with the current boundary conditions and the additional terms depending on the solution at the initial step as well as the non-linear contribution of the current step. The solution progresses to the next time step $\kappa = 2$ in a similar manner and a step-wise procedure is thus established which advances the solution until the final time step is reached. A suite of FORTRAN programs was developed for implementing this formulation. The code has already been tested and found to be reliable in the case of linear viscoelastic problems [29, 33].

Crack tip stresses

Specimen Geometry and Material Model. The developed non-linear analysis was applied to a cracked rectangular plate under step tension $\sigma_0 H(t)$. The central crack was oriented along the x_1-axis. The input data are approximately the same as those used by Moran and Knauss [14] who solved this problem using FEM. Due to symmetry relative to two orthogonal axes, only a quarter of the plate was modelled. The plate half-width was 13.44 mm, half-height 12 mm, and the crack half-length a = 1 mm. The material behaviour was represented by a standard linear solid model in shear

$$\mu(t) = \mu_0[\lambda + (1 - \lambda)e^{-\eta t}]$$

with $\mu_0 = 4800$ MPa, $\eta = 0.4$ and a constant Poisson's ratio $\nu = 1/3$. Parameter λ represents the ratio of the long-term to initial relaxation modulus. A constant Poisson's ratio means that bulk and Young's moduli have the same time dependence as the shear modulus. Plane strain conditions were assumed; this simplifies the evaluation of the volumetric strain.

In order to calculate ϕ using Eq. 7, v_0 was assumed to be 0.01, and b was chosen equal to 0.05. These values are representative of a moderately strain-softening polymer [14]. A remote tension $\sigma_{22} = \sigma_0 = 0.001E(0)$ was applied, where $E(0)$ is the initial value of the tensile relaxation modulus.

Boundary and Domain Meshing. 'Constant' boundary elements with variable element length were adopted. The two smallest elements, located on either side of the crack tip, were 0.005 mm long, the largest element at the loading edge of the plate was 3 mm long. In conformity with the boundary mesh, the domain mesh was arranged to be much denser near the crack tip, where the stress concentration and high nonlinearity occur.

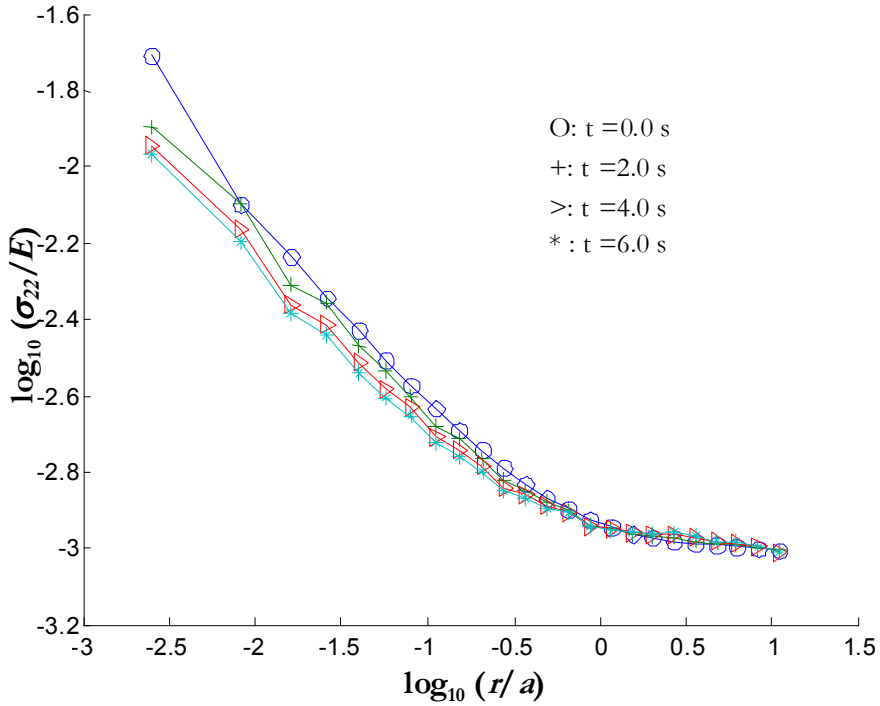

Figure 2. Normalized nonlinear stress field near the crack tip ($\lambda = 0.1$)

Nonlinear Stress Field. Fig. 2 shows the normalized nonlinear stress field near the crack tip for $\lambda = 0.1$. In a linear viscoelastic plate with a constant Poisson's ratio under step loading, the stress field has a constant time history. For nonlinear viscoelastic problems, the material undergoes considerable strain softening around the crack tip, where the high stress and strain occur. As shown in Fig. 2, the initial singular elastic response causes an instantaneous reduction in viscosity and the σ_{22} stress near the crack tip drops with time due to the strain softening; this drop slows down with time becoming less significant as the strain itself changes more slowly. The stresses far from the crack tip increase in order that overall equilibrium is satisfied. This response is similar to that predicted by FEM [14].

The program was also run with the parameter λ changed to 0.001 implying a more pronounced material time-dependence than originally assumed. From the respective results shown in Fig. 3, it was clear that the effect of nonlinearity was stronger than previously under the same loading conditions. A more significant nonlinear effect was predicted by FEM [14] but this was essentially due to the application of a much higher load in that analysis.

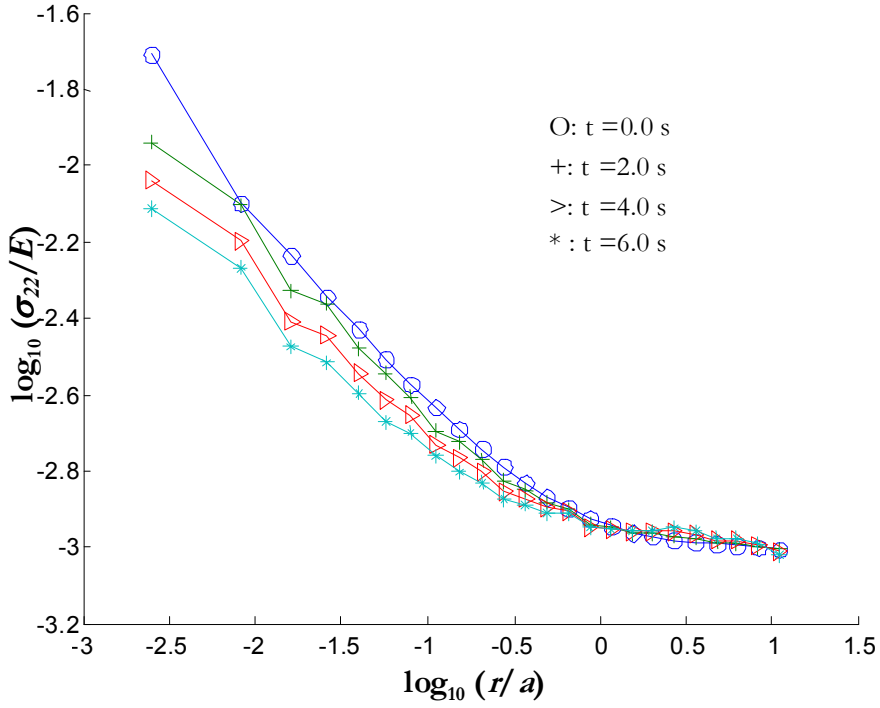

Figure 3. Normalized nonlinear stress field near the crack tip ($\lambda = 0.001$)

Concluding Remarks

A promising initial attempt has been made to apply a nonlinearly viscoelastic BEM formulation and the associated computer code to the solution of fracture mechanics problems. The numerical results obtained confirmed the expected effect of non-linearity on the stress time history, which is highest in the neighbourhood of the crack tip. They were also consistent with those reported in a previous analysis of the same problem by FEM [14]. It was noted in that study that, for materials with high viscosity ($\lambda = 0.001$), a very refined, computationally expensive mesh is required to capture the area of *K*-dominance around the crack tip. Although a domain mesh is required by the proposed BEM approach, this does not introduce any additional unknowns. Therefore, the boundary mesh can be very refined near the crack tip and thus provide reliable stress output there even in the case of highly strain-softening polymers.

The current implementation of the formulation needs to be improved to enhance the confidence in its validity and reliability. This would involve mesh sensitivity studies to establish the convergence of key results. Although the adopted boundary and domain mesh was considered acceptable for an initial assessment of the performance of the proposed method, boundary element and domain cell size distribution around the crack tip may not have been ideal for capturing the local stress concentration. Such mesh refinements may also remove an observed degree of inconsistency between the calculated boundary tractions and domain stresses. In order to explain the current discrepancy between BEM and FEM predictions, further comparisons with experimental and other numerical or analytical results should be made.

Numerical tests using the validated model can help to assess the sensitivity of the singular stress fields to various material input and solution control parameters. As shown previously in the case of LVFM [29], the proposed BEM formulation can also prove to be a very reliable and efficient numerical tool for the calculation of key fracture parameters, such as energy release rates and *J*-like integrals [18], characterising crack initiation and growth in nonlinear viscoelastic solids.

References

[1] W. G. Knauss: Appl. Mech. Rev., Vol. 26, (1973), p. 1

[2] H. K. Mueller and W. G. Knauss: J. Appl. Mech.-Trans. ASME, Vol. 38, (1971), p. 483

[3] R. A. Schapery: Int. J. Fract., Vol. 11, (1975), p. 141

[4] R. A. Schapery: Int. J. Fract., Vol. 11, (1975), p. 369

[5] R. A. Schapery: Int. J. Fract., Vol. 11, (1975), p. 549

[6] R. M. Christensen: Int. J. Fract., Vol. 15, (1979), p. 3

[7] R. M. Christensen and E. M. Wu: Eng. Fract. Mech., Vol. 14, (1981), p. 215

[8] K. Ogawa, A. Misawa and M. Takashi: Int. J. Fract., Vol. 93, (1998), p. 209

[9] D. Gutierrez-Lemini: Int. J. Fract., Vol. 113, (2002), p. 27

[10] R. A. Schapery: Polym. Eng. Sci., Vol. 9, (1969), p. 295

[11] L. W. Morland and E. H. Lee: Trans. Soc. Rheol., Vol. 4, (1960), p. 233

[12] W. G. Knauss and I. J. Emri: Comput. Struct., Vol. 13, (1981), p. 123

[13] W. G. Knauss and I. Emri: Polym. Eng. Sci., Vol. 27, (1987), p. 86

[14] B. Moran and W. G. Knauss: J. Appl. Mech.-Trans. ASME, Vol. 59, (1992), p. 95

[15] A. Wineman and R. Kolberg: Int. J. Non-Linear Mech., Vol. 32, (1997), p. 863

[16] P. J. Dooling, C. P. Buckley and S. Hinduja: Polym. Eng. Sci., Vol. 38, (1998), p. 892

[17] R. A. Schapery: Int. J. Solids Struct., Vol. 37, (2000), p. 359

[18] R. A. Schapery: Int. J. Fract., Vol. 42, (1990), p. 189

[19] W. G. Knauss and G. U. Losi: J. Appl. Mech.-Trans. ASME, Vol. 60, (1993), p. 793

[20] J. Mackerle: Model. Simul. Mater. Sci. Eng., Vol. 5, (1997), p. 615

[21] J. G. J. Beijer and J. L. Spoormaker: Comput. Struct., Vol. 80, (2002), p. 1213

[22] S. Syngellakis: Eng. Anal. Bound. Elem., Vol. 27, (2002), p. 125

[23] S. Syngellakis and J. Wu, in: *Advances in Boundary Element Techniques X*, edited by E.J. Sapountzakis and M.H. Aliabadi, EC Ltd, Eastleigh (2009).

[24] J. Sladek, J. Sumec and V. Sladek: Ingenieur Archiv, Vol. 54, (1984), p. 275

[25] B. N. Sun and C. C. Hsiao: Comput. Struct., Vol. 30, (1988), p. 963

[26] D. Polyzos, A. A. Stamos and D. E. Beskos: Commun. Numer. Meth. Eng., Vol. 10, (1994), p. 81

[27] S. S. Lee and Y. J. Kim: Eng. Fract. Mech., Vol. 51, (1995), p. 585

[28] S. S. Lee and N. H. Kim: Key Eng. Mater., Vol. 297-300, (2005), p. 2240

[29] S. Syngellakis and H. W. Wu: Eng. Fract. Mech., Vol. 75, (2008), p. 1251

[30] C. P. Providakis: Eng. Fract. Mech., Vol. 70, (2003), p. 707

[31] H. Gun: Eng. Anal. Bound. Elem., Vol. 29, (2005), p. 749

[32] E. Pineda and M. H. Aliabadi: Key Eng. Mater., Vol. (2008), p. 109

[33] S. Syngellakis and J. W. Wu: Eng. Anal. Bound. Elem., Vol. 28, (2004), p. 733

[34] M. E. Gurtin and E. Sternberg: Arch. Ration. Mech. Anal., Vol. 11, (1962), p. 291

[35] F. Hartmann, in: *New Developments in Boundary Element Methods*, edited by C.A. Brebbia, Butterworths, London (1980).

[36] H. D. Bui: Int. J. Solids Struct., Vol. 14, (1978), p. 935

[37] X. W. Gao and T. G. Davis: Int. J. Solids Struct., Vol. 37, (2000), p. 4987

Keywords Index

Authors Index